ECOLE
POLYTECHNIQUE
DE BRUXELLES

ULB

UNIVERSITÉ LIBRE DE BRUXELLES

Experimental and numerical analysis of a Pump as Turbine (PaT) in micro Pumped Hydro Energy Storage (μ-PHES)

A thesis submitted to obtain the academic degree of
Doctor of Engineering Sciences and Technology

Alessandro Morabito

Supervisor
Professor Patrick Hendrick

Departement
Aero-Thermo-Mechanics

Academic year
2020 - 2021

Abstract

In the last decade, the power generation mix and the energy markets have been affected by the growing development of distributed and renewable energy sources. Nevertheless, a significant drawback of solar and wind energy is their intermittent and weather-dependent production, which often leads to a mismatch between renewable energy production and its use. Thus, the need for energy storage is recently emerging and becoming more relevant in this era of the energy transition.

Among several technologies, today, pumped hydro energy storage (PHES) represents the largest share of the energy storage systems in the world. However, possible new investors, who might be attracted by potential profit in PHES, are repelled by the long payback period and the scarcity of adequate site topology for such power plants. Relevant design decisions can be taken to reduce the costs and improve the performance or to escape the PHES topographical requirements. For this reason, the first part of this PhD thesis reviews and provides potential assessments of some unconventional PHES systems, applied in synergy with existing infrastructures. Such is the standpoint of micro facilities near waterway locks, or underground cavities used as lower reservoirs (UPSH), or the use of pump-turbines at variable geometry to cope with fluctuating loads. Moreover, important information on PHES in micro-scale is largely missing and their potential in distributed energy systems still needs to be unveiled. In the attempt to fill this gap, this thesis provides a techno-economic overview of the design and characterization of a first-of-its-kind PHES micro facility. In micro-scales hydropower projects, the initial capital cost of a conventional hydroelectric unit is hard to be determined and often economically prohibitive. Interestingly, in order to cut the total capital investment, the micro-PHES prototype runs with a single centrifugal pump for both pumping and generating phases and exploits existing stormwater reservoirs. The variable speed regulation is also implemented and it allows the pump to constantly operate at the maximum hydraulic efficiency in order to deal with load variations. In the same way, the pump working in reverse, namely pump as turbine (PaT), runs at the most suitable speed and it keeps a high efficiency over a wide load range. In addition, the analysis of the techno-economic parameters for such a system provides an important dataset for micro-PHES feasibility breakdown.

PaTs are a legitimate cost-effective option in micro hydropower but an universal performance prediction does not exist. Their hydraulic efficiency can possibly shift from the higher efficiency of traditional hydraulic turbines. Nowadays, these reasons restrict PaTs exploitation. In this thesis, a multivariate regression method is applied to the CFD results to build a surrogate model of the PaT hydraulic characteristics as a function of the cutwater geometrical modifications. Based on this model, an optimization problem is solved to identify the most advantageous geometrical asset of the PaT cutwater to maximize the hydraulic efficiency. The presented methodology and design optimization of the cutwater in PaTs, which are extremely suited to our current energy generation needs, provides a unique and much sought guide to its performance, improvements, and adaptation to hydropower.

Acknowledgments

First and foremost, I would like to thank my supervisors, Prof. Patrick Hendrick. Thank you very much for your support over these past years at ULB-ATM and for having given me many opportunities to expand my knowledge and to build confidence in my abilities.

I would like to show gratitude and credits to all my co-authors for their precious inputs to the final version of our publications. I am also grateful to members of my PhD committee for constructive comments and suggestions: Prof. Alessandro Parente, Prof. Michel Huart, Dr. Elena Vagnoni, Prof. Pal-Tore Selbo Storli, Prof. Koen Hillewaert, and Dr. Francois Gruselle.

I'd also like to thank for their collaboration the following people and institutions:

- Prof. André Mesquita and Mr. Gilton Furtado of the Laboratory of Fluid Dynamic and Particulate (FluidPar) at Federal University of Pará, Brazil, for involving me in the study of their research facility in Tucuruì.
- Agence de Développement Territorial (IDETA), for trusting my engineering design decisions for the energy storage installation at the *Quartier Negundo* in Froyennes, Belgium.
- Dr. Elena Vagnoni of Laboratory for Hydraulic Machines at École polytechnique fédérale de Lausanne (EPFL) for inviting me in her Lab, for her advice, and for her contribution with SIMSEN software and optimisation techniques.

Getting through my dissertation required more than academic support, and I have many, many people to thank for listening to and, at times, take my mind off. In addition, a special thanks goes to Marzio, l'elegantone.

To my whole family, my parents and my brother, who have supported me even if I doubt they were fully aware of what my job tasks were. To my daughter, who's just joined us but she's already my limitless power supply. Most importantly, none of this could have happened without my soon-to-be wife Cristina: thank you for your patience, your endless support and your ardent love.

Contents

List of Figures

List of Tables

Nomenclature

Latin symbols

a_0	Guide vane opening	mm
A	Cutwater inclination angle	deg
b	Passage depth	m
B	Systematic error	-
c	Absolute velocity	m/s
c_{mix}	Celerity of the sound in a fluid mixture	m/s
C	Cost	€
C_d	Discharge coefficient	-
Cp	Static pressure coefficient	-
d	Yearly discount rate	-
dx	Average element size	m
D	Diameter	m
e	Specific hydraulic energy	J/kg
E	Energy	kWh
f	Grid frequency	Hz
g	Gravitational acceleration	m/s^2
h	Head ratio	-
h_i	Hinge function factor	-
H	Head	m
i	Incidence deviation	deg
k_i	Constant	-
K	Project duration	year
L	Length	m
m	Mass flow rate	kg/s
M	Torque	Nm
n	Rotational frequency	rot/s
np	Number of poles in a generator	-
n_{11}	Unit speed	-
N	Rotational speed	rpm
N_s	Specific speed	rpm, m^3/s, m
p	Pressure	Pa
P	Power	kW
q	Discharge ratio	-
Q	Discharge	m^3/s
Q_{11}	Unit discharge	-
r	Nominal cutwater radius	mm
R	Radius	m
Re	Reynolds number	-

S	Cutwater stretching	m
t	Time	s
u	Peripheral velocity	m/s
U	Uncertainty	-
v	General speed vector	m/s
V	Volume	m^3
V_r	Energy loss fraction	-
w	Relative velocity	m/s
W	Direction flow	-
y^+	Non-dimensional wall distance	-
z	Number of blades	-
Z	Altitude	m

Greek symbols

α	Absolute velocity angle	deg
β	Relative velocity angle	deg
γ	Blade pivot angle	deg
η	Efficiency	-
Θ	Angular coordinate	deg
λ	Blade inclination	deg
Λ	Domain	-
μ	Dynamic viscosity	Pa s
ν	Dimensionless turbine specific speed	-
ξ	Efficiency ratio	-
π	Power number	-
ρ	Density	kg/m^3
σ	Thoma number	-
τ	Slip coefficient	-
φ	Discharge number	-
ψ	Correction coefficent	-
ω	Angular speed	rad/s
Ω	Rotational speed ratio	-
Ψ	Specific energy coefficient	-

Subscripts

11	Unit factor
1	Pump inlet
2	Pump outlet
a	Available
ad	Normalised value
CFD	Numerical
cr	Critical
$curt$	Curtailment
exp	Experimental
eff	Effective
fit	Fitting
g	Geodetic
geo	Geometrical
h	Hydraulic
i	Index
in	Injected
l	Loss
L	Liquid
m	Mechanic
m	Meridional
max	Maximum
min	Minimum
md	Model
n	Nominal
opt	Optimal
p	Pump
pty	Prototype
r	Radial
rw	Runaway
syt	System
t	Turbine
th	Theoretic
u	Circumferential direction
v	Volumetric
vp	Vapour
vol	Volumetric

Acronyms

AGV	Adjustable Guide Vanes
AR	Aspect Ratio
ATM	Aero-Thermo-Mechanics
BEP	Best Efficiency Point
BF	Basis Function
CAD	Computer Aided Design
CFD	Computational Fluid Dynamic
CFL	Courant-Friedrich-Levy number
CPU	Central Processing Unit
DES	Decentralized energy sources
DNIT	National Department of Transport Infrastructure
DSO	Distribution system operator
EEX	European Energy Exchange
EES	Electrical Energy Storage
ER	Expansion Ratio
EWF	Extended Wall Function
FEA	Finite Element Analysis
FS	Factor of safety
HGS	Hydraulic Gravity Storage
IDETA	Agence de Développement Territorial
LCOE	Levelised Cost Of Energy
LCOS	Levelized Cost of Storage
MARS	Multivariate Adaptive Regression Spline
MTBF	Mean Time Between Failures
NPV	Net Present Value
OPEX	Operating Expense
O&M	Operations and Maintenance
PaT	Pump as Turbine
PHES	Pumped Hydro Energy Storage
μ-PHES	Micro Pump Hydro Energy Storage
PLC	Programmable Logic Controller
PV	PhotoVoltaic
RES	Renewable Energy Source
RPT	Reversible Pump-Turbine
SA	Spalart-Allmaras model
SPS	Seawater Pump Storage
SST	Shear Stress Transport
TSO	Transmission System Operator
UPHS	Underground Pumped-Storage Hydroelectricity
UPS	Uninterruptible Power Supply
VFD	Variable Frequency Drive

Chapter 1

Introduction

1.1 Context and motivation

The penetration of variable-renewable energy sources (RESs) (e.g. wind and solar) into power grids is constantly growing [IEA 2020]. Balancing these energy injections is a crucial topic in the energy industry all over the world [Matsuo *et al.* 2020]. Due to the flexible and rapid power adjustment of the hydraulic machinery [Pérez-Díaz *et al.* 2015, Chang *et al.* 2013], conventional hydropower plants, as well as the pumped storage, have traditionally been undertaking a large portion of the regulation and balancing tasks in many power systems [Kocaman & Modi 2017]. Research and implementation of the joint operation of hydro and RES have become more common, such as in hydro-wind [Levieux *et al.* 2019, Bueno & Carta 2006], hydro-photovoltaic [Zhang *et al.* 2019, Stoppato *et al.* 2016], and hydro-solar-wind hybrid power systems [Xu *et al.* 2019, Lian *et al.* 2019, Javed *et al.* 2020, Sun *et al.* 2019].

The operational mechanisms of storage and generation of pumped hydro energy storage (PHES) plants add significant advantages in increasing the economic benefits and availability of variable-RES [Kocaman & Modi 2017, Lian *et al.* 2019]. Specifically, the phenomenon of over-production commonly occurs in the electricity supply of oversized RESs. A combined operation with PHES enables the energy that exceeds the instant demand to be stored instead of curtailed. The reserve of energy can be used for tackling power shortages in load peak periods [e Silva & Hendrick 2016] and, for this reason, recently, the excellent complementarity with variable RES has promoted the use of advanced hydro-equipment [Bueno & Carta 2006].

Nevertheless, the widely implemented fixed-speed pumped storage plant, cannot regulate power flows under pumping operations due to their rigid operating characteristics. In this case, the pumping or generating systems cannot continuously afford the duty of mitigating the load variation, which may extremely influence the reliability of the power supply for the RES-PHES hybrid power system [Pérez-Díaz *et al.* 2015, Chazarra *et al.* 2018]. Moreover, RES are spreading in our surroundings, delivering today a vivid feeling of energy independence and environmental care and, with them, micro-distributed energy generation systems are expected to grow in this renewed energy industry [European Commission 2012a, IEA 2020]. In this context, the challenge of responsive and effective pumped storage and hydropower plants calls for flexible and high performance systems at rather

low cost of energy.

Among the several components of a hydropower plant, the turbomachinery group is the very heart of the energy production system and thus its flexibility grade affects the whole system yield. Another challenge for the turbomachine is to provide good efficiency in part load and it can be overcome by using variable-speed or variable-geometry technology, which would, nonetheless, raise the system's complexity and costs [Jain *et al.* 2015, Ciocan *et al.* 2012]. Besides, the turbine and pump efficiencies are crucial for the investment economic return of the power plant [Deane *et al.* 2010, Pugliese *et al.* 2016]. The selection of the right type of turbine for given site conditions is one of the most important factors influencing efficiency and cost. Hydraulic turbines have indeed high costs due to their punctual design and performance testing. Electromechanical elements represent between 20 - 35% of the total investment of the plant [Binama *et al.* 2017], but it can reach higher values (70%) in certain projects, where civil engineering costs are reduced by on-site pre-existing infrastructures [Binama *et al.* 2017, Jain & Patel 2014]. However, in micro scales hydropower projects, only the initial capital cost of a conventional Francis turbine generating set is often prohibitive and hard to fund [Giosio *et al.* 2015].

An effective method to shorten the costs in turbomachinery in the small-scale hydropower is the implementation of centrifugal or diagonal pumps in reversed mode instead of conventional turbines. The major benefit in using a pump as turbine (PaT) is that mass production of pumps means that they are comparatively much more cost-effective than conventional turbines [Binama *et al.* 2017, Jain & Patel 2014, Baumgarten & Guder 2005]. Pumps are massed-produced and have low initial and maintenance costs but ready availability [Motwani *et al.* 2013]. However, their performance in reverse mode is difficult to predict and, generally, they operate at a lower efficiency. Furthermore, pumps for industrial applications are not meant to run in reverse mode (opposite flow direction and rotational speed) and their performance can shift appreciably from the higher efficiency of traditional hydraulic turbines.

Many attempts have been studied and engineered to bring performance improvements in using PaTs and the hardest challenge is to hand over a considerable gain in efficiency without spoiling the outstanding cost-effectiveness of PaTs. Another possible practise in cutting down the costs for hydropower and PHES plants is given by using pre-existing structures such as natural/artificial ground conformations, or waterways locks, to set pressure head, or underground cavities, to exploit a large available capacity.

For these reasons, in the framework of the SMARTWATER project, the collaboration between the Aero-Thermo-Mechanics (ATM) department of Université libre de Bruxelles (ULB) and the Agence de Développement Territorial (IDETA) built a unique micro-pumped hydro energy storage (μ-PHES) prototype and study its performance. To its fullest, the SMARTWATER project generated some investigation tools to assess the feasibility of the rehabilitation of end-of-life quarries and mines into medium-sized PHES units. The experimental investigation presented in this PhD thesis was conducted in the facility designed and built in the framework of the

SMARTWATER project. This system benefits from using technical and material synergies that have not been discussed together before: it is equipped with a single pump for generating and storing energy, it runs with variable speed control integrated into a smart-grid scenario, and the use of a pre-existing storm-water basin as PHES reservoirs produces a relevant expense cut that endorses the μ-PHES economic accessibility. In this context, the study on PHES plants presented in this PhD thesis and the analysis of a real-life application contribute to the discussion of μ-PHES opportunity and enhance its optimisation alternatives.

1.2 Thesis objectives and strategy

The objective of this thesis is directed towards the experimental and numerical analysis of PaTs for assessing their potential measure in μ-PHES and providing a geometrical optimisation methodology to improve their efficiency for hydropower in respect of their economic advantage. The framework of this PhD thesis research objectives are introduced by the analysis of PHES technology and its economic in multiple sites, where it poses significant opportunities for energy management of decentralised systems, underground reservoirs and micro applications. Therefore, an experimental investigation is carried out on a new PHES installation to retrieve real data and evaluate the control measures of the installed PaT under variable loads. Eventually, a numerical analysis allows to build an optimisation methodology for improving the hydraulic efficiency by volute geometry modifications.

In conclusion, the plan of work is divided into three parts and it is shown in Fig. 1.1.

- The first part consists of the analysis of distinct case studies, involving different and unique topologies and energy alternatives, and it illustrates the technological and economical potential for PHES. The feasibility analysis for such energy storage plants will discuss the opportunity of using underground cavities as lower reservoirs and waterway infrastructures in hybrid power systems. Moreover, particular attention is given especially to the turbomachines and the technical advantages of variable geometry and variable speed regulation, which aims to answer to the techno-economic aspects for small PHES applications. Deriaz pump-turbines have never been reviewed and modelled in the literature nor discussed for a downsized model for μ-PHES application, which is extremely suited to our current energy generation and storage needs. In addition, the analysis of the case study facility defines the cost-effective parameters for a μ-PHES solution and it provides an important dataset for its feasibility breakdown.

- This thesis provides a technical-economic overview of the challenging design and the experimental outcomes of a first-of-its-kind μ-PHES facility. The described micro-PHES is integrated into a smart grid and it is designed to store energy produced by the connected renewable energy sources. Interestingly, this

μ-PHES runs with a single centrifugal pump for both pumping and electricity generating phases. Variable speed regulation allows the pump to constantly operate at the maximum hydraulic efficiency in order to deal with head and load variations. Moreover, it can be effective to control the operation regimes according to the grid needs and economic criteria. The research project here described aims to map the complete performance of the PaT in a case study using a wide range of rotation speed, pointing out the limitations and physical constraints. Moreover, this type of system may need to deal with variable load due to the continuing changes in the working conditions. The data collected outlines the characteristics of the turbomachine and the whole system yield, with the purpose to construct an efficient control scheme.

- Analysing the existing literature, an unexplored valuable geometrical update for this type of pump is detected to increase the global efficiency of the integrated PHES system. Because of its finite thickness, the cutwater interferes with the flow right before the runner, generating local flaw in the velocity field and deviations of the streamlines. Different grades of stretching and thickness of the cutwater are studied at variable inclination. Available experimental data is used to tune a numerical model that aims to investigate the effect of the pump cutwater design on the performance of the pump in reverse mode. For this reason, an analysis in computational fluid dynamic (CFD) is carried on to detect possible flow pattern problems and characterising the designed improvements. Hence, in light of these numerical results, a multivariate adaptive regression spline (MARS) technique builds surrogate equations of the PaT hydraulic efficiency, driven by the geometrical updates of the cutwater. Moreover, the normal pump performance of the modified geometry are discussed because the possible improvements for the reverse operation might indeed affect the normal functioning of the pump.

1.3 Thesis structure

This thesis is divided into six chapters. After the introduction, a literature review (Chapter 2) illustrates the context and gives an overview of the state of the art in pumped hydro energy storage technology and the turbomachinery selection for these applications.

The following Chapter 3 describes the framework of the thesis goals, presenting the important outcomes of three research projects in innovative pumped hydro solutions and hydropower machinery. A new PHES facility is designed along waterways for employing the pressure gap at the locks of a river in Tucuruí (Amazonia - Brazil) and endorsing the use of combined photovoltaic and storage arrangements. Other systems are discussed in preliminary analysis for PHES where the hydropower head is obtained by exploiting the depth of an underground cavity instead of elevated reservoirs. Under this concept, unexplored potential for PHES emerges, even

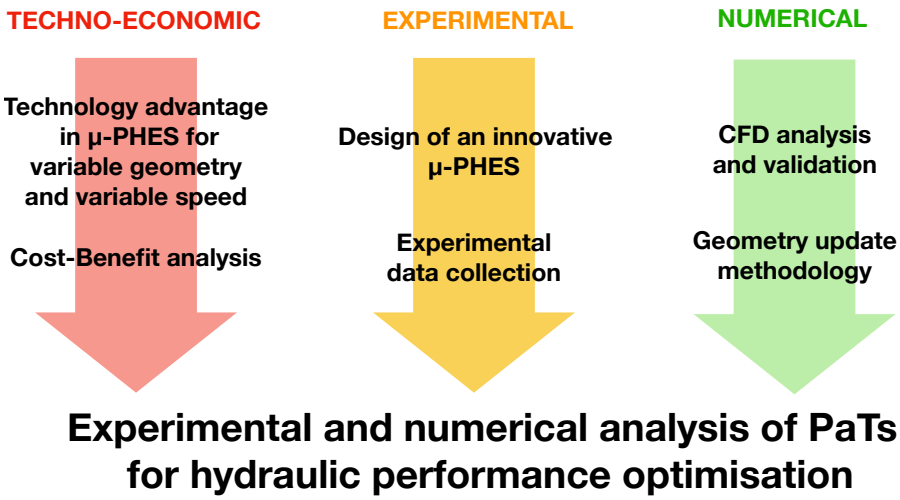

Figure 1.1: Objectives of the PhD thesis.

for those sites where geomorphology conditions limit the installation of traditional plants but unused quarries or mines are present. Finally, this chapter introduces a comprehensive work on the Deriaz pump-turbine, that represents a complementary option to PHES applications in providing a versatile solution due to its singularity. A numerical investigation is conducted in a performance analysis of a downsized model of this unique pump-turbine, suitable for μ-PHES with variable load.

Chapter 4 shows the experimental results and analyses the data compiled during the experimental study on a unique μ-PHES prototype implemented in a real smart grid. The PaT selection and the instrumentation set-up are presented. The experimental methodology illustrates the *rationale* for the management approach in the smart grid, that is based on the characterisation of the turbomachine efficiency (in pump and turbine modes) and the continuous evaluation process of the grid energy fluxes. Here, the results show the pump global performance, used in normal and reverse mode, and highlight the technological advantage in the using a variable speed control. Furthermore, the round-trip efficiency of the μ-PHES prototype is measured and a cost-benefit analysis is conducted.

Chapter 5 models computational fluid dynamic simulations for a geometrical optimisation of the PaT turbomachine applied in the μ-PHES facility. The proposed numerical investigation offers sufficient pool of data to elaborate a predictive algorithm of the hydraulic PaT performance to the finding of a cutwater optimum design. Finally, the optimized geometry of the cutwater is proposed and compared with its baseline design.

The thesis ends with the conclusions (Chapter 6), that summarizes the PhD achievements and gives the perspectives and the limits of the work produced.

1.4 Publications

The following scientific papers have been written about elements described in this work.

Peer-reviewed journal paper

- Morabito A, Vagnoni E, Di Matteo M, Hendrick P. *"Numerical investigation on the volute cutwater for pumps running in turbine mode"* Renewable Energy, 175 (2021): 807-824
- Morabito A, Spriet J, Vagnoni E, Hendrick P. *"Underground Pumped Storage Hydropower Case Studies in Belgium: Perspectives and Challenges"* Energies, 13(15) (2020)
- Furtado G, Mesquita A, Morabito A, Hendrick P, Hunt D. *"Using hydropower waterway locks for energy storage and renewable energies integration"* Applied Energy, 275 (2020)
- Morabito A, Hendrick P. *"Pump as turbine applied to micro pumped hydro energy storage"* Applied Energy, 241 (2019): 567-579
- Morabito A, e Silva G, Hendrick P. *"Deriaz pump-turbine for pumped hydro energy storage and micro applications"* Journal of Energy Storage, 24 (2019): 100788

Peer-reviewed conference paper

- Morabito A et al. *"Variable speed regulation for pump as turbine in micro pumped hydro energy storage"* E-Proceeding IAHR, Panama 100788, 2019.
- Furtado G, Morabito A et al. *"Energy alternatives for the operation of Tucurui locks"*. International Conference of Applied Energy ICAE2019, Västerås 0932-7, 2019.
- Morabito A, Hendrick P. *"Micro Pumped Hydro Energy Storage Case Study in a micro Smart Grid Application"* Proceedings of SDEWES-LA2018, 0271-9, 2018.
- Morabito A et al. *"Set-up of a pump as turbine use in micro-pumped hydro energy storage: a case of study in Froyennes Belgium"*, Journal of Physics: Conference Series, 2017, Volume 813, Number 1
- Morabito A et al. *"Pumped hydroelectric energy storage: A comparison of turbomachinery configurations"*, Sustainable Hydraulics in the Era of Global Change, Proceedings of the 4th IAHR Europe Congress, 261-268 Liege, 2017.

Chapter 2

Literature review and state-of-the-art

Contents

2.1 Introduction

At the end of 2018, global renewable generation capacity amounted to 2,351 GW [IRENA 2019]. This power capacity increase continued the recent trend of an 8-9 % yearly growth in renewable energy, including an energy production increase of about +28 % for photovoltaic (PV) panels and +11 % for wind energy compared to 2017 [IRENA 2019] (Fig. 2.1). Europe, with a renewable energy share growth of 24 GW (+4.6 %) in 2018, is second only to Asia who recorded +11 % (105 GW) growth of renewable capacity. This represents considerable progress in reducing fossil fuel usage and meeting long-term reduced greenhouse gas emissions targets [Höglund-Isaksson *et al.* 2012].

Nevertheless, a significant drawback to solar and wind energy is its intermittent production due to seasonal or even daily changes in the weather. As a consequence, there is often a mismatch between renewable energy production and its use. In

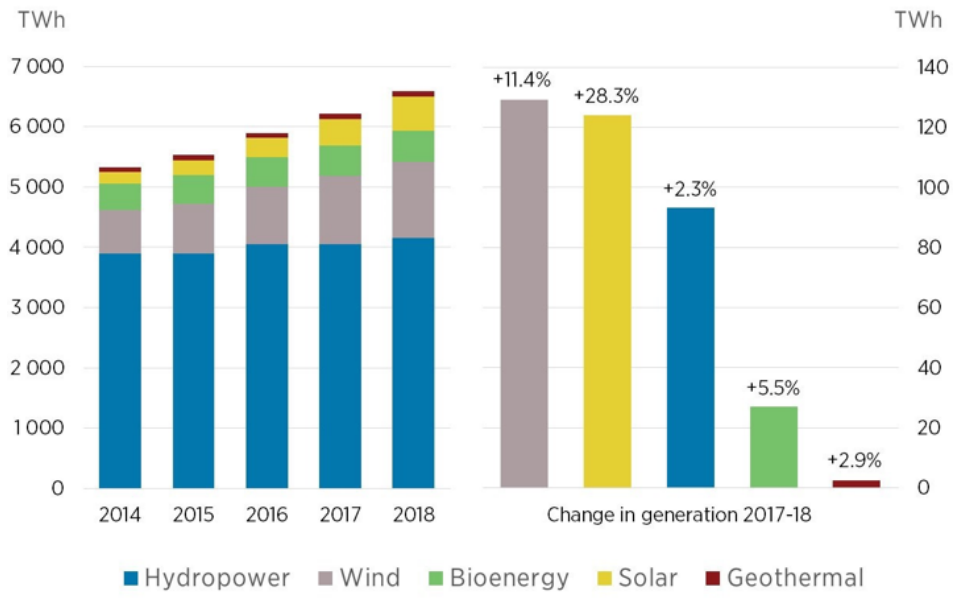

Figure 2.1: World growth in renewable electricity generation [IRENA 2019]

remote areas, this usually leads to the installation of fossil-fuel energy sources such as diesel engines to supply the base-load demand.

The integration into the electricity network of renewable decentralised energy system (DES) (small and occasionally large) is therefore a major challenge for the network's stability and flexibility [Rehman *et al.* 2015a]. Answers to these problems need to include the interconnection of European transmission networks, the dynamic management of power demand and storage, and a strengthening of the power lines [Dostál & Ladányi 2018].

In Europe, a ten-year strategy for sustainable growth has been set (Europe 2020), which aims to reduce greenhouse gas emissions by 20 %, provide 20 % of the energy needs from renewables and increase energy efficiency by 20 % (all compared to 1990 levels) [European Commission 2010]. Moreover, the EU has set itself a long-term goal (Energy Roadmap 2050) of reducing greenhouse gas emissions by at least 80 % by 2050 by reducing dependence on fossil fuels - currently the primary energy source and one of the main contributors to atmospheric pollution and global warming [European Parliament and the Council 2013]. Furthermore, the European Green Deal provides an action plan to boost the efficient use of resources by moving to a clean, circular economy, restore biodiversity and cut pollution [Commision 2020]. The plan outlines a just and inclusive transition for EU to be climate neutral in 2050 [Commision 2020]. To do this, the EU aims to sustainably renovate the existing energy network while decreasing energy losses.

Large-scale electrical energy storage (EES) is the key asset for large grid as in Europe. However, applying the concept of "*think globally, act locally*", EES can also support this transition towards a sustainable, flexible and stable energy system at residential and utility levels [e Silva & Hendrick 2016] [Reynders *et al.* 2017]. This

is particularly important for micro-scale energy systems, which offer low inertia and rapid intervention and which are expected to become ever more common with the increase in decentralized energy supply systems. Given its still largely untapped potential in most areas of the world, micro-hydropower (5 kW - 100 kW) and small hydropower (100 kW - 10 MW) provide a significant contribution to future energy needs [Bozorgi *et al.* 2013].

Hydropower is an efficient, renewable, non-polluting electrical energy source with a remarkably long lifespan at high efficiency [Balkhair & Rahman 2017]. The opportunity to use the stored energy in a sustainable way endorses the pumped hydro energy storage (PHES) instead of fossil fuel reservoirs. The PHES site requirements can therefore vary considerably whith respect to discharge and available heads of the hydropower system [Yüksel 2010] and according to this, water turbines can be designed to suit the site-specific available hydropower energy [Zeng *et al.* 2018] [Vagnoni *et al.* 2018].

In this chapter, the reader finds a brief literature review on the PHES technology in the regards to its traditional set-up and its uncommon configurations as in underground pumped-storage hydroelectricity (UPHS) and at micro-scale level. Attentions are also given to the turbomachinery options in these applications and to the PaT (Pump as Turbine), which is receiving increasing interest in the international scientific literature.

2.2 Pumped hydro energy storage system (PHES)

2.2.1 Traditional hydro power station

Among the different energy storage technologies, PHES accounts for about 97 % of the installed grid-connected electricity storage capacity worldwide, with about 160 GW across over 300 medium large sites [IEA 2020]. Key advantages in having large sites include lower costs per MWh, higher reliability and the ability to provide high levels of power for many hours. The remaining 3 % of energy storage capacity is via other technologies such as compressed air and electrochemical storage [Sandia 2016].

PHES requires two linked reservoirs located at different elevations. When electricity is needed, gates are opened and water flows through, driving the turbines, which are coupled to electricity generators. When demand decreases during off-peak periods, the energy surplus from energy sources that continue to produce power (e.g. wind turbines, PV, nuclear plants) can be stored using PHES. Powered by this surplus electricity, a pump can refill the upper reservoir. Alternatively, a reversible-turbine can pump the water up to the higher reservoir. In effect, the system is recharging the upper reservoir in order to have it ready to be used again when needed. The Fig. 2.2 represents the operation principle of PHES: pumps use the available surplus of energy for storing water in the upper reservoir and turbines operate when needed.

PHES preserves most of the advantages of hydropower plants, even if PHES

is not considered a renewable energy source as such. Especially for closed-loop configurations, which consist of two reservoirs that are isolated from a free-flowing water source, the generated energy comes solely from the storage of a second energy source that is not necessarily renewable. On the other hand, closed-loop systems have fewer environmental impacts because, after the initial filling of the reservoir, there is almost no transfer of water from a free-flowing source, thereby greatly reducing environmental impacts (fish passage, sediment migration, etc.).

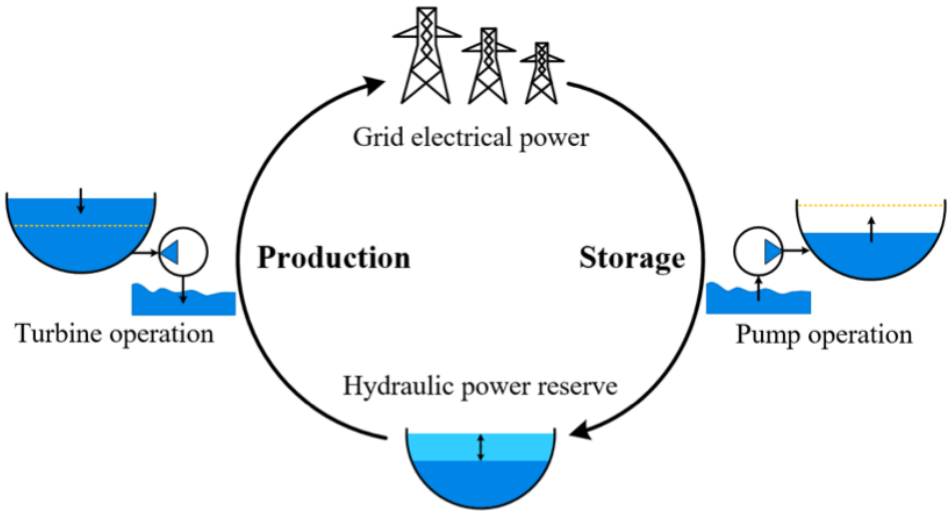

Figure 2.2: The operation principle of a PHES: it stores energy in pump operation and it generates energy in turbine operation.

The problems associated with micro-scale units (μ-PHES) are different than in large PHES units. The issues related to operation, maintenance and repair technologies are critical for the micro-scale (5 - 100 kW of power production). Manolakos et al. [Manolakos *et al.* 2004] illustrate a μ-PHES on Donoussa Island, Greece, coupled with an 18 kW-peak (kWp) photovoltaic power system. The micro-hydraulic system consists of a pump and a hydraulic turbine of 7.5 kW and two identical water reservoirs of 150 m^3 capacity each with a height differential of about 100 meters. Another hybrid system with PV and a co-generative internal combustion engine is coupled with lead-acid batteries and thermal and water storage, to satisfy the energy and water needs of a small isolated touristic resort in Northern Italy [Stoppato *et al.* 2016]. PHES technical feasibility and its economic comparison with other promising storage technologies are discussed on a small scale by Silva and Hendrick [de Oliveira e Silva & Hendrick 2016]. It appears that high cost and low efficiency compromise the competitiveness of PHES on small scales [de Oliveira e Silva & Hendrick 2016].

2.2.2 Unconventional PHES

Relevant design decisions can be taken to implement a PHES plant besides its traditional concept or to reduce costs. Underground pumped storage hydroelectricity (UPSH), based on the mature PHES technology, use underground cavities to cope with the expenses of building reservoirs from scratch and the lack of hilly areas suitable or available for pumped hydro storage [Pujades *et al.* 2017].

Another different PHES design is based on using seawater instead of fresh water: the seawater pump storage (SPS) plants [Katsaprakakis *et al.* 2013]. SPS systems can pump seawater directly from the sea, thus the construction of a lower reservoir is avoided, which further implies less land use and lower construction costs [Ioakimidis & Genikomsakis 2018]. However, the use of seawater results in increased costs related to corrosion protection and the prevention of ground contamination from salt water [Katsaprakakis *et al.* 2013]. Therefore, SPS systems comprise a solution for areas characterized by a lack of abundant natural fresh water and in proximity of the sea shore [Ioakimidis & Genikomsakis 2018]. The 30 MW Yanbaru project in Okinawa (Japan) was the first demonstration of seawater pumped storage in 1999 (Fig. 2.3) [Hiratsuka *et al.* 1993]. Another 300 MW seawater-based pumped storage project has been proposed on Lanai, Hawaii [Kroposki *et al.* 2012]. Further case studies are investigated for the island of Rhodes [Katsaprakakis & Christakis 2014], on the island of Sao Miguel (Azores) [Ioakimidis & Genikomsakis 2018], the Cultana project in Australia [Hendriks *et al.* 2018], in Southern California [Scorza 2019], for the Guadaloupe island [Brun *et al.* 2015], and in west-Ireland [Hughes 2010]

Figure 2.3: Seawater-based pumped storage plant in Okinawa, Japan.

Other innovative approaches are emerging in proposing unusual PHES facilities. The *Energy Membrane*, where energy is stored by lifting a mass of soil through the pumping of water into two impermeable membranes, represents another novel concept of energy storage system [Olsen *et al.* 2015]. The test results combined with the theoretical modelling done on such a system are indicating that visco-elastic the en-

ergy loss in the soil layer is low compared to usual energy loss by friction in the piping of traditional PHES [Olsen *et al.* 2015]. Also hydraulic gravity storages (HGS) do not outperform a conventional PHES concept. The hydrostatic head in generation mode is caused by the weight of a piston in a vertical shaft; the piston is lifted by water pressure in storage (pump) mode (Fig. 2.4). Currently, it has begun a construction on a HGS demo plant in Weilheim, Bavaria [Grid-Scale Energy Storage 2018].

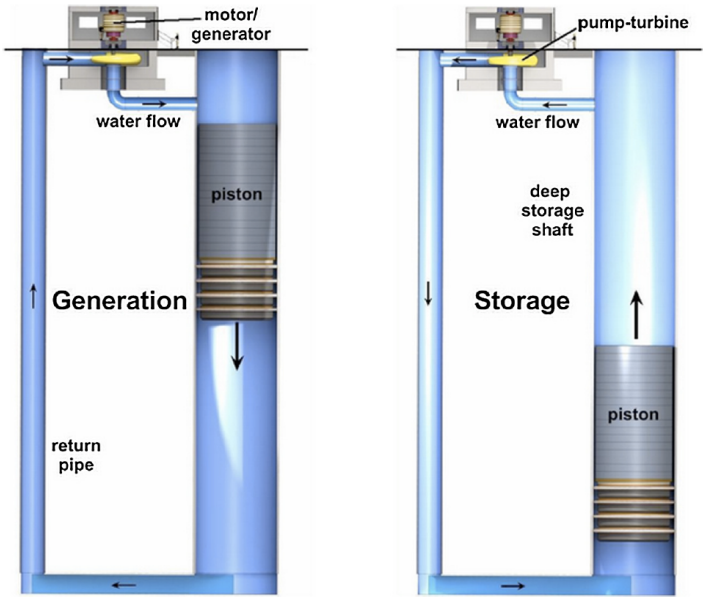

Figure 2.4: Schematic hydraulic gravity storages (HGS) facility in generation and storing phases [Grid-Scale Energy Storage 2018].

2.2.3 Underground Pumped Storage Hydroelectricity

UPSH facilities could represent a valuable solution in increasing the EES capacity in those regions where, because their geomorphology conditions, there are no promising sites for conventional PHES with sufficient head and surface [Martin 2011]. In these systems, the hydropower head is obtained by exploiting the depth of an underground cavity instead of elevated reservoirs (Fig. 2.5). However, the use of underground cavities as lower reservoirs for hydropower applications is not widespread and its technology has not yet passed the research and development phase [Pickard 2011, Pujades *et al.* 2018]. The patent for underground energy storage applied to hydropower is to R.Fesseden, being the first to record the idea of "placing the lower reservoir, not on the surface of the earth, but subterraneously, so as to have a high negative gravitation potential with reference to the earth's surface" [Fessenden 1917]. Nowadays, there is no evidence of an existing underground pumped hydro system but a few research projects worldwide in the attempt to re-valuate abandoned quarries or mines.

In the early 80s, a preliminary geological investigation has been conducted to

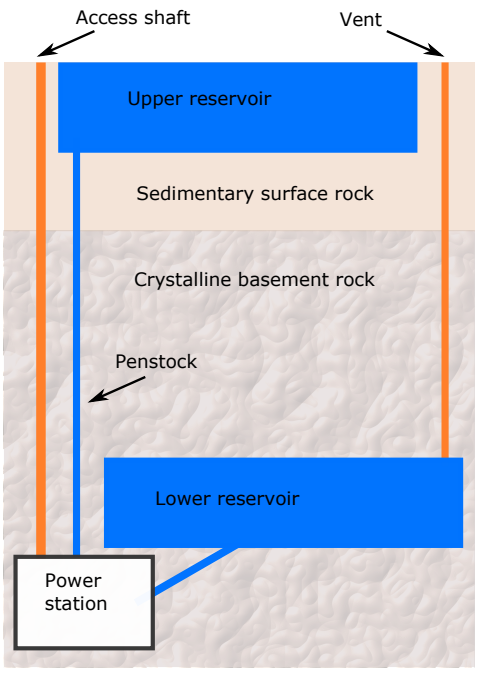

Figure 2.5: Simplified schematic diagram (not to scale) of an UPSH facility. Reality is rather more complicated than this sketch indicates.

find a suitable site in The Netherlands, pointing to the limestone rock of South Limburg to a reservoir at about 1000 m depth [Min 1984]. In Belgium, the project Smart-water had the objective of collecting the tools and information in socio-legal, economic, hydraulic, and hydro-geologic aspects to detect specific underground sites in the Walloon region for EES use [Spriet 2014, Pujades *et al.* 2017]. In another research project, because of the lack of topographical reliefs in Singapore, the Bukit Timah granite quarry has been evaluated as the lower reservoir for a UPSH plant of 370 MW, which was found economically comparable to an oil-fired plant at the time [Wong 1996]. In Germany, the coal mine of Prosper-Haniel has been studied as the lower reservoir for a closed-loop UPSH or in an open system, presenting the challenges of the rock stability, its porosity, and the composition of the used water [Wong 1996, Alvarado & Niemann 2015]. In Minnesota, USA, ten sites are analysed and explained to produce caverns that could be used as the lower reservoir in a PHES [Zillmann & Perau 2015, Martin 2011]. In New Jersey, an iron mine was proposed as the lower reservoir for a UPSH but the Mount Hope project [US Army Corps of Engineers 1981] never went further. Also, Australia, Estonia, and Finland have shown recent interest in UPSH solution with the respective Bendigo [BSG 2020], Muuga [Energiasalv 2020], and Callio [Callio 2020] projects.

In the framework of UPSH plant, not all the types of soil have adequate characteristics. Soft sediments and friable rocks cannot withstand the erosion created by the generating-pumping cycles of UPSH facilities and porous rocks are thus unsuitable as underground water reservoir [Bear & Cheng 2010]. Indeed, coal and met-

alliferous mines as slate and black marble quarries could be taken into account for their rock stability. Groundwater interactions and oscillations in piezometric heads by the influence of hydraulic conductivity of the surrounding aquifer are possible but are limited [Bodeux *et al.* 2017], as the head variation depends heavily on the discharge pumped from or injected in the cavity. Pujades E. et al. have estimated the groundwater exchanges positively as they mitigate the head variation due to regular operation of the turbomachinery [Pujades *et al.* 2017].

Still in respect to the groundwater flow impact, if the mine is totally isolated with respect to the surface, it appears that the pressure inside the chambers will increase as they are filled by water, but it does not influence the water exchanges between the underground reservoir and the surrounding medium [Pujades *et al.* 2018]. In any case, old mine rehabilitation tasks should be undertaken to adapt abandoned mines as underground reservoirs for UPSH. Thus, additional works might be required to strengthen the rock stability. Special attention must be given to the effects of increasing the connectivity between all the mine chambers or cavities. For instance, for the purpose of damping oscillations or eliminating disruptive water flows in the underground cavities, galleries homogeneously distributed between them could be drilled.

2.3 Turbomachinery options for hydropower and PHES

2.3.1 Characteristic curves

The performance of a PHES site is clearly dependent on the turbomachinery used and is sensitive to each specific local scenario [Spänhoff 2014]: pumps and turbines have to be installed according to the exploitable flow rate, available head and pipeline system characteristic curve. Although pumps and turbines are designed for a particular discharge, they operate across a certain range due to the fluctuation of the available head and/or load, as it would happen in filling from the bottom a tall column of water (Fig. 2.6). The water level may vary through the full cycle of emptying and filling the reservoirs according to its specific geometry and the flow regime, as in situation Ⓐ and Ⓑ. For pumps, the counter pressure to overcome consists in a geodetic head, namely the water levels gap from the upper and lower reservoirs, and head loss due to the water friction in the piping system, that is proportional to the square of the discharge (or the water speed). The operating condition is given by the intersection point of the system head curve, H_{syt}, and the head pump characteristic curve. Naturally, it is not assured that this point matches with the best efficiency point (BEP).

For turbines, the head available is given by the geodetic head less the pressure loss for water friction on all the walls of the system, that is proportional to the square of the discharge. However, turbines have regulations accessories, such as guide vanes before the rotor to attune the discharge or adjustable runner blades to range the load at the shaft, that extend the characteristic curve in an operating area limited by the critical conditions for incipient of cavitation and vortex development

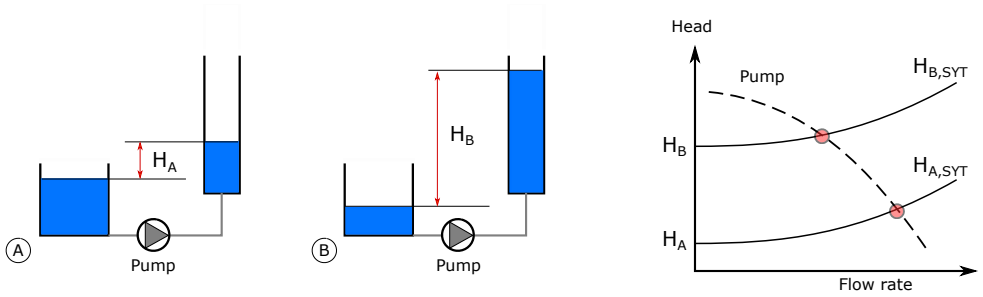

Figure 2.6: Representation of variable head during pumping water in a tall and narrow tank. Two operating points are marked when crossing the pump characteristic curve, in dashed line, and the head system ones (for case (A) and (B)).

[Guo *et al.* 2017]. The operational characteristics of a hydraulic turbine can be expressed by the performance characteristic curves (or efficiency hill chart). The intersection of head system curve and the turbine hill chart provides the possible operating range based on the turbine regulation set-up. Fig. 2.7 shows two different stationary heads for the hydraulic turbine and their consequent operating curves.

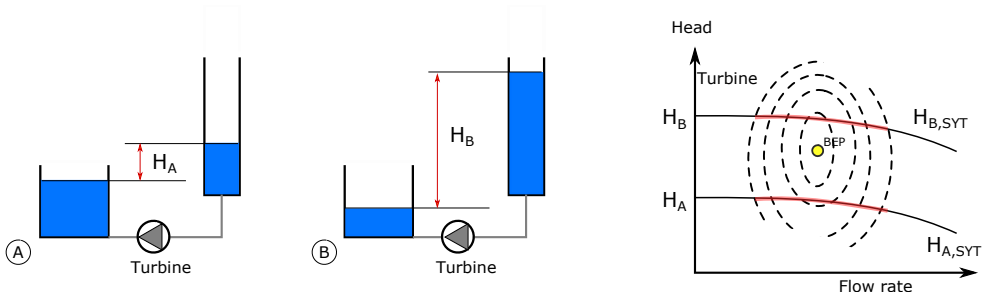

Figure 2.7: Representation of variable head during turbine generation. The operating conditions are marked on the turbine hill chart, in dashed line, and the head system ones (for case (A) and (B)).

Often the turbomachinery will temporarily work in off-design conditions during transient periods. During these conditions, the flow separates at the impeller tips, in the impeller and in the diffuser or volute. Re-circulation may occur at the inlet or at the impeller exit, where fluid might flow back from the diffuser or volute. These off-design conditions not only reduce installation efficiency but can also strongly affect its working life. Under such conditions, cavitation can damage the impeller while excessive vibrations can reduce bearing life and reliability or even cause a resonant oscillation in the entire pump system [Jonsson *et al.* 2012]. Catastrophic failures are unusual, but off-design operations for long periods of time can seriously reduce installation working life.

Care must be taken when estimating the margin of excess capacity required by the system (i.e. supplied by the pump or required at the turbine). These margins

are given by manufacturers as guidelines for the safe working range of their turbomachines. Too large margin normally causes the turbomachinery to operate far from off-design conditions but with low efficiency, reducing its reliability and working life. It is also economically important to determine whether low efficiency at nominal operating conditions (and corresponding operating costs) will balance out the losses avoided from a lack of excess capacity at unusual occasions.

2.3.2 Hydraulic turbines for hydropower and PHES

Hydraulic turbines have been broadly classified as impulse turbines and reaction turbines based on the amount of the available pressure head that is converted into kinetic energy in the nozzle. Impulse turbines first convert available hydraulic energy into kinetic energy by means of an efficient nozzle. The flow jet from the nozzle strikes a series of shaped buckets or symmetric blades fixed around a wheel. Reaction turbines transform only a part of the total available hydraulic energy into kinetic energy before the water is directed to the turbine runner. A considerable amount of hydraulic energy remains in the form of pressure energy up to the outlet of the turbine that it is sealed from atmospheric conditions. Reaction turbines are classified according to their geometric features and specific speed. Specific speed N_s ranks a turbomachine based on its working condition regardless of its size. The N_s of a pump is equal to the rotation speed in rpm of a machine of the same type working with a discharge of 1 m^3/s, under an available head of 1 meter:

$$N_{s,pm} = \frac{N\sqrt{Q}}{(H)^{0.75}} \tag{2.1}$$

For historical reasons the definition of the specific speed for turbines differs from that of pumps. The N_s of a turbine is defined by the rotation speed of a machine of the same type under a water pressure equivalent of 1 meter and a generating a power at the shaft of 1 kW. In a selected working point, defined by the rotational speed N (rpm), head H (m) and power P (kW), we obtain:

$$N_{s,t} = \frac{N\sqrt{P}}{(H)^{1.25}} \tag{2.2}$$

The specific speed is linked to the geometry of the machine and helps matching the most efficient size and working conditions.

If the fluid flows radially into the impeller the turbomachine is radial (e.g. Francis turbine) while if it flows parallel along the machine shaft, it would be axial (e.g. Kaplan turbine). The turbomachine geometry influences its use: radial machines, for instance, are better suited to smaller discharges and higher available heads than axial machines. Fig. 2.8 gives a graphical representation of the turbines' applications and an indication of the equivalent specific speed.

In some hydropower installations, it takes only a few seconds to open a high-powered hydraulic turbine to switch from a partial load to a full load. For preserving the turbomachinery lifespan, which has a high volume of investment, control and

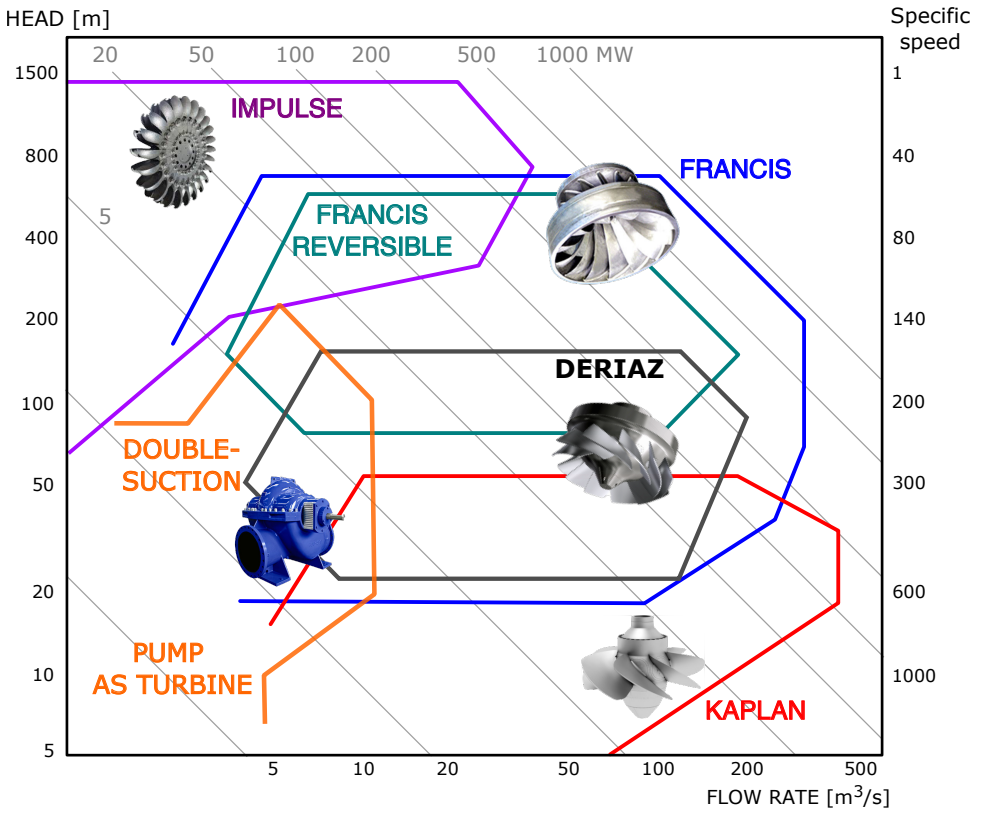

Figure 2.8: Types of hydraulic turbines in their application area Q-H. Adapted from [Johnson 2016, Paish 2002, Deriaz & Warnock 1959a] and author's data.

technical issues take precedence over other economic considerations. Francis turbines work day after day at very low openings and consequently at low efficiency. The danger of disturbance from a distribution network makes immediate emergency power necessary. In order to remedy this, a turbine with maximum efficiency at a low opening is needed, and not at approximately 80 % of the full load as for a Francis turbine of average specific speed. Fig. 2.9 shows how a Kaplan turbine might be the answer to this problem. However, Kaplan turbines are not usable under high falls (80 to 200 meters or more) due to mechanical and hydraulic restrictions. So it is, in fact, Francis turbines are used under such conditions, even though they perform poorly at partial loads. There is a need to find a hydraulic turbine of lower specific speed that works efficiently at sharp partial load and higher available head than a Kaplan turbine. Logically then, it seems that the purely axial concept of the Kaplan turbine has to be abandoned and a combination of Francis blades with variable pitch blades might be the answer: at first, ambiguously called *"Francis à pas variable"*, this was subsequently named the Deriaz turbine. In contrast to most hydraulic machines, the flow in a Deriaz turbine does not follow a full axial or radial direction but is a diagonal mixture of the two. Deriaz turbines, like Kaplan turbines,

have also adjustable blades. In fact, "*Deriaz turbine is to the Francis turbine what the Kaplan turbine is to the fixed-blade propeller*" [Deriaz 1955]. More information on Deriaz pump-turbine is reported in the next section (Section 2.4).

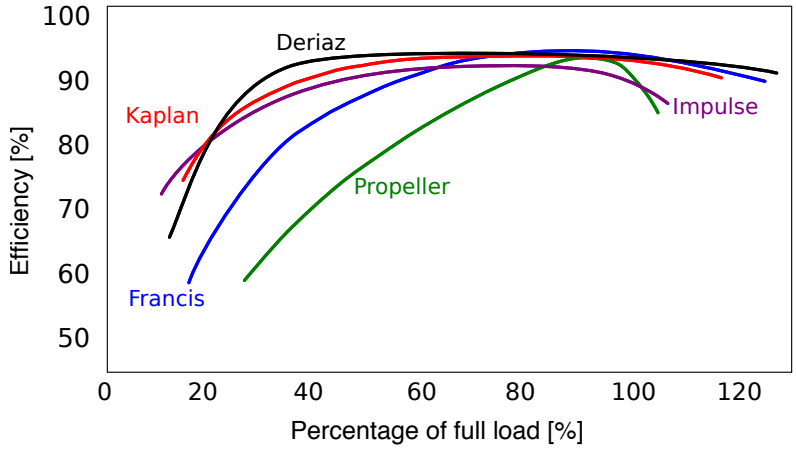

Figure 2.9: Efficiency vs load of Deriaz turbine and most common turbines.

The turbomachinery selection in a PHES, as in all conventional hydropower plants, is critical for the rated power capacity and financial availability [Martin 2011]. In pumped hydro energy storage systems, hydraulic turbines produce energy when needed from the potential energy stored in the upper water reservoir; low-cost electricity power, during the off-peak time, feeds hydraulic pumps and restore the capacity of the upper reservoir from the lower one. The hydro-mechanical apparatus can be structured by split turbomachines groups (namely the ternary solution) or completely separated pumps and turbines or reversible turbomachines solution.

2.3.2.1 Ternary set configuration

The ternary-set solution consists of three separate groups of turbine, pump, and motor/generator coupled on the same or separate shaft. Both the pump and the turbine are optimized for selected operating conditions and guarantee the highest hydraulic performance. Ternary groups operating at a drop higher than 200 or 300 m are usually composed of Francis or Pelton turbines, and the pump group is often multistage. In this hydropower set-up, the energy consumption for pumping can be different than the generation one. Ternary groups are expensive and bulkier, especially about to ducts and valves. However, they are the only ones indicated in the case where the target generated power is quite distinct from the pumping power. Their performance is also excellent because each component can be optimized separately. Finally, these groups have broad operating flexibility and make it easy to reduce significant current spikes that occur during of electric start-up. The current trend is nevertheless replacing them with reversible groups.

2.3.2.2 Reversible pump-turbine

Reversible pump-turbines (RPTs) are indeed commonly used in recent times for PHES [Akinyele & Rayudu 2014, Dixon & Hall 2010]. These machines are designed to run in both pumping and generating modes reducing the required volume (reducing excavation costs) and fittings. However, the hydraulic design of the runner implies higher costs due to its double function. Francis turbine runner and a centrifugal impeller pump have significant differences in design; in particular, the Francis runner has shorter channels and higher entrance angles that make it incompatible for a good operation in pump mode; for the latter, the flow being slowed, the boundary layers would be too exposed to flow detachment [Jaumotte *et al.* 1994, Dixon & Hall 2010]. The design of a reversible turbine must in principle be designed as a pump impeller, which, in reverse operation, will work in a turbine mode. In general, this layout makes the hydraulic efficiency of one reversible runner lower than a normal Francis runner [Jaumotte *et al.* 1994]. In this context, it is further noted that if the optimal yields in pump and turbine of a reversible runner have a similar value, the optimal operating points do not coincide at equal speed for both directions of rotation. In particular, the specific energy transferred to the fluid in pumping is larger than the available specific energy during generation. In other words, the energy available to the turbine is equal to the gross mass-energy, corresponding to the altitude difference between upstream and downstream water levels, reduced by pressure losses of the hydroelectric plant while the delivered pump's energy must be equal to the gross mass energy plus the related load losses.

The main drawback of the reversible turbine is the requirement of reversing the direction of rotational speed to pass from turbine operation to pump operation (or vice versa) [Williams 1994a], which lengthens the time required for these operations. Besides, the pump start is not easier than for a ternary group. It must be insured with an auxiliary turbine, a static frequency converter, an asynchronous generator-motor start, the pump being eventually disengaged to decrease the resilient torque. Another drawback of the reversible turbine is that the distributor-diffuser, necessary to adjust the operation in turbine mode, creates operational difficulties in pump mode; this element is then strongly stressed by pressure fluctuations at the wheel outlet, and precautions shall be taken to avoid too strong vibrations. Finally, the reversible turbine does not allow choosing a higher generated power than consumed in pumping; due to the design of this type of machine, if the rotation speeds are equal for both speeds, these powers are at most substantially equal.

2.3.2.3 Traditional turbines

Francis turbine type covers applications of the medium-high head (70-600 m) while the Kaplan turbine is used for a smaller head below 60 m. These turbines are complementary such as they cover a very wide range of available heads. Kaplan turbines have the specific feature of variable geometry, which allows them to operate at high efficiency for a different set of the blade angles, thus at different working conditions (head and discharge). Finally, pump-turbine type Deriaz merges the

characteristics of medium-head application more typical from Francis turbine and variable pitch-blade advantage of the Kaplan pump-turbine.

Pelton turbines are often used in very high head applications (not less than 300 m). An impulse turbine is one for which the pressure of the fluid flowing over the rotor blades is constant, and all the work output is due to the change in kinetic energy of the fluid. The Pelton runner is always at ambient pressure, and, for its concept, its efficiency would considerably drop if submerged in water due to disk friction and mixing. However, in some cases, the downstream water level may fluctuate in height of about ten meters. In this case, to carry out the recovery, the water is artificially lowered under the turbine wheel by compressing the air contained in the wheel chamber. Impulse turbines do not fit in UPSH plant for their operating concept unless there is not a high vertical growth of the lower reservoir. Their runner is always at ambient pressure, and its efficiency would considerably drop if submerged [Židonis & Aggidis 2015] as it could happen in a powerhouse beneath the lower reservoir.

2.3.2.4 Micro-hydropower

Recently in micro-hydropower plants ($\leq$ 100 kW), pump as turbine (PaT) can be found with downsized impulse turbines, propeller turbines and cross-flow turbines. In such a system, a pump operates in reverse mode so that it functions as a turbine (Fig. 2.10). Compared to large turbomachines, the behaviour of small pumps in reverse mode is quite different: as an industrial pump, PaT design does not have any particular need to run in reverse mode unlike pump-turbines used in large PHES [Aneke & Wang 2016]. Moreover, PaTs are not usually equipped with fixed/movable guide-vanes that are used in turbines for directing the flow: in PaTs, only the volute operates as the water flow guide [Singh & Nestmann 2010].

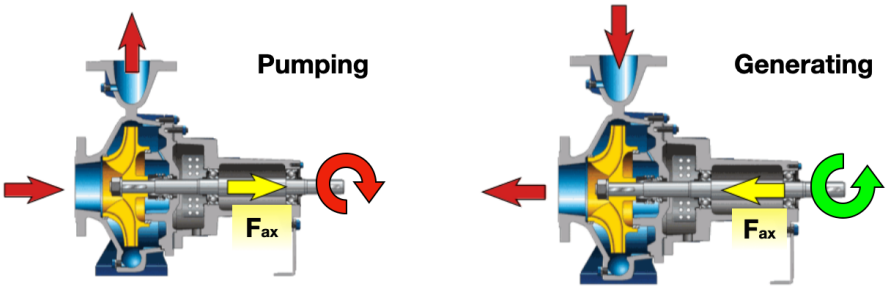

Figure 2.10: Centrifugal pump in normal and inverse mode.

Nourbakhsh et al. [Nourbakhsh *et al.* 2010b] state that pumps are relatively simple and easy to maintain and have quite competitive efficiency when compared to conventional turbines. The off-the-shelf availability of water pumps and their reduced purchase price compared to conventional hydro turbines make them an ideal technology for exploiting large portions of uncapped hydro potential that is technically viable but not financially convenient. Indeed, Baumgarten et al.

[Baumgarten & Guder 2011] state that the most significant PaT benefit is that the pumps mass production makes them much more cost-effective than conventional turbines. Such low-cost technology could help to expand hydropower exploitation in water resources worldwide, helping to reduce climate change greenhouse gas emissions. However, in the literature, the few available cost figures relative to PaT purchase price are discordant and often outdated, and such a lack of information is likely a severe barrier to a more widespread PaT implementation. Only recently, the growing interest in this subject moves researchers in action to overcome this limitation. In 2019, finally, Novara describes a specific cost model for the use of PaT [Novara *et al.* 2019] by gathering data from about 300 pumps from the industry and the literature, helping designers in the selection of the hydropower business model.

However, PaTs have a relevant drawback in efficiency, which usually lays lower than conventional hydro turbines [Nautiyal *et al.* 2011, Binama *et al.* 2017, Aneke & Wang 2016]. Difficulties arise in the prediction of the PaT efficiency [Binama *et al.* 2017]: they are not designed to run in reversed mode, and the four-quadrant diagnostic tests are not usually performed to maintain a low price. A dedicated section on PaT (Section 2.5) follows in this chapter to better understand its advantages and weaknesses.

Table 2.1 summarises the hydraulic turbines characteristics about their characteristics for PHES applications.

Table 2.1: Available turbomachinery solutions for PHES and UPSH

Solution	**Turbomachinery**	**Characteristics**
Ternary	Distinct turbine and pump groups ($H > 200$ m)	Expensive and bulkier solution. Each turbomachine is optimised for pumping or generating. Recommended in the case where the target generated power is quite distinct from the pumping power.
RPT	Variable geometry type Kaplan ($H < 60$ m) Variable geometry type Deriaz ($25 < H < 170$ m) Francis pump-turbine at fixed or variable speed ($75 < H < 600$ m)	Smaller excavation costs and civil/structural costs. An invertible rotation speed system is required. RPT design is more expensive than for traditional hydraulic turbines.

2.3.3 Variable speed regulation

The speed regulation of a turbine is an important and complicated problem. The magnitude of the problem varies with size; type of machine and installation; type of electrical load; and whether the plant is tied into an electrical grid. It should also be kept in mind that runaway or no-load speed can be higher than the design speed by factors as high as 2.6 [Johnson 2016]. This is an important design consideration for all rotating parts, including the generator. The speed of a turbine must be controlled to a value that matches the generator characteristics and the grid frequency:

$$N = \frac{120\ f}{np} \tag{2.3}$$

where N is turbine speed in rpm; f is the required grid frequency in Hertz; and np is the number of poles in the generator. Typically, np is in multiples of 4.

Regulation of speed is normally accomplished through flow control. Adequate control requires sufficient rotational inertia of the rotating parts. When the load is rejected, power is absorbed, accelerating the flywheel; when the load is applied, some additional power is available from the deceleration of the flywheel. Response time of the governor must be carefully selected because rapid closing time can lead to excessive pressures in the penstock. Opening and closing the guide vanes, which vary the flow of water according to the load, control a Francis turbine. The actuator components of a governor are required to overcome the hydraulic and frictional forces and to maintain the wicket gates in a fixed position under steady load.

On the other hand, impulse turbines are more easily controlled because the jet can be deflected or an auxiliary jet can bypass flow from the power-producing jet without changing the discharge in the penstock. This permits long delay times for adjusting the discharge to the new power conditions. With Pelton turbines, the spear on needle valve controlling the discharge can close quite slowly, e.g., in 30–60 s, thereby minimizing any pressure rise in the penstock. Several types of governors are available that vary with the work capacity desired and the degree of sophistication of control. The precision of governing necessary will depend on whether the electrical generator is synchronous or asynchronous (induction type). The induction type of generator is less complex and therefore less expensive but typically has slightly lower efficiency. Its frequency is controlled by the frequency of the grid into which it feeds, thereby eliminating the need for an expensive conventional governor.

Also, pumps can benefit from speed regulations and it is commonly used in professional applications. In order to vary delivery, centrifugal pumps are sometimes regulated by means of a bypass, namely a certain water capacity is deducted back to the suctions reservoir or elsewhere. The pump operates at its optimum point but the discharge loss in the recirculation line effect the overall efficiency. This kind of control system is normally used in simple applications with the purpose to maintain the system's robustness and in applications where saving in power consumption is not a priority. Another common and cheap solution is throttling: closing a throttle valve the hydraulic resistance increases, the system head curve gets steeper, meeting another working condition point on the pump characteristic curve.

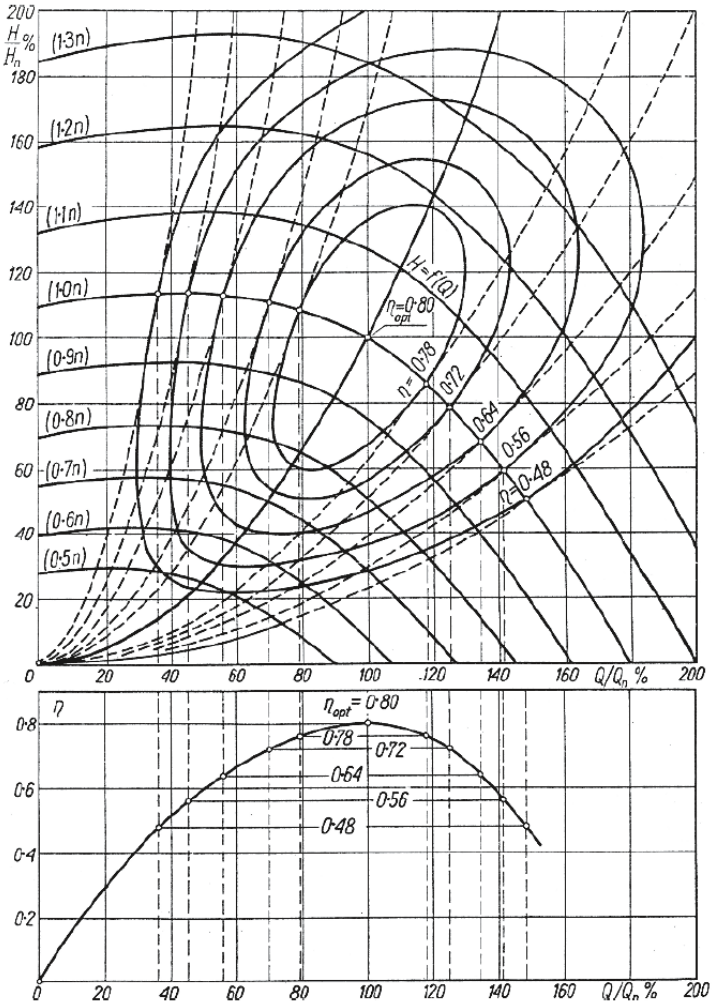

Figure 2.11: Pump characteristic curves at nominal (n) and different rotational speeds [Lazarkiewicz & Troskolanski 1965]

On the other hand, while speed control is enabled, the system head curve stays unaltered but the pump characteristic changes in accordance with the rotational speed. It moves at a higher head or lower head in raising or decreasing the speed, respectively. Where the system head curve is mostly due to friction losses, thus a quadratic curve with y-intercept close to zero, speed control offers the best solution because pump efficiency remains almost constant. If the points of the $H = f\,(Q)$ curves corresponding to the BEP at the respective speeds are joined together, a parabolic curve is obtained whose apex is at the origin and its axis coincides with the H-axis (solid line in the upper plot of Fig. 2.11). This curve represents the optimum operating conditions for the impeller. The other similar curves, dashed lines, show similar flow conditions, but at different efficiencies. In Fig. 2.11 the curves are plotted in a non-dimensional system of coordinates, where the non-dimensional characteristic curves of $H/Hn = f(Q/Qn)$ is obtained as $H\% = f(Q\%)$. Subscript

n notifies here the characteristic curve at nominal speed.

Hydraulic affinity laws can be used to predict the behavior of turbomachines over small speed changes in order to successfully manage a new duty point. When varying speed, the following equations for discharge, head and power hold good in accordance with the law of similarity:

$$\frac{Q_1}{Q_2} = \left(\frac{N_1}{N_2}\right), \qquad \frac{H_1}{H_2} = \left(\frac{N_1}{N_2}\right)^2, \qquad \frac{P_1}{P_2} = \left(\frac{N_1}{N_2}\right)^3 \tag{2.4}$$

where the subscripts 1 and 2 define the two points in similarity conditions at rotational speed N_1 and N_2. In all these points, the internal efficiency is considered constant. Affinity laws are very useful and valid over small speed changes (-5 % to +10 % [Schoenung & Hassenzahl 2003, Nourbakhsh *et al.* 2007]), and they have become predictive tools for variable frequency drives (VFDs) operation where changes may greater. However, better results can be obtained by using empirical data available from performance tests at various speeds. Obviously, phenomena such as erosion, cavitation and vibration should be reassessed over the full range of speeds.

2.4 The Deriaz pump-turbine

The Deriaz hydraulic turbomachine, developped by the Swiss engineer Paul Deriaz, was the first diagonal pump-turbine to be designed [Deriaz 1926]. The trend towards higher-head Kaplan turbines in excess of 60 m head was obvious as the hydropower potential was increased after World War II [Hager 2014]. With the conventional, axially arranged Kaplan turbine the runner hub would have become so large and the vanes so narrow that an appreciable loss in turbine efficiency resulted [Hager 2014]. The natural step was to take distance from the axial arrangement and revert to the mixed flow towards Francis frame-up. The reduction of specific speed leads to a reduction in the radial extension at the leading edge of the runner and to a loss of axial alignment thereby giving a direction mix between axial and centripetal. From a mechanical point of view, to support the increasing hydraulic forces applied to the blades, their trunnions need to be larger and more resistant. The hydraulic conditions also require more blades with an increase in the ratio of blade length to spacing, which makes the placement of the large pivot bearings very difficult. This is because the increased energy difference between the inlet and outlet requires longer blades in order to avoid blade overloading. The movable blade's length is limited at the root by the spherical geometry of the hub. Due to the limited space for the mechanism in the hub (Fig. 2.12), the number of blades is also limited. The maximum number of blades is 10. This limits the maximum head for Kaplan turbines to approximately 60 meters at reduced maximum efficiency.

The runner blade servomotor is normally a rotary type, located inside the turbine shaft or runner hub. The rotation of the servomotor piston is transmitted to the spider inside the runner hub through the piston rod. Each connection of the spider and blade arm has a slide block that conveys the rotating motion of the spider to the runner blade stem (Fig. 2.12).

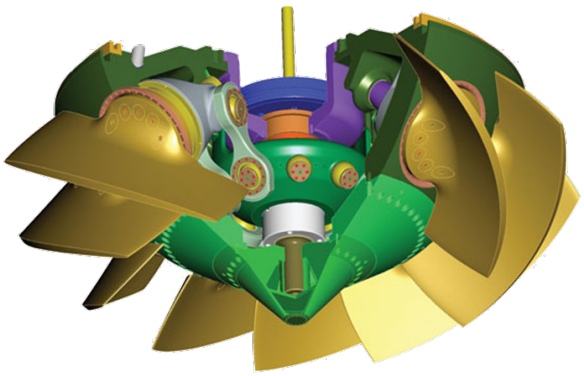

Figure 2.12: Internal view of Deriaz pump-turbine runner and of its regulating mechanism in the hub [Skotak & Stegner 2014].

2.4.1 Variable geometry regulation

The Deriaz runner is characterized by the spherical surfaces of the hub and the skirt. This allows for the rotation of the blades whilst maintaining a narrow clearance and is an essential departure from the corresponding surfaces of the Francis toroid runner (Fig. 2.13).

For a machine at constant speed, the discharge diameter of the runner has a controlling effect on the total dynamic pumped head. The variation in mean diameters of the inlet and outlet edges of the blade resulting from blade movement is a remarkable operational advantage under variable head: closing the blades, for instance, the maximum diameter decreases, or rather, the radial extension ΔR decreases (Fig. 2.13.c). The oblique position of the runner-blade pivots in the Deriaz pump-turbine gives the mixed-flow characteristics and the short radial extent of the vane-inlet edge [Deriaz & Warnock 1959b].

As mentioned before, regarding the specific speed N_s, the optimum feathering angle of the blades for higher heads is greater than for lower heads according to the accepted design of the flow speed field. The variation in mean diameters of the inlet

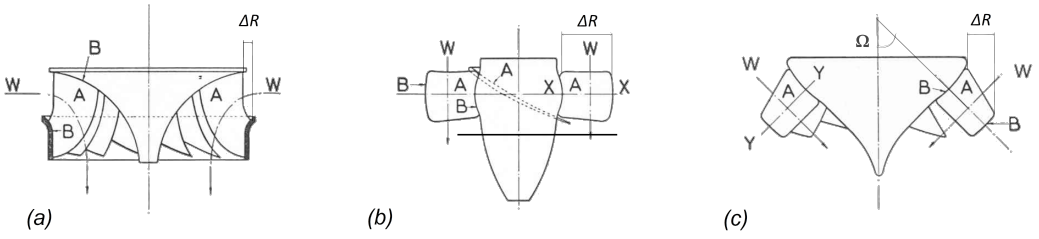

Figure 2.13: (a) Francis runner; (b) Kaplan runner (c) Deriaz runner [Deriaz 1955]. A: blades or adjustable blades; B: toroidal or spherical surface; W: direction of the flow; ΔR: radial extension of the runner blade.

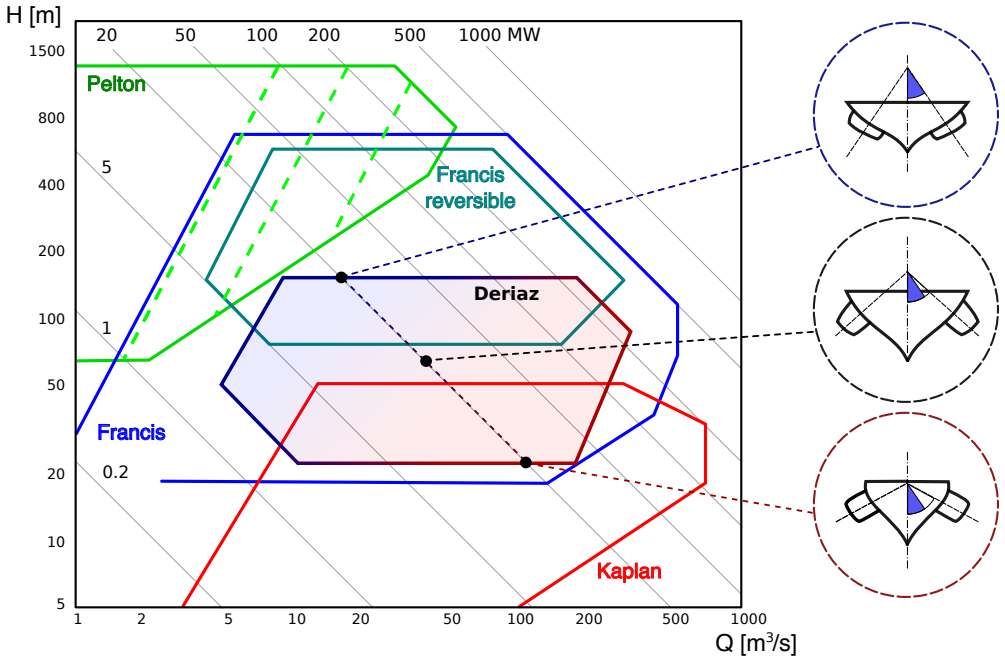

Figure 2.14: Diagram discharge over head for the most common hydraulic turbines and Deriaz turbine at different blade pivot angles γ.

and outlet edges of the blade has no equivalent in the purely axial Kaplan runner (Fig. 2.13.b), locating the Deriaz machine between Francis and Kaplan turbines in terms of functionality where it also meets the need of all the frequent border cases between Francis and Kaplan turbines. The main difference in the blades from those of a traditional Kaplan turbine, is that their axes are not orthogonal to the turbine axis: the Deriaz offers runner shape adaptation based on the head available (Fig. 2.14). Corresponding to progressively higher heads, the blade pivot angle γ decreases, moving from a mainly axial configuration to a more radial one.

Different shapes for the casing were used during the first tests in the 1950's. At first, the case was based on a conventional spiral casing (Fig. 2.15), but good research results were obtained even with a shape that remarks the oblique direction of the flow though the adjustable guide vanes or the respective diffuser in pump mode [Deriaz 1955]. During the period of design, discussion might emerge as to whether the casing should be a diagonal flow type as in the Sir Adam Beck Niagara power station or a radial type. The radial flow type is preferable for its simple construction and easy assembly although it is hydraulically disadvantageous for its slight decrease in efficiency at large flow when operated as a turbine [U. Tsuneo et al. 1964].

Another important design feature of the Deriaz pump-turbine is that it is possible to create full contact between adjacent blades for the entire length of the edges to complete the closure (Fig. 2.16). Theoretically, the machine can therefore be shut

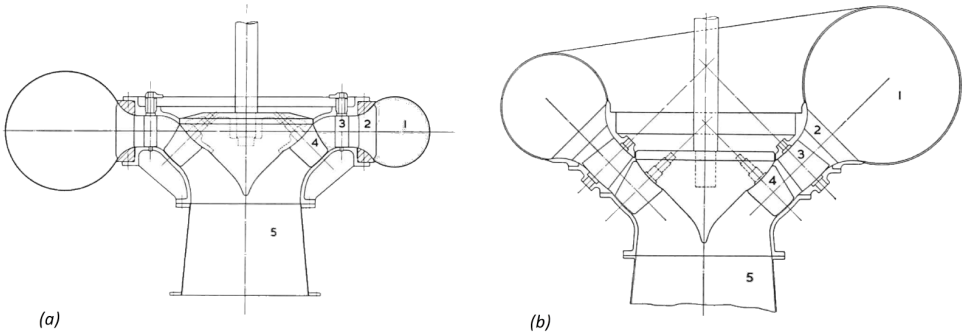

Figure 2.15: Shapes of Deriaz pump-turbine casing: (a) original shape; (b) second shape [Deriaz 1955]. 1) Case. 2) Stay vanes. 3) Adjustable guide vanes. 4) Blades. 5) Draft tube/suction pipe.

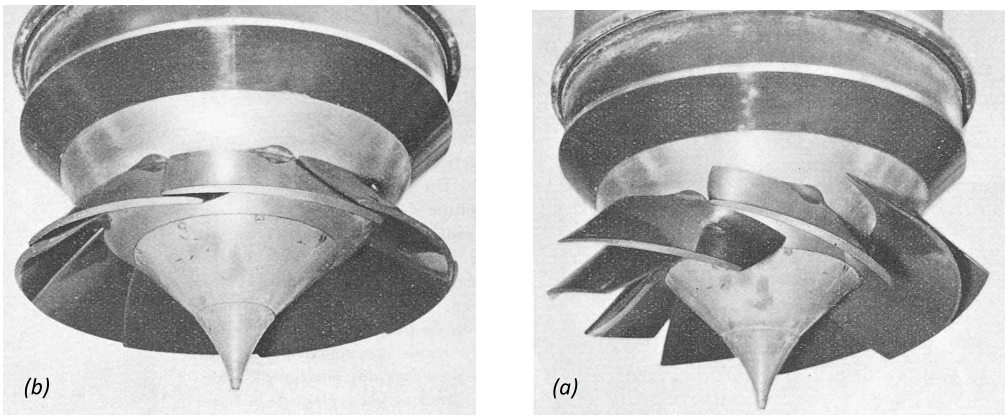

Figure 2.16: Deriaz runner normally open (a) and closed (b) [Deriaz 1955].

down without using a conventional gate apparatus or inlet valve. The omission of the closing apparatus allows considerable simplification of the plant, leading to a smaller powerhouse and reduced costs. Moreover, the versatile Deriaz turbine is designed to be used as a pump. The change of operation involves merely reversing the direction of rotation. It is only necessary to close the blade, shut it down, (even with the head gate fully opened) and then restart [Deriaz & Warnock 1959b].

Regarding a more global value such as efficiency, η, several tests comparing a Francis turbine of the same specific speed and size show how a Deriaz prototype can achieve a very flat curve and provides a better overall performance at partial load (Fig. 2.17). More recent studies have shown the improvement of a Francis solution for variable head reaching a higher maximum value of efficiency, but still over a smaller load range than Deriaz turbomachines [Skotak & Stegner 2014].

In addition to their improved efficiency over a wide load range as a result

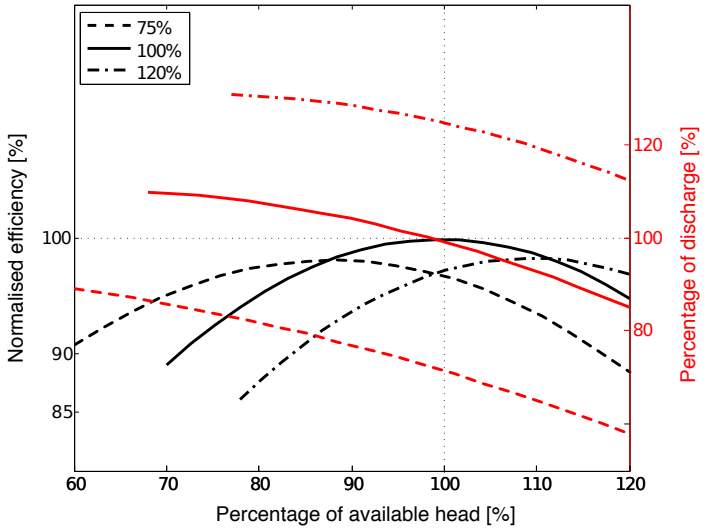

Figure 2.17: Normalised efficiency (in black) and discharge (in red) vs head for 75 %, 100 % and 120 % opening blade angles of Deriaz pump-turbine [Deriaz & Warnock 1959b].

of runner blade adjustments, Deriaz turbomachines can also work under variable rotation speeds. Some PHES systems couple the motor/generator to a frequency changer enabling a wider range of pumping or generating speeds (± 12 %) [Schlunegger & Thöni 2013]. For optimum efficiency at a designed available head, a reversible pump-turbine with fixed runner blades requires a higher pump speed than generating speed. This can result in the use of different running speeds for pump and turbine operations.

From an electrical point of view, the speed variation is achieved through a decoupling of the machine from the grid in terms of reactive power, voltage and frequency by means of a power converter. Although a Francis turbine can benefit from this technology, it has been shown that a variable speed Deriaz can take about up to 1.5 times the input capacity of a Francis turbine with VFD [Miyagawa *et al.* 1998].

2.4.2 Deriaz in PHES plants

The current focus on smarter energy use has strengthened interest in the complementary use of RES and EES systems [Koohi-Kamali *et al.* 2013]. The increasing use of RES for electricity generation, many of which have an unpredictably intermittent nature, will inevitably lead to a greater need for storage technologies.

Pumped storage is currently by far the most common form of on-grid electricity storage. During off-peak hours, energy is stored in the upper reservoir by pumping water back. During peak hours, the water is released to the lower reservoir through hydraulic turbines that generate electrical power.

The operational conditions of PHES are perfectly suited to a reversible tur-

bomachine that can function as both a pump and a hydraulic turbine. A Deriaz turbomachine is able to work in both pump and turbine mode by reversing its rotation direction. Moreover, they can adapt quickly to fluctuations in demands for electricity.

By using a reversible machine such as a Deriaz, a PHES plant can make better use of available space by reducing the size of the power house required. A Deriaz is also more efficient at partial load (Fig. 2.17). Available head might vary while the upper reservoir is refilling or emptying, which will be more evident in small PHES systems where the volumes of water are usually smaller. As a result, even though pumped storage plants generally operate at an overall cycle efficiency between 0.75 and 0.80 [Rehman *et al.* 2015b], they are economical to construct and operate due to the increased efficiency of the entire, integrated electric generating system of the utility.

The geometry of a Deriaz machine can also change by means of its adjustable runner blades thanks to a mechanical or hydraulic system inside the rotor. It is thus possible to combine a high level of adaptability and efficiency in the same runner. Table 2.2 provides a list of sites where Deriaz pump-turbine has been installed and the following subsections illustrate three of these power plants underlying some of the Deriaz pump-turbine features.

Table 2.2: Pumped storage plants using Deriaz pump-turbine.

Power station	Size* [MW]	Year	Country**	Nr unit
Adam Beck [Maricic *et al.* 2009]	29	1954	CA	6
Gangnan [Zhang *et al.* 2015]	11	1968	CN	1
Miyun [Zhang *et al.* 2015]	22	1975	CN	2
Sesquile	100	1964	CO	2
Valdecanas [Castillo 1964]	75	1964	ES	3
Naussac [Houdeline & Verzeroli 1999]	3	1995	FR	1
Culligran [Roberts *et al.* 1965]	17	1966	GB	1
Kadana [O. Thapar 2017]	61	1977	IN	4
Maharashatra [ČKD Blansko 2012b]	52	2012	IN	2
Ananaigawa	13	1964	JP	1
Kagedaira	46	1968	JP	1
Kuromata II [Imanishi 1964]	17	1963	JP	1
Masegawa I	144	1976	JP	2
Niikappu [MHI Japan 2017]	100	1973	JP	2
Takami [MHI Japan 2017]	103	1983	JP	2
Takane I	88	1969	JP	4
Niedzica [Niedzica 2017]	92	1997	PL	2
Czorstyn [ČKD Blansko 2012a]	42	1990	PL	2
Liptovsk [Slovenske Elektrarne 2017]	97	1975	SK	2
Dos Amigos [Ruud 1976]	18	1963	US	3

(∗) Power size per unit

(∗∗) Country code adopted by the two-letter Standard ISO 3166-1.

Sir Adam Beck generating station - Canada

The 174 MW Sir Adam Beck Pump Generating Station and its 300-hectare reservoir were constructed at the same time as the Sir Adam Beck II Generating Station [Maricic *et al.* 2009]. Water diverted to the Sir Adam Beck generating complex is typically pumped into the reservoir at night so it can be used to generate electricity during subsequent periods of high demand. Six mixed-flow variable-pitch Deriaz pump-turbines are installed at the pump generating station and can fill the reservoir in about eight hours. The pumped-storage scheme enables a more effective use of the water that is available for power production under the Niagara Diversion Treaty of 1950 [Maricic *et al.* 2009]. It offers a method for translating what would be surplus energy at times of low demand into primary energy at times of high demand. The change over from turbine to pumping sequence is accomplished in a matter of minutes and occurs several times each day. The guide vanes are equipped with adjustable flaps, which control the flow angle at the inlet of the turbine runner and are deflected according to the head level (Fig. 2.18). When the machine works as a pump, these vanes function as a diffuser and the flaps are placed in line with the vanes so as to not increase hydraulic losses.

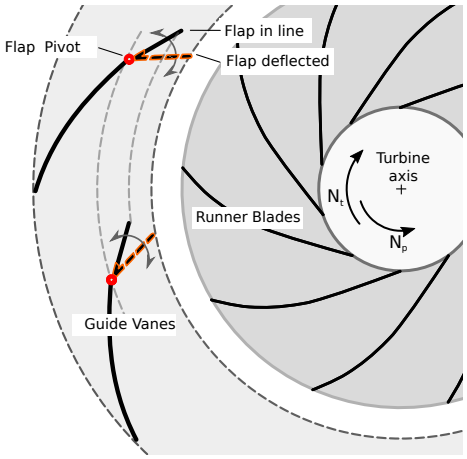

Figure 2.18: Radial view of Deriaz turbine guide vanes installed in Sir Adam Beck Station, Ontario - CA.

Culligran plant - Great Britain

The Culligran site is located in a Scottish National Reserve where a 17 MW, 10 blades Deriaz turbine is coupled with a 2 MW Francis turbine [Roberts *et al.* 1965]. Scottish and Southern Energy plc invested in an 18-month project to refurbish the 43 years old Deriaz turbine in order to extend the plant's operating life by a predicted further 30 years' without further major refurbishment or significant capital expenditure and to maximize efficiency and output. The runner chamber of the turbine was suffering from severe cavitation and it took 12 manufacturing facilities

throughout Europe to manufacture all the components [Erskine & Van Rooy 2004]. Particularly high machining precision was needed to not exceed the 1.5 mm gap between the blades and the chamber wall so as to avoid cavitation or the disastrous consequences of blades coming into contact with the chamber wall. Modern computational tools (CAD, CFD and FEA) were used in the design and testing of the new Deriaz runner to ensure that the requirements of the project were met [Erskine & Van Rooy 2004].

Kuromatagawa plant - Japan

Kuromatagawa II power station adopted a vertical shaft Deriaz pump-turbine in 1963 in order to deal with a large head variation and to attain high efficiency at partial load. The maximum available head in this case is twice the minimum operational head (39 m) [Imanishi 1964]. Moreover, the pump-turbine, coupled with a pole change generator-motor, has two speed operations in order to improve performance. The ratio of unit speeds at maximum efficiency during turbine and pump operation is about 1.1, the same as for the Francis type pump-turbine [Imanishi 1964]. In Kuromatagawa plant, the Deriaz operates at 333 rpm during pumping at high head and 300 rpm in turbine mode from an effective head of 78 m to 39 m with a maximum discharge of 28 m^3/s [Imanishi 1964].

2.5 Pump as Turbine (PaT)

Pumps behave differently when they work in reverse in terms of forces, flow and power [Binama *et al.* 2017]. A pump increases the fluid pressure by the conversion of mechanical energy; in the opposite rotational direction, the PaT exploits the head available to generate power. Since the rotational speed and the flow direction are inverted in turbine mode, the speed triangles change as a consequence. Fig. 2.19 illustrates qualitatively the complete characteristics of a pump in four quadrants.

The normal operation of a pump is represented with a positive rotational speed, $N+$, and positive discharge, $Q+$. Increasing the discharge from a normal operation above its limit, the pump is not able to deliver a positive head. $H < 0$ expresses the higher pressure at the pump inlet than at the pump nozzle: in this area, the pump runs as an abnormal turbine. However, PaT operation is located at $H > 0$ condition at negative rotational speed, $N-$, and negative discharge, $Q-$. Here, the effective characteristic curves are limited by the asymptote for torque equal to zero, the runaway limit, and the hydraulic resistance of the PaT at $N = 0$. Under $H > 0$ (higher pressure at the pump outlet than at the inlet), PAT operating conditions can range according to the characteristics defined by the rotational speed N_{T1}, N_{T2}, etc. The effective characteristic curves are limited by the runaway curve for torque, M, equal to zero. A second operational limit is reached by the characteristics of the hydraulic resistance at $N = 0$ (Fig. 2.19.b). This curve is the result of water friction inside a no-rotating runner. Fig. 2.20 illustrates diverse operating regimes of a pump for Q, N and H.

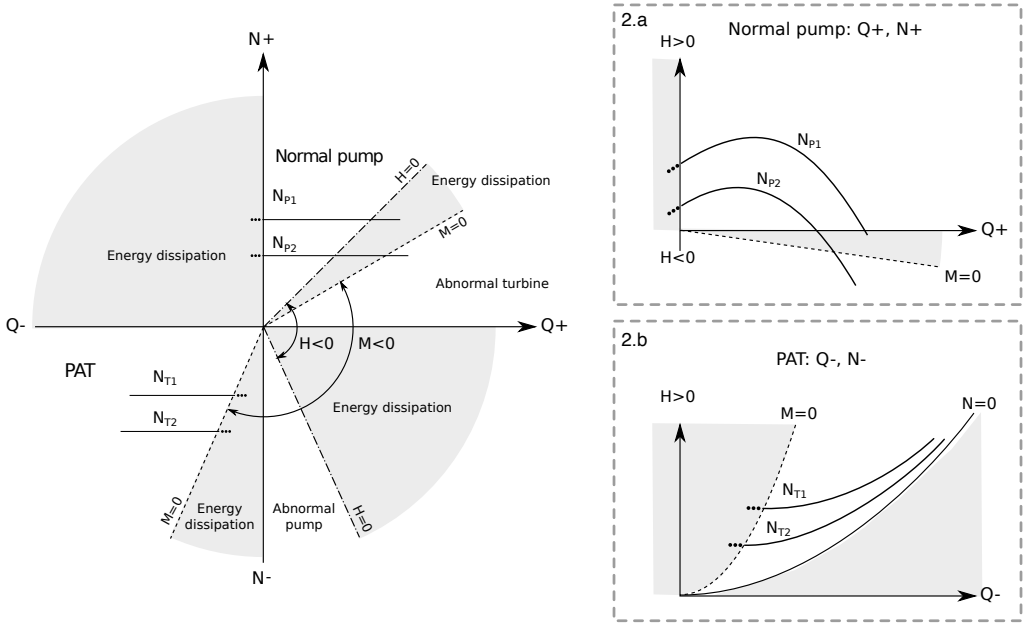

Figure 2.19: Complete pump characteristics in four quadrants defined by the rotational speed, N, and the discharge, Q. Normal pump and PaT characteristics are showed in ⓐ and ⓑ $H - Q$ quadrant.

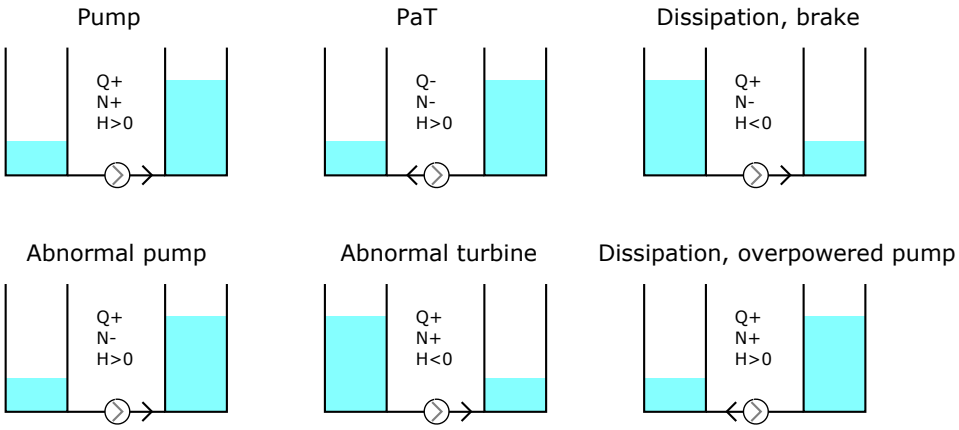

Figure 2.20: Representations of the operating regimes in four quadrants.

When the pumping system is no longer able to efficiently deliver a positive discharge against a static head, the minimum operating pump shaft speed is defined in respect of the practises for a good pump reliability at each speed (Fig. 2.21). Design engineers define the constraints for the system, such as flowrate, NPSH margin, or fluid velocity to preserve the reliability of the system [Barringer 1997].

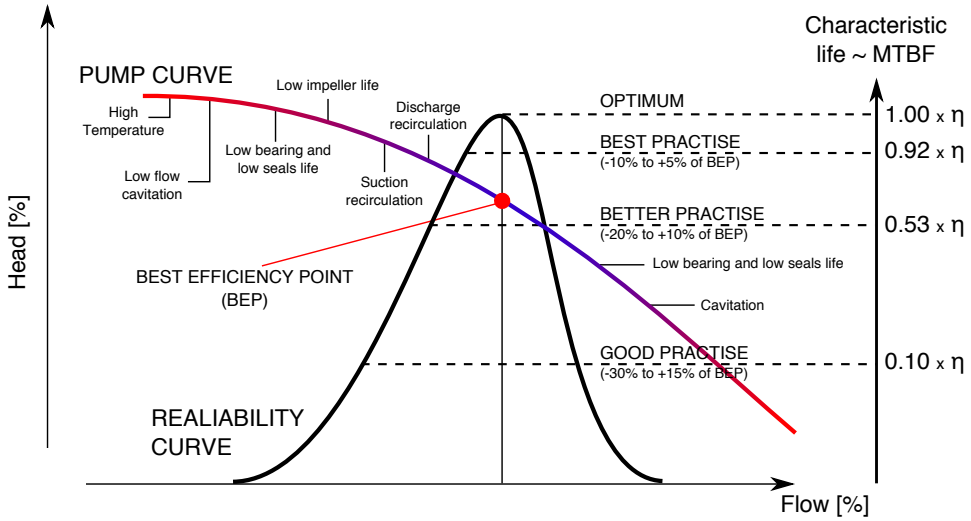

Figure 2.21: Reliability impact (MTBF) of operation away from BEP to ANSI pump, adapted from [Barringer 1997].

The characteristic defined by Mean Time Between Failures (MTBF) aside the chart in Fig. 2.21 estimates the probability that the pump will operate for its expected lifetime without a failure. The extreme operating conditions affect the total cost of the system and should be avoided. Hence, the minimum operating speed to each working condition is specific. In reverse mode, according to the velocity flow angles at the inlet and outlet of the runner at the selected rotational speed, PaTs are able to deliver a power-output or a positive torque (M $>$ 0) only above a minimum flow-rate Q_{MIN} as also showed in Fig. 2.19.b. Below this value, the PaT power output is negative. In other words, for Q_{MIN} and consequently at $H < H_{MIN}$, the power station is actually dissipating energy to maintain the runner at the constant N_T. If possible, N should be re-set, when appropriate, updating the minimum values of Q_{MIN} and H_{MIN}.

Different series of PaTs can be selected according to the performance required and the efficiency curve itself is affected whether a PaT is operating off-grid [Capelo *et al.* 2017]. With regard to the flow and pressure, multi-stage PaTs for high head and double suction PaTs for high discharge can be selected (Fig. 2.22).

One of the key advantages of PaT is that it can have a payback period five times shorter than for conventional micro hydro-turbines, although PaT hydraulic efficiency is usually reported as being lower [Orchard & Klos 2009]. Economically, PaTs below 500 kW are profitable in hydropower and allow capital payback periods of about two years [Paish 2002, Motwani *et al.* 2013]. A few manufacturers are also now producing PaTs close to 1 MW. Moreover, pumps have a larger market demand than small sized turbines, are more robust and easily installed. PaTs thus provide a solution for those hydropower sites in which conventional turbines might not be affordable.

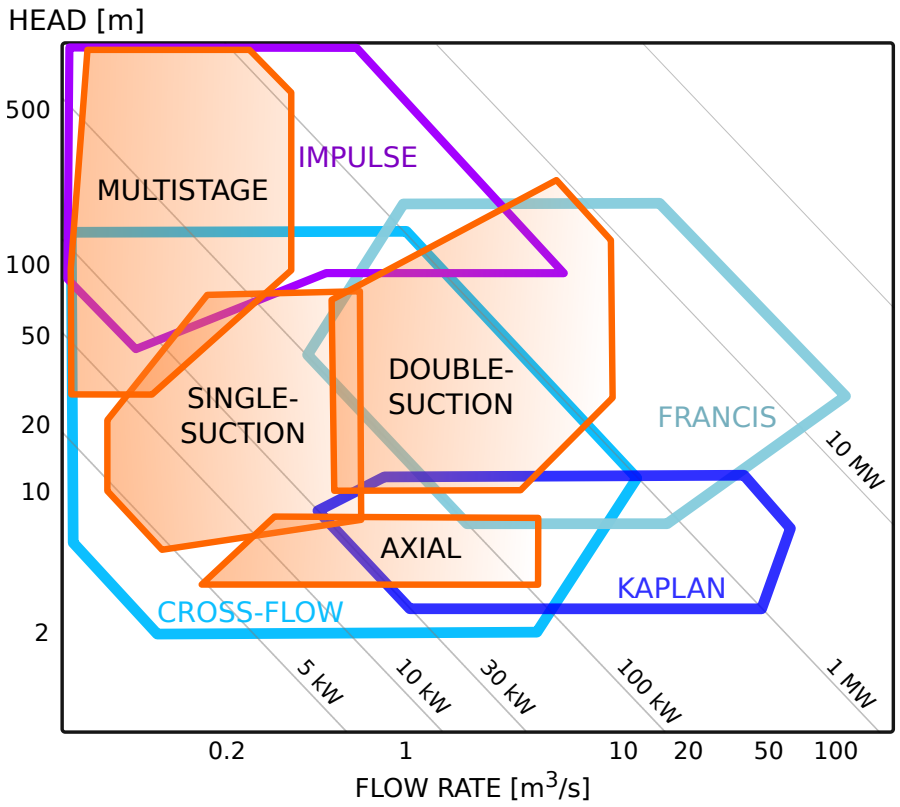

Figure 2.22: Types of hydraulic turbines and PaT (multistage, single suction, double suction and axial type) in their application area Q-H for micro-hydropower. Adapted from [Andritz 2019] [Sulzer 2019] [Paish 2002] [Pérez-Sánchez *et al.* 2017].

PaTs are most applicable to micro hydropower stations from natural water streams in rural areas [Nourbakhsh *et al.* 2010a], but also to urban water distribution networks, exploiting the excess of energy that can be present along any branch of the system [Carravetta *et al.* 2012]. The pressure along the distribution network has to be kept in balance. Usually valves are used to dissipate this excess of energy, but PaTs are an interesting technical solution that ensures both economic convenience and system flexibility [Carravetta *et al.* 2013].

Thoma, D. and Kittredge, C. [Thoma & Kittredge 1931] first investigated the use of pumps as turbines in the last century in order to recover energy from high-pressure circuits in heavy industry or chemical systems. The common alternative before that was to throttle the flow and waste energy. For decades researchers discussed the hydraulic behaviour of pumps in reverse mode and tried to formulate a function or a model able to define the hydraulic performance. A collection of proposed correlations is summarized in Table 2.3. The prediction models focus on the definition of the head and flow of the best efficiency point in reverse mode. The ratios $h = H_t/H_p$ and $q = Q_t/Q_p$ relate the BEP working condition in pump mode with the turbine mode at the same rotational speed. It

Table 2.3: Performance prediction methods for PaT.

Researcher	Criteria	Head ratio, h	Discharge ratio, q
[Stepanoff 1957a]	BEP	$\frac{1}{\eta_p}$	$\frac{1}{\sqrt{\eta_p}}$
[Childs 1962]	BEP	$\frac{1}{\eta_p}$	$\frac{1}{\eta_p}$
[Hanckock 1963]	BEP	$\frac{1}{\eta_t}$	$\frac{1}{\sqrt{\eta_t}}$
[Grover 1980]	N_s	$2.693 - 0.0229N_s$	$2.379 - 0.0264N_s$
[Hergt 1982]	N_s	$1.3 - \frac{6}{N_s - 3}$	$1.3 - \frac{1.6}{N_s - 5}$
[Sharma 1985]	BEP	$\frac{1}{{\eta_p}^{1.2}}$	$\frac{1}{{\eta_p}^{0.8}}$
[Schmiedl 1988b]	BEP	$-1.4 + \frac{2.5}{\eta_p}$	$-1.5 - \frac{2.4}{{\eta_p}^2}$
[Alatorre-Frenk 1994]	BEP	$\frac{1}{0.85\eta_p^5 + 0.385}$	$\frac{0.85\eta_p^5 + 0.385}{2\,\eta_p^{9.5} + 0.205}$
[Nautiyal *et al.* 2011]	BEP, N_s	$41.667\left[\frac{\eta_p - 0.212}{\ln(N_s)}\right] - 5.042$	$30.303\left[\frac{\eta_p - 0.212}{\ln(N_s)}\right] - 3.424$
[Yang *et al.* 2012a]	BEP	$\frac{1.2}{{\eta_p}^{1.10}}$	$\frac{1.2}{{\eta_p}^{0.55}}$
[Derakhshan & Nourbakhsh 2008a]	N_s	$f(N_p, N_t)$	$f(N_p, N_t)$

appears that PaTs usually have a BEP located at higher discharge and higher head compared to the normal pumping operation at the same rotational speed [Nourbakhsh *et al.* 2010a]. Thus, the fluid power (proportional to the product of H and Q) engaged by the turbine would be higher than the power employed by the pump rotating at the same speed, assuming an identical efficiency. The pump hydraulic efficiency is fundamental for the formulation of several prediction models: Alatorre-Frenk [Alatorre-Frenk & Thomas 1990], Childs [Childs 1962], Schmied [Schmiedl 1988b], Sharma [Sharma 1985], Stepanoff [Stepanoff 1957a] (Table 2.3). Other predictive models are based on the specific speed, N_s [Lewinsky-Kesslitz 1987, Derakhshan & Nourbakhsh 2008a, Derakhshan & Nourbakhsh 2008b], which describes the runner or impeller of a turbomachine linking mass discharge, rotational speed and energy. It ranks turbomachines based on their working conditions and it is expressed for pumps Eqn. 2.1 and turbines Eqn. 2.2 at BEP values.

The literature describes experimental studies of model prediction formulations. Errors in the sampled efficiency evaluation used for the correlation is at 25-30% [Williams 1994b, Pugliese *et al.* 2016] but in certain cases, it can even be reduced to about 8% [Nautiyal *et al.* 2011]. Recently, one-dimensional numerical codes have become available to estimate the performances of centrifugal PaTs [Barbarelli *et al.* 2016] although they require highly detailed information which is not easy to get. Further research to develop a general model for accurately calculating the h and q factors is thus needed. Fig. 2.23 shows that, beside a visible exponential trend, the discharge ratio and head ratio endure a large deviation: at the case of $N_s = 25$, h and q are subject to about $\pm$ 40% and $\pm$ 20% deviation respectively.

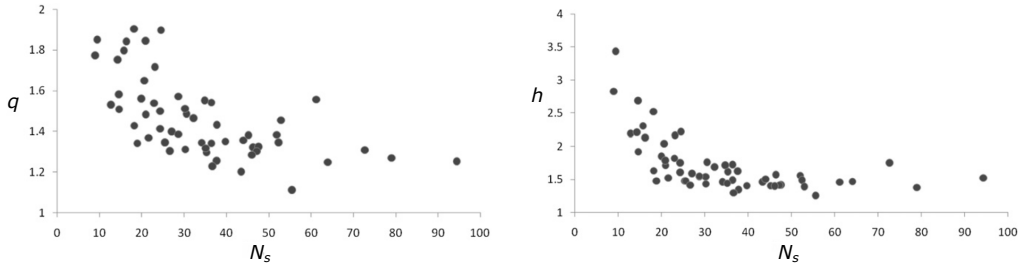

Figure 2.23: Discharge and head ratio of tested pump [Yang *et al.* 2012a]: high variation of the reverse mode performance results, especially, at low specific speed.

2.5.1 Variable speed regulation applied to PaTs

As mentioned before, PaTs are usually not equipped with guide vanes, as traditional turbines, nor with adjustable runner blade, like Kaplan or Deriaz turbines. For this reason, the operating point of a PaT at fixed rotational speed lays on a single curve and not in an operational area (Section. 2.3.3). For large installations, PATs of different sizes can be used in parallel to provide modulated power output: the smaller will define the resolution of the modulated output while the sum of all the machines is the maximum value. Another alternative is coupling to a PaT a variable frequency drive (VFD) to modulate the rotational speed hence the total output.

Fig. 2.24 illustrates a schematic representations of the variable speed control for pumps (on the left side) and for PaTs (on the right). An initial steady condition, at rotational speed N, is pointed by a yellow circle in the intersection between the characteristics of the turbomachine, H_N, and the system, H_{SYT}. Hydraulic efficiency and power values correspond to these operating conditions. A variation of the load, that can occur with a variation of the system head curve, drives the new operating points on H_N curve far from high performance, compromising the safety of the turbomachine (red points on the figure). Changing the rotational speed, the head, power and efficiency characteristics curves move in the chart in order to match with the highest efficiency point. Thus, adjusting to N_1, a new set of characteristics is given (P_{N1}, H_{N1} and η_{N1}) and a new operating point at better performance is found (final green marks on the figure).

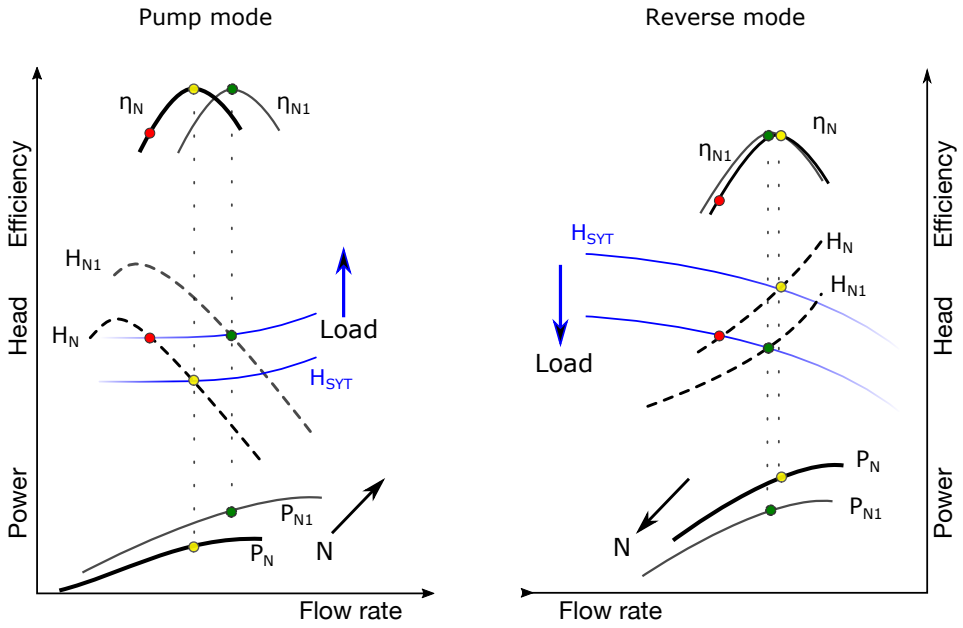

Figure 2.24: Qualitative representation of variable speed adjustments $N \rightarrow N_1$ under a raise of static head of the system (on the left) and a drop in available head for a PaT (on the right).

Variable speed driver raises the capital investment by approximately an equal cost of the pump (for micro-scale especially). Moreover, the efficiency of the driver must be also considered when evaluating the net power produced. On the other hand, the major advantages of variable speed generation, besides the objective of succeeding in load fluctuations, are:

- Fewer machines are needed with saving in space for the powerhouse and less equipment to maintain.
- The high inrush current at the start is remarkably reduced.
- Gradual changes are produced in the flow that does not upset the normal functioning of the system: pump and PaT can be ramped-up (or down) so that water hammer is reduced.
- The soft and reduced numbers of starts do not cause power dips and help the system maintenance, cutting the wearing on bearings and flexing of the shaft.

2.5.2 PaT efficiency improvements

It is clear now PaTs are good allies for the exploitation of micro hydropower in rural and remote DESs [Arriaga 2010, Ramos & Borga 1999, Teuteberg 2010]: PaTs are relatively simple, and their solid structure provides a reliable option for renewable energy provision. However, PaTs are reserving drawbacks in performance prediction, as there is not a universal model of conversion from normal operation [Pugliese *et al.* 2016, Jain & Patel 2014, Williams 1994a], and efficiency when compared to a conventional hydraulic turbine (Fig. 2.25). Many researchers have proposed analytical and experimental models in forecasting the stability and the best efficiency point (BEP) of a pump in reverse mode [Stepanoff 1957b, Schmiedl 1988b, Nautiyal *et al.* 2011]. However, the diversity of the experimental results and consequent difficulties in the validation of the developed predictive models [Binama *et al.* 2017, Rossi & Renzi 2017, Yang *et al.* 2012a] continue to motivate world-class research activities in this field, being of high interest for industry and academics in micro-hydropower [Barbarelli *et al.* 2016, Carravetta *et al.* 2013] and energy recovery instead of throttling [Carravetta *et al.* 2018].

Furthermore, pumps for industrial applications are not meant to run in reverse mode and their performance can shift appreciably from the higher efficiency of traditional hydraulic turbines. Many attempts have been studied and engineered to bring performance improvements in using PaTs. The study on coupling the effect of adjustable guide vanes (AGV) to an axial pump allowed Qian et al. [Qian *et al.* 2016] to generate a hill chart also in reverse mode and to extend the PaT operating range at high efficiency. This technology takes advantage of the variable guide vanes pitch to compose the most suitable velocity triangle at the inlet of the runner. On this topic, another experimental investigation shows the positive effect of a volute equipped with guide vanes for flow regulation [Giosio *et al.* 2015]. The act of providing inlet flow control can guarantee the PaT to operate efficiently at off-design

conditions, that could often happen in micro and mini hydropower system for the limited capacity of the water reservoir or during seasonal fluctuations of the water availability [Giosio *et al.* 2015]. However, common water pumps are not equipped with guide vanes and even less often with AGV. This additional feature affects the final cost of the pump and compromises the economic strength of PaTs unless to accommodate variable hydrological load conditions.

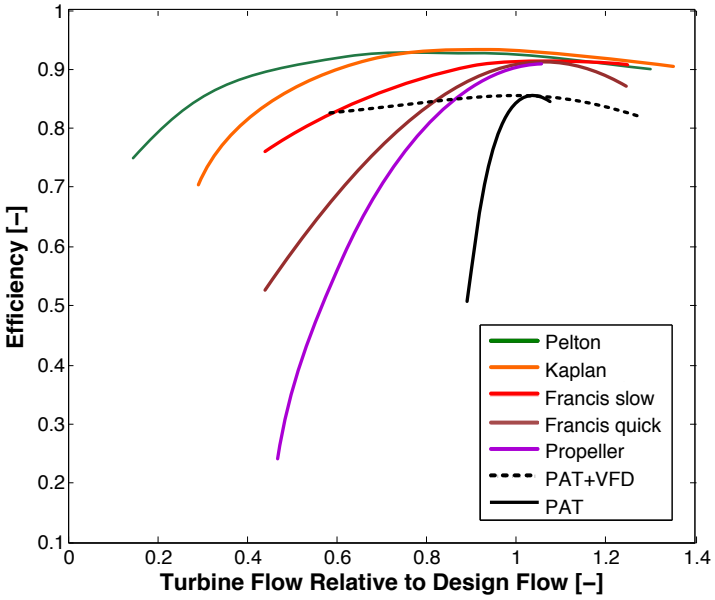

Figure 2.25: PaT hydraulic efficiency comparison with other traditional turbines for small scale hydro power plants (adapted from [Jain *et al.* 2015]).

Several efforts have been done to improve the impeller geometry. Miao et al. developped a parametric optimization of single-curvature blade profile of a PaT by combining the back propagation neural network and genetic algorithm [Miao *et al.* 2015]. Under the BEP condition, the efficiency of the PaT increased by 2.91% after optimization [Miao *et al.* 2015]. Efficiency impeller improvements for PaT operation have been presented by Derakhshan et al. [Derakhshan *et al.* 2009] by using a gradient-based optimization CAD-connected and supported by CFD validation. The new blade design results performing at about +3% better than the initial pump design and slightly reduced head and torque (-3% and -7% respectively) [Derakhshan *et al.* 2009]. Machine learning techniques, like regression models, have been applied to improve the design of an impeller for off-design and nominal working conditions by developing a multi-objective optimization problem [Asomani *et al.* 2020]. Wang et al. [Wang *et al.* 2017] conducted a numerical and experimental analysis of three new special forward-curve impellers. Although the efficiency improvements can be obtained, the impeller replacement represents a drastic and expensive re-design of the turbomachine. A less intensive geometrical modifica-

tion has been experimentally conducted on the rounding of the pump outlet edges of impeller pump blades, namely the PaT runner inlet. This operation mitigates the water shock at the inlet of the same pump in reverse mode and reduces the hydraulic losses through the blade channels [Patel *et al.* 2015]. The effect of the blade thickness on the PaT efficiency is proven by a throughout analysis of the hydraulic loss distribution in three different pumps which indicates that the total hydraulic loss in a PaT increases with the blade thickness [Yang *et al.* 2014b]. Further experimental investigations have been performed on other geometry modifications by the impeller trimming [Yang *et al.* 2012c], impeller diameter size [Yang *et al.* 2013, Jain *et al.* 2015], blade wrap angle [Yang *et al.* 2012b] and, again, impeller edges rounding [Derakhshan *et al.* 2009, Singh & Nestmann 2011, Doshi *et al.* 2017]. Moreover, the behaviour of several hydraulic components have been studied in a comprehensive investigation at BEP, part-load, and full load conditions to evaluate four different geometrical modifications in eight PaTs [Singh *et al.* 2004]: the inlet impeller rounding and inlet casing rings have been improved to increase the efficiency, while the modification of the pump suction eye enlargement and the casing eye-rib removal have shown a mingled effect on the performance [Singh *et al.* 2004, Singh 2005]. Additional theoretical and numerical analysis are present in the literature for the use of splitter blades in PaT: CFD steady-state simulations were found in good agreement with experimental results although a numerical overestimation of the efficiency due to neglected hydraulic losses [Sun-Sheng *et al.* 2012]. Capurso et al. developped a novel impeller design for low-medium specific speed double suction centrifugal pump [Capurso *et al.* 2019a] and analysed in reverse mode [Capurso *et al.* 2019b]. The novel double suction impeller is characterized by a new arrangement of its flow channels, that come up alternately on the same circumferential exit. Numerical analysis supports the performance assessment of new channel arrangement for guiding the flow at the inlet of the PaT runner in absence of a diffuser [Capurso *et al.* 2019b]. Also, a numerical analysis has shown by steady-state simulations the presence of an optimum in the PaT overall performance of the three pumps analysed by the effect of the radial gap at the rotor/stator interface [Yang *et al.* 2014a]. Finally, new designs of the volute casing have been numerically analysed to reduce radial forces affecting the pump normal and reverse operation [Arani *et al.* 2019]: the novel casing design provides a more sustainable mechanical operating conditions, allowing the PaT to run with competitive hydraulic efficiency. Recently, the same research group of the University of Tehran demonstrates the implication of the cutwater for a low-specific speed pump ($N_s = 10.3$) performance by an experimental study over the pressure fluctuation in the rotor/stator interaction [Alemi Arani *et al.* 2019]. Thanks to these few preliminary studies about the effect of the cutwater, it has been possible to foresee its design potential in reversed mode, but the existing literature concerning an effective methodology in its design optimization is missing. Chapter 5 of this thesis provides the tools for filling this gap.

Chapter 3

Definition of a framework

Contents

3.1 Introduction

As discussed in the introduction, today, humanity faces one of its most significant challenges, prompted by the limits and consequences of a historical over-reliance on fossil fuels. Renewable energy sources (RES), such as photovoltaic panels, hydropower, and wind turbines, are spreading in our surroundings, delivering today a vivid feeling of energy independence and environmental care. Micro-distributed energy generation systems (or micro-DES) are expected to grow in this renewed energy industry [European Commission 2012a]. However, questions still abound on its economics, and its "integration on an aged, capital-intensive energy infrastructure" [Braun & Hazelroth 2015], which has been supporting for about a century our economy. In the context of global digitalization and decentralization, the push in

Table 3.1: Summary of the energy infrastructure trends[Barbour *et al.* 2016, Yekini Suberu *et al.* 2014, Braun & Hazelroth 2015].

Energy infrastructure	**Overarching trends**	**Example**
Primary energy supply	De-carbonization	Increasing renewable energy share in supply portfolio
Energy transport and delivery	Interoperability and stability of electricity grid	Ensuring reliable and flexible energy supply
Energy use	Electrification	Plug-in electric vehicles
Electricity supply and storage	Decentralization	Hybrid electricity RES and storage for buffering demand variability
Grid operation	Distributed intelligence in energy management	Micro smart grid with automated regulation of local demand
Energy services	Local and individual ownership of productive energy assets	Photovoltaic system for local electricity costumers

innovation unbalances the traditional business model in energy economics and it looks at unexplored solutions. Table 3.1 summarizes and gives examples of the encompassing trends that are reshaping the energy infrastructure in these modern days.

The direction to take is clear, but the path is evolving. For instance, Elia, the Belgian transmission system operator (TSO), has recently illustrated the future prosumer-centric-model, in which the demand will follow the generation players (Fig. 3.1). There are critical challenges and opportunities in this new market, and electrical energy storage (EES) could lead this transition into successful opportunities. The evolution of renewable DESs and small- and micro-scale EES systems is today a real cost-effective solution in cutting-off the energy dependence of fossil fuel and offers a unique opportunity to reduce transmission and distribution network capacity requirements, decrease electrical losses, and potentially improve reliability and energy efficiency.

In this chapter, the outcomes of three research projects are presented with the purpose of underling the raising interest in innovative developments of PHES solutions and to illustrate their technological and economical potential.

Section 3.2 is extracted from the journal article *Using hydropower waterway locks for energy storage and renewable energies integration*, published in Applied Energy journal in collaboration with the Laboratory of Fluid Dynamic and Particulate (FluidPar) of Federal University of Pará, Brazil. Waterways are one of the most used means for shipments. Besides transportation, waterways infrastructures can also be applied for hydropower and energy storage. Their specific locations and the

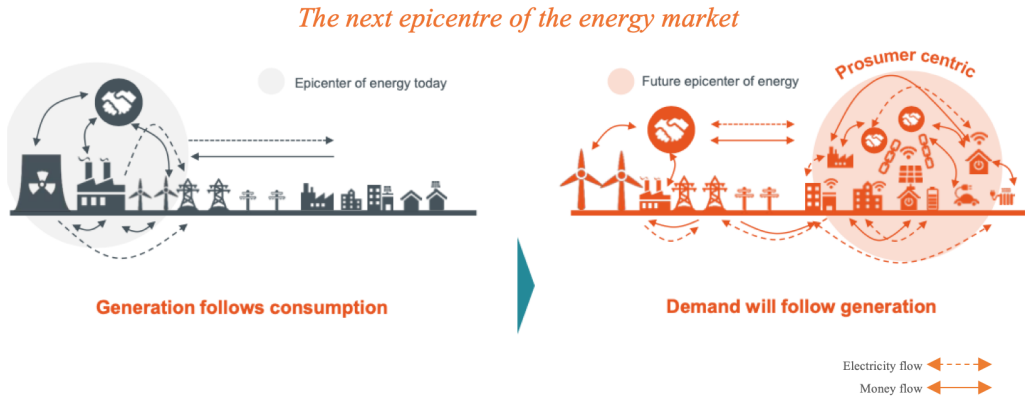

Figure 3.1: Elia vision of the shift towards "demand will follow generation" opens a new market [ELIA Group 2020].

presence of existing infrastructures lower down the initial capital investment for the integration of renewable energies and energy storage. This research analyses the energy supply solutions of the boat-lift, located in the locks of the Tocantins river in Tucuruí, Brazil. A photovoltaic power station is compared to a hybrid power generation system, which is composed of photovoltaic arrays and a micro pumped-storage facility. These two alternatives are discussed technically and economically, including the operation regime of the turbomachinery used in the EES system. Interestingly, the analysis shows that the hybrid system energy solution is the most viable alternative to the case study, and the payback time of the designed hybrid system is calculated to be 6.8 years. This system could handle up to 263 kW and 387 kW of power electricity, respectively, in turbine and pump modes. This research project gathers crucial data on the use of hydropower in waterways, and it supports the integration of renewable energies on the infrastructure of the locks.

Section 3.3 presents some of the outcomes of Smartwater project, published in *Underground Pumped Storage Hydropower Case Studies in Belgium: Perspectives and Challenges*, an Energies journal article. In order to strengthen the Belgian EES capacity, a feasibility analysis of existing underground cavities as lower reservoirs for UPHS facility is conducted. In Belgium, in the 18th century, the exploitation of coal mines became historically intense with the usage of heavy machinery for extraction and the more powerful dewatering pumps. In 1900, Belgium was counting over 300 mines for a total of about 20 million tons of national production, second only to England. After that, the production starts declining, recording the closure of the last coalfield in the Sambre-Meuse Valley in 1984. What is left today in Belgium is a very high number of abandoned mines and quarries coming from an important but now passed mineral-processing industry (Fig 3.2). In this section, two Belgian case studies for UPHS facility are presented and discussed for their singularity. A slate quarry in Martelange is discussed in technical aspects proposing three operating scenarios. Moreover, a preliminary economic analysis of the underground pumped storage system and a greenhouse gas emission evaluation

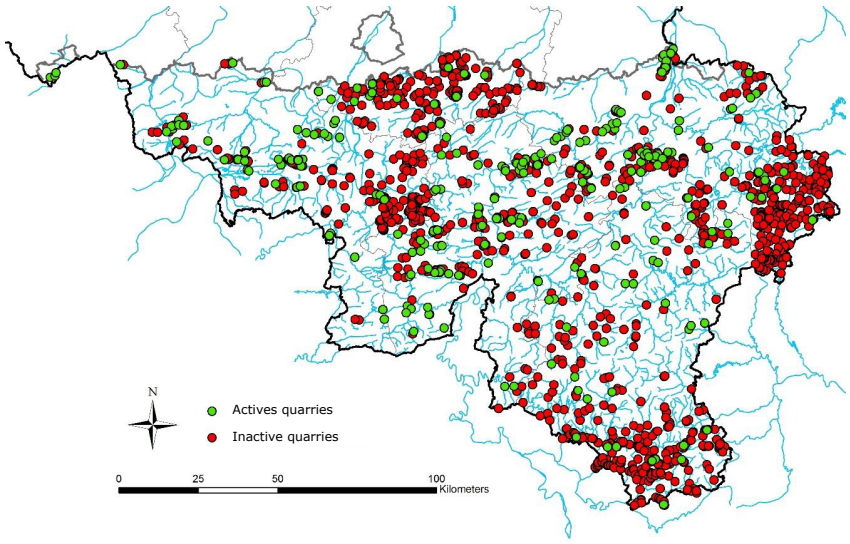

Figure 3.2: Mine and quarry exploitation in the Walloon region [Smartwater, 2017].

for the storage system's lifetime are presented. The analysis for a 100 MW power plant estimates a total initial investment of over 12 million euros. This research also proposes the use of the coal mine 500 m deep of Pérronnes-lez-Binche. The formulated representation of the mine offers a high energy capacity, but the substantial head drop of 60% (from about 500 to 200 m) challenges the selection of the hydraulic turbomachinery. A 1D simulation, computed in SIMSEN software, draws out the behaviour of the unusual hydraulic configuration of turbines in series.

Finally, Section 3.4 focuses on downsizing an existing Deriaz pump-turbine for μ-PHES applications and evaluating its performances by numerical simulations. The growing importance of the efficiency and operational range of PHES installations, especially for variable load operations, calls for the use of more efficient turbomachinery designs. As presented in Section 2.3, Deriaz turbomachines are promising candidates, since, among other advantages, they can operate as reversible pump-turbines with high hydraulic efficiency over a wide range of operational loads. Deriaz pump-turbines are largely absent from the literature and this section evaluates the Deriaz turbomachine potential and its performance, providing a unique and much-sought guide to its design, scaling, and adaptation to pumped hydro. Particular attention is given to the hydraulic characteristics and design of a downsized model (6-21 kW) suitable for micro-scale PHES applications. The analysis is supported by extensive numerical simulations for different working conditions and validated by experimental data. The results confirm the superior characteristics of Deriaz pump-turbines and validate the design process, which is described here for the first time. The complementary work on a practical and easily-built method to implement a micro Deriaz pump-turbine runner, which gives a good outline for design at high yield (about 90 %), is reported in the Appendix A. The comprehensive research, titled *Deriaz pump-turbine for pumped hydro energy storage and micro applications*, has been published in Journal of Energy Storage.

3.2 Micro PHES design: the Tucurui case study

3.2.1 Introduction to the project

Waterways are one of the most efficient means for transportation for inland infrastructure not subject to heavy congestion problems. In the city of Tucuruí, Brazil, the dam of the hydropower plant on the Tocantins river creates a water height difference of 61.7 m. Two locks allow the water transport and passage of local goods in the state of Pará. The operation of these locks is under the responsibility of the National Department of Transport Infrastructure (DNIT), regardless of the adjacent hydroelectric plant.

Several studies have been conducted over the environmental effects of the Tucuruí dam and its upper reservoir. Curtarelli et al. investigated, by mathematical modelling, the carbon emission due to the formation of the Tucuruí reservoir. The authors demonstrate the quantity emitted in the lake is of the order of 1.1 Tg of carbon per year, highlighting the importance of the carbon inventory in energy systems and the use of less environmental impact resources [Chen *et al.* 2015]. Chen et al. show the impact patterns in deforestation and forest degradation due to the construction of the aforementioned hydropower plant. The implementation of such a massive infrastructure (flooded area of about 3000 km^2) has affected the local biodiversity in addition to the consequences of urban development [Bhattacharjee & Nayak 2019]. Today, it is important to reduce the environmental and carbon footprint of the dam's appliances as the locks of the waterways. RESs are now considered an important and strategic way of ensuring the sustainability of projects [Bhattacharjee & Nayak 2019, Sun *et al.* 2019] and the coupling with EES systems contributes in their optimal exploitation in terms of reliability [Javed *et al.* 2020] operations [Rehman *et al.* 2015a, Anilkumar *et al.* 2017a] and return of investment [Lian *et al.* 2019].

The project presented in this section demonstrates the potential of using Tucuruí locks with RES and energy storage considering two possible scenarios: one with pure photovoltaic energy supply and the other one with a solar-hydro hybrid system with μ-PHES. Moreover, the economic feasibility of each alternative and the payback are investigated. The evaluation of the alternatives studied in this section shows that the hybrid system with pumped storage is more economically (around 40 %) and technically feasible due, mainly, to the head availability and the high costs of a purely photovoltaic plant.

3.2.2 Characteristics of Tucuruí locks

The Tucuruí hydroelectric plant is the sixth largest in the world and has an installed capacity of 8,535 MW, distributed in 25 hydraulic turbine units of 350 and 395 MW power capacity. The turbines exploit a 61.7 m net head maintained by an impressive dam over 11 km. Its spillway is designed for a maximum flow of 110,000 m^3/s, the world's largest spillway for a hydropower plant. The Tucuruí locks, shown in Fig. 3.3, are installed by the hydropower plant, where the irradiance PV production at an average cost of 1.8 USD/Wp. In addition, the installation is located in the same existing dam structure and it takes the advantage of the available head for self-consumption. The head variation is related to the natural seasonality of the Tocantins River and the power generation of the plant. The difference between the affluent and turbined discharge gradually changes the head, causing it to vary by up to 15 m over a year. As it shares the hydropower plant upper reservoir, the upstream lock is also subject to the same variation in head, although the downstream level, which is independent of the power plant's lower reservoir, remains constant.

The studied energy system is composed of two locks connected by a channel that allows trains manoeuvres and crossings in navigation. Each structure is 210 m long, 33 m wide and is designed to operate independently. The filling and draining operations are carried out in approximately 30 min, with capacity to handle up to 19 thousand tons of load, in trains of 200 m length, 32 m wide and 3 m draft [DNIT - National Department of Transport Infrastructure 2018].

This geographical area benefits from bright sun exposure as demonstrated by Jannuzzi and Melo [Jannuzzi & de Melo 2013]. From the experience of developed countries, the application of photovoltaic systems follows a trend established by the combination of the continuous reduction of the costs of the solar modules with the increase of the tariffs of conventional electric power [Rüther & Zilles 2011]. The data available for solar irradiation in the Brazilian territory show an enormous potential for renewable energy production, although these values are subject to overestimation [Martins *et al.* 2008].

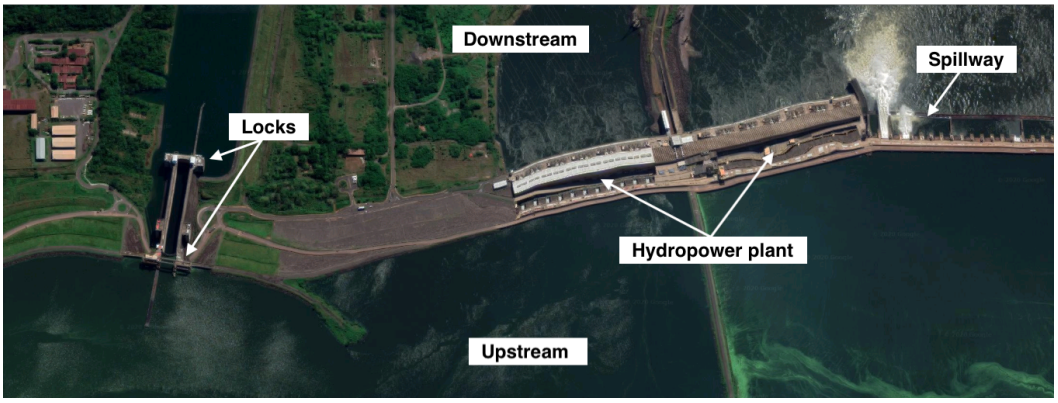

Figure 3.3: Overview of the Tucuruí hydropower dam and its locks.

3.2.3 The facility

The project consists of a facility for energy use taking advantage of the existing structure of the locks. The chamber, in its internal structure, has an unused aqueduct for communication between upstream and downstream levels independent of the filling and draining system, which can be utilized for the project. Fig. 3.4 shows the existing structure and a schematic representation of the planned project.

The hydraulic line of the hybrid system includes the set up of PaTs, selected with the aim of adopting an economic turbomachinery solution with shorter return of investment time [Derakhshan & Nourbakhsh 2008a], grid stability [Xu *et al.* 2019] and the possibility of rapid corrections in operational quantities to respond to changing demands of the facility and solar incidence on site. The total energy consumption of the locks is driven by the transportation operations (opening and closing the massive gates upstream and downstream the river) and filling and draining the locks themselves. The designed system consists of a photovoltaic solar source and a hydraulic source. The appropriate portion of PV or hydropower is carried out through an optimization process that offers the most attractive value in terms of cost and efficiency, in different consumption and generation scenarios.

Thus, the power supply for the installation can come in two ways: from the photovoltaic generation or the grid (in which energy is generated in a conventional manner, for example, at the adjacent hydroelectric plant).

A first calculation points out a 50 % split share is advantageous, although a proportion refinement is required, which will be the subject of future work. The coupled micro-hydropower plant and storage is envisaged to be formed by a group of pumps able to function also as turbines. The possibility of the pump operating as a turbine linked to a VFD guarantees the flexibility needed to meet the seasonal flow variations. The PaTs duty points are defined by the correlation between PV production and energy demand at each moment. This difference, positive or negative, is transferred to the hydraulic machine and defines whether it runs in pump or turbine mode.

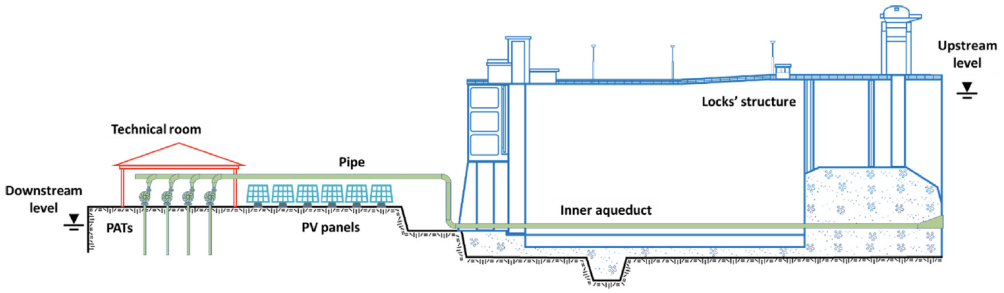

Figure 3.4: Schematic representation of the Tucuruí locks and of the installation.

3.2.4 The selection of the machines

The pump selection process is based, a priori, on the characteristics of the installation, namely the head and flow rates. The performance prediction of the pump selected to operate as a turbine will be the subject of future research on this system in Tucuruí. The suitable pump is determined considering the seasonal variations of the head due to Tucuruí lake level variation.

From the selected pump, the following procedure is performed to calculate the machine operation in variable rotational speed, guaranteed by a dedicated control system. Eqn. 3.1 shows the generic form of the pump and system equations, respectively.

$$H_p = a + bQ + cQ^2 \qquad H_{syt} = H_g + kQ^2 \tag{3.1}$$

By the similarity law for turbomachines, the quantities' rotation N, discharge Q, head H and power P are related to Eqn. 2.4, in their initial and final conditions.

By combining Eqns. 3.1 - 2.4 at the operating point, the following equation of the second order defines the relationship in $N_1 - N_2$:

$$\left[\frac{a}{N_1^2}\right] N_2^2 + \left[b\,\frac{Q_2}{N_1^2}\right] N_2 + \left[Q_2^2\left(c - \frac{H_1 - H_g}{Q_1^2}\right) - H_g\right] = 0 \tag{3.2}$$

In the configuration shown in Fig. 3.5 it is possible to grasp the modus operandi of the pumping system. This chart highlights four distinct regions that represent the possible operating areas for each set of machines. Please note only one machine turns at variable speed, operating in the region spaced between minimum (purple line) and maximum pump curves (green line). This PaT is coupled in parallel with the other three at constant rotational speed. This set-up sufficiently guarantees the pumping discharge- and head-ranges required to the installation. In the region A, a single pump operating at variable speed meets the system requirements. In the event of increased pumping needs, the facility operates in region B with the start of one more machine at a fixed speed. As the demanded flow increases, other units come into operation in regions C and D respectively in respect of the limits set by the pump manufacturers.

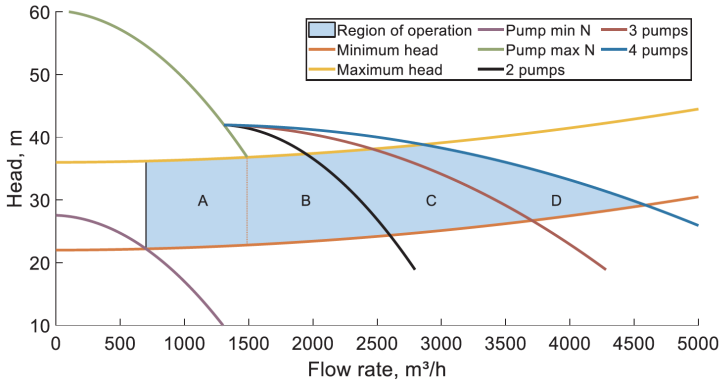

Figure 3.5: Pump mode system operation in Tucuruí micro PHES.

3.2.5 Operation scheme

Adding a micro-hydropower facility to the system reduces the amounts of PV panels, comparatively with the purely photovoltaic solution. In this arrangement, PaTs guarantee the necessary complement for supplying the energy for operation, taking into account the instant energy balance, according to $E_{PaT} = Demand - E_{PV}$. Fig. 3.6 presents the energy production by the installed photovoltaic field and by the PaT, while the negative values represent the energy consumed by the pump for storing the water upstream the river. This chart represents a case among the possible combinations of solar irradiation and demand. Therefore, in this hybrid system, the variation of the pump operating point is ensured by a dedicated speed control system, the object of research and detail in future research developments.

From the analysis of Fig. 3.6, it can be observed that the PaT operation depends on the instant balance between demand and photovoltaic production. Thus, due to the intermittent variation of the demand, it would be necessary to switch the machines often and in different power-sets. To prevent arising problems in the mechanical and electrical equipment, using the grid as an intermediate means of energy storage is proposed. In this regard, it is possible to establish a new operating schedule for pumping and generating modes, which avoids intermittent regimes as shown in Fig. 3.7. Here, while the intermittent consumption of the plant is supplied by the grid, the charge controller manages consumption and production at pump/PaT to ensure at the end of the day the balance in demand, generation and consumption.

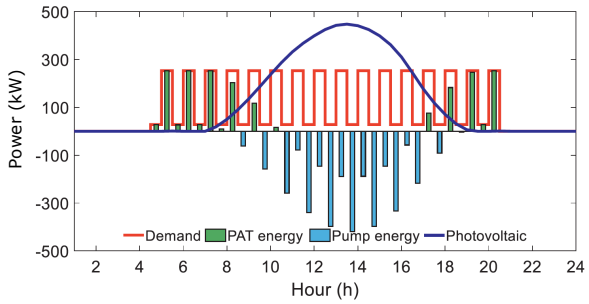

Figure 3.6: Power production in the hybrid system.

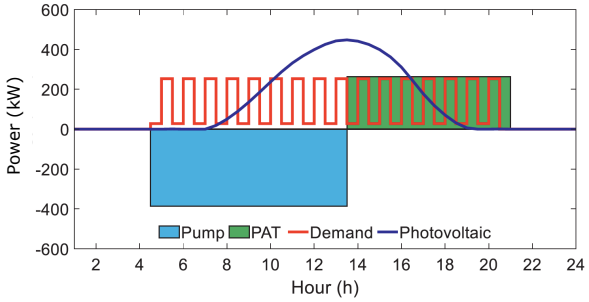

Figure 3.7: Hybrid system operation scheme.

3.2.6 Energy payback time

the payback time for photovoltaic and hybrid alternatives are calculated according to Eq. 3.3, considering capital costs C_0, operation and maintenance costs $C_{O\&M}$ and local energy tariffs (Table 3.2).

$$t = C_0/(COE - C_{O\&M}) \tag{3.3}$$

where the C refers to the estimations of local contractors, the O&M costs of these installations are considered to be 1% and 2% of the capital cost for photovoltaic systems for the photovoltaic and hybrid alternatives respectively, and COE is calculated based on the operating schedule and tariffs [National Electric Energy Agency 2018]. The complete description of the cost analysis is described in the published paper on this topic and it has been fully developed by Federal University of Pará, Brazil.

Table 3.2: Energy tariff in the Amazon region (US$/kWh) in 2018 [National Electric Energy Agency 2018].

	Peak time	**Intermediary**	**Off-Peak time**
Hour	18:30 to 21:29	17:30 to 18:29 21:30 to 22:29	22:30 to 17:29
Tariff - weekdays	0.3493	0.2241	0.1377
Tariff - weekend	0.1377	0.1377	0.1377

Fig. 3.8 shows the comparison between the proposed hybrid solutions and the conventional PV installation. It should be noted that among the alternatives the hybrid system presents better payback (6.8 years) compared to the pure photovoltaic system (11.2 years). Photovoltaic energy solutions are widely explored in the literature, applied in several cases aiming at autonomy, respect for the environment, laws and economic viability. The payback time is one of the aspects addressed to assess the viability of a project, but the facility specificity, the local regulation and energy market usually make this assessment case-specific. In systems where photovoltaic technology is present, payback is expected to be in less than 10 years [Armendariz-Lopez *et al.* 2018]: 2.3 [Peng *et al.* 2013], 4.1 [Bhandari *et al.* 2015], 4.9 [Asdrubali *et al.* 2019], 6 [Kaldellis *et al.* 2010], 7.4 [Huang & Yu 2017] and 9.6 years [Armendariz-Lopez *et al.* 2018].

Another consideration of the profitability of the investment in this case relates to the impact of the power plant adjacent to the facility. During the Amazonian humid season, typically from February to May, the dam spillway operates continuously. In view of the fact that no pumping is required during this period, the amount of energy consumed in pump operation is deducted from the calculation requirement of the hybrid system. In this way, the humid season allows the hybrid installation a constant operation in turbine mode without the need for storage. This property leads to a significant reduction of the amortization period to 5.2 years.

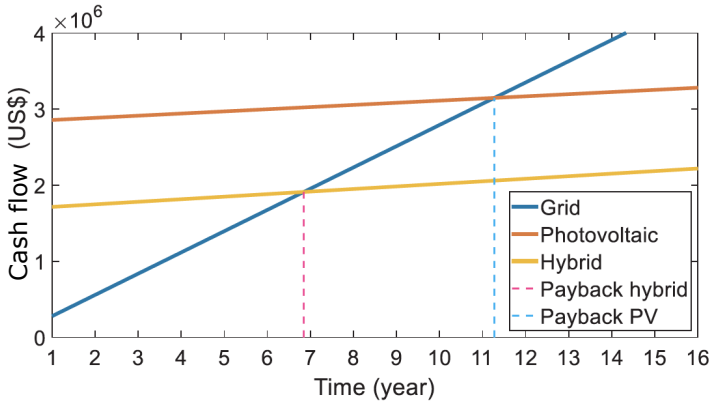

Figure 3.8: Comparison of energy alternatives payback.

3.2.7 Perspectives for the micro PHES design in tucuruí

Within the objective of comparing two complementary energy systems, the hybrid solar-hydraulic configurations with pumped storage are presented as more economically competitive for this case study. In its particularity, this project could take advantage of the local electricity grid as intermediate storage, and it allows the system to operate with a single pump/PAT conversion. This option could prevent an excessive number of starts and stops, faults and therefore maintenance. Alternatively, in the event it is impossible to connect to the local power grid, as is often the case in the nearby Amazonian areas, a more robust pump is required that can handle cyclical operations with frequent start-ups and shut-downs. In this scenario the economic analysis would show a larger initial investment, but the PHES integrated with PV still allows a better absorption of the power fluctuations favouring the optimal use of the RES.

The existing structures for hydraulic exploitation and the high costs for a standalone photovoltaic installation provide the opportunity of a pumped storage application for a more efficient and cost-effective installation. In addition, the cash flow for the hybrid system investment is comparable with the grid electricity provision in a shorter payback time compared to a pure photovoltaic facility (around -40 %) because of the high available head and the lower capital investment. Regarding a conscientious use of the water resource, the option of a hybrid system guarantees responsible use of the installation in respect of the environment by manipulating the water for energy use without additional impact on the existing hydrological dynamics.

Finally, as shown in this work, the operation of the spillway causes an important influence on the facility outcomes, with regard to economic and operational aspects. In the future work, this approach will be carried out after a statistical analysis of the historical series of the spillway's opening for further investigation in the energy solution of waterways locks.

3.3 UPSH case studies in Belgium

3.3.1 Towards PHES solutions in Belgium

The Belgian energy system is facing essential challenges in reducing its dependence on fossil fuels [Limpens & Jeanmart 2018]. Investing in energy efficiency and converting the actual energy-mix towards a higher share of renewable energy resources are the nearest goals of the country in agreement with the latest European directives [European Commission 2012b]. In the last decade, the Belgian power generation mix and the energy markets have been affected by the growing development in RES (Fig. 3.9). The green certificate system in support of RES facilities has been particularly useful as its share has increased from 3.6 % in 2000 to 26.9 % in 2018 (the production has increased by 6.6 times in 18 years) [International Energy Agency 2018]. With the spreading of this new environmentally-friendly policy, the energy transmission and distribution systems have to tackle the variability of renewable sources while the power demands from industry and householder are not diminishing [Matsuo *et al.* 2020].

To maintain the grid frequency near to its nominal values (grid quality), different wholesale markets have been set up, and they play on different time horizons, related to actual production and consumption. In the long term, producers and consumers can negotiate substantial volumes of electricity on futures markets with monthly, quarterly, and yearly maturities [de Almeida *et al.* 2003]. They protect themselves against unpredictable fluctuations in energy prices. In Belgium, futures contracts are negotiated on the ICE Endex and the European Energy Exchange (EEX). Another

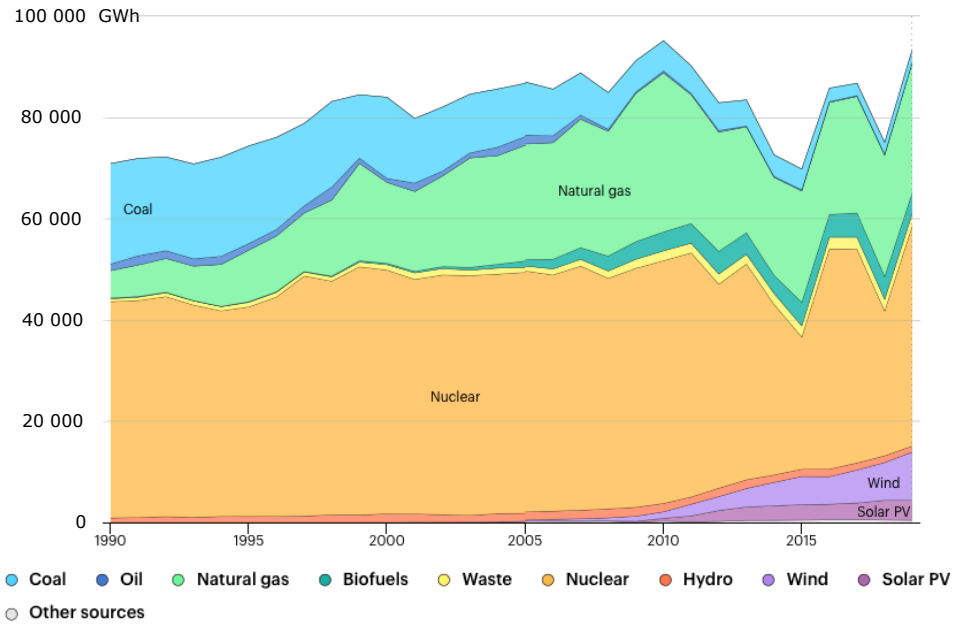

Figure 3.9: Belgian electricity generation by source, 1990-2019 [IEA 2020].

possibility is that two companies enter into a contract with each other, often referred to as an over-the-counter contract (OTC). The day before the actual delivery, a more accurate estimate of demand is possible for internal and international information and events likely to influence demand, e.g. weather data. Producers, suppliers, and large industrial consumers, therefore, negotiate on the day-ahead market. It is generally organised as an auction market, based on the economic priority curve [Vallés *et al.* 2016]. In Belgium, the day-ahead market is managed by EPEX SPOT Belgium [De Vos 2015] and electricity is negotiated on an hourly basis. In reality, the day-ahead demand forecast will never be fully accurate. The supply will also be different from expectations due to changes in wind, sunlight, or unexpected plant outages [Engelken *et al.* 2016]. This is why the third type of market has been created: the intraday market. It allows market participants to correct their injection or withdrawal on the network shortly before actual delivery. In Belgium, EPEX SPOT Belgium manages the intraday market [De Vos 2015].

In order to reduce the energy consumption and greenhouse gas emissions, the Belgian national policy is based on an integrated approach, attempting to use multiple technologies, rather than betting on one technology, to achieve its goals [Economie SPF 2019]. These technologies range from renewable resources over energy efficiency, to the technology of smart-grids. However, to tackle the challenge of the variability of renewable resources when their importance in the energy-mix increases, the policy statement looks towards an increased interconnection of the grid with the neighbouring countries but also to energy storage [CONCERE-CNC 2019].

In the most recent analysis of the Belgian adequacy and flexibility for 2020-2030, the national transmission system operator (TSO) projects a need for more 40 % increase in flexibility compared to 2020 [CONCERE-CNC 2019]. Potential sources of flexibility include flexible production, demand-side management, interconnection, and energy storage facility. Thus, given the recent developments in the power industry and the current shift to renewable generation, energy storage is increasingly considered as a future key player in the industry [Worrell *et al.* 2003, Ceglia *et al.* 2020]. As for other storage technologies to be developed, the economics of PHES must be assessed, which includes the study of the achievable revenues. These can come from two sources.

- On the one hand, from the shift of energy generation/consumption. The value arising from this action derives from price arbitrage on power markets.
- Alternatively, energy storage can provide TSOs with reserves for ancillary services, thereby taking part in the real-time balancing of supply and demand of electricity [de Almeida *et al.* 2003, De Vos 2015].

This energy reserve consists of idly running power generating systems, being able to start up very quickly, to react in cases of failures of other generators, failures on lines, or blackouts. According to the agreement, the plant must respond within seconds or minutes and for a defined amount of power [Palizban & Kauhaniemi 2016]. In order to operate as a spinning reserve, the systems need to have a quick reac-

tion time and maintain a level of charge ready to respond to promptly. A parallel pipeline dedicated to pumping needs to be installed to the one for generating to assure the constant capacity availability. However, this would represent an additional level of complexity in the frame of energy management and infrastructure [Deane *et al.* 2010].

Concerning the storage capacity required in the event of the Belgian nuclear reactors phase-out, set to be from 2022 to 2025, the various scenarios remain vague until today. The energy transition would shape the future Belgian energy-mix forward 100 % renewable in 2050, as declared by the European Union [Commission 2011], and, thus, by high variability of the power supply resources [Meeus *et al.* 2012]. What is known is that today Belgium is unable to count on sufficient renewable energy storage capacity to compensate for the nuclear shut-down. The national storage capacity is currently 1.3 GW, which is comparable to a modern nuclear power plant, but it can function for 3 to 4 hours only. Most of the totality of the capacity relies on PHES technology. Today, only two PHES facilities are located in Belgium. Table 3.3 shows their main specifications.

Table 3.3: Existing pumped hydro storage plants in Belgium.

		Coo-Trois-Ponts	**Plate-Taille**
Year		1979	1981
Power capacity	[MW]	1164	144
Stored energy	[GWh]	5	0.796
Head	[m]	250	46
Discharge generating	[m^3/s]	60 - 100	90
Pipeline diameter	[m]	6.5 - 8	4.5
Volume	[m^3]	8.52 10^6	6.5 10^6
Turbine		3x158 MW + 3x230 MW reversible Francis	4x36 MW reversible Francis
Turbine diameter	[m]	6.5 - 8	4.5
Round-trip efficiency		75 %	70 %

The Coo-Trois-points (Fig. 3.10) was constructed in two stages: the first operation in 1971 installed three single-stage reversible pump-turbines totalling 474 MW. In 1980, other three units of larger capacity were added. Coo has been built originally in a complement of nuclear development for stand-by black start power and flexibility needs. This plant is characterized by a roundtrip efficiency of 75 %, while the Plate-Taille PHES plant reaches 70 % [Geth *et al.* 2015]. The latter has a smaller power capacity and it runs four reversible Francis turbines of 36 MW each, commissioned in 1981 [Vanbellingen *et al.* 1982].

Globally, PHES is considered as a technically reliable solution, however, its investment costs, and more specifically the cost of reservoir excavation, are considered often too high [Steimes *et al.* 2016a]. Acknowledging that using existing reservoirs is economically a feasible alternative remains an important task for future design. Moreover, due to its geomorphology condition, Belgium does not have

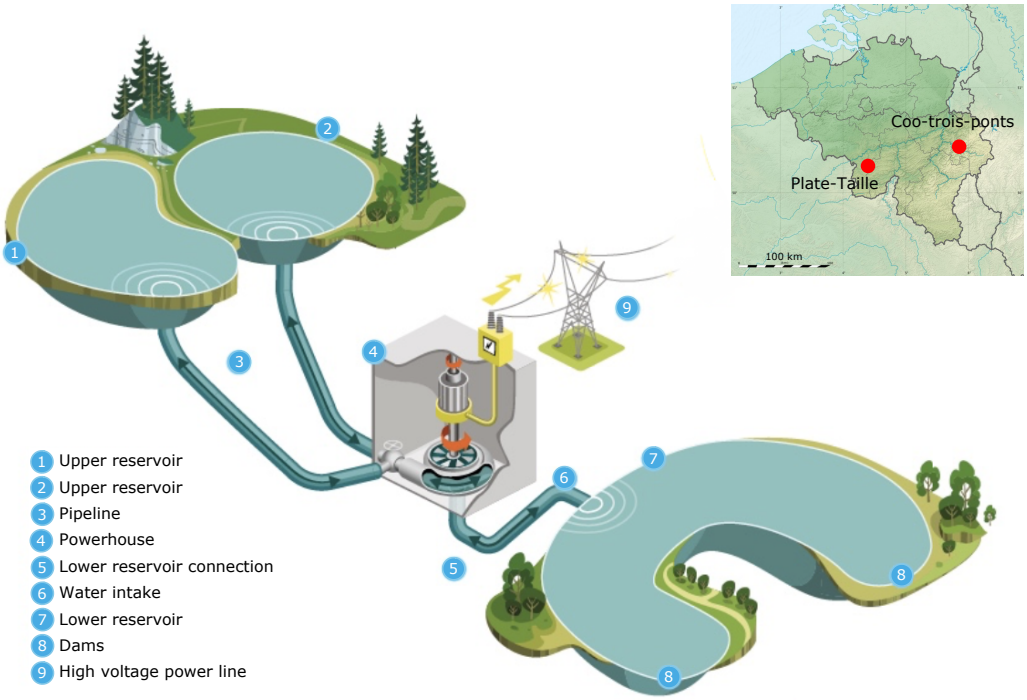

Figure 3.10: Representation of Coo-Trois-Ponts PHES plant and its location [ENGIE 2020].

promising sites for other conventional large scale PHES with sufficient head and surface [Steimes *et al.* 2016a]. Therefore, underground pumped storage hydroelectricity (UPSH) facilities could represent a valuable solution in increasing the national energy storage capacity [Martin 2011]. In these systems, the hydropower head is obtained by exploiting the depth of an underground cavity instead of elevated reservoirs. However, using of underground cavities as lower reservoirs for hydropower applications is not widespread [Spriet 2014] and its technology has not yet passed the research and development phase.

In this context, Section 3.3 provides a set of preliminary economic and technical considerations, applied to two different cases for UPSH located in the Walloon region in Belgium. This work defines and details the main characteristics of potentially exploitable sites to carry out a pumped storage arrangement reusing existing surfaces or underground cavities as reservoirs. Two UPSH case studies present different hydrogeological compositions: a former slate quarry of Martelange in Luxemburg province and a representation of a coal mine in Hainaut province. They are separately presented and each proposed analysis points out the major challenges and opportunities that this sort of energy storage system should consider and achieve. Developments of innovative hydraulic systems set-up are carried out in light of the characteristics of the investigated coal mine and the slate quarry. Furthermore, environmental and economic aspects for the Martelange case are projected at the end of its life used as a water storage reservoir.

3.3.2 The slate quarry of Martelange case study

The proposed site is situated at the edge of the municipality of Martelange at 380 m above sea level in the province of Luxemburg, Belgium, by the Sauer river. The site is an abandoned slate mine, where the last activities stopped in 1995, and many of the above-ground infrastructure still stands at the location (see Fig. 3.11.a). It should also be noted that underground quarries are generally not be included in water reservoir selection because of risks of instability of the overlying base by a relatively shallow exploitation that are too high. Slate quarries are, however, an exception in this respect, given the nature of the material mined in highly inclined decametric layers and having, therefore, led to deep cavities of impressive size, low porosity, and low permeability.

Today, rain and the underground water leaking flooded the quarry that consists of 9 distinguishable cavern structures, of which the deepest runs over 17 floors (see Fig. 3.11.b). The highest room is over 50 m in height and the longest one over 85 m in length, extending over a total depth of 180 m. The existing excavated void volume in the mine is estimated to be around 1 700 000 m^3. However, it was determined that only 800 000 m^3 is available for storage by leaving the lowest part of the cavities filled with water permanently [Spriet 2014]. In this way, it would shorten the total gross head at 160 m, but emptying the reservoir at its maximum represents additional costs and technical challenges, and finally, the major part of the available volume lies in the upper part of the quarry.

The nearby Haart hill represents a convenient location for the upper reservoir of the PHES plant in Martelange. At 470 m above sea level, the upper plateau of the hill is at a distance of approximately 550 m. Taking into consideration the

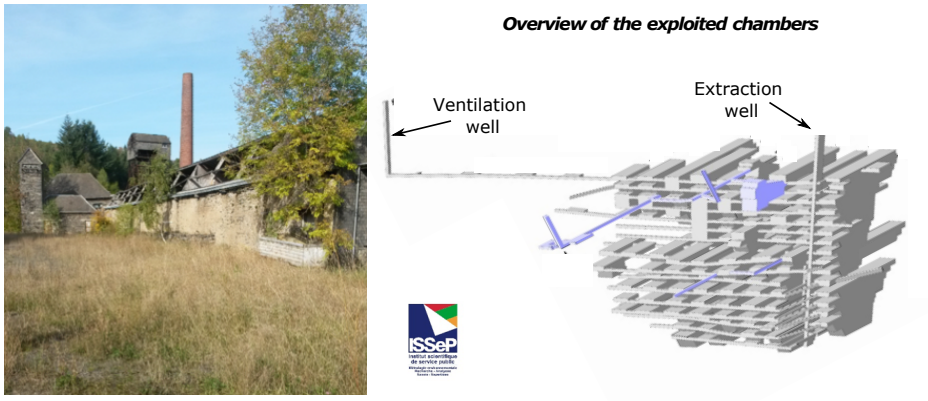

Figure 3.11: **(a)** The slate mine on the Martelange site; **(b)** 3D model of the mine made by *Institut scientifique Wallon de surveillance, de sûreté et de recherche en environnement* (ISSeP).

depth of the mine, a height difference of 250 m is thus available. On the fields on this plateau, the upper reservoir of the same capacity as the lower reservoir can be built. Here, high voltage (220 kV) power lines exist, the length of transmission lines needed from the power station towards the electricity grid is thus largely reduced, reducing the transmission losses significantly.

To determine the costs of the transformation centre and protections of network connection, fixed costs includes equipment, cubicle of high voltage, network and transformer protection units that are dependent on the rated voltage of network [Ogayar & Vidal 2009]. The transmission and access line are necessary to carry out energy distribution in high voltage to consumption points or distribution network. The length of the line will have an important influence over the project's viability.

The cadastral information shows that multiple and diverse individuals and companies own the land parcels in the zone of interest (Fig. 3.12). In order to install the upper reservoir and the penstock tunnels, agreements must be formed with all parties owning a land parcel that would be implicated in the construction. These agreements can resolute in accepting the installation on, or in transferring the ownership of the land parcel. Close to the underground caverns, the Sauer river streams, which could provide the water needed to fill up the reservoirs initially and can also provide a way of collecting the surplus water in case of emergencies. However, this river also leads to specific challenges, as this river provides drinking water to the reservoir in *'Lac de la Haute-Sûre'*, Grand Duchy of Luxembourg. Strict regulations are applied to the water quality of this river and would have important implications in terms of water potability and water supply obligations [Gronemeier & Jäckel 2013].

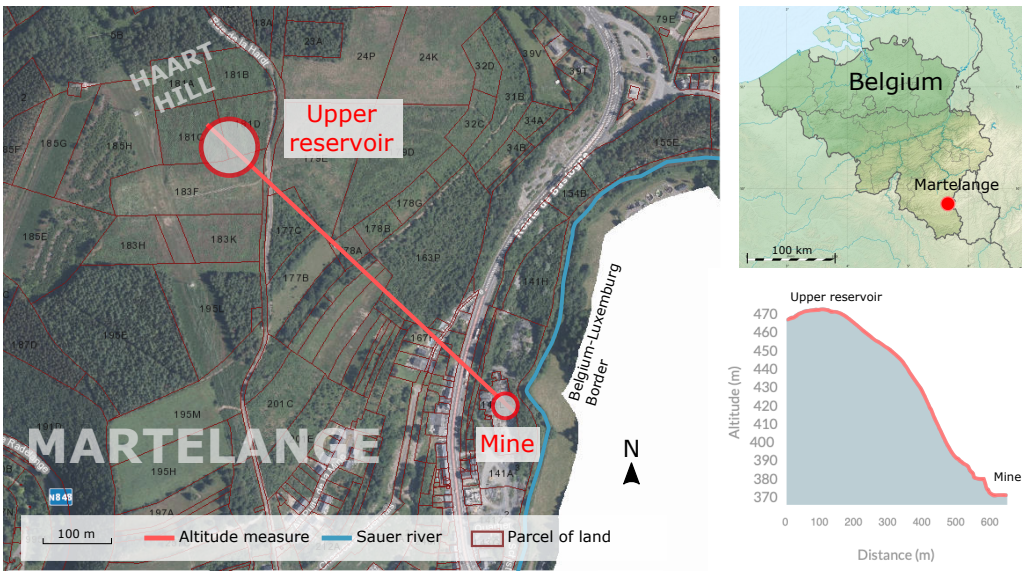

Figure 3.12: View of Martelange, the mine, and the proposed upper reservoir [Service public de Wallonie 2020].

3.3.2.1 Preliminary costs analysis

Different strategies are analysed to define pumping- and generating-period after the peak power size. Ranging from 30 to 100 MW power levels and referring to the Belpex energy price, an estimation of operation cost and revenue can be determined. A trade-off determines the optimal strategy between yearly revenue and investment costs. To estimate the profitability of the project, and estimate the time for a return on investment, a preliminary net present value (NPV) calculation is provided over 40 years, the assumed lifetime of the plant. The NPV method is particularly suitable for decisions made on the basis of long-run profitability and it is calculated by the following formula:

$$NPV = \sum_{t=0}^{t=K} \frac{CashFlow}{(1+d)^t} \tag{3.4}$$

where d the real discount rate, K is the lifetime of the system. The cash flow is yearly obtained by the difference of revenues and costs. Table 3.4 summarises the estimation of the different costs for a 100 MW peak UPSH plant.

Table 3.4: Breakdown of the total initial investment cost expressed in k€

Cost name	**Cost k€**	**Source**
Commissioning	3 000	[Deane *et al.* 2010]
Project management	5 662	[Menéndez *et al.* 2020]
Excavation upper reservoir	8 128	[Steimes *et al.* 2016b]
Upper reservoir coating	3 046	[Steimes *et al.* 2016b]
Penstock (joints, anchors, etc.)	860	[Spriet 2014]
Pumping pipe (560m)	3 140	[Andaroodi *et al.* 2005]
Francis pump-turbine	4 029	[Ogayar *et al.* 2009]
Electro-mechanical equipment	1 634	[Ogayar & Vidal 2009]
Electric substation and power-line	1 230	[Menéndez *et al.* 2020]
Protection, regulation and control	986	[Ogayar & Vidal 2009]
Powerhouse (for a single pump-turbine)	12 138	[Ogayar *et al.* 2009]
Landownership agreements	3 000	[Spriet 2014]
Other and contingencies	4 550	[Corporation 2015]
Total initial investment	51 403	

This first evaluation underestimates engineering operations and studies required for the installation. Therefore, to properly estimate the cost of such project, a multidisciplinary and professional feasibility study should be performed, encompassing legal, environmental, material and equipment provisions, hydraulic, electro-mechanical, safety and geological aspects. The project commissioning expenses include staff training, civil and structure works, review and testing of the mechanical-electrical and control systems. This entry in the cost sheets is dependent by the hired contractor. The estimation of the project management expenses is inferred by the UPSH case study presented by Menedndez et al. in regard of engineering,

construction management, security and waste mangament [Menéndez *et al.* 2020]. As reported by Fig. 3.13, contingencies at feasibility and pre-feasibility levels for PHES systems are expected to be, in average, at about 9.1 % of the total plant cost [Corporation 2015].

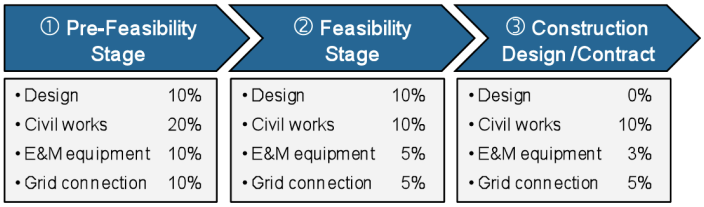

Figure 3.13: Contingencies costs in percentage of the plant total cost

Martelange quarry is not a very deep mine as coal mines and has a more favourable access to the cavities. This condition could simplify some installations aspects such as excavation, powerhouse access, electrification and ventilation of the cavern and penstock settlement. Another design parameters in a hydroelectric plant is the size of the penstock tunnel and pipes. The larger the penstock tunnel, the smaller the friction losses with the pipe walls will be, which is, of course, desirable. However, larger pipes require more massive tunnels, increasing the material and excavation costs considerably. Moreover, over time, the roughness of the internal wall of the pipe worsens due to wear and corrosion. All these factors are relevant in the penstock design. The operation and maintenance costs are calculated based on Connolly et al. [Connolly *et al.* 2011]. Their estimation is split up in a percentage of the investment, and a cost per energy consumed/produced: fixed yearly operation and maintenance cost 1.5 €/MWh and 1.5 % of the investment [Connolly *et al.* 2011].

The yearly net income is calculated on the operation parameters, and it comprises both the revenues from generating and the costs for pumping (at Belpex electricity price) according to a daily schedule of 5 and 7 hours respectively. The yearly cash flow is then: Cash flow = yearly revenue – (down payment + Operation & Maintenance costs). The capital expenditure reimbursement of the initial investment is assumed to be half within the first two years and the second half equally spread in the next 10 years. It is thus assumed those down payments are made yearly in the first 12 years of plant operation. A first stream of revenues for a storage plant lies in the arbitrage in the energy market: the plant will pump during hours with low prices and produce during peak hours, thus earning the spread between those two extremes [Deloitte 2018]. In this study, only the day-ahead market is considered; for simplicity, the storage plant does not make any arbitrage on the intraday prices or on the balancing mechanism price. The revenues from the spinning reserve depend highly on the negotiations with the transmission system operator. It is, therefore, not possible to estimate the revenue from such operation along the project lifetime; however, this is a viable exploitation option. Most actors on the energy market use long term price forecasts in order to make assessments

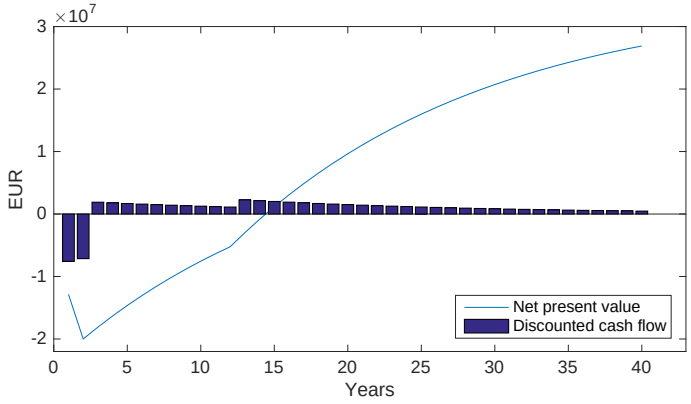

Figure 3.14: Discounted cash flow evolution and NPV of the Martelange case study.

on feasible investments. However, these outlooks are dependant on scenarios and assumptions on future national and international market developments, and hence resulting in a less foreseeable electricity price.

In order to provide a first estimation of the revenues, the yearly averaged electricity price for day-ahead market in Belgium 2019 of 39.3 €/MWh is selected [CREG 2020] and the selling price at its 75% percentile 46.2 €/MWh. In the last recent years (2015-2019), the yearly average hourly day-ahead wholesale electricity prices increased, but for a conservative approach is considered constant along the whole life span of the system. With a energy capacity of 474 MWh, a plant load factor of 0.8 and an overall efficiency in generation of 87%, it is possible to calculate the NPV for a such investment (real discount rate, d, is chosen at 0,06 and the lifetime, K, equals to 40 years). The yearly undiscounted cash flow, that comprises both the income from generating, O&M and the costs for pumping according to Belpex price, is estimated about 4.82 M€/year. The NPV and the discounted cash flow are showed in Fig. 3.14. A considerable financial outlay occurs in the first two years and the following ten years. The evolution of the NPV value marks that the time necessary to obtain a return of investment is within 15 years. Table 3.5 lists the main data used for the estimation on the NPV and the internal rate of return (IRR). IRR is a discount rate that makes the NPV of all cash flows equal to zero in a discounted cash flow analysis. On this matter different NPV values are also computed for different real discount rates.

Revenues from the control power market could further increase the price volatility experienced by the UPSH. Further studies on this subject, implying optimisation of operation between spot market and control power market, while also accounting for demanded control power volumes, would be one way to quantify the value of grid service provision for the UPSH. However, subjected to large uncertainties regarding the development and design of the control power market, such an analysis is very market specific.

Table 3.5: Data and NPV results for a preliminary economic evaluation of UPSH in Martelange.

Data	
Initial investment cost (kEUR)	51 403
Operations and maintenance costs (kEUR/year)	767
Energy per cycle (kWh)	460 000
Load factor	0.8
Annual Electricity Output (MWh)	134 320
Annual Electricity Output degradation (%)	0.01
Project lifespan (years)	40
Real discount rate (%)	6.00
Net electricity price EUR/MWh	34
NPV (kEUR)	32 170
IRR	16.19 %
Payback	15 Years
NPV (kEUR) (r = 4.00%)	51 947
NPV (kEUR) (r = 10.00%)	11 808
NPV (kEUR) (r = 20.00%)	-3 017

3.3.2.2 Turbomachiney selection

The optimal set up of the machinery depends on the required power size, pumping and generating scheduling and, indeed, economic return. In the preliminary cost analysis (Section 3.3.2.1), the turbomachines were selected for a 100 MW PHES scenario and consists in a Francis turbine and a group of centrifugal pumps. This ternary solution uses 46 m^3/s of water in generating mode and it takes about 5 hours to fill the lower reservoir. In pumping mode, the flow rate is smaller and 7 hours are needed. However, the fact that pumps are separated by the turbines gives much more flexibility on the pumps selection and pumping periods. So this can easily be modified based on the power plant business plan. The gross capacity is 460 MWh and with an overall hydraulic efficiency is 87 %.

For safety considerations, a discharge above 40 m^3/s could jeopardize the quarry's rock stability. This additional constrain influences the setup, size and discharge of the hydraulic machines due to the different head exploitable in the different scenarios. For this reason, other solutions are here presented. Purely by way of example, Fig. 3.15 shows all the configurations for a peak power production of 30 MW. Through the possible two options for the upper reservoir, one on the Haart hill or exploiting the basin by the Sauer river, different turbomachinery configurations are presented for this case of study:

A - a single hydraulic turbine type Francis under a head of 160 m and by exploiting an upper reservoir at ground level (by the river);

B - a Francis turbine installed for a gross total head of 250 meter depth by using the upper reservoir on Haart hill;

C - likewise option B, but installing a group of PaTs instead.

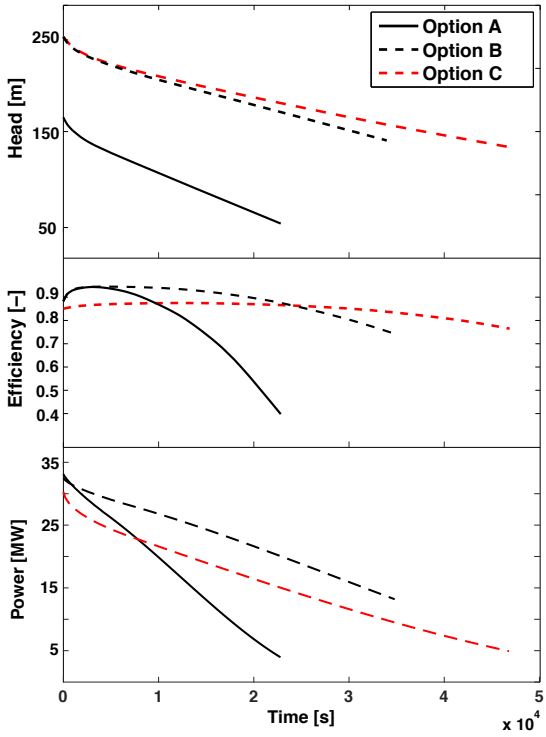

Figure 3.15: The evolution of the gross head, hydraulic efficiency and power by time for the three turbomachinery configurations A, B and C. Please note in configuration C, PaTs are coupled with a variable speed driver.

The discharge in option A must be large enough to match with the power required under a lower available head, while options B and C can afford a lower total flow rate. Comparing the cases adopting the Francis turbine, one can find a relevant variation in the peak of nominal flow rate: 26 m^3/s in the case A and 17 m^3/s in the case B. In case C, three PaTs are coupled in parallel to raise the total water discharge and to satisfy the 30 MW power target.

Francis turbines could operate within an range of working condition thanks to their guide vanes, but PaTs are required to run with variable speed to cope with the underground reservoir water level variation. Variable rotational speed allows characteristic curves to shift accordingly to meet a new working condition point at high hydraulic efficiency. In point of fact, fully exploiting the reservoir capacity implies a raising water level from the bottom up to its maximum, namely about 100 m higher, and regulating measures must be taken. The total flow rate in option C stays between the values of about 16 m^3/s at available high head and 10 m^3/s at low head and lower speed (Fig. 3.15). The reduced total flow rate in option C (Fig. 3.16) causes a more extended period in generating.

In case A, the load floats from a deep part-load of 35 % up to 107 % of the nominal value: this wide range produces a significant variation in hydraulic efficiency

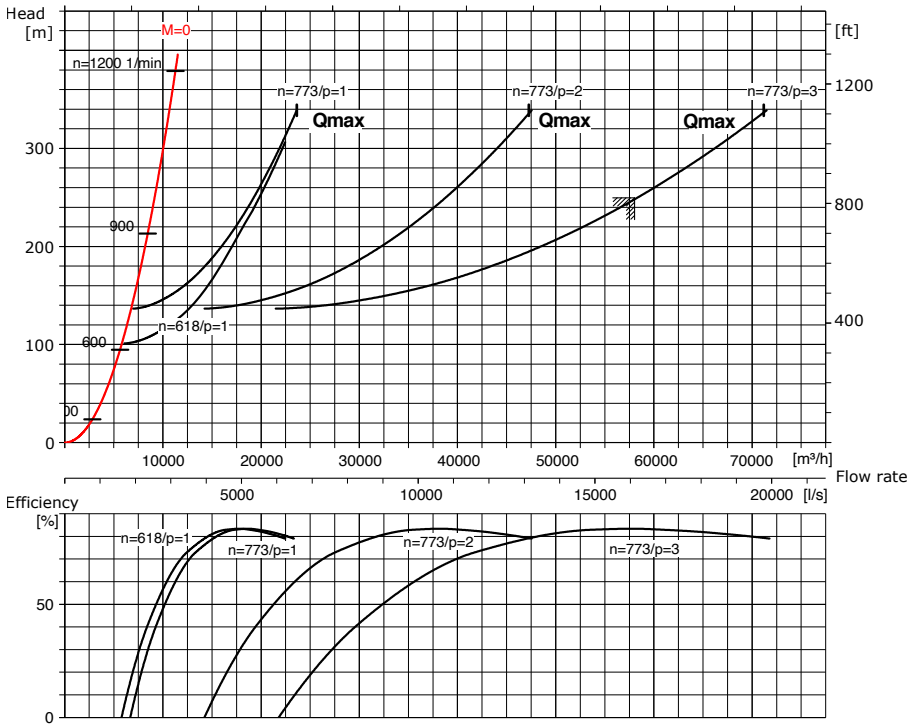

Figure 3.16: Estimation of the performances of the 3 double suction PATs in parallel (p=3) under 250 m gross head. In the graph other characteristic curves are presented: performances for two PaTs in parallel (p=2) and a single PAT (p=1). In red the runaway limit in which no positive torque is produced.

for strong cavitation vortex during refilling of the reservoir, and it would drastically limit the energy capacity. Installing the upper reservoir on a higher altitude (as in cases B and C) cuts down the off-design range, which is relevant and affecting the turbine performance in case A. For option B and C, the load varies from 65 % to 104 %. Due to a weaker efficiency and a lower flow rate, the power output in configuration C is lower than when using the Francis turbine in case A or B.

3.3.3 The coal mine of Péronnes-lez-Binche case study

3.3.3.1 Hydropower plant description

The case study discussed here is a simplified formulation of the existing site due to the limited knowledge of its network of galleries and tunnels. The topology definition of a coal mine is hard to be defined and standardize as every site has its specific structure in terms of size, galleries, drainage system, geology and hydrology. However, this reduced configuration could provide a valid case study in hydro-mechanical design, and preliminary performance analysis and challenges.

The proposed theoretical case study represents the configuration of the Péronnes-lez-Binche: two vertical wells (4 m diameter) reach the depth of 500 m and are

crossed by three extensive horizontal galleries at 200 m, 350 m and 500 m depth each. Usually, secondary galleries are entirely spread along the central tunnels and are the heart of the coal extraction. They could represent a substantial raise of available volume even if their length is usually a fraction of the main galleries. However for lack of information, the secondary galleries are neglected.

The main challenge for this site is the high variation of the available head in the regular operation of the system. The three horizontal galleries, of 5000 m^3 each, provide a quasi-steady condition for the turbines and pumps. The first vertical well is employed to give access from the ground level to the powerhouse at the bottom of the mine for construction works and to place the penstock. The second well represents the primary connection to the horizontal galleries, which form the tailwater level reservoir (Fig. 3.17). Due to the limited volumetric capacity of the vertical well, a modest change in water volume produces an abrupt variation in the water level and thus in the piezometric pressure along with the vertical pit. The head switches from the maximum gross head capacity of 500 meters down to 200 meters during the complete refilling of the mine as the lower reservoir. The operating conditions would suffer relevant head variations during the transition between two galleries in the vertical well.

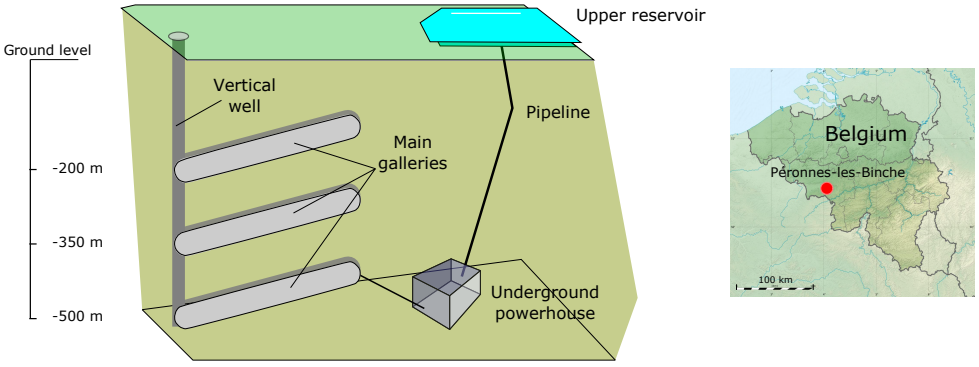

Figure 3.17: Scheme of the coal mine. The lower reservoir of the UPSH plant consists in three main galleries and the mine shaft.

3.3.3.2 Turbomachinery selection

There is no hydraulic turbine able to tackle alone this high variation of load. Variable speed regulation aim to work under the similarity laws and allows the turbomachinery to adapt to different working conditions. Similar flow conditions guarantee the adimensional velocities are constant, but this is based on the assumption that the coefficient of losses is independent of the net head. The similarity is confirmed until the net head is not too large (>130 %) [Jaumotte *et al.* 1994] or the draft tube reaches lower pressure than water vapour pressure [Dixon & Hall 2010]. The extremely large fluctuation in energy generation by the filling or emptying of the mine during a full cycle requires a combination of multiple turbomachines. In principle,

the sum of the turbine energy production aims to cover the net head peak and the smallest turbine defines the resolution of the system power output.

In this case, a series of three Francis turbines could be implemented to split the full charge, due to the net head variation in the three main galleries. With the assumption of adopting an upper reservoir at the ground level, the full group of Francis turbines needs to operate under 500 m gross head, two turbines at 350 head and only the last, when the water reaches the third horizontal gallery, at 200 m depth. Additional connecting pipes and turbine by-pass fitting are therefore necessary to modulate the turbines group operational load and isolate one or two, when required because of the head variation.

Fig. 3.18 provides an overview of the possible turbines group arrangement. The penstock coming from the upper reservoir has direct access to the spiral casing of the turbine I or it can deviate the water flow to the next machine. Similarly, turbine II can operate or be by-passed into turbine III. This configuration presents high hydraulic efficiency per turbine but it requires important investment costs since three hydroelectric units are needed. Moreover, the fittings and by-pass connectors, required by this unusual configuration in series, add non-negligible head losses. Furthermore, the new design of the draft-tube of each turbine represents a further engineering challenge, since the draft-tube plays the critical role of recovering energy by reducing the flow's kinetic energy [Valentín *et al.* 2017] and it is crucial to avoid the perturbation of the operating conditions of the following turbine in the series.

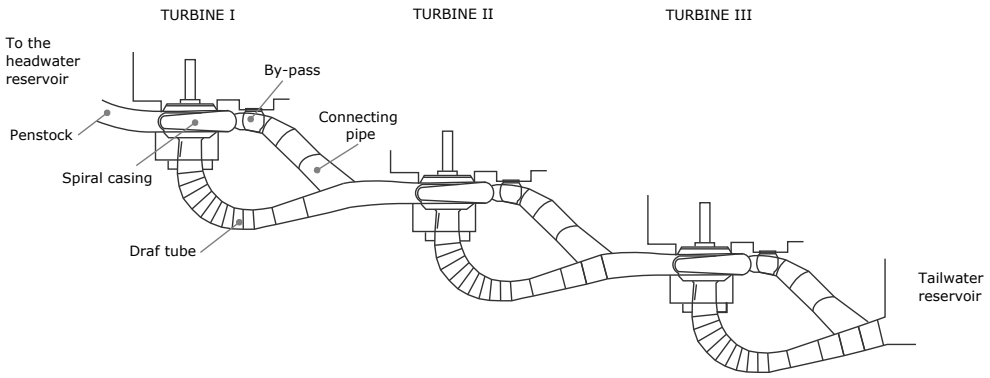

Figure 3.18: Schematic representation of turbine I (for 200 m gross head), II and III (both at 150 m gross head) in series.

A 1-D numerical model of the proposed hydropower plant, as illustrated in Fig. 3.17, has been developed in collaboration with École polytechnique fédérale de Lausanne (EPFL) to perform a feasibility study on the selection of the hydraulic turbines and to predict the machines behaviour under different operating scenarios. For this purpose, the SIMSEN software is used, in which mass and momentum conservation equations are modelled according to their electrical equivalent, as presented in [Nicolet 2007, Nicolet *et al.* 2002]. The SIMSEN components representing

the power plant are illustrated in Fig. 3.19. The integrated dynamic behaviour of the whole system is simulated in the time domain through a set of first-order non-linear ordinary differential equations [Nicolet *et al.* 2007]. The model features the upper reservoir located at ground level, the penstock with diameter $D_P = 0.9$ m and length $L_P = 545$ m, the powerhouse located at -510 m and the lower reservoir whose depth varies as a function of time and of the flow discharge. The following equation is implemented to simulate the head variation $H_t(t)$ of the power plant during each transition between two horizontal galleries through the well:

$$\begin{cases} H_{t_1}(t) = \min(H_2, H_1 + \frac{Q \times t}{A}) \\ H_{t_2}(t) = \min(H_3, H_2 + \frac{Q \times t}{A}) \end{cases} \tag{3.5}$$

where H_1, H_2 and H_3 are the depth of the three horizontal galleries, respectively, Q is the discharge at the outlet section of the turbine III and A is the cross-section of the well. A distributed model of the losses in the penstock is adopted, as presented in [Landry 2015, Nicolet 2007], by assuming that the piping system will be made by stainless steel, material preferred to polyester pipes reinforced with glass fibre at high head hydropower plant [Ogayar *et al.* 2009].

Three identical Francis turbines are selected with a D = 0.55 m runner diameter and the specific speed $\nu = 0.13$ [-] is defined as follows:

$$\nu = \omega \frac{Q^{1/2}}{\pi (2e)^{3/4}} \tag{3.6}$$

where ω is the angular speed of the runner [rad/s], Q is the discharge [m^3/s], and e is the nominal specific energy [J/kg].

Two scenarios for the turbines operating condition have been simulated:

- SCENARIO A: the machines operate only during steady head conditions. During head variation the turbines are bypassed until a new steady condition happens;
- SCENARIO B: it implies the continuous operation of the hydraulic turbines also during transient head conditions. A by-pass strategy depending on the head variation is proposed.

In the first investigated operating condition, Francis turbines operate in series with $H = 500$ m and all by-pass valves are closed. As soon as the first horizontal gallery is filled-up, all turbines are switched off and the flow discharge is pass through the by-pass piping system. When the water level reaches the second horizontal gallery, the valves of the by-pass of the turbines II and III are closed and only turbine II and III operate at $H = 350$ m. When the second horizontal gallery is filled-up, all turbines are switched-off, as for the first transition, and all valves are open to let the flow discharge pass through the by-pass piping system. Finally, only the turbine III operates at $H = 200$ m, when the third horizontal gallery is reached.

The results of the simulation during the whole transition process are illustrated in Fig. 3.20. It can be observed that the available turbine head is shared equally

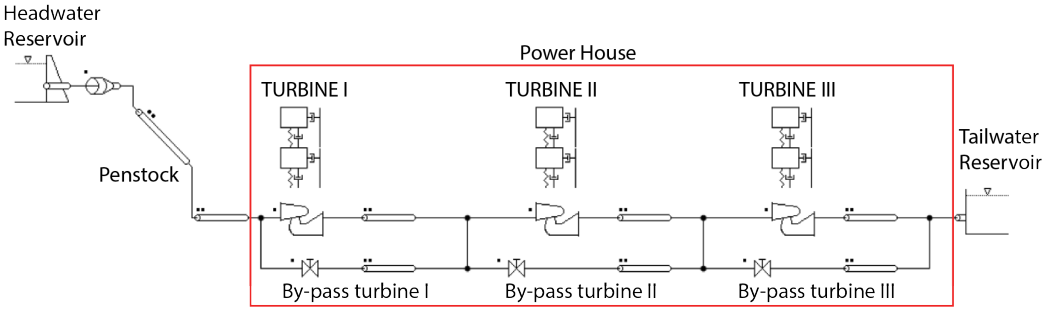

Figure 3.19: SIMSEN components to simulate the Péronnes-lez-Binche power plant.

between the machines and this allows maintaining an acceptable head variation throughout the power plant operation. The head range for which the turbines have to be designed is within 165 m and 200 m. The discharge is set within 1.6 m^3/s and 1.8 m^3/s to operate at the highest efficiency depending on the head.

The first scenario's operating condition implies a dramatic energy loss. During the transition from one horizontal reservoir to the following one, the flow discharge is not exploited for energy production to avoid a part-load operation of the hydraulic machines due to the dynamic change of the head. This energy loss E_l [J] corresponds to about 6 MWh by considering the integral of the available power over the transition time between the horizontal galleries, computed as follows [Dunlap 2020]:

$$E_l = \int_t \rho g Q(t) H(t) dt \tag{3.7}$$

where $Q(t)$ and $H(t)$ are the instantaneous discharge [m^3/s] and available head [m], respectively and ρ is the water density [kg/m^3]. Furthermore, it is important to notice that numerous start-up and shut-down of the machines, as well as several modifications of operating point, lead to unsteady loading, and this might result in fatigue collateral damage and additional cost in maintenance [Ye *et al.* 2020].

The second investigated scenario implies a continuous operation of the hydraulic machines during the transition between the horizontal galleries. Therefore, an investigation on the feasibility of the machine operation during the dynamic head changes is performed. The optimization of the strategy for switching-on and off of the turbines is out of the scope of this investigation as well as the study of the machines' start-up and stop transitions since this will be strictly dependent on the final design and performance hillchart of the machines.

Important variations in head would require the selected Francis turbines to operate in part-load and full conditions, which can cause several vibrations and induce to dangerous cavitation phenomena [Muller *et al.* 2016, Favrel 2019, Pereira 2019]. Fig. 3.21 illustrates the three phases in which three turbines are operating until the lower load limit is reached, then only two turbines, and, eventually, a single Francis turbine is in function. During the first transition, the selected machines enter in part-load regime after a decrease in head of 14 %. Therefore, the first hypothesis of this scenario is to shut down turbine I after a variation of $\Delta H = 105$ m to the gross

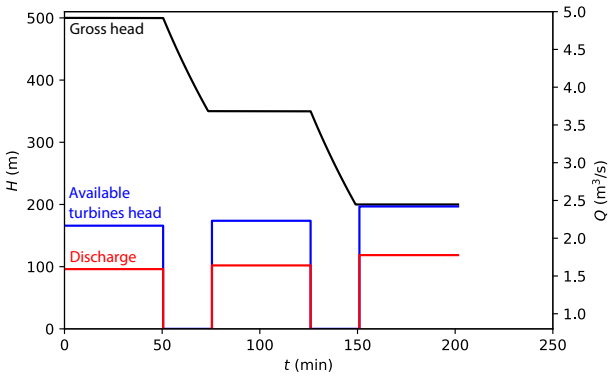

Figure 3.20: Time history of the gross head, available head and discharge of each Francis turbine operating at maximum efficiency for the given head (Scenario A).

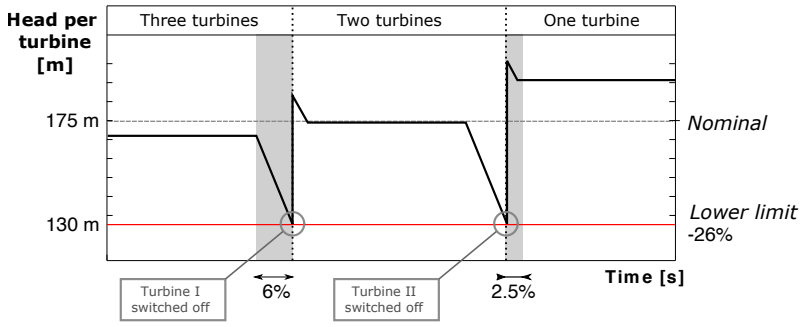

Figure 3.21: Operating sequence of the three Francis turbines in series to cope with 300 m gross head variation of the power plant.

head of the power plant, which corresponds to a variation in the available head of each turbine equal to the 26 % of the nominal head. The turbines would operate in part-load condition, but only for a limited time, about 900 s, which corresponds to the 6 % of the operating time and this is not critical for the machine safety [Favrel 2019]. After the stop and by-pass of the turbine I, the turbines II and III would experience an increase of the head and discharge allowing the machines to leave the part-load condition until the second horizontal gallery is reached, which corresponds to the nominal operating condition for both machines.

Similarly, during the second transition to reach the third horizontal gallery, both turbine II and III operate until a variation in available head on each turbine equals to the 26 % of the nominal head is reached. Then, turbine II is stopped and by-passed. The turbine III now operates alone and at full load condition until the third horizontal gallery is reached, corresponding to the 2.5 % of the operating time. The results of the numerical simulation of this operating condition of the hydraulic machines are presented in Fig. 3.22.

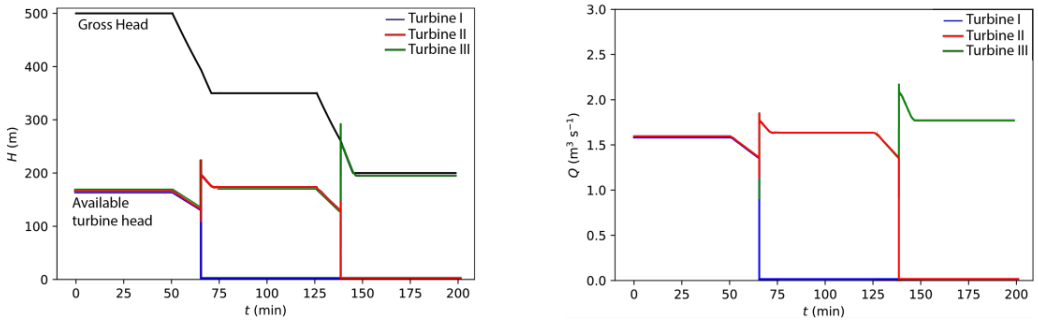

Figure 3.22: Time history of the gross and available heads (left) and discharge (right) of each Francis turbine for the operating condition in the scenario B.

3.3.4 UPSH in Belgium - Discussion

3.3.4.1 The quarry of Martelange case study

Martelange mine has a very peculiar geometry and it is impossible to maintain a fixed available head during a full generating cycle: head is actually changing from 250 to 150 m. That is one of the crucial challenges for UPSH exploiting abandoned mines. The preliminary cost analysis is based on a system of 100 MW peak. However, the peak power is reachable only when the mine is at its minimum water level (which differs from being dry due to a safety margin). From then on, the head drops progressively and the machinery group adapt their flow rate too, reducing the total power output: the time averaged power production is about 62 MW.

The preliminary cost analysis conducted in Section 3.3.2.1 provides important economic insights. The specific cost of the initial investment for UPSH at the quarry of Martelange of 514 €/kW$_{peak}$ underlines the economic advantage of this kind of systems. PHES is a mature energy storage technology [Sabihuddin *et al.* 2015, Rehman *et al.* 2015a] and expenditures are statistically defined in the literature. The annual OPEX is estimated about 6-10 % of the total initial investment [Albadi *et al.* 2017, Chen *et al.* 2009, Poullikkas 2013a]. At these terms, Martelange UPSH lifetime cost can be estimated at about 920 €/kW in line with the lower values of the capital cost range of 530-2700 €/kW [Nikolaidis & Poullikkas 2018, Albadi *et al.* 2017].

Although, the analysis considers only the main economic items such as upper reservoirs, installation, pipeline, turbomachinery, and purchase of land parcels for the upper reservoir. The economical comparison with other PHES in the literature shows that the case in Martelange is more convenient (about 830 €/kW of initial capital investment at averaged power 62 MW). The reasons are multiple. Any evaluations have been done in regard to the lower reservoir rehabilitation works from its actual (and unclear) condition. These tasks would require to dewater the mine for working under dry and safe conditions [Pujades *et al.* 2018]. This assessment results too specific and it is improbable to deliver an correct estimation. On the other hand, building from scratch the lower reservoir could cost additional 6-7 mln € for a

traditional PHES. Assuming the same price, capacity, and methodology used for the upper reservoir, the lower reservoir cost is estimated about 11 mln € (excavation and coating) in addition to land ownership (3 mln €), and commission and contingencies costs. The specific cost of the initial investment would then reach 1056 €/kW instead of 830 €/kW.

A drawback of the UPSH configuration is that hydrochemical related issues and groundwater exchanges could rise further costs and affect the system's performances [Pujades *et al.* 2018]. The soil on-site in the Martelange mine is slate. Slate is highly water-impermeable, an essential quality in PHES reservoir, and this is the reason why the mine is currently flooded. However, the mine has known an incoming water flow over its entire lifetime, and the water pressure is lower than the hydrostatic pressure necessary for fracking (meaning that the slate layer won't be fracked by the water pressure) [Spriet 2014]. It can be expected that no significant damage will occur to the soil and that the cavity will remain intact, during the operation of the UPSH system [Gronemeier & Jäckel 2013]: the quarry is expected to withstand the cyclic pressure due to filling and emptying of the reservoir [Gronemeier & Jäckel 2013].

A study on the Martelange Mine interactions with the groundwater flow has been conducted [Pujades *et al.* 2020]. Influence of water exchanges on the hydraulic head can be observed in periods during which water is not pumped nor discharged, especially when the hydraulic head is located at the top or at the bottom of the underground reservoir [Pujades *et al.* 2020]. When the hydraulic head is located at the top, it decreases slightly because water flows from the underground reservoir towards the surrounding medium. On the contrary, when the hydraulic head is located at the bottom, it increases because water is entering from the surrounding medium [Pujades *et al.* 2020]. The influence of water exchanges on the hydraulic head in the underground reservoir of Martelange is relatively small but enough to limit the discharge of some of the pumped water. In addition, efficiency is impacted since some of the energy used for pumping cannot be recovered discharging water into the underground reservoir [Pujades *et al.* 2020].

3.3.4.2 The coal mine of Péronnes-lez-Binche case study

The selection of the hydraulic turbomachinery configuration relies on a technical feasibility analysis. For a given reservoir capacity there is probably an advantage in using fewer machines as far as the powerhouse volume (and therefore its construction and excavation costs) is concerned [Tam & Clinch 1979]. Specific costs for the turbomachinery selection are related to the type of arrangement and the expected fittings and connections. Interestingly, the size of the turbine runners can affect the construction methodology and setup of the powerhouse. The runner diameter would insert additional constrains in its transportation and installation. In the presented case, the vertical well's diameter, as it is, limits the maximum transportable breadth. Although, it presents an already existing access to the mine and drives the plant-construction cost down [Steimes *et al.* 2016a].

The simulations of the turbines series have shown their behaviour in case of two different operation regimes: the first one avoids the high head variation by shutting-off the turbines' group and fully bypassing the water flow when the vertical wells are met; the second regime operates in continuous but it bypasses a turbine at the time and split the available head to the remainder of running machines. The latter scenario records a higher capacity, 27 % gain in energy production, it reduces the total number of start-up and stop for turbine II (-50 %) and turbine III (-100 %) due to the by-passing system, and it does not require the bypass piping system between the turbine III and the tailwater reservoir. On the other hand, the turbines are operating in the variable head, although limited, which could compromise the machines' safety if the operation is prolonged in this condition.

The creation of multi-stage turbines has precedents in responding to reduce the cost of investments for a given power by seeking to use sites of high fall with low flow rates, while single-stage turbines did not allow to exploit such great heads [Jaumotte *et al.* 1994]. An example is the 1217 m head multi-stage pump-turbines of the same type without wicked gates in Super Bissorte power stations in the Alps close to the Italian – French border, operating since 1987 [Truong *et al.* 1988]. Since these machines with fixed diffusers do not allow any variable power load, the system can be combined with other turbines for partial flexibility.

As an alternative to the analysed configuration, a Deriaz turbine could be employed. The pump-turbine type Deriaz because its unique features, can run within broad range of operation (40 % - 120 % of the nominal load) at high hydraulic efficiency. A literature review on this pump-turbine is presented in Section. 2.4. Moreover, additional information and data elaboration on Deriaz pump-turbine for PHES can be found in Section 3.4.

Deriaz pump-turbine needs to adjust vane ring and runner blade according to the currently available head and consequently its water discharge as well [Deriaz & Warnock 1959a]. The flow rate varies in this configuration, catching up a more significant total period of the power generation phase if compared to the scenario all series of Francis turbines are switched off during the wells transitions. Deriaz pump-turbine can be installed in providing a more compact solution to the exploitation of two galleries. However, historically, Deriaz pump-turbine has not been favoured over Francis turbine because of its mechanical complexity and cost [Erskine & Van Rooy 2004]. A study on the investment costs between the solution with a Deriaz turbine and the solution with the series of the three Francis turbines should be assessed to compare the two solutions.

Finally, variable speed solutions can be also implemented to tackle the fluctuation of the load. The solution consists in rotating the reversible turbine at different rotational speeds in pump and turbine mode, but it is not primarily used due to its complications in the alternator-engine connection level. Variable rotational speed could provide a +10 % gain in hydraulic efficiency in partial load for specific Francis turbine applications [Iliev *et al.* 2019] but additional drops in the global efficiency need to be considered from the variable speed devices.

3.4 Deriaz pump-turbine

3.4.1 Deriaz hydraulic model

Nowadays, the need of a more flexible turbine operation and PHES plants, makes the Deriaz turbomachine an emerging technology in this context, being able to work in pumping and generating modes. The characteristics and the strengths of Deriaz pump-turbine stand on its high flexibility at variable flow rate and adaptation to head variation by using double regulation of the guide vanes and runner blade. Implementing such a pump-turbine presents a lighter solution for PHES than the bulkier installation of a ternary set-up or a series of turbines. However, the cost-benefit advantage of installing a compact and advanced-technology pump-turbine, such as Deriaz turbine, can be partially reduced by the additional costs in the mechanical apparatus as required for adjustable runner blades. On the other hand, the conception and design of a pump-turbine at fixed-geometry require additional tests in pump mode (four quadrants) in comparison with a pure turbine anyway. Also, the costs of fixed-geometry turbines coupled with variable speed are compounded by the high price of the frequency driver.

Under the lens of the energy decentralization and micro-grids trends, a high grade of turbine flexibility can display profitability for those PHES applications discarded before. In this context, the following section presents a numerical performance analysis of a micro-scale model Deriaz pump-turbine (md), designed on the geometry of an existing prototype case (pty). The fulfilment of scaling laws for the downsizing and the design of the blade profiles are described in Appendix A. The traditional method *point by point*, which defines the geometric parameters along streamlines from the leading edge up to its trailing edge of the pump blade [Stepanoff 1957a, Lazarkiewicz & Troskolanski 1965, Gulich 2010], is used. The design aims to provide an outline of a Deriaz pump-turbine for micro applications. The hydrodynamic and mechanical solutions are designed in such a way that efficiency is not a priority criterion for micro-hydropower plants, but rather a relatively high performance over a wide range of partial load.

3.4.1.1 Prototype Deriaz pump-turbine in Naussac

The prototype is installed in the power/pumping station of the Naussac II in Lozère, France (44°44'55.8"N 3°49'31.9"E). This is the second phase of the expansion of the Naussac I reservoir, which is used to maintain the low-water flow in the Allier and Loire rivers below its confluence with the Allier. Specifically, the plant of Naussac II is intended for the support of low-water mark of Allier and the Loire; the functioning of machines was thus optimized in pump to favour the filling of the reservoir, and not the hydroelectric production which is a by-product [Thépot *et al.* 1999] .

This installation was preferred over a double or multi-speed Francis machine which would have required a much larger and higher pumping basin. This would have required intake work on the dam of more than 10 meters height but only 2.30 meters with Deriaz machines [Houdeline & Verzeroli 1999] - a much better scenario

ecologically and for its reduced impact on the landscape. In addition, polluting fluids such like oil from the moving parts of the machine in contact with the water have also been partially eliminated [Houdeline & Verzeroli 1999], addressing water quality concerns. The hydrostatic seal-joint and the controls of the blades of the runner have a waterproof ceramic coating, as do the gates downstream.

The existing installation was commissioned in 1983, creating a reservoir with a capacity of 190 Mm^3. The power station has three identical Deriaz pump-turbines of 0.950 meters in diameter with a unitary power of 3 MW during pumping, each able to generate a maximum of 2.6 MW. Each group is coupled to an asynchronous classic motor-generator, all fed by a single transformer of 12 MVA (5.5 kW/ 63kW). Fig. 3.23 shows a cross-section of one pump-turbine installed in Naussac II. The synergy of the blade and guide-vane regulations allows the groups to function well under the variable working conditions (Section 2.4). The unit pumping flow is variable from 2 to 5,5 m^3/s under a head varying from 32 to 57 m. The Naussac II plant is primarily intended to support the low-water mark of Allier and the Loire rivers. So, the machines were optimized to fill the reservoir by pumping rather than for hydroelectric production.

During the start-up phase, the regulator select the rotation direction and maintains the machine close to the synchronous nominal speed, allowing it to be coupled to the network. Once the group is coupled with the network, the regulator maintains the optimal water flow rate for pumping or generating. During normal functioning, the machine is relatively noisy due to cavitation until the extreme minimum flow rate of about 3.5 m^3/s, after which it becomes quiet [Houdeline & Verzeroli 1999]. This is considered admissible if the wheel blades are made of a stainless material to limit excessive damage.

The regulator has two conjugate cams, one for the functioning of the pump, the other one for the functioning of the turbine. This ensures the best combination of blades and vanes giving the greatest possible efficiency over all the variable conditions for pumping or generating. The prototype is moderately sized, adapted to the maximum flow value of the project and interest in preserving the basin water level. The main mechanical characteristics are shown in Tables 3.6 and 3.7.

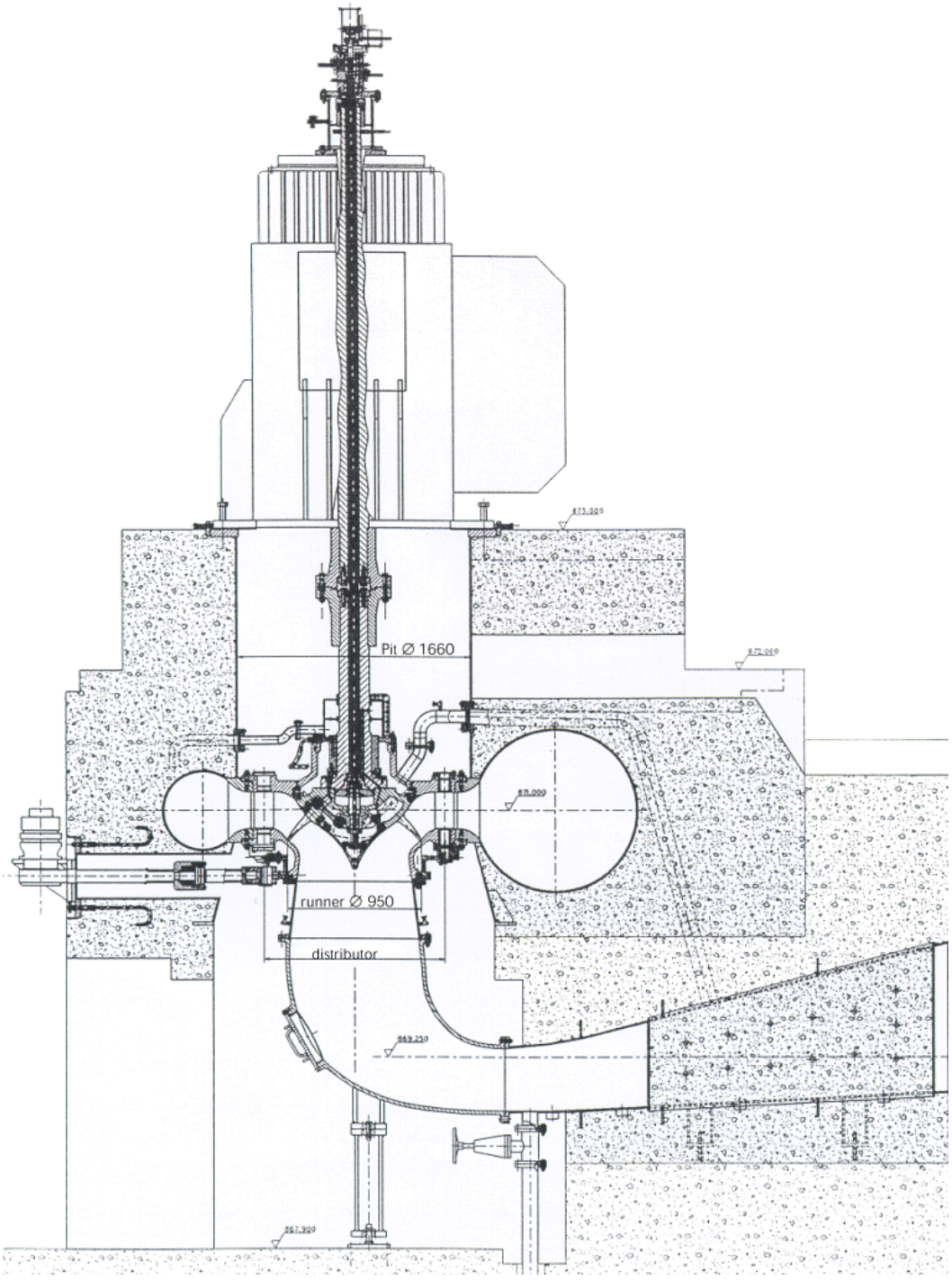

Figure 3.23: Overall cross-section of a Deriaz pump turbine in Naussac II powerhouse [Thépot *et al.* 1999].

Table 3.6: Mechanical data of Deriaz prototype working in Naussac II. In Figure a view of Naussac II power-house. [J.Kirejczyk 2001]

Turbine Specifications		
Rotational speed, N	750	[rpm]
Diameter of the spiral case entry	1.140	[m]
Number of fixed stay vanes	12	[-]
Number of mobile wicket gates	24	[-]
Height of the distributor	0.257	[m]
Distributor boring diameter	1.286	[m]
Runner diameter, D	0.950	[m]
Number of runner blades, z	8	[-]
Blade pivot angle, γ	45	[deg]
Width of the draft tube outlet	2.592	[m]
Height of the draft tube outlet	1.130	[m]

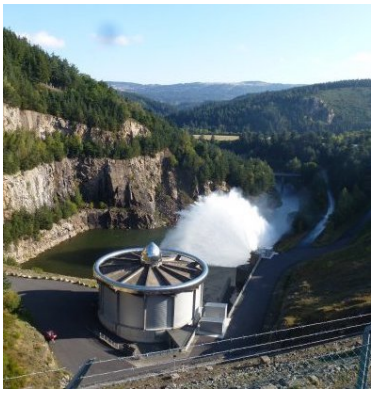

Table 3.7: Operational data in pumping and generating Deriaz prototype in Naussac II power-plant [J.Kirejczyk 2001, Houdeline & Verzeroli 1999].

Pump mode		
Geometrical reference, D	0.950	[m]
Rotation speed, N	750	[rpm]
Nominal power used per unit, P_p	3	[MW]
Corresponding flow per unit Q_p	4.6 - 5.5	[m^3/s]
For a total vertical height, H_p	48.7 - 58.2	[m]
Total losses for max height	1.2	[m]
Number of units in service	3	[-]
Efficiency, $\eta_{t,h}$	85.5	[%]

Turbine mode		
Geometrical reference, D	0.950	[m]
Rotation speed, N	750	[rpm]
Maximum power per unit, P_t	2.65	[MW]
Corresponding flow per unit, Q_t	5.4 - 6.0	[m^3/s]
For a net head height, H_t	50 - 57	[m]
Total losses for max height	0.5	[m]
Efficiency, $\eta_{t,h}$	92.8	[%]

3.4.2 Selected model case

The hydraulic study of these diagonal reversible turbines with double a regulation type Deriaz is conducted on a reduced scale model with a reference diameter of 0.3 m at 1054 rpm. Table 3.8 summarises the mechanical data and predicted performances of the downsized model obtained by the application of the scaling laws (Appendix A). Experimental performance analysis on this model size ($D = 0.3$ m $N = 1054$ rpm.) has been conducted and reported by the manufacturer in occasion of the Naussac II hydropower plant [Zavadil & Meduna 1981a, Zavadil & Meduna 1981b]. The small size of these machines makes manufacturing them more complex; the construction of the operating mechanism for eight blades tends to be more difficult in a smaller space than for a bigger prototype or for a Kaplan turbine. For these reasons, a diagonal flow turbine has a compact arrangement for the runner blade operating mechanism, as shown in Fig 2.12.

In the scale model only the hydraulic internal passage design has been converted, using the diameter ratio between prototype and model D_{pty}/D_{md}, as the geometric scale ratio. Geometrical similarity in both downsized and full-size turbomachines may be attained without great difficulty. In general, it is more difficult to attain similarity in relative roughness and for the clearances between the runner and stationary elements, both from a technological and a hydrodynamic point of view.

The Reynolds' law of similarity assumes that friction losses are the same in both machines. However, this assumption is not valid everywhere. In fact, the friction is a function of the surface roughness and Reynolds number, *Re*. Therefore, defining water as the working fluid at comparable temperatures, the same viscosity is assumed for the model and the full-size prototype although adjustments must be taken into account as depicted in the following sections. Moreover, the performance of the model could be more efficient, mostly due to the simpler hydraulic system and components [Zavadil & Meduna 1981a]. The study described in this research project starts by analysing the numerical performance of the machine in turbine and pump modes under different blade angles, $\delta\beta = [0°; +15°]$, and opening gate vanes, $a_0 = [17\ \%; 100\ \%]$.

Table 3.8: Mechanical data of the downsized Deriaz pump. In Figure a downsized model of a Deriaz pump-turbine [Erskine & Van Rooy 2004].

Downsized model		
Geometrical reference, D	0.3	[m]
Design pumping head, $H_{p,n}$	10	[m]
Rotation speed, N	1054	[rpm]
Design pumping flow rate, $Q_{p,n}$	0.24	[m^3/s]
Pump efficiency, $\eta_{p,h}$	82.7	[%]
Turbine efficiency, $\eta_{t,h}$	91.4	[%]

3.4.3 Numerical analysis

Turbomachines are the most critical components in hydro-power plants because they affect the cost as well as the overall performance of the plant. For the cost-effective design of any hydro-power project, it is therefore very important to predict the hydraulic behavior and efficiency of hydro turbines before they are used. An experimental approach would be much more costly and time consuming [Versteeg & Malalasekera 2007]. Using CFD it is possible to gain significant insight into issues such as energy transfer and fluid flow details in hydraulic turbines [Choi *et al.* 2013, Wu *et al.* 2012, Minakov *et al.* 2015]. Only the final fine-tuning has to be done experimentally [Wu *et al.* 2007].

This section presents the results of the first step of a CFD integrated design analysis for a Deriaz pump-turbine runner. The computations were carried out with the aid of the Numeca software FINE^{TM}/Turbo solver, with the additional assumption of stationary flow and using a second order discretization scheme. Carried out to double precision, the computations required around $3{\cdot}10^3$ iterations. Modifying the angle position of the runner blade involves adapting the mesh at blade-to-blade structure: closing the passage stretches the mesh, increasing skewness. In order to protect the mesh, different block definitions and more mesh points are used.

3.4.3.1 Solid prototype modelling

The Deriaz pump-turbine studied in this project was modelled with the CatiaV5 CAD tool. To avoid problems during the CFD analyses the investigated domains must be properly designed. Problems may occur during the grid generation phase if unwanted surfaces or solid parts remain from the solid modelling. The surfaces were drawn with the fewest features possible, using the original drawings in order to avoid any imperfections (e.g. sharp edges, open surfaces). Computational domain and the runner profiles are shown in Fig. 3.24.

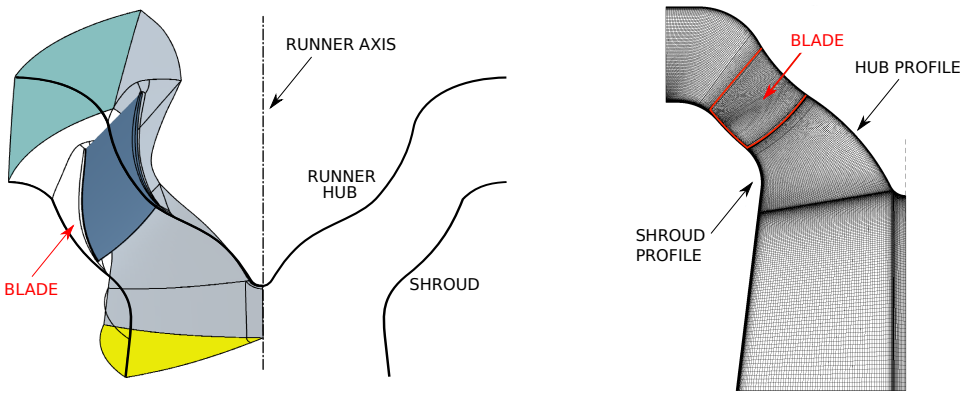

Figure 3.24: Runner domain blocks and boundary condition surfaces (on the left) and meridional view of the axisymmetric mesh (on the right).

3.4.3.2 Discretization process

Generating the mesh is a critical step in CFD turbomachine applications. Generally, over 50 % of the time spent in industry on a CFD project is devoted to the definition of the domain geometry and grid generation [Versteeg & Malalasekera 2007]. Since a grid in these types of applications includes many technological effects (rotor tip clearance, hub leakage flow [Gicquel *et al.* 2011, Schiffer *et al.* 2017]), it might require over 2 million points for one blade passage. All available experience in CFD applications indicates that the mesh definition and quality have a considerable influence on accuracy and convergence properties. The boundary layer is iteratively corrected in preliminary tests for the walls that define the geometry: the shroud, the hub, the blades and tip gaps between rotor and stator. Each surface has a different environment, and therefore needs to be treated differently. The velocity field is more complex in the gap rotor and stator than in the surrounding zones: the passage narrows abruptly and contains a rotating component. To assess the independence of the grid on the accuracy of the solution, a mesh convergence test is conducted (Table 3.9). It is considered sufficient to choose a mesh close to the stable solution of the hydraulic efficiency, η_h, of $\pm$ 0.05%, that corresponds to an initial mesh of the domain of about 3.1 million of nodes Fig. 3.24. Care must be taken when evaluating the quality of mesh suitable to the selected turbulence model. A summary of the mesh characteristics is presented in Table 3.10. The discrete domain is composed by five blocks whose features change according to the operating conditions. A higher number of nodes are needed for the narrower blade to blade passage in order to maintain a minimum quality level.

Table 3.9: Mesh convergence test on the same project case at $\delta\beta = 5°$, a_0= 56 % and mass flow of 0.18 [m^3/s]

	Nodes (million)	Min skewness	Efficiency, η_h	Torque, M [Nm]	CPU time [h]
Mesh 1	0.9	25	0.7858	234.2	3
Mesh 2	1.2	25	0.7872	228.0	4
Mesh 3	3.1	28	0.7956	230.5	11
Mesh 4	5.4	29	0.7980	230.8	16
Mesh 5	8.2	29	0.7976	231.9	27

According to the method accounting for viscous effects close to the wall, the turbulence models require a domain discretization adequate for computing the boundary layer. The high-Reynolds turbulence models assume that the flow near the wall behaves like a fully developed turbulent boundary layer and prescribe boundary conditions by employing wall functions. The viscous sub-layer will not be resolved. In FINE™/Turbo, both standard wall function and extended wall function are available [NUM 2013]. The low-Reynolds turbulence models resolve the entire boundary layer, including the viscous sub-layer where the viscous diffusion is much larger that the turbulent one. Thus, sufficiently fine grid should be used inside the boundary

Table 3.10: Mesh quality summary for turbine case at $\delta\beta = 5°$ and closing runner blade at $\delta\beta = 0°$

Case	Block	No. of nodes (million)	Minimum skewness	y^+_{max}	y^+_{min}
$\delta\beta = 5°$ $a_0 = 50$ %	Pump bulb inlet	0.6	71	1.4	0.8
	Blade topology	1.3	28	5.2	0.8
	Tip radial clearance	0.7	28	6.0	3.6
	Pump Outlet	0.5	86	1.6	0.6
	Entire mesh	3.1	28	6.0	0.8
$\delta\beta = 0°$ $a_0 = 50$ %	Pump bulb inlet	0.6	71	1.4	0.8
	Blade topology	1.9	14	8.1	1.2
	Tip radial clearance	0.9	15	12.1	3.5
	Pump Outlet	0.5	86	1.6	0.9
	Entire mesh	3.9	28	12.1	0.8

layer so that the sharp gradients can be resolved.

The relation between the parietal coordinate y^+ and width of the first cell close to the wall y is driven by the Blasius equation, expressed as follows for turbulent flows [NUM 2013]

$$y_{wall} = 6 \left(\frac{V_{ref}}{\nu} \right)^{-\frac{7}{8}} \left(\frac{L_{ref}}{2} \right)^{\frac{1}{8}} y^+ \tag{3.8}$$

where y_{wall} is the distance of the nearest grid point to the wall [m]; v_{ref} is a reference velocity of the flow, for instance the inlet velocity [m/s]; ν is the kinematic viscosity of the fluid [m^2/s], L_{ref} is a reference length of the test case 0.300 [m]; $y^+ = v_\tau y/\nu$ is the non-dimensional value of parietal coordinate. The thickness of the cells near the wall, y_{wall}, is so estimated. This estimation is then corrected on the whole geometry iteratively: the shroud, the hub, the blades and tip gaps between rotor and stator. Each surface is bathed differently and it has to be treated in a different way. While the blade and rotor are spinning at the rotation speed ω, the shroud is still. The velocity field is more complex in the gap rotor and stator as in the surrounded zones: the passage narrows abruptly and involves a rotating part.

3.4.3.3 Numerical modelling of turbulent fluid flow

The grid size of the Deriaz runner comprises only one of 8 repetitions of the blade block. For selected cases, the accuracy of different meshes are examined in order to import a good mesh without using a large number of cells. The bigger the mesh, the more equations the software has to solve.

Simulations are computed with *coarse grid initialization* that allows starting the iteration with a coarser level of the mesh and rapidly get closer to the possible finest level of the mesh until the convergence. The Courant-Friedrich-Levy number (CFL) is set equal to 3 for the proposed settings. This number globally scales the time-step sizes used for the time-marching scheme of the flow solver. A higher CFL number

results in a faster convergence, but will lead to divergence if the stability limit is exceeded [NUM 2013].

A mesh linked to a result of an hydraulic efficiency within a range of ±0.05% is selected and it correspond to a grid with around 3.1 million nodes initially. The time required to obtain results from the simulation is defined by the condition of convergence. It is therefore crucial to check for and assess convergence, and not only by examining residual levels. To gauge convergence properly, it is necessary to monitor other values: overall mass, momentum, energy and scalar balances are obtained. The net imbalance is recorded to be less than 0.3 % of the net flux through the domain.

An analysis sequence in post-processing confirms the assumptions made during the design of the mixed-flow pump (Appendix A): in Fig. 3.25, streamlines are shown coming from the inlet surface up to the leading edge of the pump blade; the flows appear orthogonal and uniform at the blade leading edge.

An appropriate turbulence model is chosen based on the specific application [Gicquel *et al.* 2011]. In this research project the choice of the turbulent model used is pragmatically based on the CPU-time required to reach convergence, even though the results obtained are within reasonable range of those given by the other solutions [Shah *et al.* 2013].

Close to the wall the flow is influenced by viscosity effects and does not depend on free stream parameters. The mean flow velocity depends on the distance from the wall, fluid density, fluid viscosity and the wall shear stress.

The selection of a suitable turbulence model is of paramount importance for the accuracy of the expected results. Choosing the wrong model may result in divergence from achievable results. This is particularly important when experimental verification is not feasible. Anyway, under such circumstances, the choice must be guided by specialist experience, generated mesh parameters (appropriate y^+) and available CPU. To validate the range of the results of the simulations, another turbulent model test is carried out and summarized in Table 3.11.

Table 3.11: Turbulent model test for an assigned mesh of 3.1 nodes: Spalart-Allmaras (SA), SA with Extended Wall Function (EWF), k-ε models, k-ω, Shear Stress Transport (SST) and v2 code model (a seven equations model).

Model	$\Delta\dot{m}$ [%]	ΔP [kPa]	M [Nm]	η_h [%]	$\Delta\eta^*$ [%]	CPU-time [h]
SA	0.030	148.0	232.2	79.84	1.641	12.84
SA EWF	0.053	145.0	231.9	80.15	1.331	7.20
k-ε Yang Shih	0.123	145.1	232.0	80.64	0.841	18.67
k-ε EWF	0.197	143.0	235.0	81.26	0.221	18.56
k-ω	0.005	143.3	238.5	83.44	1.959	16.35
SST EWF	0.024	143.8	238.6	83.32	1.839	14.69
v2 code	0.312	145.9	239.3	81.63	0.149	23.17

($*$) Difference by the reference value of $\eta = 81.481$

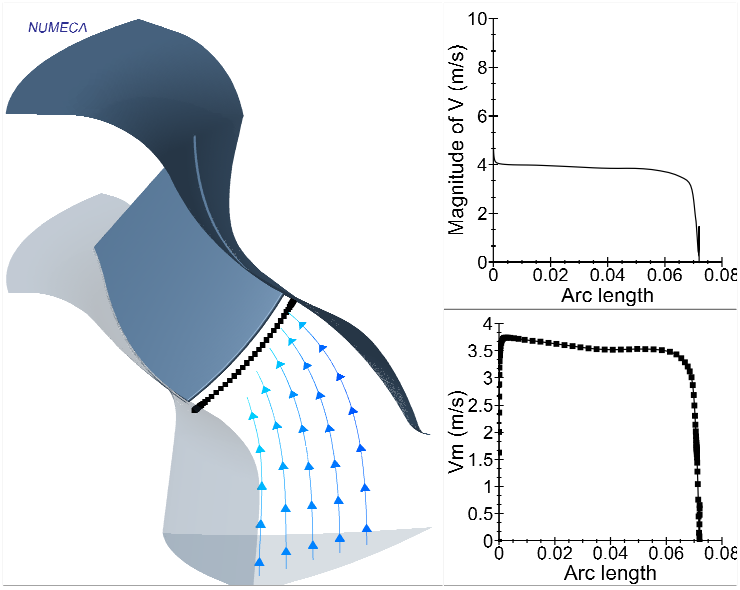

Figure 3.25: Flow streamlines at the pump inlet and flow speed distribution at the leading edge.

3.4.3.4 Pump mode

The computed volume is limited to the runner and the boundary conditions are fundamental to impose the correct equation sets to be solved. The velocity fields need to be set to define the guide vanes peculiarities: in turbine mode the they defines the inlet angular momentum at the runner and in pump mode are considered fully open to reduce possible obstruction effect. The behavior of the Deriaz type model was experimentally tested [Zavadil & Meduna 1981a] with a fixed static head of 10 meters at the inlet under different angles of regulation of the guide vanes. The chosen rotational speed, N, is 1054 [rpm]. The boundary conditions are set to agree with the experimental data (Table 3.12). The pump mode testing simulations of the Deriaz machine aim to define the working points with the developed design. Its characteristic curves defined by positioning the angle of the runner blade at 0, +5, +10 and +15 degrees.

Due to the unknown flow distribution at the entrance of the machine, some adaptations are necessary. In order to facilitate the discharge, the mobile parts of the diffuser (the inlet guide vanes at in turbine mode) are kept fully open ($a_0 = a_{max}$ =100 %) and their effect is considered negligible in pumping. This case was computed under the following settings: inlet pump total absolute pressure fixed at 201000 Pa for all related patches and the velocity normal to the inlet of the domain (no pre-swirl). The inlet pressure is actually irrelevant, for an incompressible computation. Cavitation phenomena only change if a cavitation model is implemented which then introduces the sole dependence on the absolute pressure level.

The point of maximum efficiency of the machine in pump mode is slightly more than 0.82 and was recorded at maximum rotor blade aperture ($+10° < \delta\beta < +15°$) close at the design point of 0.24 m^3/s, $\delta\beta = +15°$. Even more interesting is the possibility to maintain a higher efficiency of 0.79 for a wide range of flow rates: from about 0.12 to 0.28 m^3/s, the equivalent of $Q_D \pm 40$ %. Fig. 3.26 depicts the pump characteristic curves for the model of the Deriaz turbomachine with fully open turbine guide vanes at different blade angle positions.

Table 3.12: Adopted boundary conditions for the CFD simulations.

	Pump mode	Turbine mode	Turbine mode (2nd case)
Inlet	P_T at 201000 Pa Velocity normal	P_T at 351000 Pa Variable flow direction	Mass flow Variable flow direction
Outlet	Mass flow	P_T at 201000 Pa	P_T at 201000 Pa
Solid	Rotating at 1054 rpm Rough wall type	Rotating at -952 rpm Rough wall type	Rotating at -952 rpm Rough wall type
Blade angle	$0° < \delta\beta < +15°$	$0° < \delta\beta < +15°$	$\delta\beta = +5°$
Guide vane	Fully open	$17\ \% < a_0 < 100\ \%$	$17\ \% < a_0 < 100\ \%$

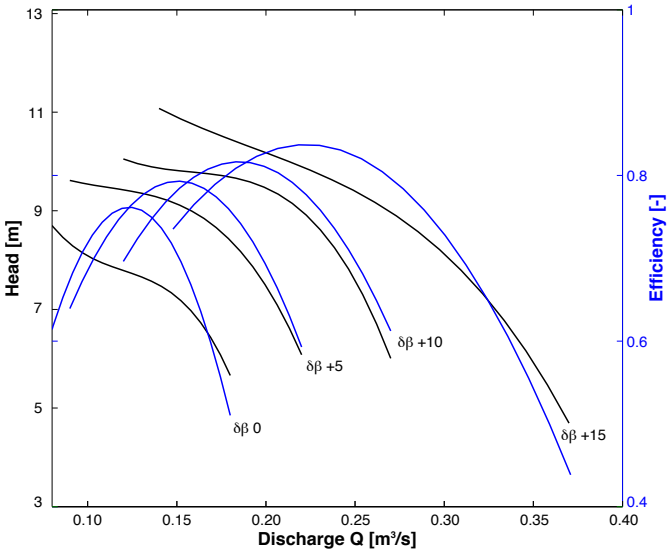

Figure 3.26: Head and efficiency of Deriaz pump-turbine in pump mode at 0, +5, +10 and +15 blade angle position.

3.4.3.5 Turbine mode

During a complete design of the machine it is necessary to carry out several tests at the most important blade geometry and rotation speed, N, settings as well as for the guide vanes angles, β and γ. The design process is iterative in that it tries to refine the design in the light of the results obtained at each design step. In generating mode tests the runner is rotating in the opposite direction than during pumping. This section illustrates two different cases of the machine in turbine mode.

The first case is with a variable blade pitch at fixed available head. Regulation is carried out by the adjustable blades of the runner blades. The inlet turbine (the outlet in pump mode), this time has a total absolute pressure fixed at 351 kPa with a variable flow direction to simulate the guide vanes. The turbine is submerged with an outlet static pressure of 201 kPa.

The designed downsized Deriaz pump turbine provides a good picture of the performance in turbine mode. In order to provide a qualitative comparison with the experimental data, an important overview of the efficiency curve is shown from manufacturer report tests in [Zavadil & Meduna 1981a, Zavadil & Meduna 1981b, Zavadil & Meduna 1981c] and represented by Fig. 3.27. Mechanical losses, not implemented in the CFD simulation, appear to be the main cause of small discrepancy in the efficiency peaks.

In the second case the impeller has fixed geometry and runs with variable guide vanes opening. In this test, the chosen pitch angle of the rotor blades is selected to +5 degrees. The simulations have the following inlet conditions: mass flow and flow directions (Table 3.13). The outlet draft tube has the averaged static pressure set at 201 kPa with back flow control. In this case study, the selected turbine Deriaz has a fixed runner blade angle of $\delta\beta = +5°$ and fixed rotation speed. The different open gate vane values, a_0/a_{max} [%], admit a controlled mass flow rate and allow the required ΔP to change. All the possible combinations of settings are thus mapped. The flow direction at the entrance is defined by the angle α ranging from 0° to 43° respectively at closed and fully open guide vanes. The throat passage at the vanes changes from 0 mm to 36 mm, affecting flow rate and direction (Table 3.13).

Table 3.13: Inlet condition for the flow direction in turbine mode.

Throat vane [mm]	6	8	12	18	22	26	30	36
Opening a_0 [%]	17	22	33	50	61	72	83	100
c_r/c	-0.113	-0.151	-0.227	-0.341	-0.422	-0.500	-0.568	-0.682
c_u/c	-0.993	-0.988	-0.973	-0.940	-0.906	-0.866	-0.822	-0.731

Fig. 3.28 shows how an excessive opening of the flow affects the orientation of the current which then fails to apply a torque to the rotor blades. This lowers efficiency and, also, it does not succeed in disposing a higher flow rate than was theoretically expected.

For a turbine at limited available head, H, the peak of hydraulic efficiency (91 %) coincides with the combination of a rotor blade closer to level $\delta\beta = +5°$ and an inlet

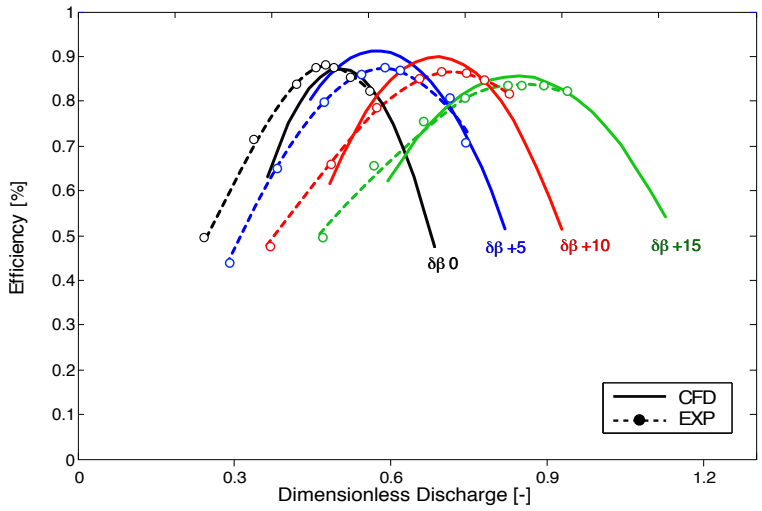

Figure 3.27: Measured and numerical performance in turbine mode at variable runner blade angle at fixed vanes versus dimensionless discharge Q/Q_n.

direction flow generated by 50 % of the maximum granted by the guide vanes: such direction helps achieve an effective angular momentum in the energy balance to the turbine. Furthermore, although the mapping efficiency was realized exclusively in the case of a turbine at $\delta\beta = +5°$ at different flow orientations, it does illustrate the full versatility over a broad area of high efficiency (Fig. 3.29). Forces and torque are calculated from the pressure and velocity fields on the walls, including rotating solid boundary characteristics (Fig. 3.30).

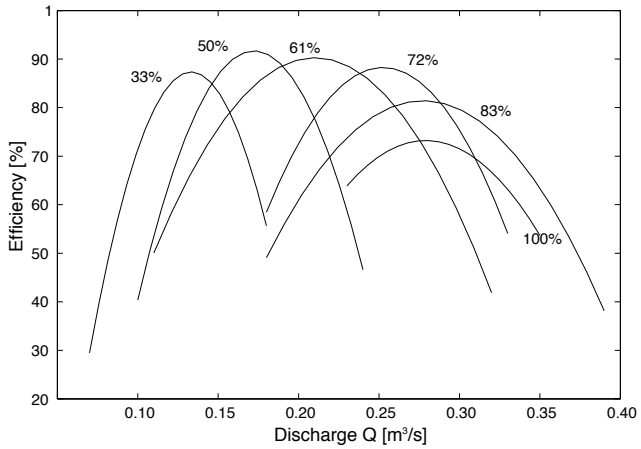

Figure 3.28: Efficiency map of Deriaz turbine at $\delta\beta + 5$ blade angle and variable guide vane direction: opening from 33 % up to 100 %.

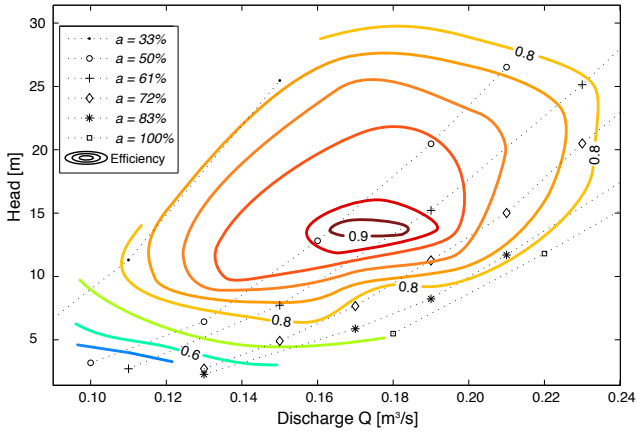

Figure 3.29: Hill chart of Deriaz turbine at fixed runner blade angle $\delta\beta + 5$ and variable guide vane direction.

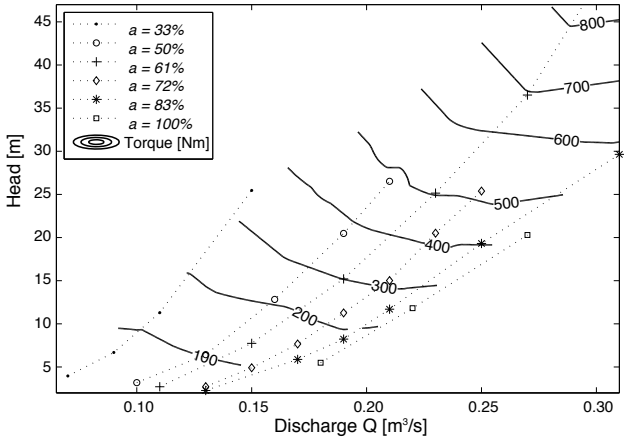

Figure 3.30: Torque map of Deriaz turbine at fixed runner blade angle $\delta\beta + 5$ and variable guide vane direction: opening from 33 % up to 100 %.

3.4.4 Final remarks on Deriaz pump-turbine

Worldwide, PHES is the most established and common storage technology [IEA 2020] and Deriaz pump-turbines provides a valid solution to its impelling requirements in flexibility and high hydraulic efficiency. In this context, this preliminary analysis of Deriaz turbomachine aims to deliver insights on advantages of a pump-turbine with variable geometry regulation. This governing measure could compete with variable speed regulation, that appears to be more frequent in pumping systems and for hydropower plant at higher head.

The results show clearly how the downsizing of the prototype can conserve versatility over a wide range of partial loads. According to the data collected and produced in this research, the application ranges of the micro-size of Deriaz turbine can be now compared to the other hydraulic turbines and be plotted in solid black line in Fig. 3.31. The shaded region marked in a dashed line shows the predicted

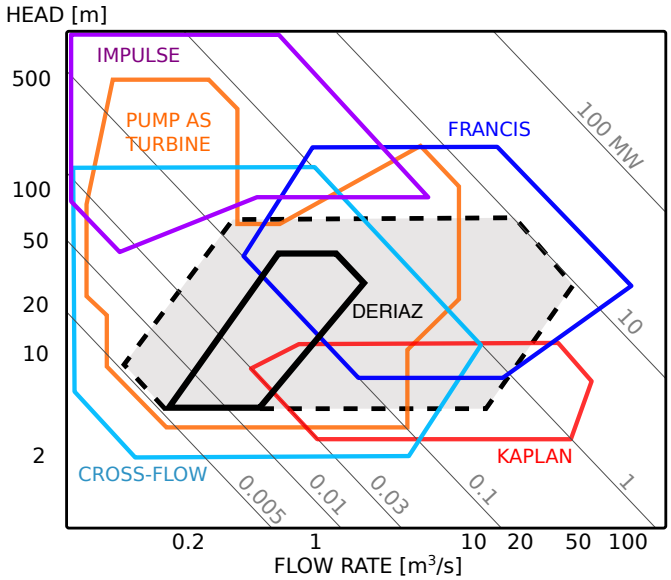

Figure 3.31: Types of hydraulic turbines and Deriaz turbine in their application area Q-H for μ-hydropower. Adapted from [Andritz 2019] [Sulzer 2019] [Paish 2002] and authors' data.

extension of the Deriaz application range thanks adjusted angle blades and different runner sizes.

In the framework of this thesis, the analysis on the pump-turbine type Deriaz enhances the discussion of PHES and μ-PHES and their new unexplored opportunities. It is also relevant to underline the complexity of pump-turbine design in opposition to pure hydraulic turbines or even more with a PaTs, simply by its concept design. To produce a pump-turbine, a pump impeller usually gives the designing starting point. Indeed, common turbines have usually lower performance in pump mode. For instance, the blades relatively short of a Francis turbine runner lead to an excessive slowing down of the water-flow in pump mode, producing flow detachment and efficiency loss. Moreover, the Francis turbine blade's angle is too large to produce a stable characteristic in pump mode [Jaumotte *et al.* 1994, Dixon & Hall 2010]. The concept of pump-turbine as a trade-off between pump impeller and turbine runner is required. Besides, the optimal functioning point of the common hydraulic turbomachine in turbine mode does not match with its operation in pump mode. At constant speed, the best efficiency point in turbine mode corresponds to a higher head than the one for the pump optimum. Since the turbine operates below the static head, which is reduced by hydraulic losses, and since the pump delivery head is larger than the net delivery head, which is to be pumped, the divergence in pump and turbine performance increases. The design of Deriaz pump-turbine with double regulation by guide vanes and runner blades solves the discrepancy between pumping and generating modes. In this way pressure pulsations and cavitation can be avoided over the range of variation in flow and head. Compared to the Kaplan turbines, Deriaz

prototypes use a diagonal flow direction to enlighten the hydraulic load and can be applied under higher head, competing with Francis turbines. For low head Francis turbines, part-load operation at higher head than the design head is a general problem [Turton 2012] which can be avoided by using adjustable blade turbines. Within this frame, the Deriaz pump-turbine fills the gap left by the reversible Francis and Kaplan turbines.

In addition to their improved efficiency over a wide load range resulting by the runner blade adjustments, Deriaz turbomachines can also work under variable rotation speeds. Some PHES systems link the motor/generator to a frequency changer, enabling a wider range of pumping or generating speeds ($\pm$ 12 %) [Schlunegger & Thöni 2013]. Although a Francis turbine can also benefit from this technology, it has been shown a variable speed Deriaz can take about 1.5 times the input capacity of a Francis turbine with variable frequency driver [Miyagawa *et al.* 1998].

3.5 Chapter conclusions

Nowadays, the need for energy storage reflects economic, environmental, geopolitical, and technological considerations. The growing global demand for fossil fuels, the resulting rise in prices, and the political turmoil in several producing countries have made the energy supply partly uncertain [Barbour *et al.* 2016]. Energy storage is, therefore, a geostrategic asset and an ineludible need to limit losses during overproduction, thus reducing energy consumption. Pumped hydro energy storage represents the most used technology for storing energy today [IEA 2020] but has definite geomorphic limitations [Rehman *et al.* 2015a]. In the smaller scales, PHES could overcome some of these impediments by integrating other applications and working on synergies.

The example of the μ-PHES project on the locks of Tucuruí in Brazil underlines the spread interest in this type of installation, that takes advantage of existing infrastructure that would reduce certainly economic barriers and the aforementioned geomorphic limitations. The crucial key-factors for the energy options offered by solar and hydraulic sources at the site are explored, and they define the hybrid option as a viable solution at the Tucuruí Locks facility. Therefore, this project provides the much-sought information regarding the design of a hybrid energy source system to be implemented to waterway locks and dams, promoting the growing debate in energy sustainability.

The underground pumped storage hydropower technology is another research development of PHES that aims to evade geomorphic limitation. UPSH installation does not require steep topography because the lower reservoir is a cavity in the underground. Although the Belgian landscape is relatively flat, it counts hundreds of mines and quarries into disuse. The main features of two different cases are described with concern of the significant challenges in geometry complexity and actual potential capacity with a multidisciplinary approach by considering both economic and

technical aspects. The analysis on the turbomachinery selection highlighted that the steep variation of the head during generating cycles is critical for the machine reliability and it calls to non-traditional turbine setups for preserving a profitable energy capacity, as well as to safeguard the turbines.

From the options adopted in the Martelange case study, part-load conditions space from 35–107 % to 65–104 % and both Francis turbines and PATs with variable speed can be implemented to tackle high available head stretches. Multi-stage pump-turbines, driven by a full-size frequency converter, offer a compact and reliable solution.

For the coal mine case study of Péronnes-lez-Binche, a series of separate Francis turbines can also be installed to deal with the extreme variable head operations. This concept is unusual and the cost analysis of this solution should be assessed and compared to other hydroelectric units. In this regard, 1D numerical simulations have been carried out to investigate the operation's feasibility in the coal mine case study. The Francis turbines succeed in balancing the instant available head according to the operation in full series or in by-pass. Interestingly, the SIMSEN 1D simulation proved the 6 MWh saving in the applied system by letting the turbines continuously run instead of shutting off the system during head high gradient periods.

The high incidence of part-load operation in non-traditional pumped storage plants calls for a valid solution respecting high hydraulic efficiency and adaptability. The Deriaz pump-turbine is a rare double regulated machine (guide vanes and runner blades) like Kaplan turbines but for medium-head plant. Therefore, the advantage of Deriaz turbines comparing to Francis turbines is the high efficiency operation over a wider range of head and discharge as well as an extended region with limited pressure pulsations. The results show clearly how the downsizing of the prototype can conserve its exceptional versatility over a wide range of partial load. The presented research on this topic concludes that the computational analysis method and the design parameters employed in this study can be effectively applied to the hydraulic design and optimization process of a Deriaz mixed-flow pump-turbine runner.

Deriaz pump-turbines have never been reviewed and modelled in the literature nor discussed for a downsized model for μ-PHES applications which is extremely suited to our current energy generation and storage needs. This section describes the Deriaz pump-turbine and all the preliminary steps of its design. The robust and accessible hydraulic modelling, here presented, favours designs capable of operating at high efficiencies over wider operating ranges. The analysis is conducted on a downsized model of the Deriaz pump-turbine for μ-PHES applications and it evaluates its potential, providing a guide to its design, scaling, and adaptation to pumped hydro.

The runner design, the CFD and experimental results are found to be in agreement regarding the characteristic curves and performance. Although a further refinement of the model design might give a slightly hydraulic performance improvement, this work provides a practical and easily-built method to implement a Deriaz pump-turbine solution which gives a fine outline at its first iteration. In pump mode, a minimum of hydraulic efficiency of 80 % is registered for a wide range of discharge

load $Q \pm 40$ %. In turbine mode, the peak of hydraulic efficiency is modelled at 91 % with opening guide vanes. As expected, the combined use of a variable blade pitch with moving guide vanes provides a wider range of highly efficient working conditions, enacting a Deriaz pump-turbine a suitable turbomachine solution at high-variable load.

Chapter 4

Micro-PHES prototype

Contents

4.1 Introduction

This Chapter describes a μ-PHES that has been designed and implemented in reality in the industrial suburb of Froyennes in Belgium. The designed μ-PHES has a close-loop configuration, which consists of two reservoirs that are isolated from a free-flowing water source. Thus, the generated energy comes solely from the potential energy of the stored water in the upper reservoir. Because of its micro scale and the peculiarity of the system, the operating conditions need to deal with variable load given by the geometry of the reservoirs and by the interconnection with intermittent renewable energy sources. To cope with system requirements, a centrifugal pump equipped with variable speed technology is selected to be able to supply water into the upper reservoir (normal operation) and to work in reverse mode (or PaT) both with a high global efficiency. The selection of the PaT respects the specifications of site and the requirements of the micro EES system.

As pointed out in Section 2.5, PaTs are most applicable to micro hydropower stations from natural water streams in rural areas [Nourbakhsh *et al.* 2010a], but also to urban water distribution networks, exploiting the excess of energy that can

be present along any branch of the system [Carravetta *et al.* 2012]. The pressure along the distribution network has to be kept in balance. Usually valves are used to dissipate this excess of energy, but PaTs are an interesting technical solution that ensures both economic convenience and system flexibility [Carravetta *et al.* 2013]. The introduction of PaTs in the water-energy network offers a large potential in promoting energy savings practises [Capelo *et al.* 2017]. One of the key advantages of PaT is that it can have a payback period 5 times shorter than for conventional micro hydro-turbines, although PaT hydraulic efficiency is usually reported as being lower [Orchard & Klos 2009]. Economically, PaTs below 500 kW are profitable in hydropower and allow capital payback periods of about two years [Paish 2002] [Motwani *et al.* 2013]. PaTs thus provide a solution for those hydropower sites in which conventional turbines might not be affordable. For decades researchers discussed the hydraulic behaviour of pumps in reverse mode and tried to formulate a function or a model able to define the hydraulic performance. A collection of proposed correlations is summarized in dedicated reviews [Binama *et al.* 2017] [Jain & Patel 2014].

4.1.1 Goals of the analysis

The objective of this chapter is to explore the performances of a unique μ-PHES system equipped with a single pump in a smart grid scenario (represented in Fig. 4.1). The outcomes of the analysis have been also published in Morabito A, Hendrick P. *"Pump as turbine applied to micro pumped hydro energy storage"* Applied Energy, 241 (2019): 567-579 .

This chapter presents data of real-life pumped energy storage application in micro scale, using technical and material synergies that have not been discussed together before:

- Instead of having a group of pumps for charging and a separate group of turbines for generating, in the μ-PHES a single commercial low-cost pump operates for both modes. The adopted solution reduces the number of hydraulic machines needed and reduces the space required for pipeline fittings, thereby cutting costs. There is no other μ-PHES equipped with only a pump that copes with variable load in generating or storing energy. The literature describes experimental studies of PaT model prediction formulations but errors in the sampled efficiency evaluation used for the correlation are at 25-30 % [Williams 1994b] [Pugliese *et al.* 2016] [Nautiyal *et al.* 2011]. Further research and data to accurately calculate the PaT performance model are thus needed and here provided. The turbomachine selection method is applied and discussed and integrated with the methodology implementation of pump/PaT operations in μ-PHES.

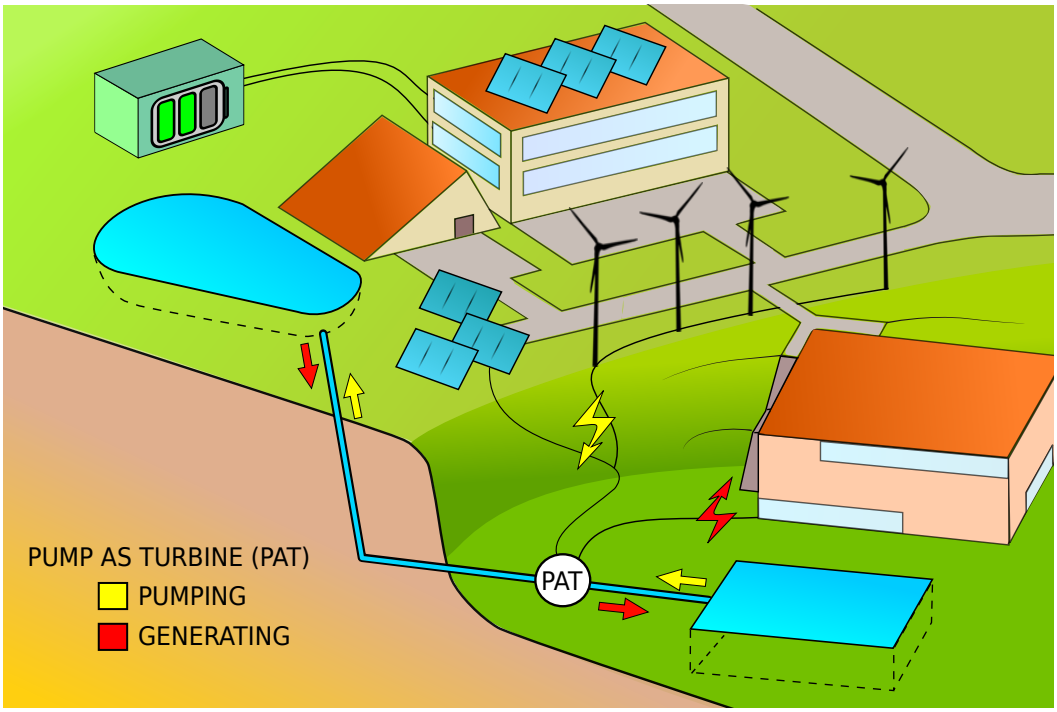

Figure 4.1: Schematic representation of the implemented μ-PHES, integrated in its micro smart grid.

- Load fluctuation and operational flexibility have become a new orientation [Ciocan *et al.* 2012] within the targets of rentability and high efficiency [Chazarra *et al.* 2018] [Pérez-Díaz *et al.* 2015] even with off-grid electricity generation in case of emergency conditions. Hence, evaluating the advantages and demonstrating the additional value of speed regulation is a relevant and practical topic [Yang & Yang 2019]. In the present study, a variable frequency driver is coupled to the motor/generator in order to change from pumping to generating mode and to react efficiently to the load fluctuation. This has been managed via monitoring the energy consumption profile of the smart grid.

- Pumped storage plants are characterized by high capital expenditure and the excavation costs, where needed, constitute one of the greater direct expense [Steimes *et al.* 2016b][Witt *et al.* 2016]. Methods of exploiting water distribution network [Carravetta *et al.* 2012] and underground cavities [Pujades *et al.* 2017] for hydroelectricity production have been previously modelled in the literature. Few other methods have been simulated in micro storage application as in aquifers and flooded quarries [Poulain *et al.* 2018] or residential areas [Anilkumar *et al.* 2017b] [Carravetta *et al.* 2018]. In the presented μ-PHES, a stormwater basin is concretely implemented as a cost-effective solution for a water reservoir.

The existing literature on PHES describes the technology in details [Rehman *et al.* 2015a] [Barbour *et al.* 2016] but information about real-life application are still needed [Aneke & Wang 2016] [Deane *et al.* 2010] especially in micro-size system [de Oliveira e Silva & Hendrick 2016]. Moreover, this paper defines the techno-economic parameters for a μ-PHES cost-effective solution. A Levelised Cost of Energy (LCOE) analysis provides an important dataset for μ-PHES feasibility breakdown.

This chapter is structured as follows: Section 4.2 starts with an overview of the smart grid where the PHES is installed. The PaT selection methodology is then discussed and the set-up application is described. Section 4.3 presents the results of the experimental investigation of the hydraulic system performance and on the use of variable speed. The economic advantages of a decentralized energy source (DES) integrated in a smart grid and a cost-benefit analysis of the μ-PHES prototype are described in Section 4.4, followed by the conclusions.

4.2 Micro-PHES in the "*Quartier Negundo*"

The PHES case study is located in Froyennes, Belgium (50°37'05"N 3°20'38"E) (Fig. 4.2). It is integrated into a smart grid agglomerate, which includes offices and conference centres, called Negundo (*le Quartier Negundo*). Several buildings in this district have an interconnected power supply network as well as sharing various sources of wind and solar energy. The μ-PHES is managed by IDETA (Agence de Développement Territorial - Territorial Development Agency) with the collaboration of the Aero-Thermo-Mechanics Department at the Université libre

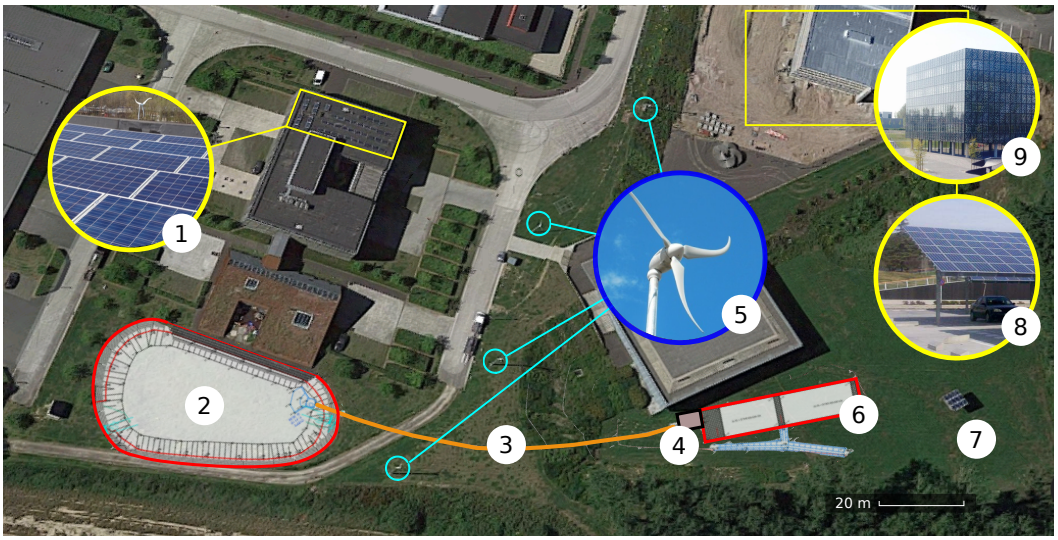

Figure 4.2: View of the *Quartier Negundo*: ① PV panels; ② upper stormwater reservoir; ③ pipeline; ④ technical room; ⑤ micro wind turbine; ⑥ lower stormwater reservoir; ⑦ solar flower; ⑧ solar carport; ⑨ building integrated PV panels.

de Bruxelles. IDETA gives technical and administrative support to businesses to help them set-up and/or develop their project plans. IDETA has also shown an increasing interest in renewable energy sources and energy efficiency by partnering several projects concerning solar, wind, biomass, hydro energy sources and electric vehicles. In Negundo, a solar flower of 5.2 kWp and two other groups of photovoltaic panels of 10 kWp and 15 kWp are installed. Four wind turbines of 2.4 kWp each are also present. 60 kWp building integrated PV panels are installed and an adjacent solar carport facility provides 20 kWp.

Today, the micro energy grid, illustrated schematically in Fig. 4.3, has two EES systems which support the energy consumption in the connected buildings. In order to store the energy surplus in night time and weekends a μ-PHES and a vanadium redox-flow battery 100 kWh at 10 kW are implemented in the grid. The battery, installed next one of the two buildings, is usable only for a severe hourly regulation to safeguard its durability and preserved mostly for the available electric vehicle charging station of the *Quartier Negundo*. The μ-PHES (of about 17 kWh) is equipped with a single PaT that provides a peak of 7 kW_{el} production. The maximum theoretical amount of energy stored, namely capacity E in kWh is given by

$$E = \rho V g H / 3600 \tag{4.1}$$

where ρ is the water density and g is the gravity acceleration. In a more accurate way, the energy generated is the product of the capacity and the total efficiency of the system in generation mode, $E_t = E\ \eta_t$. The amount of energy consumed in storing energy in the whole upper reservoir is equal to the capacity over total efficiency of the system in pumping mode, $E_p = E/\eta_p$. To design PHES, the capacity of the site has to be defined according to the available water volume V in m^3 and head H in m. About 650 m^3 are available from a stormwater basin used to collect run-off water from local roofs and roads in order to prevent flooding or erosion.

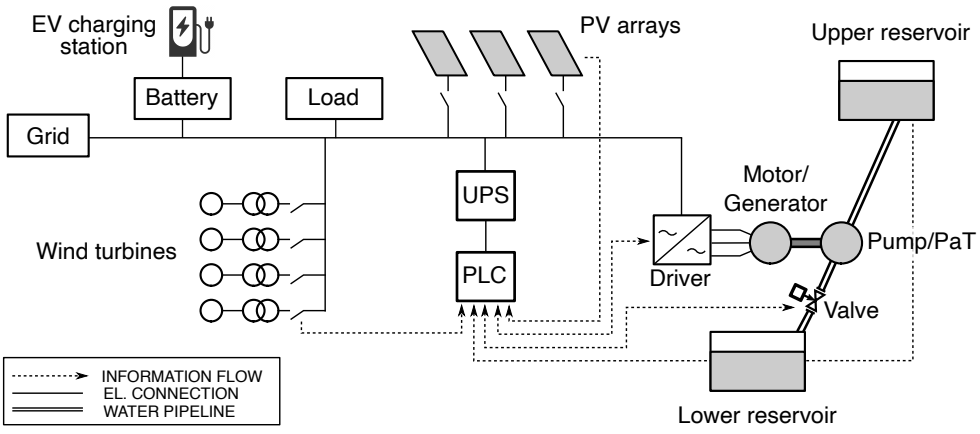

Figure 4.3: Interconnection scheme of *Quartier Negundo* smart grid.

Stormwater basins (or retention basin) - as frequently used in rural and in urban areas for flood prevention and management - provide a vegetative buffer that can withstand dry or wet conditions. They constitute an innovative solution to be applied in hydroelectricity and EES systems. Due to its location, this basin is used as the upper reservoir for the μ-PHES (Fig. 4.4). The lower reservoir, conceived as an extension of the stormwater basin, has been built with a capacity of 650 m^3 next to one of the buildings in the street block (Fig. 4.5). Building the reservoir out of prefabricated water-resistant concrete components simplifies both its installation and maintenance, which would not be possible if it was made from a series of single interconnected tanks. The final size and locations of the powerhouse has been set according strong constraints given by civil engineering considerations and economic factors. As depicted in areal view of the *Quartier Negundo* of Fig. 4.2, the technical room ④ is wedged between the nearest building and the uphill bank that the upper reservoir is located upon ②.

Figure 4.4: View of the upper reservoir in *Quartier Negundo*.

Unlike the upper reservoir, which is wide and not very deep (about 1 meter), the lower reservoir needs to fit among the existing building in the surrounding area. 650 m^3 are contained in a reservoir 3,1 m deep, 6.3 m large and 33.3 m long. The maximum depth of the lower reservoir is reached only in proximity of the pump (about 5 m) to guarantee a minimum submergence level at the pump suction side and, thus, leaving a safety margin for cavitation phenomena. Due to its geometry (deep and narrow), its water level varies considerably during the normal working cycle of charging and discharging. The minimum water level is set at $Z = 29.1$m and the maximum capacity is reached at $Z = 32.2$m. In fact, the total water level fluctuation (about 4.5 meters) is relevant to the modest maximum differential height (11 meters). Fig. 4.6 shows a schematic view of the μ-PHES in *Quartier Negundo*, tracing the absolute altitude for the reservoirs and the pump installation. In order to deal with a possible severe variation of the available head, a new feature has been tailored to this μ-PHES. A VFD is coupled to the turbomachine, allowing the

Figure 4.5: Internal view of the lower reservoir of the μ-PHES.

pump to rotate in inverse direction when working as a turbine. If it were not for the working condition variations, a gearbox would provide two rotational speeds on the shaft: one suitable for pumping and the second applied for generating mode, but no speed adjustment would be possible. The VFD modulates the rotational speed in order to operate at high efficiency under the changing working conditions: the most suitable rotational speed can be selected for the available head. As well as dealing with load fluctuation, there are other major advantages of variable speed

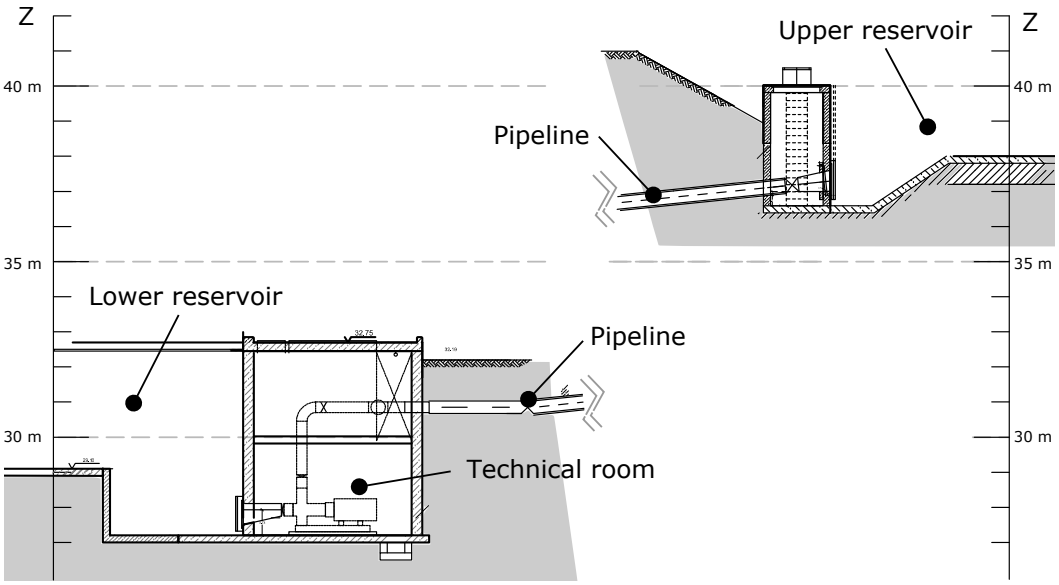

Figure 4.6: Traversal view of the reservoirs and the technical room in *Quartier Negundo*. For the sake of clarity and ease of comprehension, the pipeline is severed to fit the system in a single figure.

generation. The high inrush current at the start is remarkably reduced and gradual changes are produced in the flow that do not upset the normal functions of the system. In addition, having fewer start-ups avoids power dips, reducing the need for system maintenance as a result of the wearing of bearings and flexing of the shaft. Variable speed control does however add rather high extra costs and complexity to the system.

The PLC system is equipped with an uninterruptible power supply (UPS) to guarantee a safe shut-down procedure in case of main power fail. In unexpected power disruption or error event, the commands of shutting down the electric machine and closing the valve are sent as an alarm message.

4.2.1 Pipeline and pressure losses

The two reservoirs are connected by about 80 meters of pipeline, with an internal diameter of 355 mm made from PE100, which provides long-term strength, oxidation resistance and a low friction coefficient. In the technical room, where the pump is installed, the pipes are made of stainless steel and the diameter reduced to 200 mm (pump discharge side) and 250 mm (at pump suction side). The pipeline sinks more than 8 meters and has to cross under a bank, a pedestrian way and a sewer line. For these reasons, it has not been possible to keep the penstock outside or to bury it as usually done. Instead, directional drilling practice has been employed, adding additional cost to the pipeline installation. From the upper reservoir, a well is piloted to reach the technical room that would otherwise be inaccessible with traditional drilling practices. According to the Colebrook-Prandtl relation

Figure 4.7: Photo of the trashrack cleaner at the upper reservoir pipeline inlet installed to protect the hydraulic system. The grid is removable for easing the periodic cleaning and maintenance. A similar grid is installed at the pump suction side.

[Nourbakhsh *et al.* 2007], the head loss due to the losses in the straight pipe (in polyethylene) is about 0.6 m at the maximum measured flow rate (133 kg/s). Two grids protect the pump from external objects at the price of further losses (about 0.2 m each) and a flanged diffuser is necessary to connect two pipes of different diameters. In order to reduce these undesirable effects two diffusers are installed on each pipeline inlet. Local pressure drops have been estimated between 0.52-1.10 m for the diffuser/convergent, curved pipefittings and valves. Moreover a straight pipe of length L $\geqslant$ 2D should be fitted before the impeller pump to avoid non-uniform condition entry. However, for technical reasons and space limitations in the powerhouse, a butterfly valve is located at the pump suction side in between the convergent and the pump.

The formation of swirling eddies on the water surface at the lower reservoir is caused by asymmetric flow into the suction pipe. The velocity distribution in the sump depends on many factors: shape of the sump, disposition of the suction pipes, vertical or horizontal pump axis and the how water is fed into the sump [Nourbakhsh *et al.* 2007]. The two pipe inlets are equipped with fine grid to protect the pump, located in the technical room next to the lower reservoir. Three valves are needed to maintain accessibility to the devices and thus allow maintenance. Due to the presence of large and heavy equipment units, the powerhouse stability must be completely secured. The minimum distance between the water level in the lower reservoir and the end of the suction pipe is also important to avoid any undesired pre-swirl cavitation phenomena.

4.2.2 Turbomachinery selection

In the case study, the exploitable available head is not very large and varies considerably during a whole cycle. A traditional hydro-turbine would have been too expensive [Orchard & Klos 2009] and it would often operate in off-design conditions, reducing the overall system efficiency. To overcome these difficulties, a single pump is selected in order to charge the upper reservoir but it is able to run in reverse, as a turbine, to generate hydroelectricity. The pump must obviously be able to recharge the upper reservoir up to at least $H_{p,max} = H_g + H_{max,l}$. The pump manufacturer catalogues provide the Q_p, H_p and N_p.

The prediction models for reverse mode operations (PaT) focus on the definition of the head and flow at the BEP conditions. The ratios $h = H_t/H_p$ and $q = Q_t/Q_p$ relate the BEP working condition in pump mode with the turbine mode at the same rotational speed. It appears that PaTs usually have a BEP located at higher flow rate and higher head compared to the normal pumping operation at the same rotational speed [Nourbakhsh *et al.* 2010a, Binama *et al.* 2017]. Thus, the fluid power (proportional to the product of H and Q) engaged by the turbine would be higher than the power employed by the pump rotating at the same speed, assuming an identical efficiency. The pump hydraulic efficiency is fundamental for the formulation of several prediction models: Alatorre-Frenk [Alatorre-Frenk & Thomas 1990], Childs [Childs 1962],

Schmied [Schmiedl 1988b], Sharma [Sharma 1985], Stepanoff [Stepanoff 1957a]. Other predictive models are based on the specific speed, N_s [Lewinsky-Kesslitz 1987, Derakhshan & Nourbakhsh 2008a, Derakhshan & Nourbakhsh 2008b], that describes the runner or impeller of a turbomachine linking mass flow rate, rotational speed and energy. Recently, one-dimensional numerical codes have become available to estimate the performance of centrifugal PaTs [Barbarelli *et al.* 2016] although they require highly detailed information, which is not easy to get.

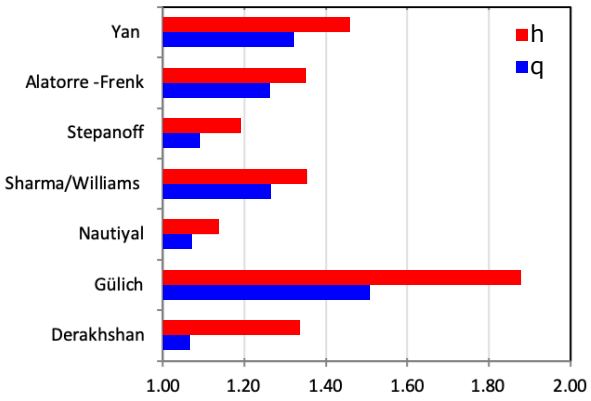

Figure 4.8: Estimation of h and q ratios by different methods (Table. 2.3) of the same selected pump of the case study.

A comparison between different predictive methods depicts a weak reliability in the pump selection: Fig. 4.8 shows the flow and head ratio calculated a posteriori on the selected pump for the μ-PHES in *Quartier Negundo*. A different approach is finally necessary because of the scattered results of the PaT performance models. Then, a statistical/empirical method is used instead. Subgroups of tested pumps in the literature [Derakhshan & Nourbakhsh 2008b, Singh & Nestmann 2010], defined by the impeller diameter, lead to a better match with the experimental values of h and q. According to the manufacturer catalogue, pumps between 0.25 m and 0.30 m impeller diameter suit the requirements in Q and H on the Froyennes site. For this pump impeller range, the following equations in dependence of N_s are found, fitting the experimental data available (Fig. 4.9) :

$$h_{fit} = 5.196\, {N_s}^{-0.323} \qquad q_{fit} = 3.127\, {N_s}^{-0.219} \tag{4.2}$$

The pump specific speed is calculated based on the pump BEP (Eqn. 2.1) and thus, the ratio h and q are obtained.

As stated before, q and h are usually greater than 1, which locates the PaT BEP at a higher flow rate and required head. A new rotational speed value must be set in order to match with the actual head offered on site $H_t = H_g - H_l$. For this passage, the so-called affinity laws help us to determine the new flow, head and power. The affinity laws, which are actually corollaries of Buckingham Pi theorem

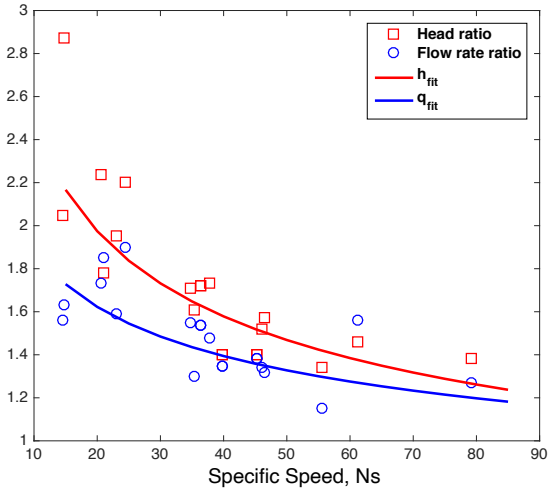

Figure 4.9: Regression for head ratio h and discharge ratio q of available PaT experimental data .

[Buckingham 1914], define the non-dimensional groups

$$\varphi = \frac{Q}{uR^2} \qquad \Psi = \frac{gH}{u^2} \qquad \pi = \frac{P_p}{\rho u^3 R^2} \tag{4.3}$$

As long as these dimensionless parameters are maintained from application to application, it is possible to obtain a good prediction of the speed scaling by a resulting scale factor. The direct scaling yields with $D_a = D_b$ and $\rho_a = \rho_b$ are the following:

$$Q_b = Q_a \frac{N_b}{N_a} \qquad H_b = H_a \left(\frac{N_b}{N_a}\right)^2 \qquad P_b = P_a \left(\frac{N_b}{N_a}\right)^3 \tag{4.4}$$

Dimensionless parameters (Eq. 4.3) are often used for turbomachinery scaling but the Reynolds number is also fundamental. The Reynolds number, Re, is the ratio of inertial forces to viscous forces of a fluid subjected to movement. Changes in the Re results in relevant hydrodynamic effects and losses. With this in mind, an efficiency correction for the modification due to PaT speed variation is necessary. The transposition is in agreement with the methodology provided by International standard IEC code NO.60193 [Commission *et al.* 1999]. In this case, a reference Reynolds number of $7 \cdot 10^6$ is considered to define the performance correction by speed variation:

$$(\Delta\eta_h)_{a\to b} = \delta_{ref} \left[\left(\frac{Re_{ref}}{Re_a}\right)^{0.16} - \left(\frac{Re_{ref}}{Re_b}\right)^{0.16} \right] \qquad \text{with : Re} = \frac{\rho v l}{\mu} \tag{4.5}$$

where $\delta_{ref} = (1 - \eta_{h,\ a,\ opt}) / \left[\left(\frac{Re_{ref}}{Re_{a,\ opt}}\right)^{0.16} + \frac{1 - V_r}{V_r} \right]$ with V_r equal to 0.7 for operation as a turbine and 0.6 for operation as a pump [Commission *et al.* 1999].

The values of $\Delta\eta_{h,\ a\to b}$ diverge from the experimental results by 0.18 %, thus within the data accuracy.

Another selection criteria in the PaT selection is the determination of the operating condition at torque $M = 0$ and, consequently at zero power output. This condition of no load defines the runaway characteristic which connects all the points H(Q) which occur for $M = 0$ at various speeds. Gulich [Gulich 2010], defines the following equation for the runaway flow rate, Q_{rw}, and the runaway head, H_{rw}, by elaborating the data offered in [Engeda 1988, Schmiedl 1988a, Yang 1983]

$$H_{rw} = H_{t\,BEP}\,(0.55 - 0.002\,N_{s,\,p}) \tag{4.6}$$

$$Q_{rw} = Q_{t\,BEP}\,(0.45 + 0.0067\,N_{s,\,p}) \tag{4.7}$$

According to the affinity laws (Eq. 4.3) with $Q_{rw} \propto N$ and $H_{rw} \propto\ N^2 \propto Q^2$, the runaway characteristic curve is obtained as a parabola through the origin of the coordinate system $H - Q$.

The numerical procedure for performance prediction and selection is illustrated in Fig. 4.10. Based on the characteristics of an available pump from the manufacturer's catalogue, the most suited performance prediction model can be used. The parameters h, q are defined as the parameter ξ, which estimates the efficiency ratio η_p/η_t [Derakhshan & Nourbakhsh 2008b] (*step 1*). Thus, the working conditions of the selected pump in reversed mode rotating at the pump rotational speed are found (*step 2*). Applying the affinity laws, the rotational speed scaling is performed to suit to the site constrains: the flow rate and the available head are site depending (*step 3*). The revised rotational speed and best efficiency point are determined (*step 4*) and, by using the Eq. 4.5, the PaT hydraulic efficiency is adjusted (*steps 5-6*). In this iterative procedure, continuous checks must be performed to avoid cavitation phenomena and crossing runaway conditions. Minimum operating pump shaft speed is defined as that at which the pumping system is no longer able to deliver a positive flow rate against a static head. Hence, it is specific to each working

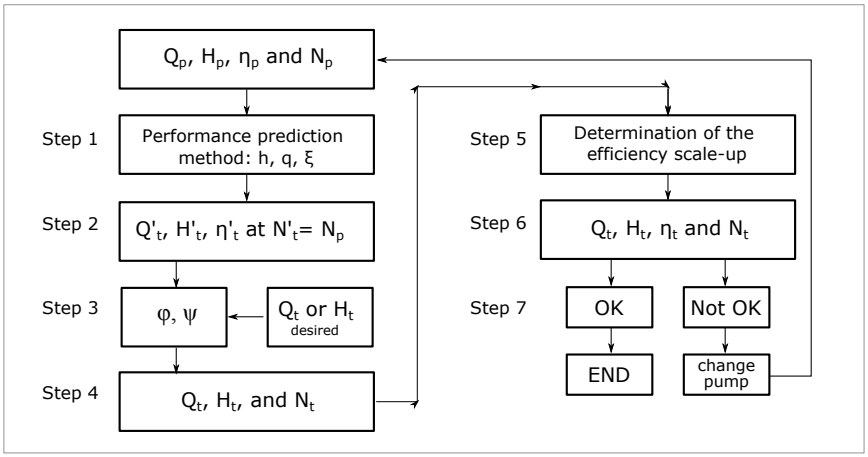

Figure 4.10: Decision tree for PaT selection.

condition. The minimum operating speed in reverse mode depends strongly on the running condition. According to the velocity flow angles at the inlet and outlet of the runner at the selected rotational speed, PaTs are able to deliver a power-output (torque $M > 0$) only above a minimum flow-rate, $Q_{PAT-min}$. Below this value, the PaT power output is negative. In other words, for $Q_{PAT-min}$ and consequently $H < H_{PAT-min}$, the power station is actually using energy to maintain the runner at the selected N. If possible, N should be re-set, when appropriate, updating the minimum values of $Q_{PAT-min}$ and $H_{PAT-min}$. The new operating condition at the set rotational speed must take into account PaT stability and the avoidance of incipient cavitation. If these prerequisites are not respected, a new pump must be selected (*step 7*).

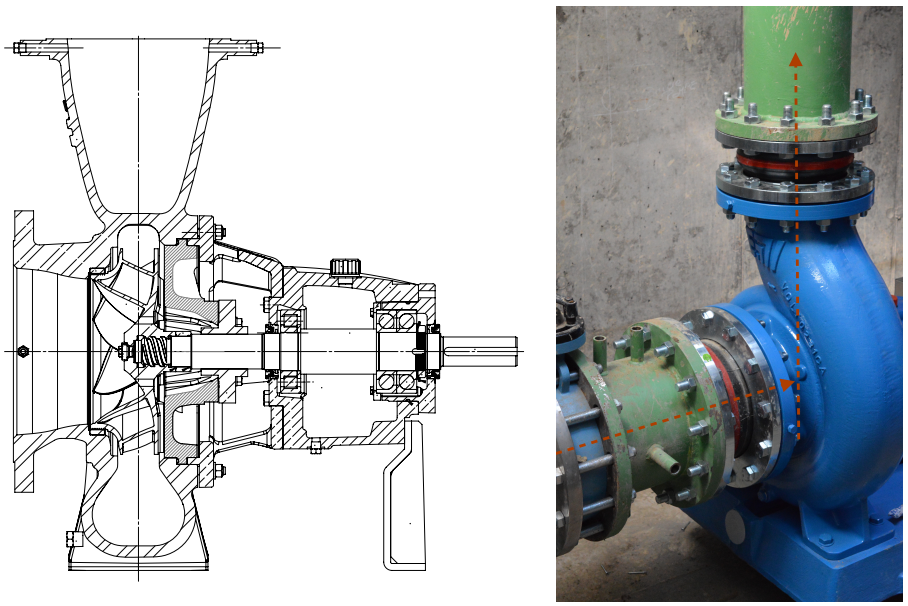

Figure 4.11: Sectional view and photo of the pump/PaT of the μ-PHES in *Quartier Negundo* - Froyennes

Concerning the case study, in the end, a centrifugal pump with an impeller diameter of 296 mm from Ensival-Moret/Sulzer was chosen. The pump has a horizontal axis configuration and the discharge pipe centerline is crossing the axis of the motor-impeller (Fig. 4.11). The main parameters of the pump are listed in Table 4.1 and photos of the facility technical room are shown by Fig. 4.12. The pump suction and discharge sides have diameters of 250 mm and 200 mm respectively. The specific speed of the selected pump at 1000 rpm results in 55 (rpm, m^3/s, m). This pump is in agreement with the specifics of the PaTs adopted for the formulation of Eq. 4.2.

According to Eq. 4.2, the pump running in reversed mode at 1000 rpm has its BEP at 13.5 meters of head for about 117 kg/s of water. Due to the geographic limitation of the site, the system is not able to provide the required head to run the PaT at its estimated BEP. By the similitude given by Eq. 4.4, the rotational speed

Figure 4.12: The two floors of the powerhouse or technical room of the *Quartier Negundo*. At the upper floor the electric panel and control system is set. In the lower floor the centrifugal PaT and the electric motor is installed.

suitable for 6.5 meters available head is about 700 rpm and it will be provided by the VFD.

As previously depicted by Fig. 4.6, the pump axis is located below the minimum water level height at the lower reservoir, and precisely at 1,3 m. This set-up has been chosen as additional factor of safety to avoid cavitation. To assist preliminary pump selection procedure and coordinate civil engineering works, in terms of excavation depth of the technical room, the net positive suction head available ($NPSH_a$) has been calculated. The critical condition for cavitation can be avoided by placing $NPSH_a$, a measure of how close the fluid at a given point is to cavitation, greater than $NPSH_r$, namely the head required to keep the flow from cavitation and given by the manufacturer. $NPSH_r$ is often defined as the working point in which 3% head loss is produced by a reduced hydraulic performance [Dixon & Hall 2010]. The maximum height for the pump suction side, Z, is defined by the following definition of $NPSH_a$ in [m]:

$$NPSH_a = H_{bar} - Z - H_{vp} - H_l - \sigma H \tag{4.8}$$

where H_{bar} [m] is the barometric pressure at the lower reservoir, H_{vp} is the water vapour pressure [m], H_l is the head loss in the suction side of the pump and σ is the Thoma number. Fundamental notes on the cavitation parameters are also given in Appendix B. Assuming the scenario for the μ-PHES in *Quartier Negundo* (about 30 m above sea level) operating at high water temperature of 20°C ($H_{vp} = 0.234$ m) and with unfavourable weather condition ($H_{bar} = 0.90$ atm), $NPSH_a$ equals to 5 m and, thus, greater than the $NPSH_r = 1.97$ (Table 4.1). The factor of safety of 3 m is set by σ according to Fig. B.2 and a pressure drop from the lower reservoir and the pump of 0,5 m (at the pump maximum discharge).

4.2.3 Set-up and instrumentation

The system is monitored in order to measure the performance of the turbomachine in pump and in reverse mode. Data is acquired in steady state operations with a frequency of 1 Hz by sensors placed in key sections of the facility line, as represented in Fig. 4.13.

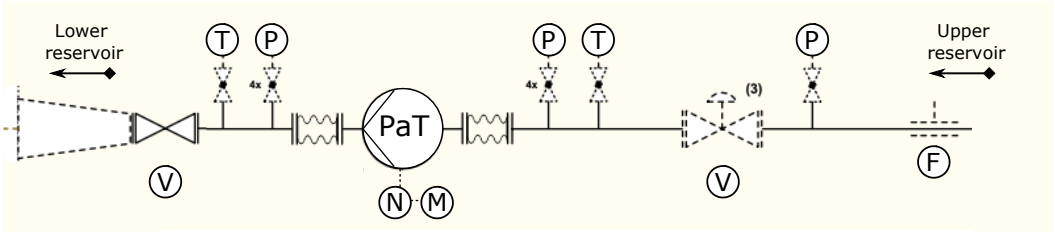

Figure 4.13: Schematic view of the micro-hydropower station and location of the valves (V) and measurement devices: (P) pressure sensors; (T) thermo-couples; (N) tachometer; (M) torque-meter; (F) flow-meter.

Table 4.1: Extract of the pump data-sheet Main parameters of the pump installed at the micro pumped storage facility plant.

Pump main parameters	
Installation year	2017
Horizontal axis	
NPSHr at BEP pump	1.97 m
Pump BEP rotational speed, N_p	1000 rpm
PaT BEP rotational speed, N_{PaT}	-700 rpm
Diameter suction side	D250
Diameter discharge side	D200
Number of blades	6
Blade thickness at exit	2.8 mm
Blade thickness at mid-channel	5.2 mm
Specific speed	55
Impeller exit diameter	296 mm
Impeller exit width	45.6 mm
λ hub	33°
λ shroud	31°
β_2 hub	33.6°
β_2 shroud	31.5°

One pressure transmitter (Unik5000) is installed on the PaT inlet side and another one at the PaT discharge side. These pressure taps are manifolded (Fig. 4.14) and each tap is valved separately [Commission *et al.* 1999]. A third pressure sensor access to the pressure upstream the control valve for operational reasons.

Detailed illustrations of the instrumentation are collected in Fig. 4.15 and 4.16. An ultrasonic flow-meter is installed upstream of the PaT where a sufficient straight pipe length is available to ensure a fully developed symmetrical flow profile. The

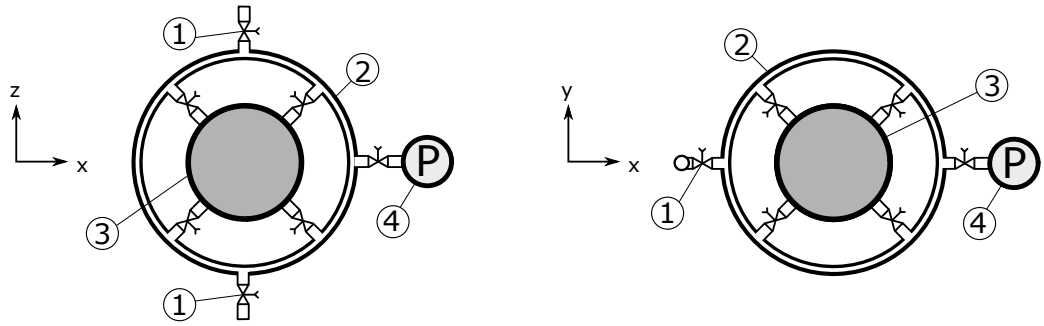

Figure 4.14: Pressure transmitted manifold practise for horizontal and vertical pipes: ① air purge/water drain; ② manifold ring; ③ pipe section; ④ pressure sensor.

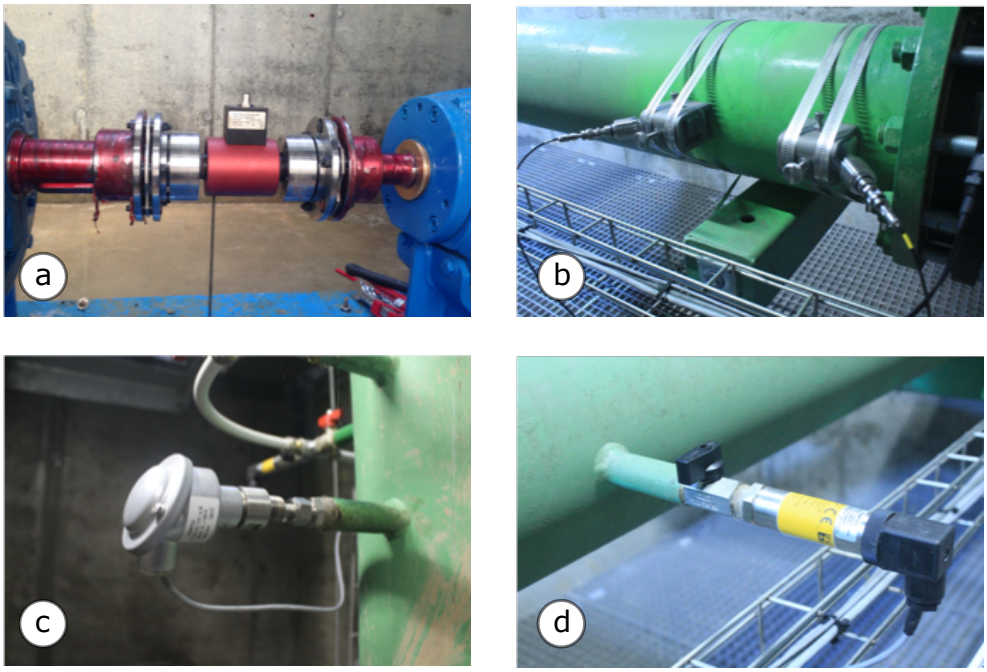

Figure 4.15: ⓐ torque-meter; ⓑ ultrasonic flow-meter sensors; ⓒ thermocouple; ⓓ pressure sensor.

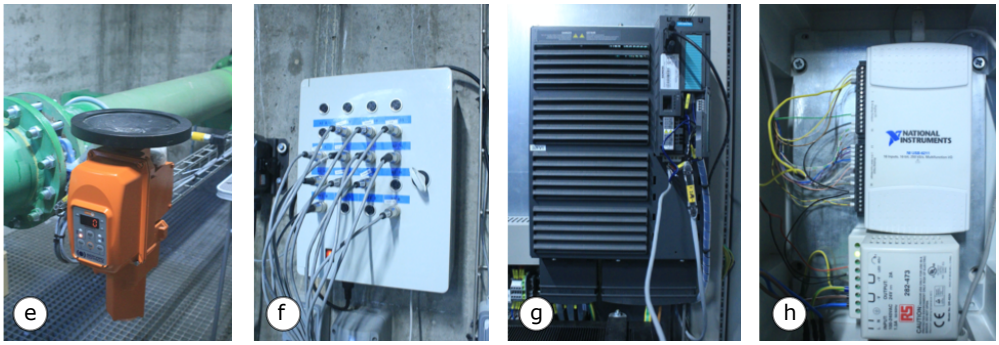

Figure 4.16: ⓔ electromechanical valve; ⓕ shunt box and connectors; ⓖ frequency driver; ⓗ acquisition card and sensors' electric tension supply.

ultrasonic flow-meter can be clipped directly onto the pipe and measures the flow rate in both directions. Mechanical torque and rotational speed measurements are obtained by a torque-meter mounted onto the turbine shaft. Water temperature is measured in order to adjust the flow-meter setting as dependent on the sonic path and to alert to the possibility of ice formation in the volute, sealing and pipeline. When water freezes and becomes ice, its expansion can be devastating. Ice growth at -8 °C can exert pressures as high as 92 MPa [Otero & Sanz 2000], pressures that not all the components of the pipeline and of the pump can withstand.

The signals outputs are connected to an acquisition card and managed by LabView for real-time measurement acquisition and control. The system is able to detect irregular flow by alarms from the driver, the presence of tension as well as from the flow-meter. The instrumentation range, accuracy and expected measurement ranges for the air side of the installation are listed in Table 4.2.

Since the PHES control system pilots the VFD via MODBUS and an electromechanic valve, it is possible to modulate the discharge rate and speed to best suit the operating conditions. Gradual changes are produced in the flow that do not upset the normal functioning of the system: the pump/PaT can be ramped up (or down) to reduce water hammer, which could have dangerous consequences on the integrity of the whole pipeline. If it were not for the variation of the working conditions, a gearbox would provide two fixed rotational speed on the shaft: one suitable for pumping and the second applied for generating mode.

Table 4.2: Instrumentation range and accuracy summary.

Apparatus	**Quantity**	**Sensor**	**Range**	**Accuracy**
SPT100	T_{IN}	Thermocouple	0 - 50 °C	±(0.3+0.005T)%
	T_{OUT}	Thermocouple	0 - 50 °C	
DATAFLEX 32/300	M	Torque-meter	± 300 Nm	± 0.2 % FS
	N	Rotational speed	0 - 2000 rpm	
Diris 60A	P_{syt}	Wattmeter	scalable	± 0.5 %
UNIK 5000	P_A	Pressure sensor	-0.9 - 0.6 bar	± 0.2 % FS
	P_B	Pressure sensor	0 - 2.0 bar	
	P_C	Pressure sensor	0 - 1.5 bar	
AquaTrans T600	$\dot{m}$	Ultrasonic flow-meter	± 150 kg/s	± 1.5 % FS

4.2.4 Error measurement propagation

The experimental results are averaged values over a total number of 300 samples per steady operating condition. The precision of a given single parameter is computed with the following uncertainty model:

$$U = \pm[(B_{err})^2 + (t_{95} S_{\overline{X},err})^2]^{1/2} \tag{4.9}$$

where U is the uncertainty of the parameter, B_{err} is the systematic error (or bias error), $S_{\overline{X},err}$ is the precision index error (or random error), and t_{95} is the Student's t degree of freedom and is computed with the Welch-Satterthwaite approximation [Dieck 1997]. The precision index error is determinate by the square root of the sum of the square random uncertainties $S_{\overline{X}_i}$:

$$S_{\overline{X},err} = \sqrt{\sum_{i=1}^{K} (S_{\overline{X}_i})^2} \tag{4.10}$$

The $S_{\overline{X}_i}$ is the standard deviation divided by the square root of the number of samples for the i^{th} element. The high number of samples acquired in these tests reduces $S_{\overline{X},err}$ making it negligible. Therefore, only the systematic error, that remain constant in the whole test [Abernethy *et al.* 1985], is taken in consideration. It is calculated by the square root sum of the square of the single systematic error B_i:

$$B_{err} = \sqrt{\sum_{i=1}^{K} B_i^2} \tag{4.11}$$

The error measured for each parameter propagates in derived results though the following propagation relationship:

$$\frac{\partial f}{f} = \sqrt{\left(\frac{\partial f_1}{f_1}\right)^2 + ... + \left(\frac{\partial f_k}{f_k}\right)^2} \tag{4.12}$$

in which $f = f(f_i)$ is the combined results, ∂f is the associated uncertainty of the quantity f, while ∂f_i are the uncertainty of the independent parameters f_i. The bias and the random error should be taken in consideration separately until summed as seen in Eq. 4.9, but since we consider the random error negligible only the bias error will be considered for the error propagation.

Fig. 4.17 shows the propagation of the relative error for the different parameters measured and the derived system efficiency, expressed as $\eta = M\omega/\rho g Q H$, in function of the discharge number $\varphi = Q/\pi\omega D^3$.

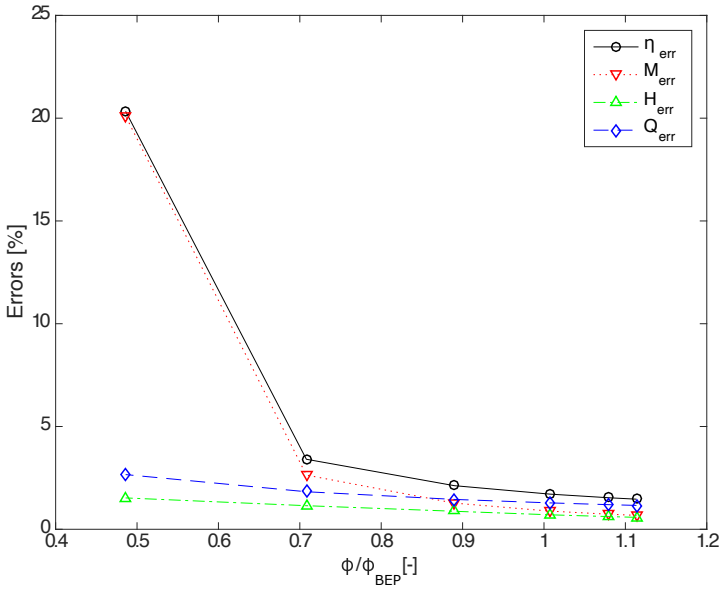

Figure 4.17: Error propagation in function of the dimensionless discharge number.

4.2.5 Experimental methodology

The power generated and consumed by the pump installed in normal and reversed operations are:

$$P_p = \frac{\rho g\, H_p Q_p}{\eta_p}, \qquad P_t = \rho g\, H_t Q_t\, \eta_t \tag{4.13}$$

where H_p and H_t are obtained by the total pressure gap measured in the pump discharge and in pump suction side. The flow rate is directly measured by the flowmeter, which is able to detect possible flow irregularities resulting from, for example, the presence of a mixture of vapour or air and water in the pipeline.

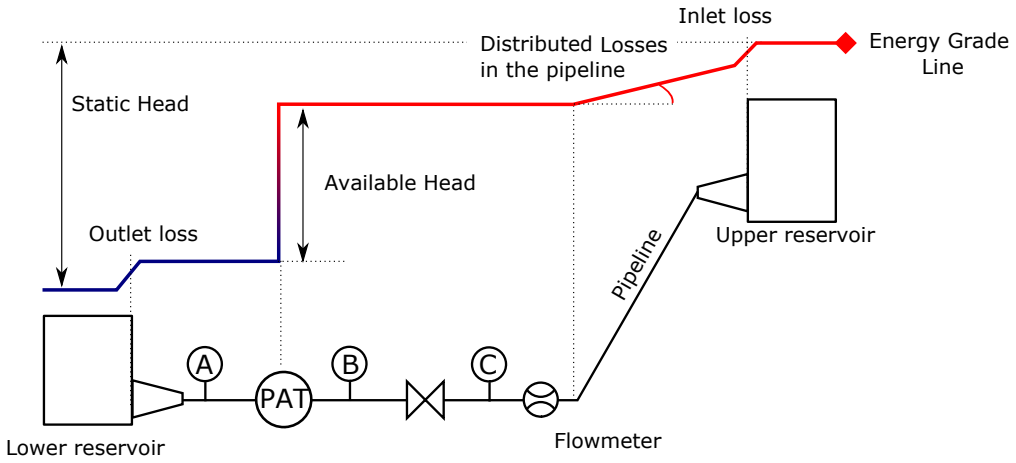

Figure 4.18: Schematic layout of the set-up and graphical representation of the energy grade line of the system in generating mode.

Fig. 4.18 illustrates the schematic layout of the set-up and the positions of the pressure sensors (pressure sensors A, B, C). Pressure transmitter A faces the lower reservoir and measures the water-level height when the system is not running. The pressure transmitter C is always in communication with the upper reservoir measuring its water-level when the valve is closed. The water-level height measure needs to be continuously calibrated to the atmospheric pressure. In Fig. 4.18, the energy grade profiles during the hydropower generation by mean the PaT is qualitalevly depicted. The available head reduction due to the distributed losses in the straight pipe (in polyethylene) is about 0.6 m at the maximum measured flow rate. Local pressure losses are also produced by the different fittings of the pipeline. Two grids protect the pump from external objects at the price of further losses (about 0.2 meters each) and a flanged diffuser is necessary to connect two pipes of different diameters. To reduce these undesirable effects, two diffusers are designed and installed on each pipeline inlet.

Every test begins with recording the water levels of the reservoirs to provide the initial theoretical available head (gap from transmitters C and A in Fig. 4.19). While the valve is still closed, the machine is set in motion and it produces turbulences

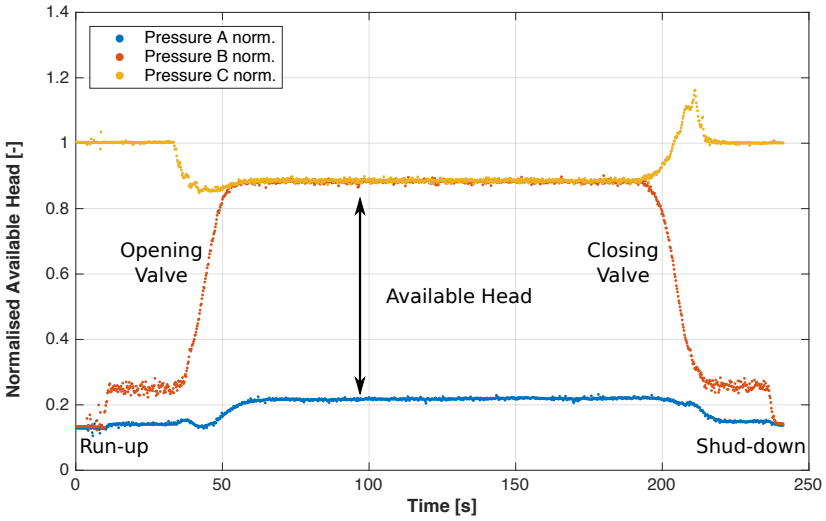

Figure 4.19: Pressure measurements for sensor A, B and C facing PaT run-up, opening valve, normal operation, closing valve and shut-down.

(fluctuations of measurement of sensor B in Fig. 4.19). Once the machine starts the valve is progressively set open at 100 %. Within 25 seconds the electromechanical valve is cleared. From then on, until the closing of the valve, sensors A and B define the available head. Water starts flowing in the piping system and, due to friction, energy losses are encountered: the available head is now reduced by a factor dependent on the square of the flow rate. Sensors B and C, are now recording a lower available head that geodetic value and the pressure sensor A checks a higher pressure available needed to over pass the local losses due to the draft tube and the protection grid. The plot on the total pressure development shows that the available head is really affected by the working conditions up to a shortening of 23 %. In shutting the valve, the flow rate slows down and conditions similar to the initial status are reached again for sensors A and B. Remarkable is the pressure peak recorded by the sensor C in closure. The water flow in the pipeline is subjected to an abrupt stoppage of the flow (albeit fairly slow) and a pressure wave is formed. Since liquid is not compressible, any energy that is applied to it is instantly transmitted. The velocity of the flow, the sizes of the pipe and the closing speed of the valve are crucial to define the water hammer effect. The pressure waves created at rapid valve closure can reach five times the system's working pressure [Nourbakhsh *et al.* 2007], causing bursting of the pipeline and pump casing as well as fracture in the pipe fittings. For this reason, it is essential to understand under what conditions these pressure waves are produced and reduce the pressure rise as much as possible in the piping system. The slowness of the electromechanical valve has been set to transform this phenomenon harmless.

For the exploration of the entire operating range in pump and turbine modes, multiple tests are conducted. The efficiency is defined as the power transferred

between the available hydraulic power to the shaft:

$$\eta_p = \frac{\rho g\, H_p Q_p}{M\omega_p} \qquad \eta_t = \frac{M\omega_t}{\rho g\, H_t Q_t} \tag{4.14}$$

where ω is the rotational speed in rad/s and M is the torque in Nm. Eq. 4.13 includes mechanical losses in the shaft seals and bearings, and the volumetric efficiency, which applies to leakage across impeller shroud rings and balancing drums [Karassik *et al.* 2001].

The logic of energy management of the μ-PHES is realised by a programmable logic controller (PLC) connected to a computer. Table 4.3 summarises the key points for a correct functioning of the μ-PHES installed and Fig. 4.20 frames the interfaced developed in LabView available on site. The rationale for the management approach in the smart grid is based on the characterisation of the pump performances (in pump and turbine modes) and the continuous evaluation process of the grid energy fluxes. The objective functions for the integration of the μ-PHES into the smart grid have been developed in the pursuit of a safe and efficient EES facility and are available to the PLC. Nevertheless, the system has only been activated under manual control so far for testing and under steady working operations. Future work concerns deeper analysis of the interaction between the energy source units and storage and the plug-in of the automated system.

In pumping mode, the PLC aims to maintain the highest efficiency setting the proper, N_p, at the given instant pressure gap available at the pump extremes (p_A and

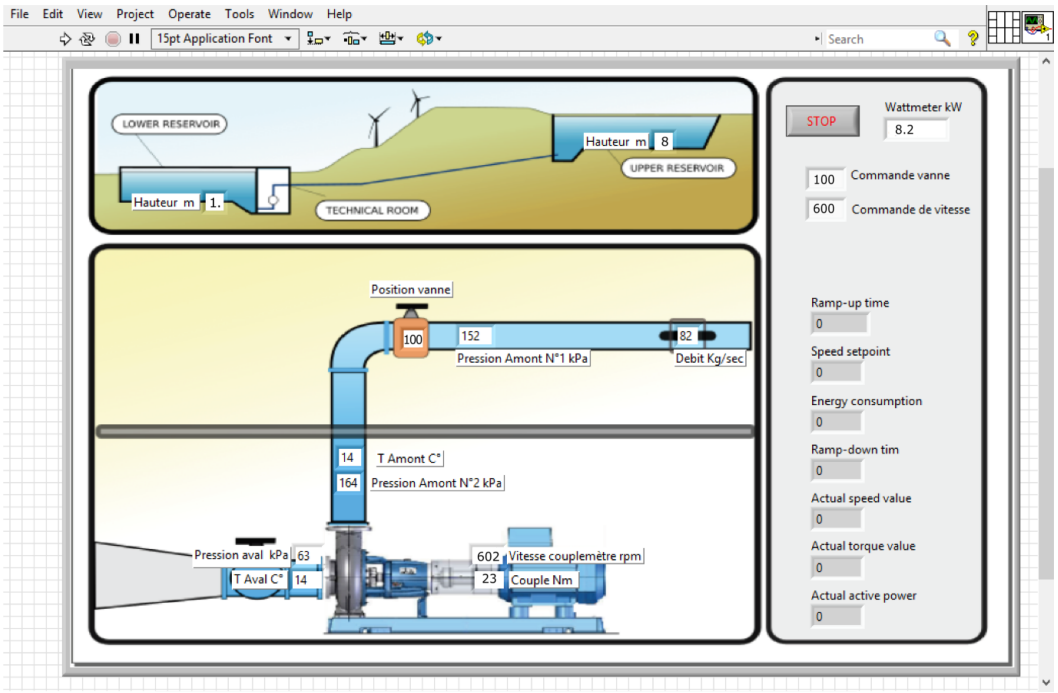

Figure 4.20: Human-machine interface developed on the LabView for real time control and analysis.

Table 4.3: Summary of PHES control and command actions.

Step	**Description**
Instrumentation check	Check on system alarms, electric tension and consistency of the measurements.
Measurements	The acquisition data system is ready and running in continuous for real time control and command.
Evaluation of energy surplus	Instant difference of load demand and RES production. With positive surplus, pump is ready in pump-mode. With negative surplus, pump is ready in turbine-mode. Evaluate the requirements*.
Detection of the water levels	Definition of the stationary head among the two reservoirs by pressure measurements.
Mapping	Forecast the working conditions based on surplus and water levels (rpm, m^3/s). Estimate losses and compute the available head. Re-assess the operating condition and requirements.
Run-up	The pump runs (pump-mode or turbine-mode)
Synchronisation	Rotational speed adjustments based on available head fluctuation and instant energy surplus.
Shut-down	Operating conditions or requirements are no longer met.
Stand-by	Maintain the system ready.

(∗) Water levels of both reservoirs in the limits agreed under security and safety reasons.

p_B) corrected by the pressure losses along the hydraulic system. As speed changes, efficiency peak follows a parabolic curve with apexes at the origin. Efficiency is therefore independent of limited changes in rotational speed except for a slight shift reliant on the Reynold number. Absolute minimum pump shaft speed, N_{min}, is defined as that at which the pumping system is no longer able to deliver a positive flow rate against a static head. The absolute maximum speed, N_{max}, is linked to the maximum flow rate on the $H-Q$ curve which limits the operation due to cavitation and mechanical constraints. Hence, it is specific to each working condition. The minimum operating speed of the installed pump occurs when the lower reservoir is full (minimum geodetic head between the water levels of the two reservoirs). On the other side, the maximum rotational speed occurs when the lower reservoir is about to be empty (maximum geodetic head). The set pump power consumption, P_p, is determined by Eq. 4.13 and it comes from the difference of power generated by the RES installed in *Quartier Negundo*, P_{RES}, and the electric load consumed by the smart grid consumed, P_{load}. This surplus, $P_{RES} - P_{load}$ can exceed the required power in storing at μ-PHES and curtailment would be needed (P_{curt}). On the other hand, if $P_{RES} - P_{load}$ would not be sufficient, electric power could be purchased

from the grid or injected by the vanadium redox-flow battery of the smart grid, P_{in}. For the sake of energy efficiency and economics, the amount of the purchased P_{in} can be limited to a fraction of P_{RES}, such that the power surplus would be adequate for at least 90% of P_p ($k_{in} = 0.1$). The PLC objective reflects the following problem to solve Eq. 4.15.

$$\max_{\eta_p} : \quad \eta_p = f(H_p, Q_p, N_p) \tag{4.15}$$

$$\begin{aligned} \text{Such that} : \quad & H_p = (p_C - p_A) + H_l(Q) \\ & P_p = \rho g \, H_p Q_p / \eta_p \\ & P_p = P_{RES} - P_{load} + P_{in} - P_{curt} \\ & N_p \in \Lambda_N \qquad \Lambda_N = [N_{min}, N_{max}] \\ & P_{curt} \in \Lambda_{P-curt} \qquad \Lambda_{P-curt} = [0, P_{RES}] \\ & P_{in} \in \Lambda_{P-in} \qquad \Lambda_{P-in} = [0, k_{in} P_p] \end{aligned} \tag{4.16}$$

Another operating strategy in pumping is not based on running the pump at the highest efficiency point but, when possible, fully exploiting the power surplus that the connected RESs can offer and avoiding extra injection of power ($P_{in} = 0$). Indeed, increasing N at constant H, the flow rate Q and power P raise accordingly. This practise prefers to not curtail the instant RES's exceeding power but to store it as potential energy in the upper reservoir. The energy management objective can be thus expressed as follow:

$$\min_{P_{curt}} : \quad P_{curt} \tag{4.17}$$

$$\begin{aligned} \text{Such that} : \quad & H_p = (p_C - p_A) + H_l(Q) \\ & P_p = \rho g \, H_p Q_p / \eta_p \\ & P_p = P_{RES} - P_{load} - P_{curt} \\ & N_p \in \Lambda_N \qquad \Lambda_N = [N_{min}, N_{max}] \\ & P_{curt} \in \Lambda_{P-curt} \qquad \Lambda_{P-curt} = [0, P_{RES}] \end{aligned} \tag{4.18}$$

However, this strategy would probably not operate the pump at BEP conditions most of the time and could compromise the pump lifetime and the system safety.

The primary goal of using PaT with variable speed is to maintain a nearly constant high efficiency regardless of the head availability. In practice, the PLC tunes the rotational regularly to take advantage from the instant available head and help the system's RES to fulfil the P_{load}. T he two water levels are always changing, mostly because of the considerable depth of the lower reservoir.

A different objective function related to the economic viability of the smart grid can also be set but a punctual cost-benefit analysis of the whole smartgrid business model (resources and appliances) is required. An hybrid methodology, that envisages turbomachinery safety and maximum assests profitability, would be the scope of future work.

4.3 Results

4.3.1 Experimental characterisation

The use of variable speed pumping in PHES integrated into a smart grid aims to give flexibility to EES [Mercier *et al.* 2019, Pérez-Díaz *et al.* 2015, Chazarra *et al.* 2018, Marchi & Simpson 2013]. Whenever possible the pumping station only uses the intermittent and fluctuating surplus energy from the rest of the system. The manometric head provided by a pump or exploited by a PaT is dependent on the rotation speed of the impeller. For this reason, one method to adapt the characteristic curves of a turbomachine with fixed geometry is to change its peripheral speed. The hill chart in Fig. 4.21 shows the characteristic curves of a pump installed on the site in Froyennes at different rotational speeds from 800 to 1100 rpm. Peak of hydraulic efficiency is measured as being 72.7 %. The mechanical power consumption is thus re-traceable according to Eq. 4.13 and is shown in Fig. 4.22. The pump can use a relatively wide range of electrical power moving from 5 kW (low speed) up to almost 17 kW (high speed) for storing energy in the upper reservoir.

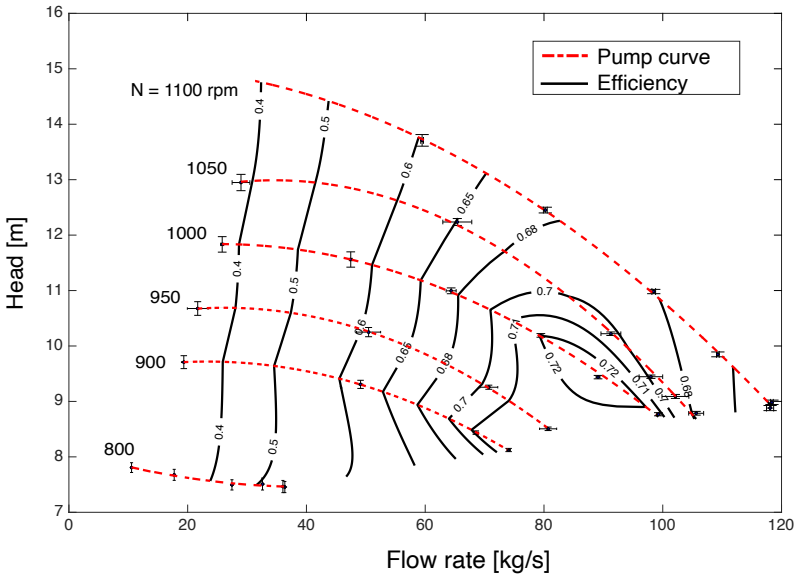

Figure 4.21: Experimental results of the pump characteristics and its hydraulic efficiency.

In reverse mode, the efficiency is higher than 70 % over all the available head range offered by the site. To operate at high performance under a wide range of available head the rotational speed must be adjusted, as described previously in Section 2.5.1. Consequently in this case, the rotational speed is scaled up to 800 rpm for highest available head on-site (Fig. 4.23). Finally, a round-trip hydraulic efficiency of 52 % is achieved by the experimental investigation in pump mode and turbine mode.

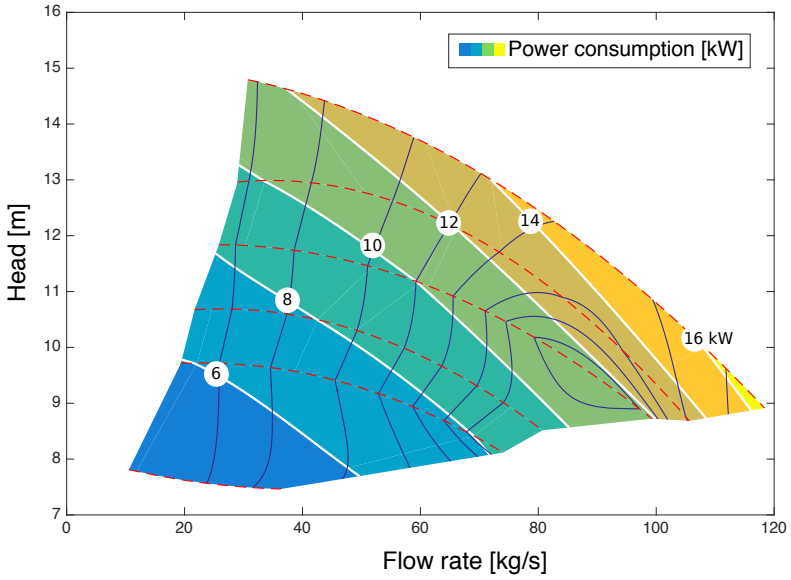

Figure 4.22: Experimental results of the pump and its power consumption.

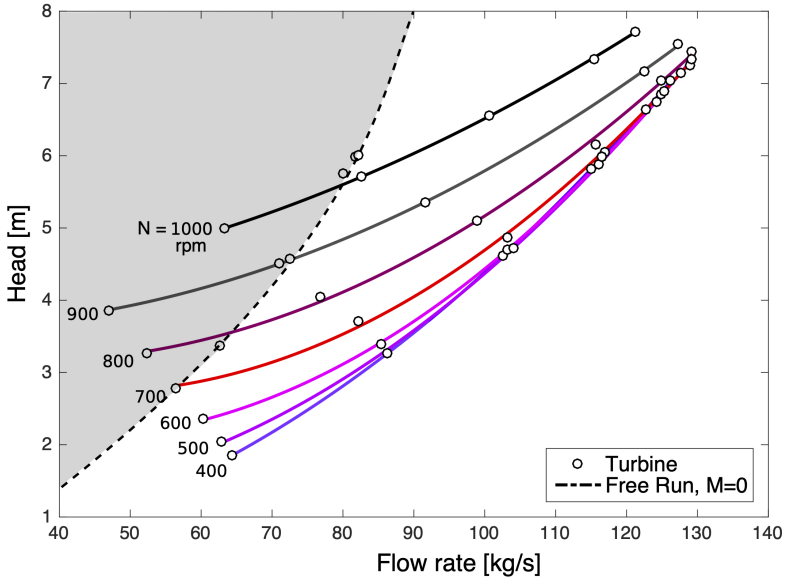

Figure 4.23: Experimental results of PaT characteristics in Q-H plot limited by the runaway curve.

The PaT characteristic curves are showed in Fig. 4.24 which compares the efficiency curves obtained by the measurement at fixed speed N_{PAT} with a variable regulation of 500 - 800 rpm. The black line is the efficiency curve of the PaT as it would run at the pump nominal synchronous speed N_{PUMP} and displays the rele-

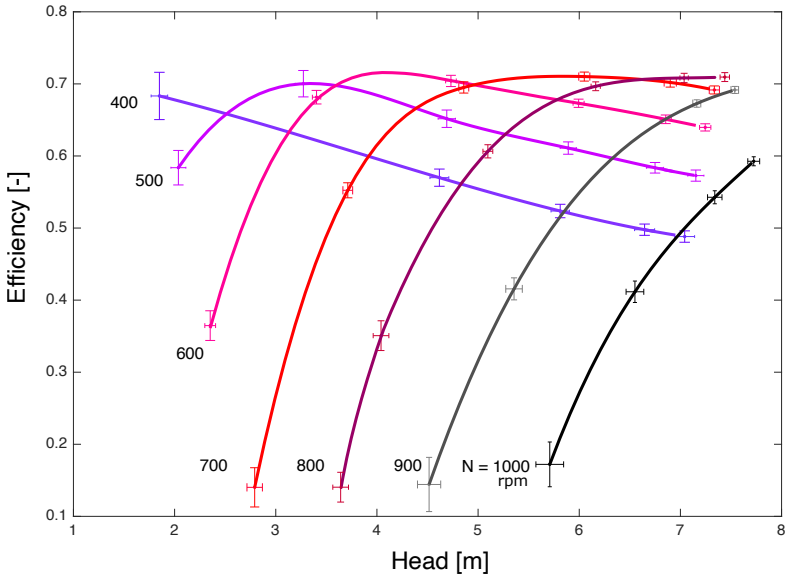

Figure 4.24: Experimental results on PaT efficiency over the variable head, H.

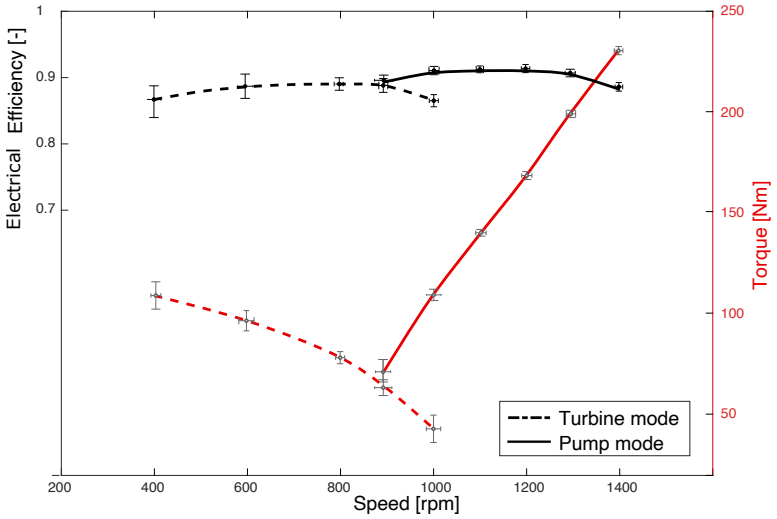

Figure 4.25: Electrical efficiency and torque over the variation of the rotational speed for turbine and pump modes.

vant efficiency improvement of using speed adjustment. The runaway curve, where $M = 0$, limits the area of energy production as already depicted in Fig. 4.23. The range of flow rate at high efficiency (>70 %) in reverse mode is 1.2 times larger than in pump mode regardless of the reduced speed: 65 - 105 kg/s in pump mode and 80 - 135 kg/s in turbine mode. At minimum load conditions, the PaT runs with a geodetic head reduction of about 55 % from its maximum. Lower rotational speed

allows the PaT to adapt to the running water regime at reduced available head and to preserve high efficiency.

The motor generator is a 30 kW WEG type 380/660 V 50 Hz 6P and it is characterized by an efficiency of 92.1 - 92.8 % in the range of 50 - 100 % of the load. The total effect of the motor/generator and the VFD is presented in Fig. 4.25. In pump mode, the total efficiency does not differ substantially from the motor manufacturer data-sheet. However, in turbine mode, the driver lowers the total electric efficiency and differently according to the speed. The overall efficiency of the system including charge, discharge and conversion turns out to be 42 % (electrical round-trip efficiency). The round-trip efficiency obtained for the installed μ-PHES is not comparable with large scale PHES of 75 - 80 % [Jülch 2016] or lithium batteries (65 - 93 %) [Tan *et al.* 2017].

4.3.2 Variable rotational speed efficiency gain

The pumping station is capable to use only the surplus of energy given intermittently by the RES of the system. Indeed, the pump is capable to use a wide range of electrical power moving from 5 kW (low speed) up to 17 kW (high speed) for storing energy in the upper reservoir. As rotational speed changes, efficiency follows parabolic curves with their apexes at the origin of the graph. The pump power consumption is affected by the different flow rate at the variation of the rotational speed and the turbomachinery efficiency Thus, except for a slight shift dependent on Reynold number, the peak of efficiency is independent of rotational speed. Fig. 4.26 pictures the hydraulic efficiency gain by using the pump with variable rotational speed compared to fix nominal rotational speed (1000 rpm):

$$Gain_p = \eta_{VFD} - \eta_{1000} \tag{4.19}$$

In this chapter, the head is normalised based on the nominal pumping head. Rotational speed is normalised on the nominal value in pump mode, such that $N_{ad} = N/Nn$. N_p needs to adapt to the system required head accordingly. The pump working range stays between $N_{ad} = [0.960, 1.16]$. This method allows the installed pump to operate at heads otherwise not accessible at the nominal rotational speed Nn and, thus, to record very high efficiency gains.

The primary goal of using the installed PaT with variable speed is to maintain nearly constant high efficiency all the time regardless of the head availability. Practically, the two water levels are fluctuating because the limited space in the reservoirs. Referring to the nominal speed of the installed pump, the minimum operating pump speed is at 65% when the lower reservoir is full (minimum static head) and at 90% when the lower reservoir is about to be empty (maximum static head). At the minimum load conditions, the PaT runs with a static head reduction of about 55% from its maximum. Lower rotational speed allows the PaT to adapt to the running water regime at reduced available head and to preserve high efficiency in partial load.

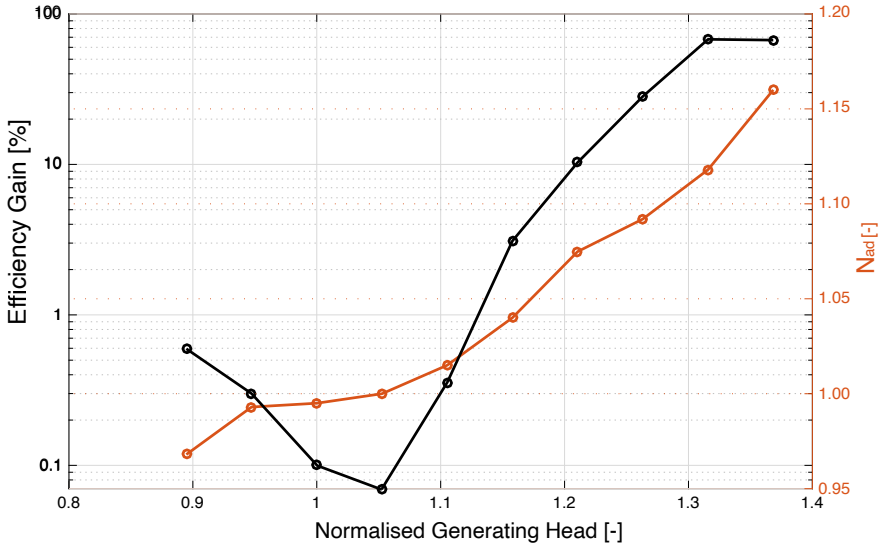

Figure 4.26: Gain in hydraulic efficiency in pump mode by using variable speed over the variation of the head

As shown by Fig. 4.27, the use of PaT at $N_p = N_n$ (black line) is clearly not sustainable nor affordable. At this working condition, the PaT could work in a very limited operation range and reach only the 73% of its efficiency maximum. However, the PaT records better performance at lower rotational speed in lower head conditions. For instance, at the selected speed of $N_{ad,PAT} = 0.6$ (blue line), PaT reaches its maximum for normalised head equal to 0.7 and preserves high values for greater available heads. If the available head decreases further, vibrations are detected and they suggest a consequent adjustment to slower the rotational speed. If it were not for the working condition variations, a gearbox would provide two rotational speeds on the shaft: one suitable for pumping and the second applied for generating mode, but no speed adjustments would be possible.

The green line in Fig. 4.27 depicts the efficiency line of variable speed command though a wide range of available head. The difference in efficiency in turbine mode of operating at the variable speed and fixed speed of $N_{ad,PAT} = 0.6$ is defined as:

$$Gain_{PAT} = \eta_{VFD} - \eta_{600} \tag{4.20}$$

Fig. 4.28 describes the gain in hydraulic efficiency by using variable speed over the fluctuation of the available head, showing the rotational speed path to obtain the maximum efficiency in whole operating range. The rotational speed and head are still normalized at the nominal pump conditions) The gain in production and improved turbomachine lifespan (i.e. avoiding dangerous working conditions) would balance the cost of the VFD and allow a longer life expectancy.

The example of flexibility provided by the experimental data constitutes an alternative to upgrading μ-PHES in smart-grid: peak-loads are shaved by exploiting the capacity of the PHES and the intermittent energy injections produced by the

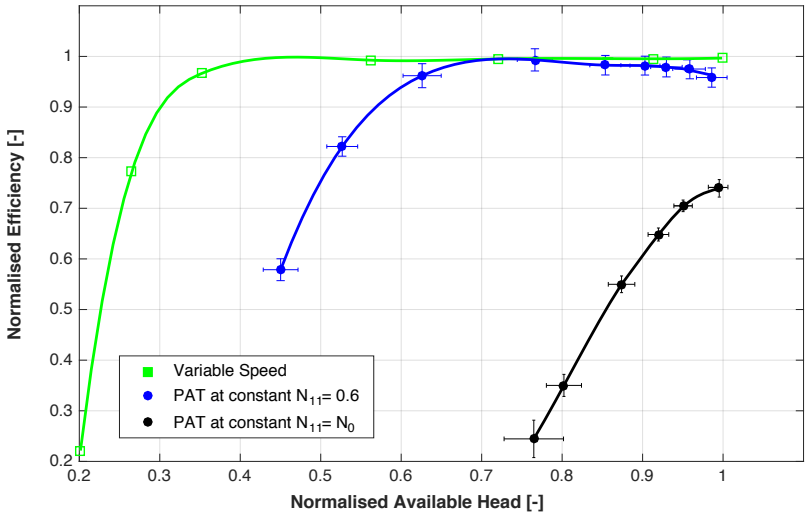

Figure 4.27: η_{PAT} normalized to its maximum over H at different speed regimes

renewable sources are properly stored in the hydraulic reservoir. This is successfully obtained by installing a PaT with variable speed control: it provides conditions for achieving a higher energy yield while avoiding the onset of operation instabilities caused by the part load.

Fig. 4.28 and Fig. 4.26 illustrate on the right axis the progression of the most suitable rotational speed to keep high efficiency during a head alteration H/H_n.

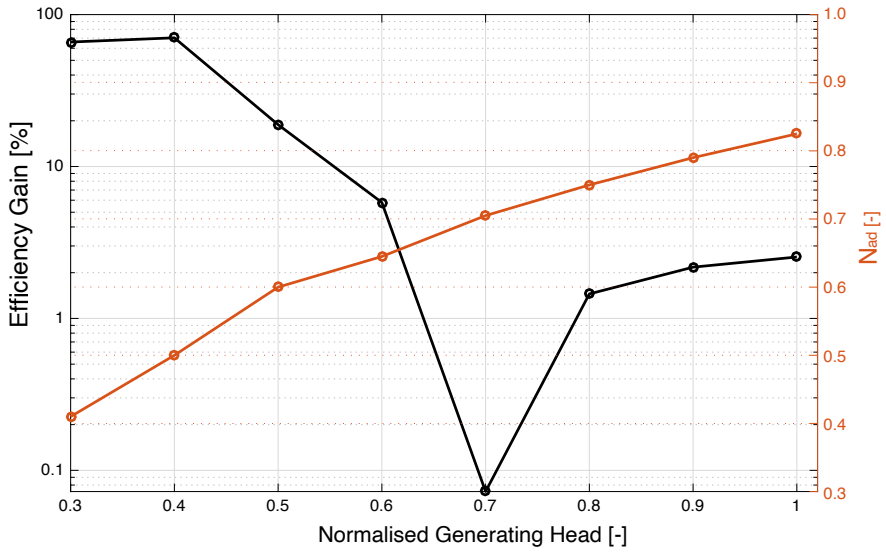

Figure 4.28: Gain in hydraulic efficiency in turbine mode by using variable rotational speed over the variation of the head.

Eqn. 4.21 and Eqn. 4.22 are the quadratic trendlines for the pump mode and PaT mode, respectively:

$$N_{ad,pump} = 0.6181\left(\frac{H}{H_n}\right)^2 - 1.0137\left(\frac{H}{H_n}\right) + 1.3874 \qquad R^2 = 0.9880 \qquad (4.21)$$

$$N_{ad,PAT} = -0.5149\left(\frac{H}{H_n}\right)^2 + 1.2485\left(\frac{H}{H_n}\right) + 0.0862 \qquad R^2 = 0.9968 \qquad (4.22)$$

it can be conclude that PaTs at variable speed are valid turbomachinery alternatives to conventional micro turbines in exploiting variable hydraulic power. The use of the same machine for pumping and generating is related to the objective of saving cost of energy, space and maintenance. The PaT hydraulic efficiency recorded in the case study (about 72 %) may be slightly smaller than with regular micro turbines but still very competitive. It emerges that this μ-PHES requires a calibrated evaluation of the hydraulic system performance, taking into account energy fluctuations and the turbo-machinery working conditions. The extra cost applied for VFD is mitigated by the advantage of installing a PaT instead of an expensive customized micro hydraulic turbine. The extraordinary adaptability recorded on the site in partial load until 30% clearly endorses the coupling of the PaT and the VFD.

4.3.3 A simulated day of the micro-PHES

A crucial element of innovation for energy fluxes in a smart grid management is the technology of measuring and orientating electrical loads. Such a system recognizes the "electric footprints" that all the connected appliances produce while the are in operation. A power line communication needs to be developed to link the dedicated instrumentations for measurement and operational purposes: renewable energy production, consumption, shift-loading, and storage.

Today, the system monitoring can allow easy-to-read energy consumption and an instant evaluation of safety measures, costs and efficiency. Purely by a way of example, Fig. 4.29 presents the simulated system operation and modelled performance on the 21^{st} of April 2017 at the *Quartier Negundo* smart grid. This day could be considered as a typical week-day of the month of April.

The load diagram shows the intense use of heating and ventilation system from the early morning, when the first consumption peak occurs (at about 06:00 AM). Later on during the morning, RESs help covering the energy demand as the PV panels production raises. With real-time power measurements, as used in μ-PHES set-up (Section 4.2.3), the surplus of energy eventually recorded is assigned directly to the pump and used in charging the upper reservoir. For the sake of clarification, this simulation is conducted on the real load profile recorded on site and a monthly averaged RES production. In accordance with Table 4.3, the geodetic difference of the water levels of the two reservoirs is constantly measured by the pressure sensors, which defines the starting rotational speed of the pump following Eqn. 4.21. The rotational shaft speed is modulated iteratively as it suits with the actual available

water levels (net of the hydraulic losses). The pump can operate in reverse mode (negative rpm) when the PV groups and wind turbines do not cover the electricity demand. The fluctuations of the turbine rotational speed indicate that there are periodically operating changes according to the imposed frequency of PLC command loop (Table. 4.3). Besides the load fluctuations given by the unbalance between RES production and load profile, the volume of water is waving for charging and discharging of the reservoirs. In case of a protracted period of generation, as it happened after around 16:15 in that day of April (Fig. 4.29), the upper reservoir is emptying and the lower reservoir is filling-up: the available head decreases progressively as the rated rotational speed (Eqn. 4.22). Interestingly, the hydraulic efficiency is maintained at its maximum value until the cycle is completed (within 70 - 72%) as expected.

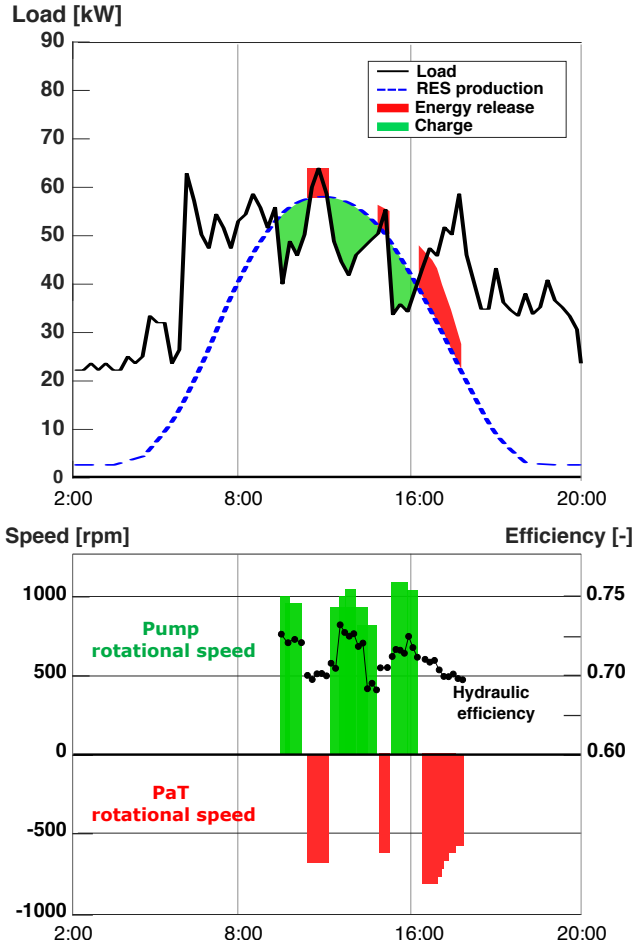

Figure 4.29: Absorbed and produced power by the storage system according to the load profile and RES production. Related rotational speed and hydraulic efficiency, values between 02:00 - 20:00 (21^{st} April 2017).

4.4 Cost-benefit analysis

4.4.1 Sector description of smart-grid business model

Since the first European directives of the late 1990s, introduced the opening up of the network industries to competition, the energy sector has undergone profound changes [Limpens & Jeanmart 2018]. First of all, many markets have developed in markets which are differentiated both by their temporality ("on-spot", at hourly steps or half-hours, at term, etc.) but also by their functions (trade forecasting function over time, real-time balancing functions, etc.). Secondly, the development of competition had to be regulated, in particular, because of the dominant positions of operators on national markets and the existence of a natural monopoly (the electricity network). Finally, energy and supply security are now part of the public service's tasks. They are giving space to the active contribution of privates at industrial [Trianni *et al.* 2016] and residential levels [Avilés A. *et al.* 2019]. The research presented in this section is carried out in the continuity of the European trend forward new business and economics in DES and the social interest in a green energy provision.

The European Union is currently pursuing several objectives related to the liberalization of energy markets and the fight against climate change as in the United Nations Climate Change Conference held in Paris 2015. The complexity of energy systems and the relationships between goals requires the appropriate application of several measures or instruments. Also, in the context of energy consumption increase in Europe in recent years [International Energy Agency 2013], applying regulatory and competitive policies on several alternative technologies seems to be the right path to take for the ambitious targets given. In this direction, rising interests in energy efficiency and sustainability involve everyday economics and industry [International Energy Agency 2013], thus politics.

To achieve the envisaged objectives of the competition, security, and climate, among the new technologies, the integration of renewable energies in markets, the promotion of storage technologies as well as the deployment of smart-grids technology are currently being researched in fields as diverse as economics, sociology and engineering [Coll-Mayor *et al.* 2007]. The effects of the development of smart-grids and DESs should result in reduced consumption and peak periods, better use of networks (regulation by the quality of service), and easy integration of renewable energies, electricity storage, or energy demand management instruments.

4.4.1.1 Renewable energy grows in Belgium

On 9/12/2017, the Climate Change Department of the FPS Public Health, Food Chain Safety and Environment in Belgium published the results of the 4th National Climate Survey (after 2005, 2009 and 2013 editions) [FPS-Public Health 2017]. This survey revealed, among other things, that increasingly the Belgians – significantly more than in 2013 - saw climate change as an urgent problem to be tackled. They were in favour of a gradual transition towards a low-carbon economy

and society, and expect greater efforts by governments to address climate change [FPS-Public Health 2017]. Recently, a survey revealed that the pulse of Belgians' concerns is increasing in climate and its impact on health [RTBF 2017]. It is the youngest, the 18-25-year-old, who seems to be the most concerned and the most numerous to cite the negative health impacts of global warming [RTBF 2017]. This growing consciousness of the need for a green alternative to other pollutant energy sources has pushed up the decentralized PVs. Small systems (<10 kW-peak), perfectly suitable for residential level, represented in 2018 the 84% of the yearly added national capacity [APERe 2019]. In other words, in 2018, approximately one household over ten owned a PV system: 450 000 PV sites are online over 4 800 000 houses [APERe 2019]. Thus, the prosumers are the emerging figure in the field of the energy sector. The prosumers are identified as the final user of the electricity, but it is also capable of playing the role of producer and contributing actively in the energy market with RES or fossil fuel-fired systems. The prosumers' potential in buying and selling electricity increases the complexity of the energy transmission and the regulations of the energy sources.

RESs are regulated in Belgium according to regional competences and they may differ between all the three regions. In the past decade, the number of PV installations has been strongly affected by legislation support, which has drugged the market, and, once the subsidies have been cut down, it left a reduced perception of the economic attractiveness of such systems. The first identified revenue by using decentralized private energy sources and energy storage units is the reduction of the electricity bill. In this context, the literature defines the self-consumption metric: it is given as the ratio between the renewable power that is locally consumed (directly or after storage) and the total production [Luthander *et al.* 2015]. The higher the self-consumption, the lower the electricity purchase from the grid supplier. Moreover, Belgium allows producers to generate another revenue: producers can feed-in (or injecting) electricity generated by their systems to the national grid at the agreed price. This practice will need a different electric meter able to track the consumption and generations. The balance between import and export would represent the final electricity bill: the injections of the electricity in the grid stand according to limit (in Brussels no more than 70% of the production can be injected) and agreements defining the rate (about 3-5 €/MWh in Brussels depending by contracts) [Brugel 2020].

Another element to add to the revenue is the federal (or regional) subsidies to renewable energy production. In Belgium, the green certificate (GC) system is adopted (in French certificat vert - GC, in Flemish Groenestroomcertificaten - GSC). It is a form of retribution based on the obligation of generating a share of "green" energy for all the producers. On the one hand, the "green" and decentralized producers have the right to get GCs at the rate of 1.81 each megawatt-hour of 100% green energy produced (the number of GCs changes according to the type of energy system implemented). On the other hand, those suppliers, who do not reach the minimum, are obliged to buy GC from the firsts to balance their pollutant energy production. These certificates are subject to a market price of demand/offer. In

Belgium, several suppliers are willing to buy GCs from DER, and today, they reach a price market of about 93 € each [Brugel 2020]. Brugel deals with the mechanism of compensation of GC in Brussels. Yearly, Brugel updates the coefficient of premium for each type and size of the installation and communicates the proposal to the Belgian Ministry of energy for approval. The calculated coefficients are practically based on the average costs, actual subsidies, electricity price, and a targeted return of investment for a small PV system of seven years and five years for the cogeneration system [Brugel 2020]. GCs are emitted for the first ten years of the RES online in the grid. The new coefficients apply to only the new installations [Brugel 2020] to protect the investment of previous facilities. These values may fluctuate in the years, and they are essential to evaluate the possible investment in RES. Table 4.6 summarizes the coefficients used in Belgium.

Table 4.4: Value for green certificate in Brussels, Belgium, from June 2020.

	Unit	**Values**				
Power size	kW	< 6	$6 - 50$	$50 - 100$	$100 - 250$	>250
Coefficient	Rate/1.81	1.375	1.155	0.935	0.880	0.770
Rate	GC / MWh	2.5	2.1	1.7	1.6	1.4

4.4.1.2 Structures and players of the Belgian energy power grid

Today, the deregulation of energy markets has been widely adopted, based on the same basic principles set in the 1980s: distinction of the competitive and non-competitive components of the sector, regulation of the non-competitive part, and development of a competitive market for the remaining. Typically, the electric power industry has been working as a one direction system with electricity being generated in power stations by the producer and then delivered to the consumer. The chain can be divided into sub-segments: generation, transmission, distribution, and retail. Electricity generation is strictly the production of electricity from sources of primary energy such as coal or uranium or renewable sources. Transmission is the transfer of electricity at high voltage for reduced losses, from the power stations to the distribution grids. After transmission, electricity voltage is reduced and enters the distribution grid, which delivers electricity to the endusers (residential, industrial, or tertiary level). The sale of this electricity to the user is made by the electricity retail industry or suppliers [Burke 2017].

In Belgium, the market is regulated at the national level by the CREG, the regulating commission for electricity and gas (in French, Commision de regulation de l'electricite et du gas), which ensures that the electricity and gas markets are competitive, transparent, and seek the vital interests of the consumers [CREG 2020]. This report includes an overview of the main national legislative changes, an overview of developments in the electricity and natural gas markets [CREG 2020]. Also, at the national level, there is a single transmission system operator (TSO), Elia, which is responsible for market facilitation as well as maintaining and developing the electrical

grid and ensuring the operability with neighbouring countries. Given its monopolistic activity, it is subject to the supervision of the regulators [ELIA Group 2020]. The Brussels capital region has a regional regulating commission for energy, the Brugel [Brugel 2020]. There is also a single distribution system operator (DSO)in Brussels, Sibelga, which is responsible for maintaining and developing the distribution grid and energy metering [Sibelga 2020]. In February 2017, Brugel presented a list of 36 licensed electricity and gas suppliers in the Brussels region [Brugel 2020]. These retailers supply power to the consumers by buying electricity from producers, based on long-term contracts or markets such as the Belpex (the Belgian electricity spot market). Users and prosumers of Brussels region are then in agreement with theses licensed retailers for energy provision or injection (prosumer). Table 4.5 enumerates the players in the electricity market in Belgium.

Table 4.5: List of the main players in the electricity market in Belgium. Edited from [Nolden *et al.* 2020, de Oliveira e Silva 2017].

Category	**Operation**	**Belgian player**
Producer	Produces electricity	Independent power producers like farmers with a CHP, Engie Electrabel, EDF Luminus
Consumer	Consumes electricity	Industry, tertiary and households
Prosumer	Consumes and produces electricity	Households or company with DES
Transmission system operator (TSO)	Transmission of electricity on the high-voltage grid	Elia
Distribution system operator (DSO)	Distribution of electricity on the low-voltage grid	Eandis, ORES, Infrax, Sibelga, RESA
Energy supplier	Sells the electricity to small consumers	Eneco, EON, Electrabel, EDF Luminus, Lampiris
Balancing responsible party (BRP)	Balances electricity injection and intake at its access point	Large consumers or producers are their BRP. The supplier arranges the BRP for small end-consumers
Regulator	Defends the free market from monopoly and influences by large players	CREG, VREG, CWaPE
Power Exchange	It is the energy trading platform at bids of 15 min	Spot Belgium EPEX

4.4.1.3 Why flexibility?

Belgian research stakeholders are advancing the challenges of managing electricity demand through the smart grid. With scheduled consumption profiles, some consumers are willing to play an active role in the market. Several tariffs are offered by electricity retailers in Belgium, as in other European countries, in respect of a dual tariff [Huart 2019], and they award the electricity management.

Flexibility in electric systems is defined as the flexible operation of consumption and production. According to a high demand period, the electricity price would be higher than the standard tariff, but in other periods, off-peak hours, the electricity price is remarkably lower. However, these assessments do not calibrate their prediction on specific measurement but a statistic based databased for different users. Synegrid, the federation of electricity and gas system operators in Belgium, publishes a synthetic load profile, obtained and processed from several and different users. The synthetic load profiles are used to bill customers until there is a real, measured consumption. Today, the validity of these predictions is criticized by the agency of protects customers' interests. Before, companies were used to inflate the "estimated consumption" for short-term investments at the expense of the consumer [Fischer *et al.* 2015].

Flexibility does not gain value in the use of electricity for a convenient tariff contract only. Planned flexibility can also be sold in the day-ahead trading for the "Belgian SDAC Price" [EEX GROUP 2020] or during intra-day auctions on the quart-hour basis [EEX GROUP 2020] for the Demand-Response (DR) energy market. The challenge for the electricity sector is present in the generation systems as for consumers. Regarding the electricity production framework, flexibility aims to shape the instant production according to the grid's fluctuating energy demand. It is well known that the power plants which cover the bulk of the demand are usually subject to a long period of inertia in modifying their output. Nuclear power plants, for instance, could not be turned on/off easily and coal-fired plants have slow answer-time to adapt at the daily changes of the grid. Fast-starts or part-load high efficiency are more and more quested to adapt quickly from a baseload demand to peak hours. Power generations and demand need to stay in balance to cope with the margin level of 50 Hz grid frequency [ELIA Group 2020], and thus, avoiding electricity fails and blackouts. Out of this threshold (± 0.05 Hz), social danger, and the technical issue occurs [ELIA Group 2020]. To restore the equilibrium quickly, the system regulator has multiple choices and, for instance, could run immediately other appliances to raise the consumption (or turn of other generation plants). Whoever offers the energy flexibility, in this case, is participating in a remunerating open market for providing ancillary services.

All forecast scenarios provide a national energy mix with a higher share of distributed and renewable energy, which can be partially predicted at its best as good as weather forecasts. Running clouds in the sky instantly deflect the production of the photovoltaic panels, and wind intensity blows differently every hour. Relying only on RES without an adequate EES apparatus at an international level, Belgium

cannot reach 100 % fossil-fuel-free [Limpens & Jeanmart 2018].

To improve its security of supply and environmental performance, fast and responsive flexibility is required. Energy flexibility is not limited to the electricity generation sector. Consumers can use the advantage of this rising market of flexibility. They can indeed play a beneficial role in the electricity grid management if they cancel their demand at the right time (load shifting) or eliminate short-term demand for avoiding too high peak (peak shaving).

Demand-side management (DSM) was initially technical and industrial, and it has been practised in recent years among large electricity consumers. It has gradually given rise to a new service activity focused on the industrial sector: the aggregation of voluntary demand-side response capacities made available to network operators at the right time [Huart 2019]. Elia offers online the quarter-hourly basis electricity price for the agreed flexibility. Fig. 4.30 shows an example of the evolution of the power imbalances (in orange) in Belgium (MW) and the related electricity price (€/MWh) paid by Elia in the daily compensation of energy flexibility: based on the foreseen imbalance gap (positive or negative) the electricity price fluctuates appreciably.

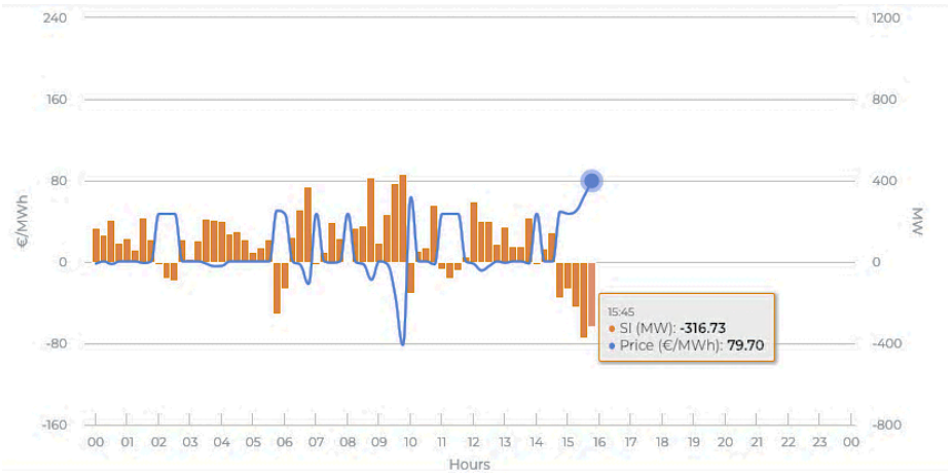

Figure 4.30: Imbalance power (SI) and prices of 30/04/2020 at a quarter-hourly basis [ELIA Group 2020].

4.4.1.4 Demand-Response (DR) opportunity

The objective of remunerating the demand-side flexibility aims to support the quality of the electricity transmission for balancing purpose or ancillary services. The electricity price has been rising for households in Belgium of +47% from 2010 [Statista 2018], and DSM can encounter economic viability for all the activities, or industrial process in which timing is not a strong constrains and managing the own energy consumption would result in a positive income.

Unlike adopting an energy-saving approach based on reducing energy consumption, the offered strategy relies on the scheduling and timing of the processes or

activities. Thus, opportunities are emerging for companies or householder agglomerate able to adopt successful business models applied to the actual energy market by the leverage of distributed RES and the opportunity of demand-side flexibility.

In Europe, the active commitment in energy management and energy efficiency motivated by socio-economic reasons is preparing and educating a society willing to exploit its flexibility portfolio. When smart-grids equipped with DES participate in dual tariff and DR, their electricity consumptions need to be adapted according to different solutions:

- the energy consumption is cut down during demand peak usually at higher electricity cost (peak-shaving strategy);
- shift energy consumptions to a different period for a low exchange price (shift load strategy);
- consuming on-spot the generated energy, thus reducing their electricity bill (selfconsumption strategy);
- sell the surplus of power generated to the distribution network (feed-in strategy);
- store the surplus of power generated for later consumption (self-sufficiency).

Fig. 4.31 illustrates an example of energy management action on a smart grid consumption profile. The operation measures provide an optimised schedule of the daily activities by peak-shaving at a high-priced electricity period and shifting the power consumption to cheaper hours of the day (from the grey area to the orange one). High-priced electricity periods can be avoided also by using previous stored energy by batteries or PHES systems.

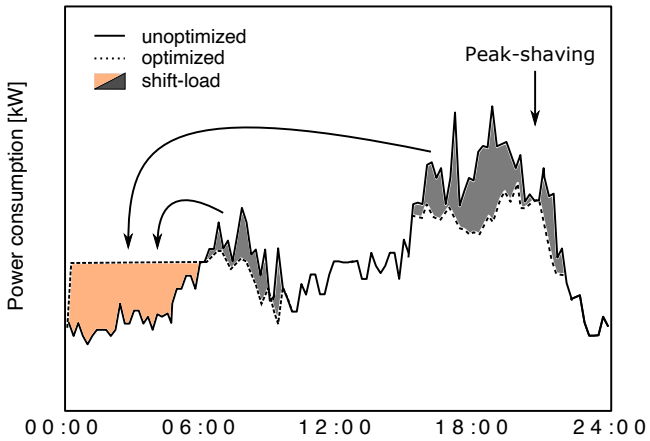

Figure 4.31: Schematic representation of reducing the consumption at peaks and shifting load during the night for lowering the electricity bill.

4.4.2 μ-PHES prototype in the *Quartier Negundo.*

A cost-benefit analysis is performed to the operating μ-PHES in the *Quartier Negundo*. The system will not operate intensively and in continuous, thus the expected lifetime span K of the system is 30 years, few years above the average. Moreover, a yearly degradation in efficiency (-0.2 %/year) and the operation and maintenance (O&M) yearly cost (30 €/kW/year) are are considered for the analysis.

The RESs on site are not meant to be connected to the grid and the injection of excess power into the grid is therefore not possible. If it is not consumed or stored, the produced energy is curtailed. The electricity required for charging the upper reservoir is fully provided by the surplus of the RES systems installed on site whose costs are already considered amortised. In order to avoid the necessity to pay for electricity to charge the upper reservoir, the use of RES is crucial to reach a high number of PHES cycles and the low LCOE values. The PV panels and wind turbine capacity factor (Table 4.6), defined as the ratio of the power generated and the rated peak power, drastically affects the annual energy yield and leads to the possibility of an over-dimensioned RES installation. The wind turbine capacity factor average varies seasonally and it has not a predictable profile on an hourly basis. Fig. 4.32 shows the case for the month of April 2017. However, its impact on the total RES implemented in the *Quartier Negundo* is very low: the total peak power for wind turbine equals to less than 10% of the whole nominal installed RES.

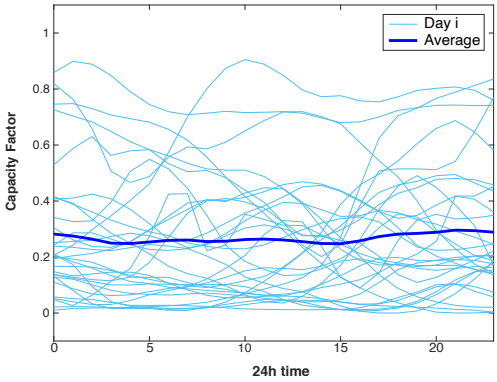

Figure 4.32: Wind turbines capacity factor during the month of April, 2017 in Froyennes. Data extracted from [Elia.be 2018].

Table 4.6: Averaged capacity factor for the PV panels and wind turbines in Belgium 2017. Data extracted from [Elia.be 2018].

Period	PV capacity Factor	Period	Wind turbine Capacity factor
April	0.74	Spring	0.27
July	0.67	Summer	0.22
October	0.61	Fall	0.26
December	0.43	Winter	0.29

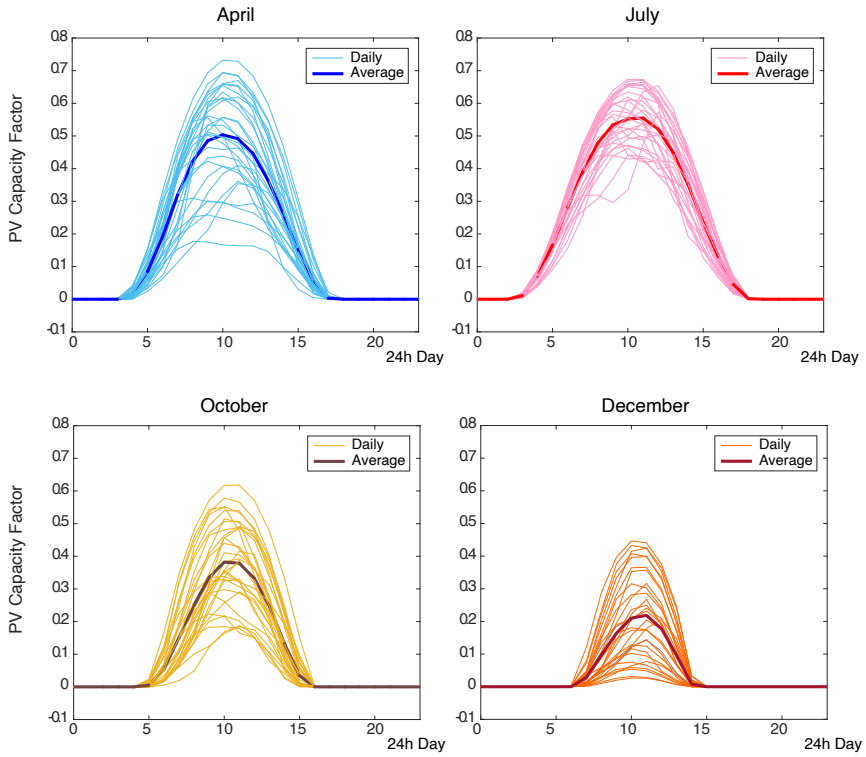

Figure 4.33: PV panels capacity factor in Tournai, Belgium 2017 during the months of April, July, October and December. Data extracted from [Elia.be 2018].

In Fig. 4.33, the daily and monthly averages of the capacity factor for PV panels in Belgium are shown for the months of April, July, October and December 2017 [Elia.be 2018]. More than one daily full cycle is possible as plotted as an example in Fig. 4.34. The electricity load consumption is mainly due to the heating, ventilation, and air conditioning systems of the adjacent buildings. The load fluctuates at high peak during weekdays with reduced consumption during Saturday and Sunday. Both PV and wind energy production profiles are formulated as a monthly average taking into account the associated capacity factor. During night time the RES power production drops to the wind turbine contribution only, which results be very limited.

The PHES operating control is able to match quickly with the available head value, H, and, if possible, start the pump at the most suitable rotational operating speed with the exact surplus of power generated by RES in *Quartier Negundo*. For the cost-benefit analysis calculation of the μ-PHES, the capital costs of the first year are equal to about 108 k€, with 42 % going to pipeline related costs and 26 % for the motor-pump group coupled with the electric driver. The collected list of costs, expressed in Table 4.7 includes materials, accessories and manpower. The reservoir costs are not applied in this calculation because one already exists as a stormwater basin and the other one is considered as an extension of the first.

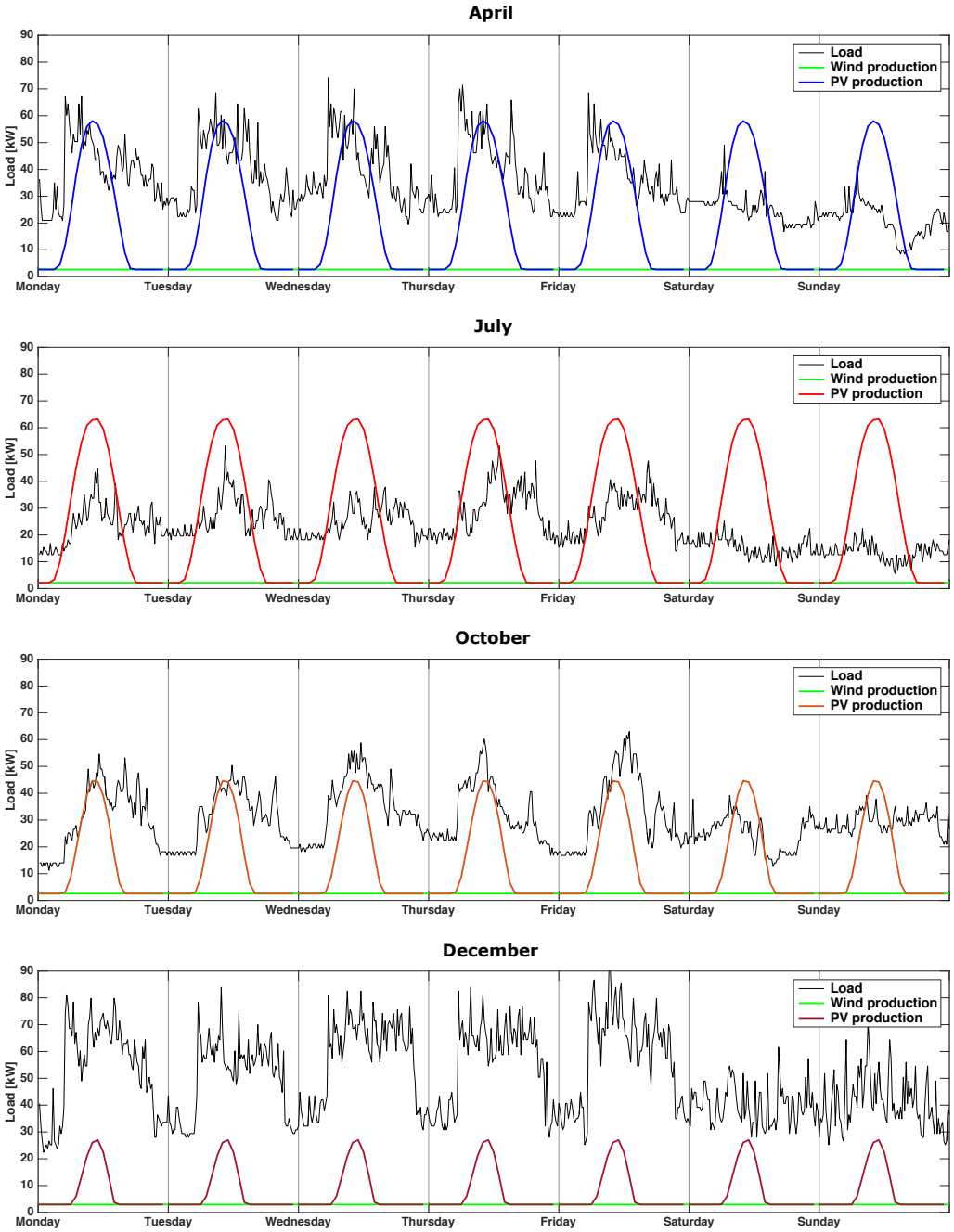

Figure 4.34: Load consumption of *Quartier Negundo* during weekdays and weekends and averaged empowered RES production on site (PV and wind turbines) in April, July, October and December 2017.

4.4.3 μ-PHES case study

Another case study is here assumed based on the μ-PHES prototype in the *Quartier Negundo* but with different realistic contingencies for an industrial PHES project. It is known that a larger available head makes the hydropower plant more energy proficient with the same amount of stored water (Eq. 4.1). Assuming that a four-story building is situated at the ground level of the upper reservoir in Froyennes, its rooftop could provide the space for an upper reservoir 20 meters higher than the previous one. The dimensions and structure of the roof would respect the limits defined by the minimum load according to the law (1500 kg/m^2) [European Committee for Standardization 2002]. 800 m^2 are sufficient for a total water volume of 625 m^3. However, the roof surface must be adapted from the standard coating with a reinforcement waterproofing of about 36 €/m^2 to apply to the vertical containing walls as defined by the contractor. Roofs by law must withstand rain even in case the drainage system is clocked but certaim measures must be taken for safety. This extra cost could be mitigated by possible synergies in the building's water infrastructure. External open-air tanks are subjected to environmental phenomena and are not always suitable for a potable water network. However, they can find valid applications for rainwater harvesting systems.

Today, Belgian national legislation requires that all new constructions have a rainwater harvesting system that can be used for toilet flushing and external water uses [Cornut *et al.* 2006]. This legislation has been devised to help reduce the demand for mains supply water and to collect and use rainwater as part of sustainable drainage systems [Cornut *et al.* 2006].

In this second case study the pipeline needs to be extended a further 20 meters to reach the roof of the building adding some extra costs. However, directional drilling process can be avoided in a more convenient situation where no pedestrian way nor a sewer line need to be crossed. The flow rate is considered to remain equal to the μ-PHES in Froyennes but the new available head requires selecting a PaT with lower specific speed (Eq. 2.1). As the specific speed decreases, the ratio of impeller diameter to impeller eye diameter increases. As a consequence, a larger

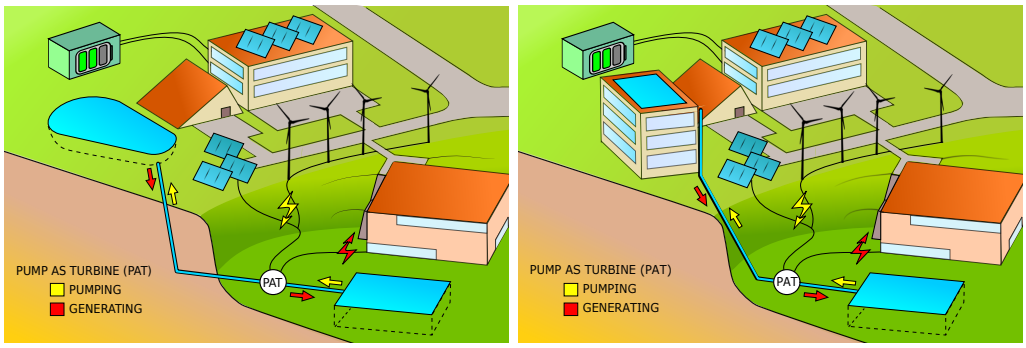

Figure 4.35: illustration of the μ-PHES prototype in the *Quartier Negundo* (left) and a second case study (right)

radial extension blade is required. However, the water flow rate is the same, and the flanged diameter on the discharge and suction side are thus unchanged. This means that only a different impeller shape of whole pump-block needs to be changed. The pump price is not drastically higher, but the motor and driver must be able to manage a larger electric load. Nevertheless, the electric system size of μ-PHES prototype in the Quartier Negundo is over-dimensioned by large security factor. In an industrialized and commercial apparatus the dimensioning would better match with the expected capacity of the system. The new costs have been estimated by the constructor and summarized in the Table. 4.7. The PaT and pump hydraulic efficiencies in the case study are considered equal to those in the Negundo site.

Table 4.7: Capital costs for μ-PHES in *Quartier Negundo* and cost estimation for the second case study.

	Quartier Negundo [€]		**Case study [€]**	
Motor-pump group	12900		18000	
Frequency drive	15600		40000	
	28500	26 %	58000	48 %
Electric panel and control	19700		19700	
Electro mechanic valve	1700		1700	
Acquisition data system	2300		200	
Connections and cables	2100		2100	
	25800	24 %	23700	19 %
Directional Drilling	28400		-	
Pipeline	17300		24400	
	45700	42 %	24400	20 %
Upper reservoir	-		6200	6 %
Others	8300	8 %	8300	7 %
Total	108300	100 %	120600	100 %

4.4.4 Economic-evaluation methods

Economic-evaluation methods provide the energy community of tools to compare different energy technology investments. Power supply, energy storage and energy appliances need guidelines and benchmark for making economically efficient energy-related decisions. In the following sections, only some of most used methods are presented. They provide sufficient guidance for a cost-benefit analysis of the presented case study, computing measures of economic performance for relatively simple investment choices.

4.4.4.1 Net present value

The net present value (NPV) method finds the excess of benefits over costs, where all amounts are discounted for their time value. The NPV method is also used in Section 3.3.2.1 for a preliminary economic analysis of a PHES using pre-existing infrastructure and underground reservoirs. The NPV method is particularly suitable for decisions made on the basis of long-run profitability from an investment, such as an investment in energy efficiency or renewable energy systems, but it is not very useful for comparing investments that provide different services. It is calculated by the following formula:

$$NPV = \sum_{t=0}^{t=K} \frac{CashFlow}{(1+d)^t} \tag{4.23}$$

where K is the lifetime of the system and d the real discount rate. The discount rate is the interest rate that discounts or reduces future amounts to their lesser value in the present. The discount rate, called also the required rate of return, depends on the riskiness of investments. The higher the risk, the higher the discount rate. The real discount rate includes externalities as the inflation rate. The cash flow used in the NPV calculation is yearly obtained by the difference of revenues and costs. Many assets yield cash inflows at the end of their useful lives because they have residual value. Such a residual value is discounted as a single lump sum when the asset is sold or terminated (at time $t = K$). A positive NPV means that the project earns more than the requires rate of return. A negative NPV means that the project earns less that the required rate of return.

4.4.4.2 Internal rate of return

Another discounted cash flow method for capital budgeting is the internal rate of return or IRR. It is the interest rate that makes the NPV of the investement equal to zero. The IRR is one method that allows them to compare and rank projects based on their projected yield. The investment with the highest internal rate of return is usually preferred but using IRR exclusively can lead to poor investment decisions, especially if comparing two projects with different durations.

4.4.4.3 Levelised cost of energy and storage

The levelised cost of energy (LCOE) is a method to evaluate the economic value of an energy project. It provides the price per energy unit (€/kWh) that balances out all the costs of the project. An energy system that reaches grid parity, it is a system whose produced electricity has the same cost (or LCOE) equal to the grid price. All the costs incurred are divided by all the energy provided along the project duration, K (years). The values must take into account the time-varying value of money with

the real yearly discount rate, d (%). The LCOE is obtained by:

$$LCOE = \frac{\sum_{k=0}^{K} C_k/(1+d)^k}{\sum_{k=0}^{K} E_{out}/(1+d)^k} \tag{4.24}$$

where C_k is the cost in the year k in €, E_{out} is the energy output in year k in kWh.

Such a measure could allow for simple verification of the economic viability of certain storage technologies in a given electricity market. The same formulation as for the LCOE but employing energy storage technology characteristics, instead of traditional electricity generators, calculates the Levelized Cost of Storage (LCOS). To this matter, storage characteristics and perspections must be used. Generally, the absolute price at which electricity is discharged is of minor importance. Rather, the average price spread between charged and discharged electricity determines the revenue of the investment [Belderbos *et al.* 2016]. Then, the cost of efficiency losses and self-discharge phenomena affect the possible obtainable price spread. Moreover, due to the limited energy storage capacity, the system cannot always provide the energy transfer in the most suitable moments. If any corrective coefficients are adopted the LCOE and LCOS represent the maximum profitable values.

4.4.5 Analysis results

The NPV analysis shows that μ-PHES solutions requires a relevant initial investment per installation and not strictly per rated power of the storage system, until height and reservoirs are supported by pre-existing infrastructures. The price per kilowatt it highly affected by the available head: 13.5 €/W, for the low head as in the *Quartier Negundo*, is reduced to 3 €/W for the second case study at higher head. However, both designs profits of economic and structural advantages. The use of a stormwater basin as a reservoir is an important cost-effective solution. According to the type of implemented tank [de Oliveira e Silva & Hendrick 2016], the equivalent cost for a 625 m^3 reservoir would have laid between 43 - 187 k€, translating the use of the existing reservoir into an expense reduction of 28 - 61 %.

Fig. 4.4.5 illustrates the discounted cash flow and NPV of the μ-PHES in the *Quartier Negundo* and in the second case study. The real discount rate, that includes inflation rate is set at 6%. The energy output per cycle is crucial to the profitability of μ-PHES and only the modified case study, with almost four times the annual electricity output, get a positive NPV in 30 years and IRR of 8%. An overview of the NPV data is given by Table 4.8.

According to further scenario modifications it is possible to explore the second case without variable frequency driver but equipped with a gear box to switch the direction and amplitude of the rotational speed: gear-box lifetime and cost are 17 years and 5 k€respectively. Fig. 4.37 illustrates the latter scenario and the NPV outcomes by increasing the grid electricity price by 0.5 % per year.

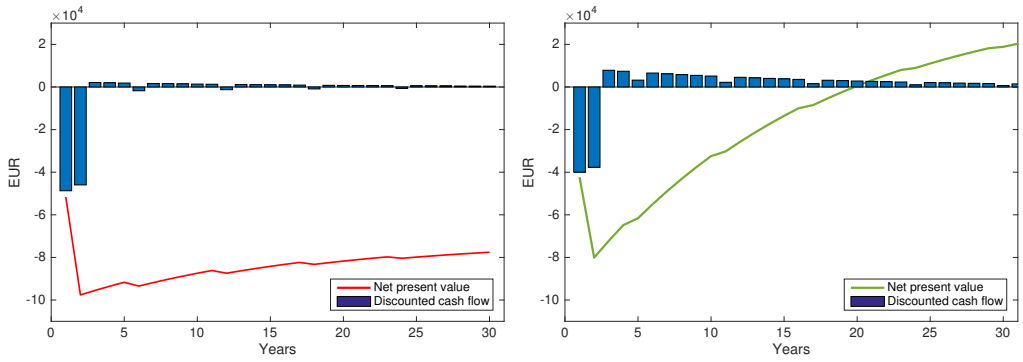

Figure 4.36: Discounted cash flow and NPV of the μ-PHES in the *Quartier Negundo* (left) and in the second case study (right).

Table 4.8: Data and NPV results for a economic evaluation of μ-PHES.

Data	*Quartier Negundo*	Case study
Initial investment cost (kEUR)	108.3	120.6
Operations and maintenance costs (EUR/kW)	30	
Annual electricity output (MWh)	10.6	36.7
Annual electricity output degradation (%)	0.02	
Project lifespan (years)	30	
Real discount rate (%)	6.00	
Net electricity price EUR/MWh	28	
NPV (kEUR)	-78	27.7
IRR	neg	8%
Payback	-	20 Years
NPV (kEUR) (r = 4.00%)	neg	59.4
NPV (kEUR) (r = 10.00%)	neg	-7.5

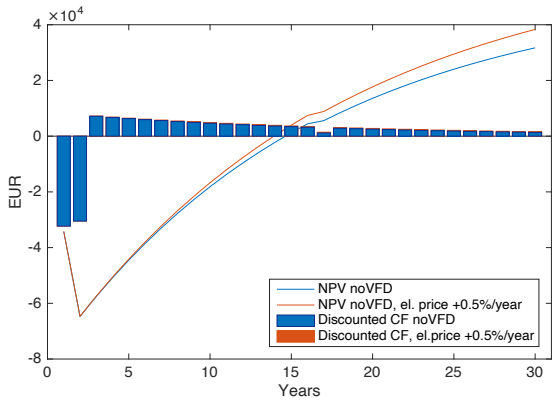

Data of noVFD	
Initial investment cost (kEUR)	85.6
Annual electricity output (MWh)	34.6
Electricity output degradation (%)	0.03
NPV (kEUR)	33.6
IRR	11%
Payback	15 years

Data of noVFD with el. price raise	
Initial investment cost (kEUR)	85.6
Electricity price raise (%/year)	0.5
NPV (kEUR)	40.3
IRR	11%
Payback	14 years

Figure 4.37: Estimations of the NPV of the μ-PHES of two further scenarios: without VFD but coupled with a gear-box and with a progressive electricity price raise (+ 0.5%/year)

Despite its small capacity and high flexibility, the prototype μ-PHES in the smart grid of *Quartier Negundo* does not operate during winter time due to the high consumption for heating and low RES production. Only during sunny seasons μ-PHES can profit largely of renewable energy surplus. By a yearly averaged regime of 1.5 cycle per day, the LCOE calculated is equal to 1.06 €/kWh. Fig. 4.38 shows a specific sensitivity analysis for the variation of certain parameters over a range of ±20 %. As expected, it emerges that LCOE can be reduced significantly by raising the total energy output, improving efficiency and/or exploiting a higher available head. Pumps with a hydraulic efficiency higher than about 70 % are available for this power size. Presumably they also have a higher efficiency in reversed mode. A reversible micro turbine could have a better hydraulic efficiency, but hardly higher than 80 % because its modest size ($\Delta\eta$ = +12.6%). However, this customised turbomachine wouldn't be easily accessible and its price would raise at least five times more than a PaT [Motwani *et al.* 2013, Baumgarten & Guder 2005], the cost of which is 12.9 k€ (8.4 k€ for the pump and 4.5 k€ for the motor/generator) for the μ-PHES in *Quartier Negundo*. Thus, an estimation of a traditional hydraulic turbine at equal power output results 42 k€, respectively, a total capital cost raise of 31% (Table 4.7). According to the correlation illustrated by Fig. 4.38, ΔC = +31% corresponds to a LCOE growth by 28.6%. An efficiency improvement of $\Delta\eta$ = +12.6% generates only a LCOE reduction of -11.2%. The net effect of a high performance turbine results in a LCOE raise of 17.4%.

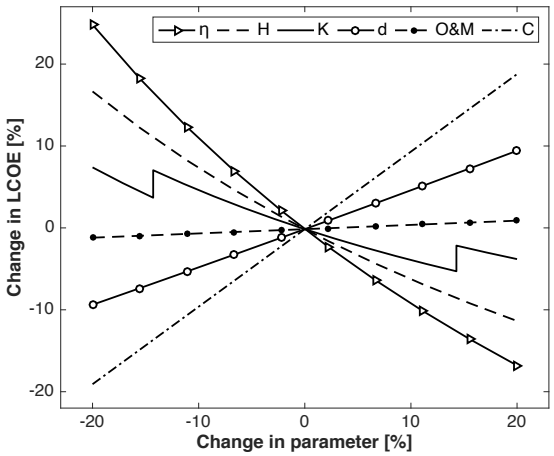

Figure 4.38: LCOE sensitivity analysis using the μ-PHES in *Quartier Negundo*.

A longer lifetime, K, also has a positive effect on the final LCOE. The steps presented in the LCOE sensitivity analysis in Fig. 4.38 for K are due to the periodical maintenance that involves mild reparation of the electrical apparatus. In this regard, the VFD is subject to an expensive check-up at least every five years.

Obviously, the capital cost has a big impact and should be reduced in order to reach grid price parity. Directional drilling cost is an exceptional expense that it was required for these specific cases: 26 % of the total capital cost in Negundo. Furthermore, the pipeline cost is relevant here due to the ratio of pipeline length

and geodetic head (L/H) in the Negundo layout which is about 8. In a hydropower system, L/H can often be close to 4 and thus it underlies the considerable scope for improvement in this subject for other future μ-PHES. Lowering the L/H tends to lower costs and increase cycling efficiency [Botterud *et al.* 2014]. O&M costs have quite a limited influence on the total outcomes: the most common practises on site are to routinely inspect and maintain the trash rack cleaning systems so as to keep the aspiration and discharge channels free of any major obstructions. With the insight of the existing facility and the data analysis available, it is possible to propose a second case study.

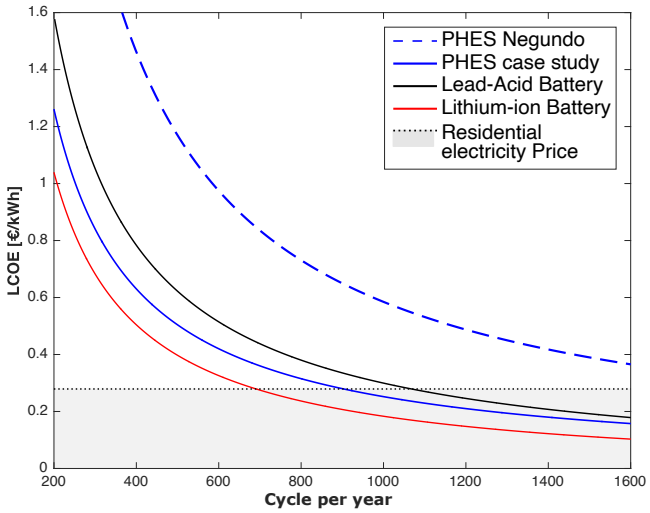

Figure 4.39: LCOE comparison of the μ-PHES in the *Quartier Negundo* with other technologies and the electricity price in Belgium for household consumers in 2017 (0.2877 EUR per kWh) [Statistical Office of the European Communities 2018].

For the sake of completeness, the results of the LCOE calculations are plotted over the number of PHES full cycles in Fig. 4.39. The LCOE results of the μ-PHES in the *Quartier Negundo* and the second case study are compared with other storage technologies. In this plot, lead-acid batteries shall be regarded as having an efficiency of 85 % [Ferreira *et al.* 2013], a capital cost of 200 €/kWh, 300 €/kW, the lifespan of 5 years [de Oliveira e Silva & Hendrick 2016] and a depth of discharge of 10 %. Besides the higher capital cost of about 2500 €/kWh, 3500 €/kW, [Ferreira *et al.* 2013], more competitive LCOE is obtained with lithium-ion batteries due to their durability of about 20 years and an efficiency of 90 % [Ferreira *et al.* 2013]. PHES is the most cost-effective storage technology in long-term and for large scale application [Jülch 2016]. However, micro PHES meets different outcomes. The μ-PHES operative in Froyennes is not competitive with other storage technologies neither under high cycle of charging/discharging per year. Only increasing the system power and energy capacity, as in the second case study, μ-PHES results to be more competitive with other storage technologies

4.5 Conclusions on micro PHES solution

The description of the site and μ-PHES facility presented here provides technical insights into micro energy storage and into reversible pump (or PaT) applications. The experimental results and data obtained on site allow for cost improvements and contribute to the awareness of μ-PHES performance and feasibility.

The μ-PHES in Negundo described in this chapter adopts a single centrifugal PaT for both pumping and generating phases. By using VFD the pump can operate in normal and reverse modes to maintain the highest hydraulic efficiency over a span of 40-120 % of the nominal load design. At such extreme working conditions, a standard hydraulic turbine at fixed rotational speed is subjected to cavitation and instability, both of which reduce the performance. The maximum efficiency measured in reversed mode is approximately 1-2 % less than the efficiency of the turbomachine in pump mode. With a peak of 71 %, the PaT hydraulic efficiency recorded is smaller than with regular micro turbines [Paish 2002] [Jain & Patel 2014], but still very competitive at this power-size.

The results of the economic analysis of these two case studies highlight crucial and imperative design arrangement. The limited revenues create the main economic barrier for micro μ-PHES solutions. The *"micro"* amount of energy managed by such a bulky system defects the profitability of this investment. Using the same machine for pumping and generating is an outstanding solution to save cost-energy, space and maintenance but a cost-benefit analysis proves that the installed μ-PHES have not reached parity to other small scales EES, but yet the results are promising if higher system head is available. A significant reduction in cost investment is reached by using an already existing stormwater basin on site, by reducing the construction costs of at least 28 %. A LCOE of 1.06 €/kWh is obtained for the micro PHES realised in Negundo, but for the same amount of cycles per year it could reach 0.46 €/kWh, as shown in the further case study. The latter shows possible additional improvements linked to the specificity of the site: cutting costs and increasing the total energy output, E_{out}, by increasing the exploitable available head. Moreover, the LCOE sensitivity analysis here discussed provides a rational basis for making the most economically informed decision, possibly leading to more future inspirations within the academic and professional communities.

Chapter 5

Numerical investigation

Contents

5.1 Introduction

Previous research investigations in the PaTs performance, presented in Section 2.5.2, underline the growing interest in improving its efficiency and promoting their implementation in micro hydropower. However, drastic geometrical updates would not preserve the PaTs economic advantage, but they may require a considerable amount of resources instead. On the contrary, cutwater modifications are confined in a modest area of the volute and do not alter the runner geometry. Because of its finite thickness, the cutwater interferes with the flow, generating local excess velocities and deviations of the streamlines affecting the flow orientation at the inlet of the PaT runner and consequently its performance. Thanks to the few preliminary study

about the effect of the cutwater, it has been possible to foresee its design potential in pumps in reversed mode, but the precedent literature concerning an effective methodology in its design optimization is limited.

To fill this gap, this chapter, in part published at Renewable Energy journal under the title *"Numerical investigation on the volute cutwater for pumps running in turbine mode"*, presents a new approach for a geometry improvement based on numerical investigations. The produced data allow building a regression model of the PaT efficiency and to detect with good accuracy the geometry optimum for the new cutwater design thanks to the solution of an optimization algorithm. The analysis is conducted on the variations of the rounding, length and angle inclination of the volute cutwater of the radial-pump implemented in the μ-PHES analysed in Chapter 4. For this purpose, Section 5.2 announces the problem statement and introduces the developed methodology. Section 5.3 firstly illustrates the hydraulic domains, giving a view of the phenomenological problem driven by the cutwater modifications. The numerical approach and the available experimental data are then discussed. Finally, the regression model and the optimization strategy are presented. The CFD validation and results are described in Section 5.4 and they address the finding of the cutwater optimum design. The proposed numerical investigation offers sufficient pool of data to elaborate a predictive algorithm of the hydraulic PaT performance. The optimized geometry of the cutwater is proposed and compared with its baseline design. A performance analysis of the geometry improvement on the turbomachine in pump mode is provided in Section 5.4.7. At last, the conclusions are stated in Section 5.5.

5.2 Problem statement

In order to optimize a centrifugal pump running as a turbine, the present study aims to detect the global maximum of hydraulic efficiency under the constraints of the cutwater geometric variables. An overview of the investigated geometry is given by Fig. 5.2. The cutwater is modified from its initial design (baseline geometry) by length, tip thickness and tilt deviation. The geometrical updates are conducted on case-by-case basis by a computer-aided design software and adapted for numerical simulations. To secure reliability of the selected numerical model, the computational results of the baseline geometry are validated by experimental measurements in respect of their relative accuracy. Therefore, CFD simulations build a complete data-set, including the PaT head and efficiency characteristics. The retrieved data allow the development of a regression model for understanding the effect of the different geometrical variables on the hydraulic efficiency. Moreover, this model is able to predict the PaT performance in relation of the cutwater design and lessen the investigation time appreciably. Finally, an optimization problem, targeting the highest efficiency point, processes the regression model and converges in an ultimate optimal design of the cutwater.

5.3 Methodology

The workflow and the tools used in the methodology are described in the Fig. 5.1. First, the methodology is validated on the baseline geometry by the available experimental data. Then, simulations of multiple geometrical assets of the cutwater generate the numerical dataset for solving the optimization problem.

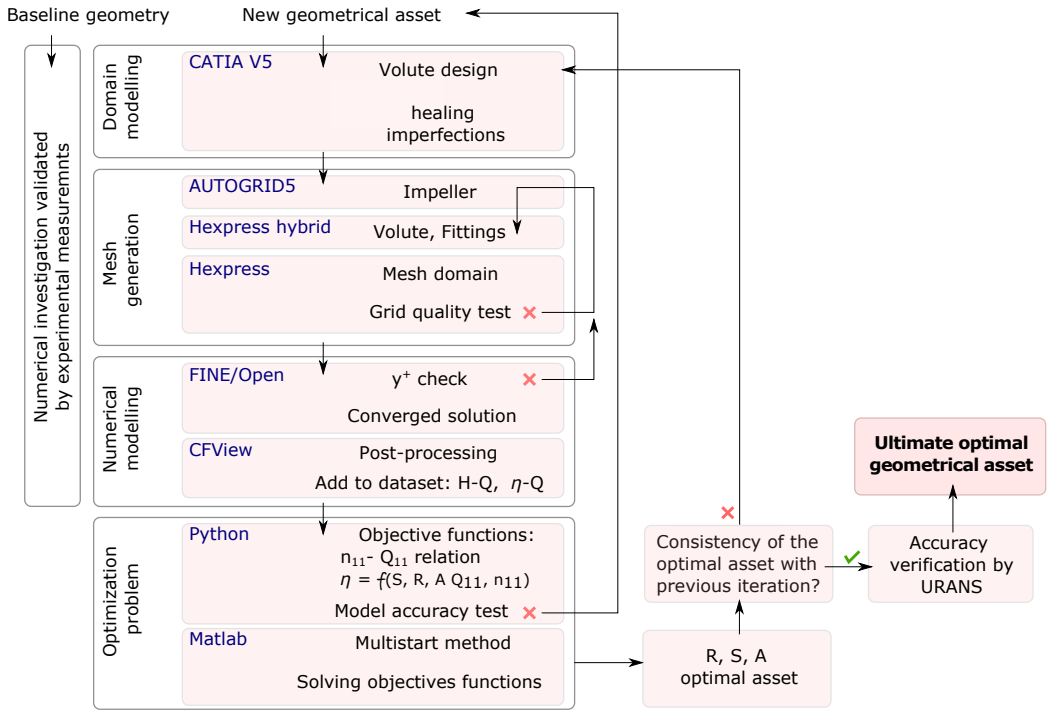

Figure 5.1: Numerical investigation workflow and used tools in the methodology. Iterations and corrections are foreseen if *mesh quality test, y^+ check*, and *regression model accuracy test* were failed.

5.3.1 Experimental setup

In this study, experimental tests are used to validate the numerical simulations performed on the centrifugal pump. The pump specific speed N_s, a designing value that helps characterize the shape of the impeller pump, is equal to 55 and it is calculated as follows:

$$N_s = \frac{N\sqrt{Q}}{(H)^{0.75}} \tag{5.1}$$

where N [rpm], Q [m^3/s], and H [m] are related to the pump BEP. The radial pump is applied in the micro pumped storage plant facility described in the Chapter 4. In this installation, the pump without any modifications is used for both pumping and generating operations by variable speed control.

5.3.2 Hydraulic domain modelling

The domains implemented for the generation of the computational grid count four sub-domains: the pump impeller, the volute and two straight pipes (or fittings) at the suction and discharge sides of the pump (Fig. 5.2). The additional volumes are meant to uniform the imposition of the boundary condition during the solver calculations without affecting the solution of the simulation [Štefan *et al.* 2020]. Despite the increase of simulated flow and thus the larger use of computational resources, both sub-domains allow the flow to reach the full developed conditions and avoid severing the computation right at the interested research sections.

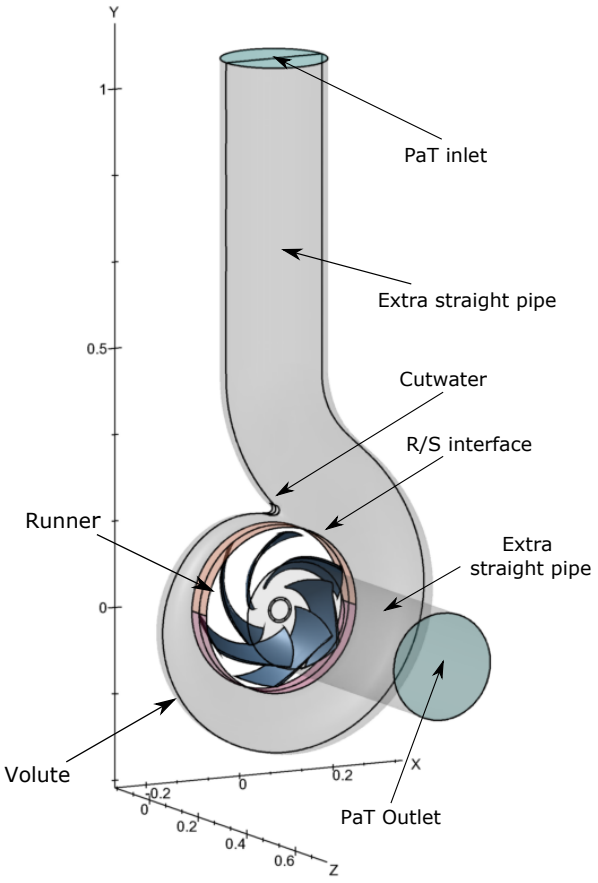

Figure 5.2: Overview of the simulated domain. Dimensions are expressed in meters

To reproduce the operating domains of the pump, its technical drawing, provided by the manufacturer (Ensival-Moret/Sulzer), have been imported in CATIA V5 [Dassault 2019]. The design of the cutwater modifications are conducted by the structure of five symmetric profiles that respect the definitions of the imposed design variables. Fig. 5.3 depicts the CATIA view of the original cutwater, fragmented in numerous separated surfaces, and an example of modified cutwater: the yellow area is the new geometry and the parallel profiles are enlightened in red.

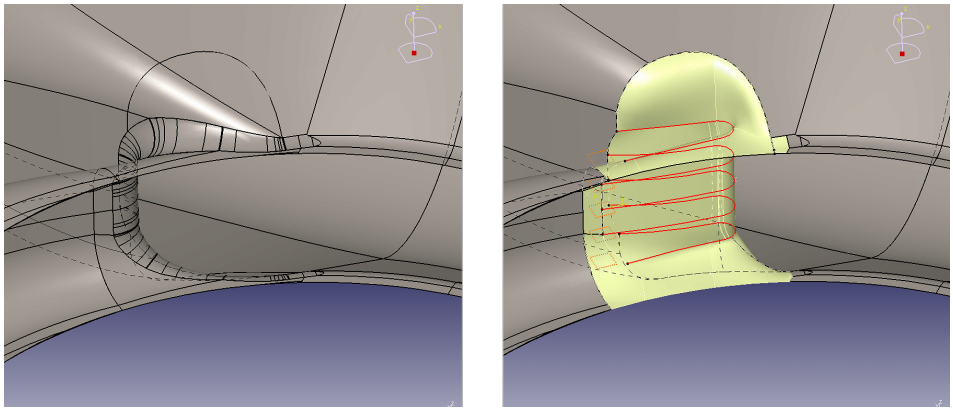

Figure 5.3: Detail of the geometry in CATIA for the baseline cutwater (on the left) and a tested configuration (on the right).

The original CAD .IGES files, provided by the manufacturer, have been converted and healed by geometrical imperfections, such as disconnected surfaces and missing intersecting points. The CAD needs to be watertight: no surface fractions are allowed nor for inlets and outlets bounds. Numeca meshing tool software requires closed surfaces and all the gaps needed to be filled. A dedicated smoothing-CAD process is applied to the investigated sub-domains in order to emulate fine and smooth surfaces nearabout the cutwater (Fig. 5.4). Moreover, parts that are supposed to touch/intersect, are better imported in the mesh generator if merged in respect to their tangent constraints. In this way, erroneous sharp edges and inaccurate defects are removed from the domain modelling, saving critical geometrical spots, such as bulges and cusps, to the mesh generation process and numerical computations.

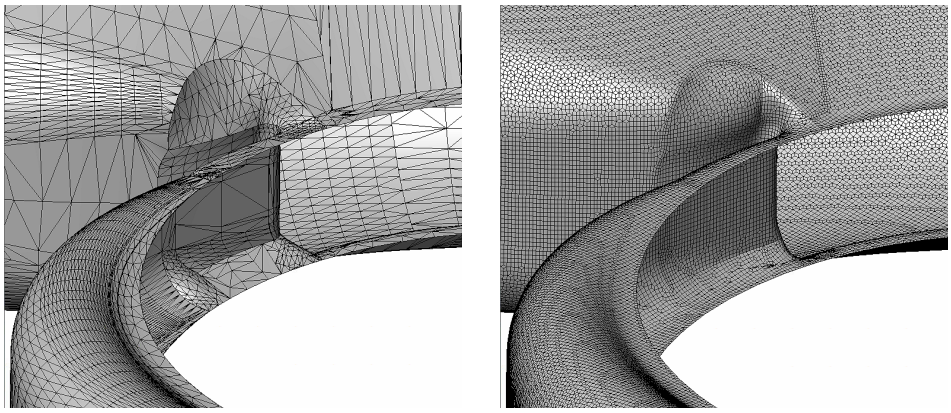

Figure 5.4: Geometry improvement by rebuilding the cutwater's adjacent surfaces. Here for a stretched version: before (on the left) and after the surface improvements (on the right).

5.3.2.1 Reproduction of the real geometry

A key aspect in every simulation process is the difference between the real geometrical model and the simulated one; there are discrepancy between the models used in CFD and the real components [Montomoli *et al.* 2015]. Firstly, the computational domain does not usually take into account all geometrical features, such as fillets and steps at the runner. Another aspect is the limited knowledge of the components manufacturing. For instance, surface roughness and interplatform gaps could affect and generate local complexity hard to detect in numerical simulations [Adami *et al.* 2007]. Therefore, in many cases the geometries are subjects to approximations in favour of reducing model complexity as computational time and improving stability of the simulation process.

In the present case study, the geometry received by the pump manufacturer is already limited in characteristics and details: the CAD files do not include gaps between the rotor and stator parts nor sealings apparatus nor manufacturing tolerances. It follows that no impeller clearances have been considered. The hydraulic friction losses related and the drag loss at the back of the impeller are not simulated, but the losses in these zones (non-flow zone losses) are mainly due to disk friction and secondary flow effects, and they can be estimated [Doshi *et al.* 2017, Derakhshan & Nourbakhsh 2008a]. To reduce the discrepancy from the experimental data [Yang *et al.* 2014a], the losses have been computed according to empirical formulations provided in literature [Doshi *et al.* 2017, Gulich 2010]. The power losses created by leakages have been estimated a priori, according to an empirical 1-D model, because the pump seals and the balancing holes of the impeller have not simulated and need to be accounted to compare experimental and numerical values:

$$\eta_v = \frac{Q}{1 + \dfrac{Q_l}{Q} + \dfrac{Q_e}{Q} + \dfrac{Q_h}{Q}}, \qquad Q_l/Q = \frac{a\,z}{N_s^m} \tag{5.2}$$

where $a = 0.15$, $z = 2$ and $m = 0.6$ are parameters set according to the literature for $N_s > 27$ pumps with balance holes [Gulich 2010] for defining the volumetric efficiency η_v. The leakage (Q_e) through devices for axial thrust balancing and the additional fluid (Q_h) that may be circulated within the pump for auxiliary purposes such as feeding a hydrostatic bearing, flushing, sealing or cooling, are considerate negligible for this case.

Additional power detriment is due to the radial gap volute-impeller tips and disk friction, i.e. it includes the friction at the axial thrust balance device as the energy dissipated through wall shear stresses on the impeller and the sidewalls (on the rear and front). Because of a lack of information on the surfaces roughness and axial spacing, which are essential parameters for metering such a proportion of power loss [Poullikkas 1995, Daily & Nece 1960], the gap and disk friction, η_f, cannot be computed but estimated [Mikhail *et al.* 2001, Yang *et al.* 2012b].

Finally, the mechanical efficiency can be calculated at BEP by [Gulich 2010],

[Giosio *et al.* 2015]:

$$\frac{P_m}{P} = 0.0145 \left(\frac{1}{Q}\right)^{0.4} \left(\frac{1500}{N}\right)^{0.3} = (1 - \eta_m) \tag{5.3}$$

All these considerations allow to reproduce the overall pump and PaT characteristic curves for comparing the numerical output (CFD) with the experimental efficiency data (exp) such as:

$$\eta = \eta_h \, \eta_m \, \eta_v \, \eta_f \tag{5.4}$$

Eq. 5.5 explains the conversion in a greater efficiency ($\eta_{CFD} > \eta_{exp}$) due to a reduction of simulated power loss P_{loss}:

$$\begin{aligned} \eta_{CFD} &\simeq \eta_{exp} + \frac{P_{loss}}{\rho g Q H} \\ &\simeq \eta_{exp} + \frac{H_{loss}}{H} \end{aligned} \tag{5.5}$$

5.3.2.2 Volute characteristics in pump mode

In the normal operation of a centrifugal pump, the discharge leaves the impeller with a strong tangential component. The flow is led to follow the volute curvature and, by reducing its velocity, to limit consequent energy losses. In most of the common centrifugal pumps, volutes are not equipped with vanes. However, as the capacity and size increase, the hydraulic efficiency is more relevant and different kind of diffuser (with parallel walls, divergent walls, vaneless or with vanes) must be used [Nourbakhsh *et al.* 2007]. The conservation of mass and conservation of momentum describe the normal fludynamic process in the pump casing:

$$rV_u = k_1 \qquad \rho V_m A = k_2 \qquad \tan\alpha = \frac{V_u}{V_m} \simeq \frac{k_1/r}{k_2/\rho 2\pi r b C_d} = b\rho k_3 \tag{5.6}$$

where A is the passage section, b is the passage depth, C_d is the discharge coefficient A_{eff}/A_{geo} and k_i are constants. The angular momentum is linked to the angular momentum at the exit of the impeller. However, about 5 % to 15 % may be destroyed as the flow proceed in the vaneless diffuser [Japikse *et al.* 1997]. In a normal operation of a centrifugal pump at constant rotational speed the tangential flow can be considered in first approximation constant along the volute and resulting to the meridional velocity at the throat, V_7. Fig. 5.5 shows the approximations of the flow states in the spiral volute and the preserved flow conditions of Eq. 5.6.

Fig. 5.6 illustrates a qualitative representation of a volute with a tangential exit. It is apparent from the rectilinear transformation of the volute flow that the pressure loading is important around the cutwater. Johnston et al. recommend that the volute exits should curve about the axis for quite a distant downstream from the tongue to limit the loading in the cutwater area [Johnston & Dean 1966]. In result, more common commercial pumps, the centerline of the discharge pipe is crossing the axis of the motor-impeller. This is also the case of the analysed pump in this

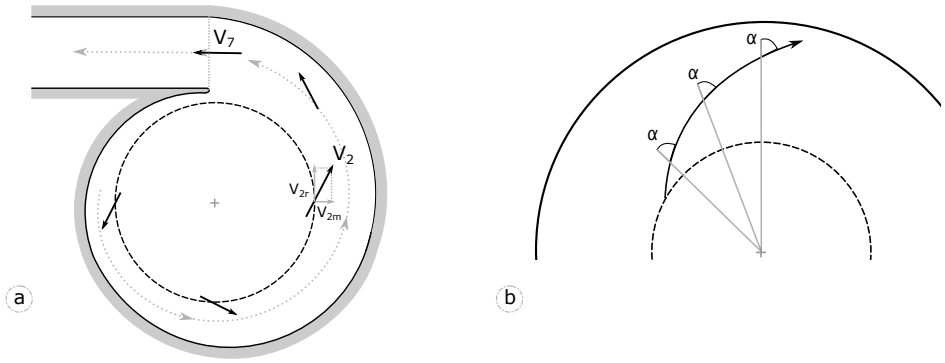

Figure 5.5: (a) Volute flow states (b) Flow path with constant flow angle α in logarithmic spiral

research (Fig. 4.11). The Fig. 5.6 indicates that fine modifications of the volute cutwater are likely to have modest effect on the flow, and that most of the pressure distortion is produced by the abrupt turning in the exit passage [Japikse *et al.* 1997].

However, particular complexity of the flow can appear in a vaneless diffuser and especially around the cutwater region in off-design operating conditions [Lazarkiewicz & Troskolanski 1965, Johnston & Dean 1966]. Besides, the effective velocity passing the volute throat is determined by the mass flow and the local flow area. In the other hand, the design point of a pump volute is specific and matches with the design intent of the BEP [Japikse *et al.* 1997]. At high flow rates the water velocity through the throat increases more than what the peripheral velocity at impeller exit gains. Thus, the V_u need to accelerate along the volute. At lower flow, the opposite occurs and the flow slows down and diffuses to fill the empty room in the volute. The volute operates as nozzle at high flow rate ($V_2 < V_7$) and as diffuser at low flow rate ($V_2 > V_7$). Furthemore, it is important to mention the disturbed and separated flows that can usually occur in off-design regimes, particularly in the vicinity of the cutwater [Brennen 1994].

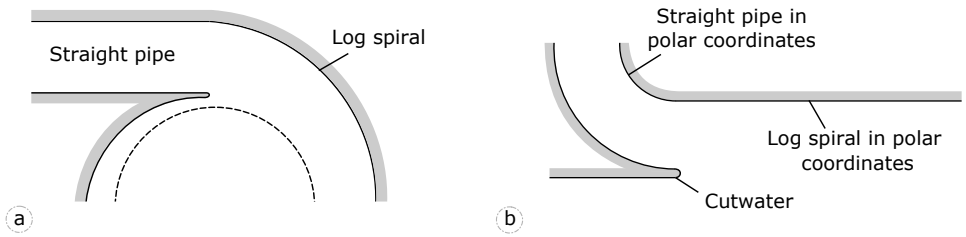

Figure 5.6: (a) A two dimensional volute (b) Volute transformation in cartesian plane (x, y) of the polar description of geometry (Θ, r).

5.3.2.3 Design of experiment

In this research, the modifications of the cutwater's length, thickness and tilt angle report to the baseline design of the volute. The original dimensions are denoted by the length of 15,6 mm (L) and a tip thickness for 6,5 mm (radius, r). The inclination angle (A) of the original cutwater is set to 0°. The limits of proposed modifications reflect geometrical constraints. The maximum inclination is defined to avoid the contact with the rotor and the minimum thickness and length by structural and manufacturing issue. The investigation analyses the cutwater's radius at full, half and quarter of the baseline size (Fig. 5.7). The effects of cutwater's length are covered by CFD simulations on multiple sample stretching values i.e. two, three and four times the baseline length (Fig. 5.8). Finally, the inclination of the cutwater represents an additional optimization parameter: cutwater with positive and negative angle deviations are explored (Fig. 5.9).

As a factorial investigation, the design of experiment produces 60 responses of the variables and 60 consequent different characteristics. The effects of interactions between the factors on the global hydraulic efficiency are expected, defining the new operational regimes and cutwater geometry.

The modifications performed on the cutwater geometry are investigated within the ranges summarised in Table 5.1. The research space covers the operative intervals of Q_{11} and n_{11} where high efficiency is performed. Q_{11} and n_{11} are defined as follows:

$$Q_{11} = \frac{Q}{D^2 H^{0.5}} \qquad n_{11} = \frac{nD}{H^{0.5}} \tag{5.7}$$

The investigated geometry alterations would affect the flow pattern at the entrance of the PaT runner such as the absolute water speed c_2 direction, α_2. The hydraulic performance of the PaT depends on the specific energy, which increases through the turbomachine according to Eq. 5.8 [Gulich 2010]:

$$\begin{aligned} E = gH &= u_2 c_{2u} - u_1 c_{1u} \\ &= u_2 c_{2m} \cot(\alpha_2) - u_1^2 + u_1 c_{m1} \cot(\beta_1) \end{aligned} \tag{5.8}$$

An overview of the nomenclature and the velocity triangles in pump running in turbine mode is provided by Fig. 5.10.

Table 5.1: List of independent variables describing the cutwater.

Variable	Domain
Stretching, S	$\Lambda_S = [L, 4L]$
Rounding, R	$\Lambda_R = [r/4, r]$
Angle, A	$\Lambda_A = [-25°, +10°]$
Discharge unit, Q_{11}	$\Lambda_{Q11} = [0.33, 0.50]$
Speed unit, n_{11}	$\Lambda_{n11} = [65, 105]$

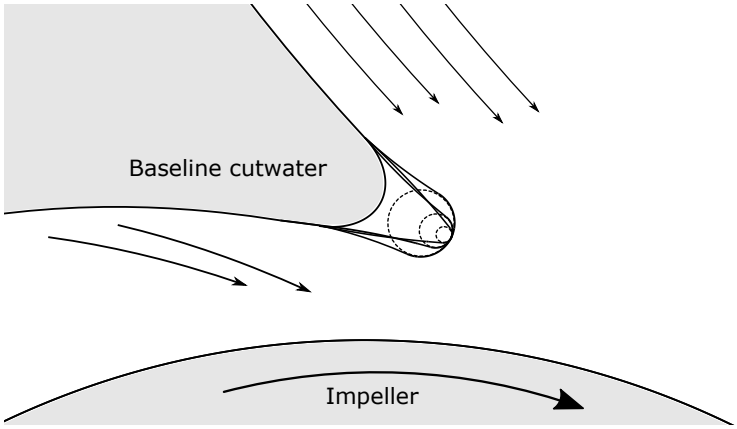

Figure 5.7: Variation of the cutwater rounding variable R.

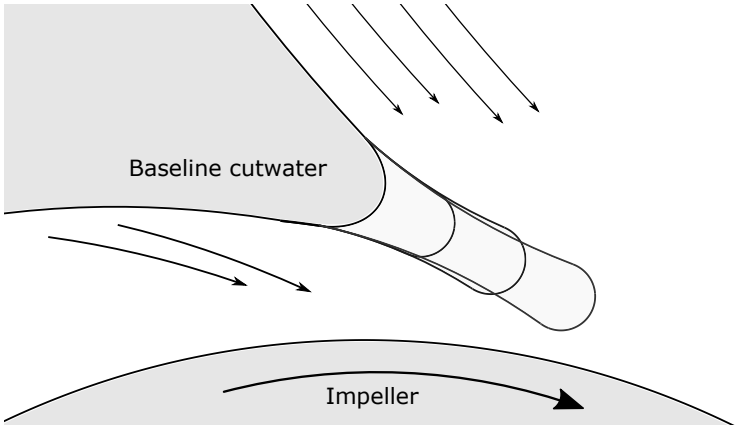

Figure 5.8: Variation of the cutwater length variable S.

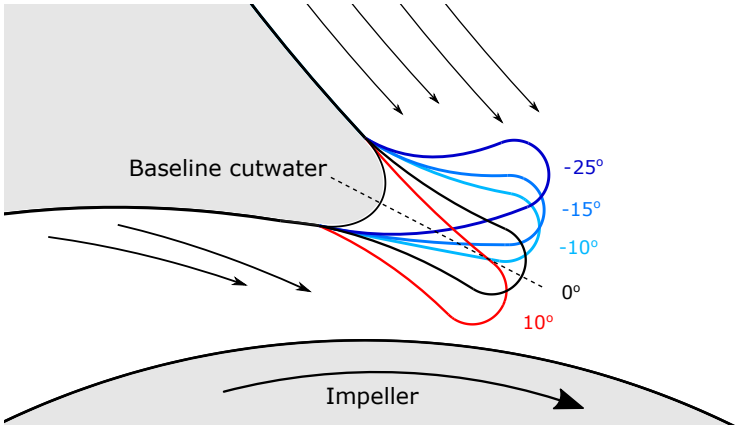

Figure 5.9: Variation of the cutwater tilt angle variable A.

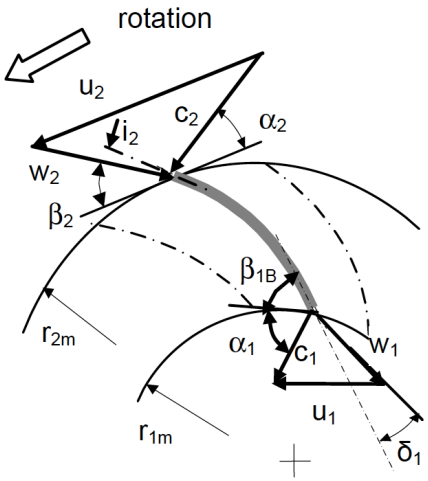

Figure 5.10: Velocity triangles at the entrance (station 2) and exit (station 1) of the PaT runner [Gulich 2010].

5.3.3 Mesh generation

The domain discretization has been generated separately for the sub-domains by utilizing commercial CFD codes from Numeca. AutoGrid5^{TM} software [NUM 2019a] produces a structured mesh of a single passage of the six-blade-runner. The solver will then implement the full periodicity of the runner blade passages for achieving the numerical results. On average, the 3D solid mesh of the pump impeller has 73 paths from the hub and shroud, 33 % of which are used for the core flow. Fig. 5.11 represents a scheme of the cell point distributions at the blade to blade level. Fig. 5.12 shows a full repetition of the six blade impeller mesh and the blade to blade grid passage in angular (theta) and radial (dm/r) directions at mid-flow span. In here, two repetitions of one blade channel are represented. The generated grid blocks, that are marked in red lines for one blade channel, refer to the inlet of the pump impeller, the leading edge, the channel, the trailing edge and the impeller outlet.

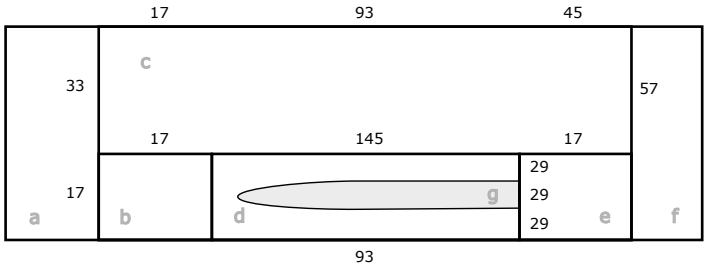

Figure 5.11: Blade to blade topology map of the mesh blocks and cell point distributions: a) inlet; b) leading edge; c) blade channel; d) blade skin; e) trailing edge; f) outlet; g) blade.

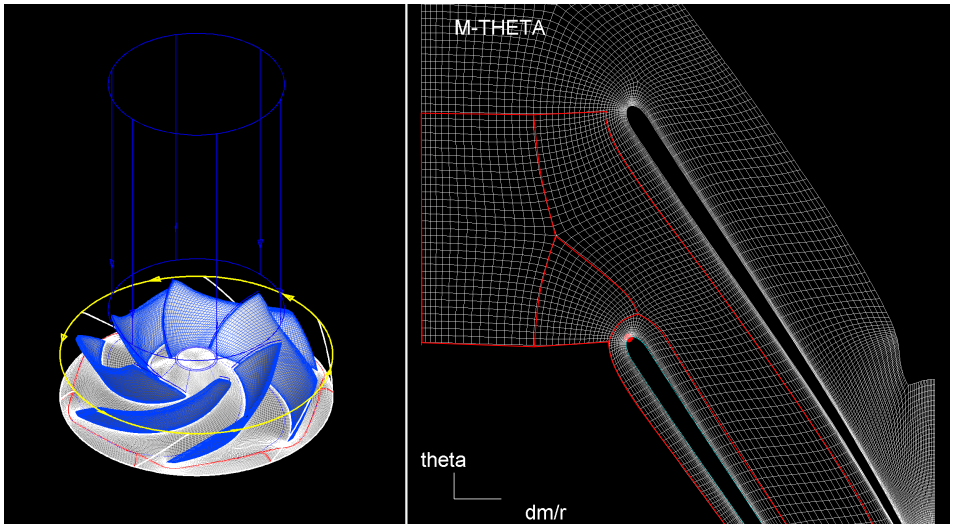

Figure 5.12: Full mesh illustration of the pump impeller (left) and blade to blade topology for two blade passages at mid-flow span. In red, the edges of the blade grid blocks.

Hespress [NUM 2019c] and Hexpress-hybrid software[NUM 2019d] are used for the unstructured mesh of the other sub-domains and the final merged mesh. Fig. 5.13 illustrates the whole volute mesh surface and a cut-view of the mesh. All the available experienced numerical simulations confirm the relevance of the grid quality as a crucial factor for convergence and simulation reliability [Asomani *et al.* 2020, Štefan *et al.* 2020]. For this purpose, a grid sensitivity analysis is conducted with an increasing number of mesh points and improved quality (Fig. 5.14), in respect of the maximum level of orthogonality (average skewness $>$ 75°), average expansion ratio ($\overline{ER} <$ 5), acceptable ER at viscous layer ($ER \leq 1.2$) and average aspect ratio ($\overline{AR} \leq 5$). The final mesh is considered acceptable when the generated outputs do not show great sensitivity to local or global grid refinements [Alemi Arani *et al.* 2019, Arani *et al.* 2019, Wang *et al.* 2017]. The convergence criterion is set at 10^{-4} and, until the converged values for efficiency and torque exceed the range of 0.04 % from the solution obtained with a finer mesh, the number of the grid points are further increased. Table 5.2 illustrates the details of the mesh in the four sub-domains used for the baseline case study. $\overline{ER}$ and $\overline{AR}$ give an index of the mesh quality and dx estimates the average element size, calculated as $dx = (V/n_{nd})^{1/3}$, where V is the domain volume [m^3] and n_{nd} is the number of mesh nodes.

The non-dimensional wall distance y^+ defines the requirements for a sufficient and accurate description of the turbulence at the wall. Hence, it is crucial to monitor that y^+ ranges in the admissible values in solving the boundary layer, according to the adopted turbulent model. An iterative adjustment of the first-cell size and grid refinement are conducted to find the adequate set of mesh for different discharge regimes. The shift in flow velocities affects the Reynolds number, and thus, the

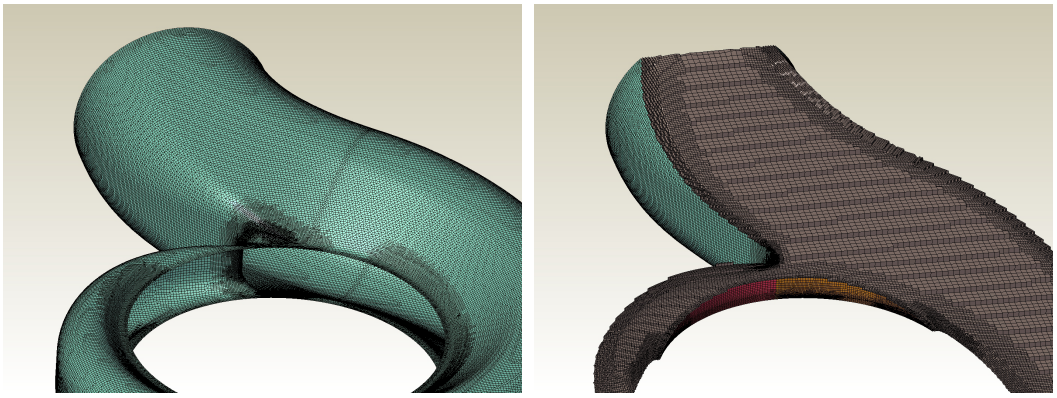

Figure 5.13: View of the wall surfaces of a volute (right) and cut-view of a volute mesh. Denser regions are created to deal with the wall boundary layer and refining the cutwater zone.

approach in estimating the boundary layer. The y^+ values reported in Fig. 5.15 are representative for all the investigated cases and simulated discharge values. A whole mesh system of the four sub-domains between $4.8{\cdot}10^6$ and $6{\cdot}10^6$ cells is found satisfactory. The cell number variation is mostly due to the turbulence model selection and the additional refinements near to cutwater during its modifications: the wider the inclination angle and length, the larger the required number of grid cells. Finally, the mesh for unsteady simulations, that requires the same grade of periodicity between rotor and stator, counts a 360 degree domain of the runner (6 blades) and approximately 10^7 cells.

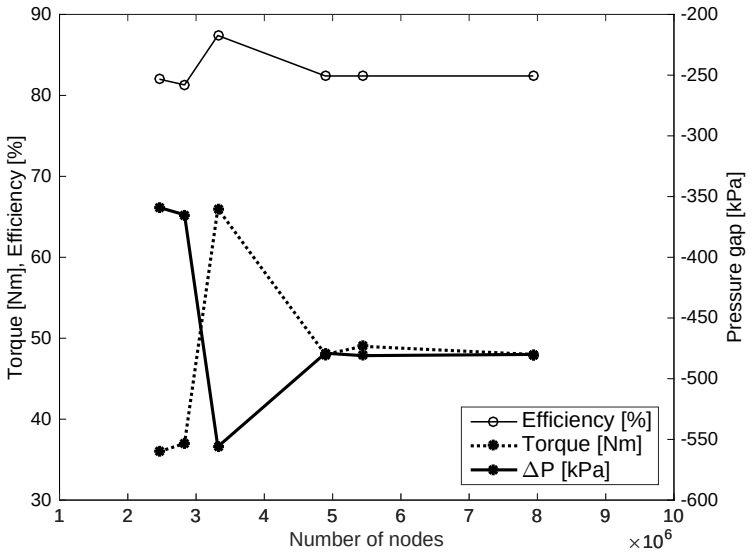

Figure 5.14: Mesh convergence test conducted to assess the independence of the grid on the accuracy of the solution.

Table 5.2: Mesh details for the baseline case study domain

Sub-domain	Volume [m^3]	Nodes	dx [m]	$\overline{AR}$	$\overline{ER}$
Inlet	0.0198	450 953	0.0035	1.01	1.16
Volute	0.0247	2 791 970	0.0021	1.01	1.10
Blade	0.0095	1 190 496	0.0019	1.72	1.25
Outlet	0.0201	460 359	0.0035	1.01	1.16

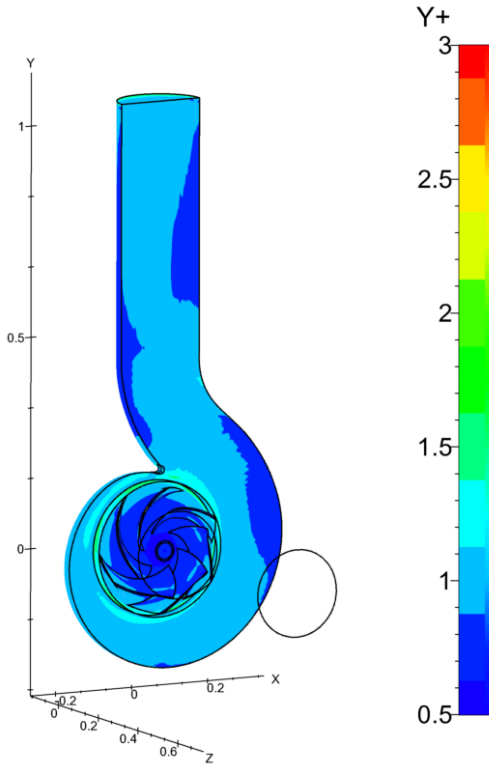

Figure 5.15: Evaluation of non-dimensional wall distance y^+ for the volute and impeller in the baseline case.

5.3.4 Numerical Modelling

The selection of a suitable turbulence model is of crucial importance for the significance of the simulations. Six different models have been tested to solve the incompressible Reynolds time-averaged Navier-Stokes (RANS) equations. The simulations run in steady-state and aim to look at the design validity of the cutwater, describing the flow field perturbations in the volute and velocity angles at the inlet of the runner. Thoroughly solving the relative motion between rotor and volute requires an unsteady and viscous flow solver with the capacity to manage enormous data storage. One way to optimize the calculation requirement is to resolve the steady flow field on a truncated computational domain. This requires the so-called mixing plane approach, an averaging process to be performed at the rotor/stator (R/S) interfaces [NUM 2019b]. In this condition, the PaT cutwater does not locally influence the inlet of the runner but the circumferential averaged flow quantities are exchanged at R/S interfaces. However, the resultant simulation is still capable of predicting with reasonable accuracy the blade-to-blade flow-field and the rotor and stator's overall performance [Corsini *et al.* 2013, NUM 2019b]. This physical approximation tends to become more acceptable as the rotational speed is increased [NUM 2019b]. Finally, the mixing plane approach decreases the needed computational effort by up to an order of magnitude compared to unsteady simulations, that is too time-consuming for use in routine design [Pinto *et al.* 2017, Denton 2010] because it requires different definitions of the spatial and temporal scales of the problem. In this first part of the research investigation, a mixing plane approach is implemented in the RANS simulations with a full non-matching technique that allows for not congruent topology of mesh patches on both sides of the R/S interfaces.

Nevertheless, the employed steady-state CFD simulations can lead only to a partial understanding of the problem that may occur when the pump is operating in turbine mode, especially far from its BEP. On the optimal geometry obtained in this investigation, unsteady verifications are computed by the means of Unsteady Reynolds Averaged Navier-Stokes (URANS) equations to assess the correctness of this optimum. The 2^{nd} order scheme is used to discretize the time dependent terms of the governing equations and 200 maximum inner iterations are considered in one time step of $t = 6.66 \cdot 10^{-4}$s, corresponding to a 4° runner rotation angle.

In agreement with other numerical investigation on internal flow with relevant gradient pressure, k-ω SST better reproduces the revised characteristic curves of the pump and PaT [Capurso *et al.* 2019c, Bardina *et al.* 1997, Arani *et al.* 2019]. This turbulence model is used for all the simulations presented in this investigation. Table 5.3 represents an extraction of the aforementioned turbulence model test over a mesh in a range of 3.9 - 4.6 million nodes. This grid difference is due to the different approach to resolve the boundary layer for extended wall function (EWF) and standards model. In EWF treatments, each wall-adjacent cell's centroid should be located within the log-law layer, namely $30 < y^+ < 300$. Therefore, EWF requires a greater first cell height, thus, a reduced total number of nodes than a standard model ($y^+ \simeq 1$).

Table 5.3: Turbulent model test applied to a PaT: Spalart-Allmaras (SA), k-ε models, k-ω with or without Extended Wall Function (EWF).

	Pump mode at 1000 rpm			PaT mode at -700 rpm		
Model	Δp [kPa]	T [Nm]	η_h [%]	ΔP [kPa]	T [Nm]	η_h [%] [h]
SA	996	98.2	88.24	-455	-45.9	82.2
SA EWF	1005	97.8	89.4	-451	-45.9	82.8
k-ε Yang Shih	1000	98.1	88.65	-525	-57.1	83.0
k-ε EWF	1013	97.7	90.1	-525	-56.0	83.4
k-ω SST	992	98.6	87.9	-479	-48.0	82.4
k-ω SST EWF	1011	96.8	89.6	-525	-53.4	82.8
Experimental data*	920	98	80.8	-492	-49	78.2

($*$) Values revised by the experimental-numerical discrepancies measures (Section 5.3.2.1).

The simulations are computed in FINE/Open solve [NUM 2019b] and the numerical discretization scheme is set central and of the second order. For smoothing the calculations, *multigrid initialisation* is employed: multiple levels of initial coarser grids are used to prepare the computation with the finest grade. Providing an initial data field that is close to the final solution for steady-state cases means the solver has to do less work to reach the converged result [NUM 2019b]. Therefore, this reduces simulation time. The mesh used to discretise the space can have multiple grid levels in each direction of the computational domain $\vec{x}, \vec{y}$ and $\vec{z}$. The *multigrid initialisation* enables, before calculating the flow on the mesh contained in the Hexpress files, to perform a preliminary flow calculations on a coarser mesh the final one. This provides a rapid estimation of the flow. The feature is accessed via the text user interface and re-orders the grid as part of the process [NUM 2019b]. Depending on the case the initial value have been set differently in pressure and in velocity field. A specific setting for the initial solution that divides the domains in sectors and they will be oriented following the boundary conditions, has been chosen for this numerical investigation. Anyway it is correct affirm that in a valid steady state simulation that the same solution should be obtained regardless of initial conditions, but a proper initialisation can accelerate the convergence.

A no-slip boundary condition is applied to all the internal wall. The boundary conditions adopted for the numerical simulations are summarised in Table 5.4. The mass flow direction is set normal to the PaT inlet section and static pressure constant value at the PaT outlet. At the low pressure side, 1.5 bar static pressure provides a safe pressure threshold to avoid the inception and development of cavitation phenomena that would affect the global performance of the simulated turbomachine. Local low pressure regions are anyway detected, not in absolute values, but in relation to the gauge pressure from the inlet. Individuate this spots is fundamental because cavitation could produce critical effects in hydraulics and its development is a serious treat to the normal operation of the system. However, a comprehensive analysis on this phenomenon requires additional analysis for transient isolated

Table 5.4: Adopted boundary conditions for the CFD simulations.

	Pump mode	Turbine mode
Inlet	p at 150000 Pa	Mass flow imposed Velocity normal to the inlet
Outlet	Mass flow imposed Velocity normal to the inlet	p at 200000 Pa
Solid	Rotating at 1000 rpm Rough wall type	Rotating at -700 rpm Rough wall type

bubbles, or attached/sheet cavities or cavitating vortices [Franc & Michel 2006]

The numerical settings for the pump mode are alike to the PaT mode but with switched inlet and outlet definitions and opposite direction of the rotational speed. De facto, in the μ-PHES system, where this PaT operates, the machine can operate both in generating and pumping modes and the BEPs are found at -700 rpm and 1000 rpm, respectively (Section 4.2.2).

The performance of the turbomachine and the cutwater influence are analyzed for a series of discharge values. The time required to obtain converged results is on average above four and a half hours (with 12-core parallel calculations). The convergence criterion is not defined unequivocally by examining the residuals, that, by default, each variable will be reduced to a value of less than 10^{-3}. The residual values provided are normalized to 1 in the first iteration. Hence, if the simulation starts with initial conditions largely different than the steady state solution, the residuals will rapidly fall and appear to level off long before the simulation has actually converged. On the other hand, if an initial conditions that are very near the steady state solution are used, the residuals will never fall very far, and a valid converged solution can be reached with residuals above 10^{-1}. This is why the convergence rules are finally based on residual values and, also, confirmed from the imbalance of mass and momentum (usually lower than 1%), and stable outputs.

5.3.5 Multivariate regression model

Relying on the data-set produced by the simulated operating points, a surrogate model of the PaT performance is built by employing the multivariate adaptive regression spline method (MARS) [Friedman 1991]. The MARS algorithm is a non-parametric multivariate regression method that approximates a nonlinear correlation by a series of spline functions on different intervals of the independent variable. The sequence of these spline functions is articulated by recursive partitioning, or hinge functions, which includes branched equation modelling and assures the continuity of the resulting analytical function and of its first derivative. Hinge mapping of the developed MARS model can be expressed as:

$$BF_i = h_i * \mathrm{Max}[0, (x_j - k)] \tag{5.9}$$

where i and j are the indices for basis functions (BFs) and input variables (x), respectively, and k is a constant referred as *knots*. The $(x-k)$ condition greater than zero enables the related function factor, h. In this way, MARS builds regression based surrogate models by adding BFs as a mechanism that defines variable intervals severed by *knots*. Fig. 5.16 shows examples of fitted regression of two-variables relationship; a linear (a) and polynomial (b) regression models are compared with linear MARS model outputs with a single *knot* (c) and 4 *knots*.

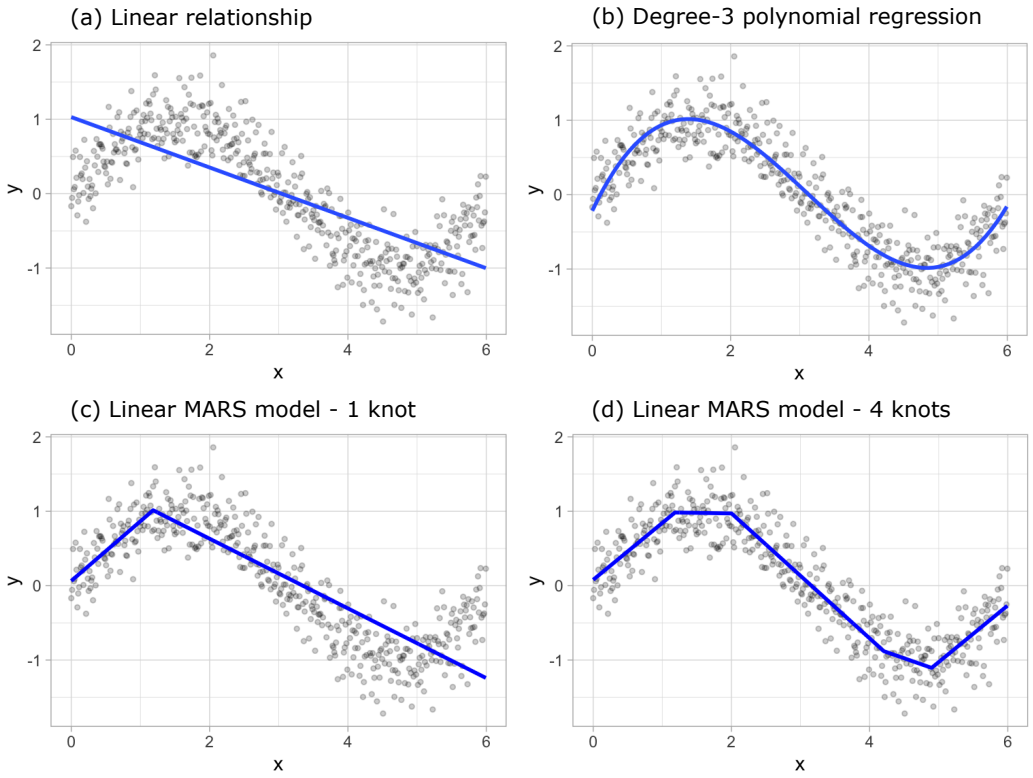

Figure 5.16: Examples of fitted regression of two-variables relationship as in $y = f(x)$ [Boehmke & Greenwell 2019].

Once the full set of basis functions combinations has been created, the algorithm sequentially removes individual basis functions that do not significantly contribute to the model equation [Kuhn *et al.* 2013]. In the backward-pass process of the MARS implementation several BFs are discarded from the final model expression as not significant or held in more influencing hinge functions [Kuhn *et al.* 2013]. For this reason, some BFs are pruned in the final formulation of the surrogate model.

The target of the model is to compute a formulation of the predicted PaT efficiency, $\hat{\eta}$, by the investigated variable ranges, as previously listed in Table 5.1. $\hat{\eta}$ is given by a function dependent on the operating conditions (Q_{11} and n_{11}) and by the geometrical variables (S, R, A) that define the modification of the cutwater. In addition, in order to set consistency of the $\hat{\eta}$ formulation with the feasible PaT

working conditions, an admissible design space of the Q_{11}-n_{11} relation needs to be resolved. Therefore, an analytical function $\hat{Q}_{11} = g(S, R, A, n_{11})$ is established by applying the MARS method to the available numerical data. Because of this second correlation of Q_{11}, the model of the PaT efficiency also respects the admissible operating conditions imposed by the H-Q predicted characteristic curves. The surrogate model of the PaT hydraulic performance is generated with *py-earth*, a library of machine-learning methods written in Python [Rudy 2013], and it is defined as showed in Eq. 5.10:

$$\begin{cases} \hat{\eta}_{PAT} & = f(S, R, A, Q_{11}, n_{11}) \\ \hat{Q}_{11} & = g(S, R, A, n_{11}) \end{cases} \tag{5.10}$$

The correlation coefficient R^2 and the generalized cross validation (GCV) [Golub *et al.* 1979] are used to evaluate the performance of the surrogate model.

5.3.6 Optimization problem

The purpose of the geometry optimization of the cutwater is to guarantee a better PAT performance in energy recovery ability, thereby reducing its energy losses. The calculations are performed in MATLAB [Mathworks 2016] environment and the optimum geometry is detected by solving an optimization problem targeting:

$$\min_{\hat{\eta_{PAT}}} : \quad 1 - \hat{\eta}_{PAT} \tag{5.11}$$

$$\begin{aligned} \text{Such that} : \quad & \hat{\eta}_{PAT} = f(S, R, A, Q_{11}, n_{11}) \\ & S \in \Lambda_S, \qquad Q_{11} \in \Lambda_{Q11}, \\ & R \in \Lambda_R, \qquad n_{11} \in \Lambda_{n11}, \\ & A \in \Lambda_A \end{aligned} \tag{5.12}$$

The global minimum of this model function can potentially be located in the interior of the search space or on its boundaries, indicating that there might be multiple feasible regions and multiple minimum points in each region. In order to solve this non-convex problem a multi-start method is applied [Hickernell & xiang Yuan 1997, Tu & Mayne 2002]: the non-linear solver runs from different starting points, reaching different locally optimal solutions. To keep high probability that the global optimal solution has been found with accuracy, a large number of runs is carried out. Therefore, approximately four thousand different initial values are used for the solver in the basin of attraction of the multi-variable global optimum value. Precisely, a systematic sampling of the search space of the independent variables S, R, A, n_{11} is set and explored in all the variable ranges.

5.4 Results

5.4.1 Validation of PaT numerical simulations

This section compares the CFD results with the available experimental data of the baseline case in order to validate the numerical model. The CAD geometry obtained for the numerical simulation does not include the gaps between the rotor and stator parts nor manufacturing tolerances. It follows no impeller clearances have been considered. The hydraulic friction losses related and the drag loss at the back of the impeller are not simulated, but the losses in these zones (non-flow zone losses) are mainly due to disk friction and secondary flow effects, and they can be estimated [Doshi *et al.* 2017, Derakhshan & Nourbakhsh 2008a]. To reduce the discrepancy from the experimental data [Yang *et al.* 2014a], the losses have been computed according to empirical formulations provided in literature [Doshi *et al.* 2017, Gulich 2010]. The power losses created by gap friction (η_f = 98 %) and leakages (η_v = 98.87 %) have been estimated a priori by Eq.5.2, according to empirical 1-D models [Gulich 2010], because the pump seals and the balancing holes impeller have not simulated. In addition, the mechanical efficiency has been calculated equal to 95.4 % at BEP (Eq.5.3) for the size and wear of the implemented pump, also in agreement with the accepted range value 89-96 % in the literature [Giosio *et al.* 2015, Gulich 2010]. All these considerations allow reproducing the overall characteristic curves of both pump and PaT modes.

Fig. 5.17 compares the pump specific energy coefficient Ψ and pump efficiency η_h with the numerical results. The curves are found in good agreement, despite the CFD simulations over perform at higher flow rate. There are elements in the pipeline that are required for operations and for measuring (Fig. 4.13) but they affect the flow turbulence and possibly spoil the optimal performance conditions. The butterfly valve located near to the suction side of the pump (or PaT outlet) introduces an uneven flow into the eye of the impeller increasing pressure drops.

In Fig. 5.18, the PaT's specific energy coefficient, $\Psi = gH/(\omega D)^2$, and the hydraulic efficiency, η_h, of the numerical simulations are compared with the experimental data over the PaT's discharge coefficient at N_{PAT}. It should be noted that discrepancies between computations and experimental data could be partly due to the uncertainties in measurements and unavoidable numerical uncertainties. The uncertainty analysis gives a relative error of about ± 3 % in pressure and head at BEP operating conditions (Fig. 4.17).

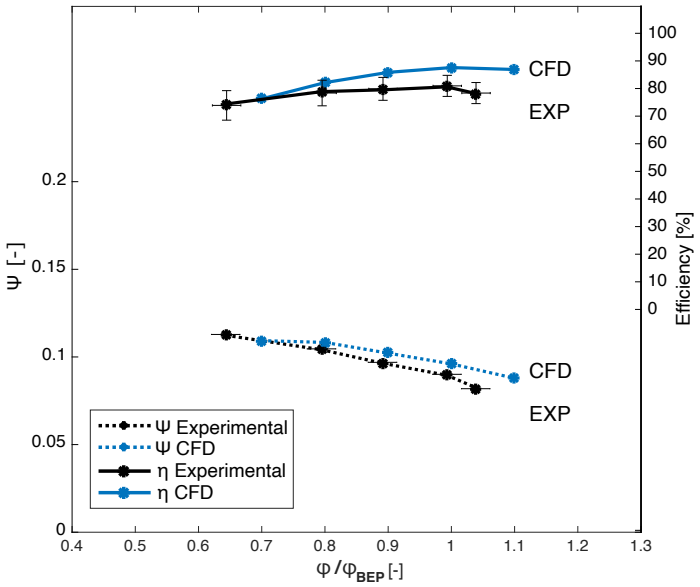

Figure 5.17: Numerical simulations and experimental data comparison for the pump specific energy coefficient Ψ and pump efficiency η_h over the relative discharge number.

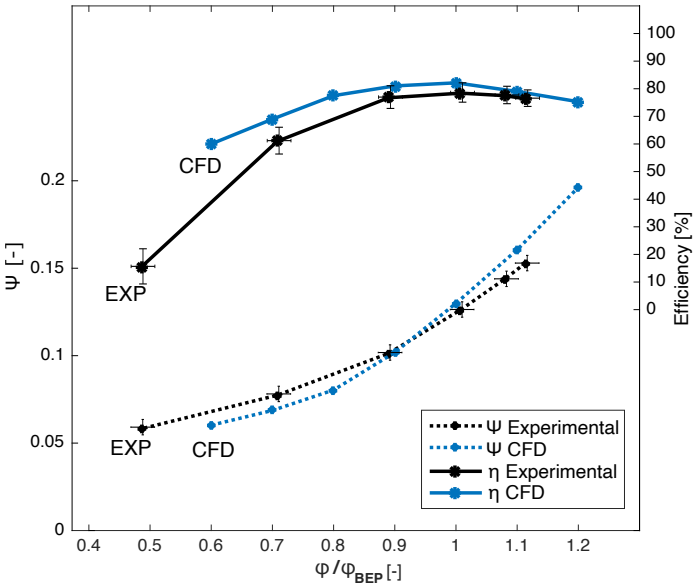

Figure 5.18: Numerical and experimental comparison for the PaT specific energy coefficient Ψ and PaT efficiency η_h over the relative discharge number.

5.4.2 Performance evaluation

After quality evaluations of the simulations by means of the convergence history, y^+ checks, momentum- and mass-balances, the numerical results can be analysed. Immediate observations can be acquired by the development of the flow field in the cutwater nearby. Velocity contours illustrate if the flow momentum is well distributed or uneven at the impeller entrance. This condition would affect the optimal and balanced flow pattern in the runner downstream. Streamlines and the absolute velocity angle describe the flow deviation and incidence to the rotor/stator (R/S) interface. Fig. 5.19 shows the velocity field near the cutwater in baseline design. The flow coming from the PaT inlet is following a dominant radial direction to the R/S interface; only revolving around the volute, the streamlines are subject to a more circumferential component, as shown in the cutwater-gap before mixing with the incoming discharge. Beneath the baseline cutwater, there is a complex three-dimensional flow, which forces to recirculation through the tip gap and consequently is forcing fluid down into the runner: the flow separation and secondary flow created under the cutwater certainly complicates the flow field at the rotor.

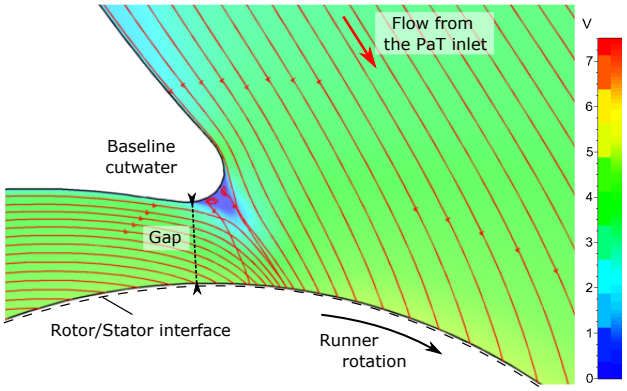

Figure 5.19: Flow field for the baseline cutwater at φ_{BEP}.

Fig. 5.20 depicts the PaT flow fields and the absolute velocity angles ($\text{atan}(V_r/V_t)$) for three of the simulated cutwater assets S, R, A. $-25°$ tilt angle slows down the flow before the cutwater on its side and broadly deviates the flow coming from the PaT inlet into a more circumferential direction. However, the lifted shape favours volute recirculation by enlarging the final passage of the volute log spiral, affecting the velocity angle (Fig. 5.20-a). On the other hand, a positive inclination ($+10°$) insufficiently bend the water streamlines and a velocity flaw is generated directly in front of the cutwater tip (Fig. 5.20-b). A straight ($A = 0°$) and long cutwater ($S = 4L$) smoothly leads the flow towards the volute spiral, but the velocity flow angle does not appear completely even, especially in the volute closure gap (Fig. 5.20-c).

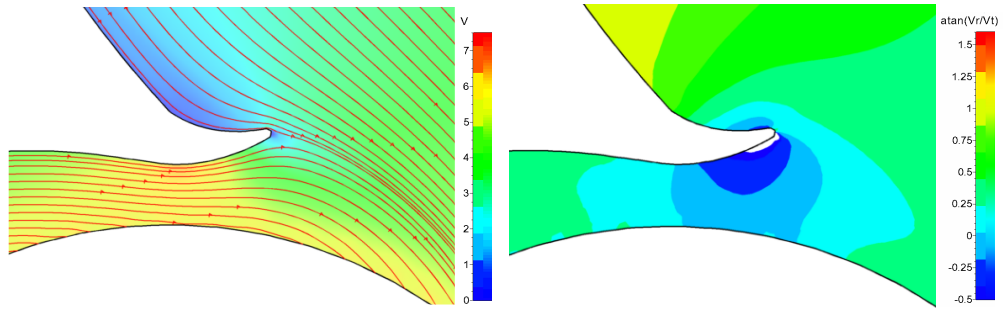

(a) Flow field for a cutwater of $S = 3L$, $R = r/4$ and $A = -25°$

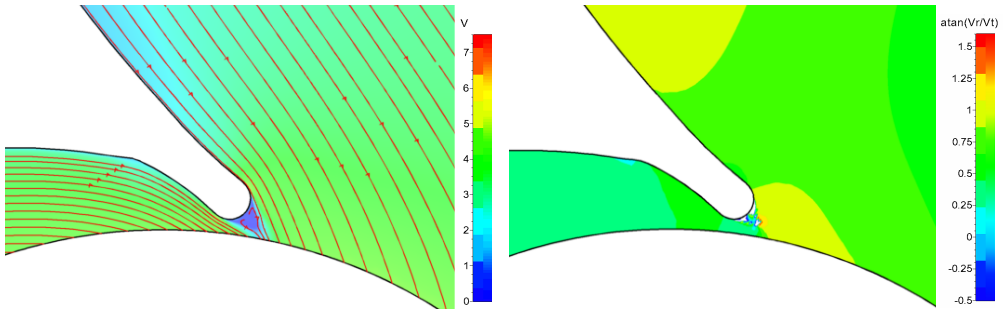

(b) Flow field for a cutwater of $S = 3L$, $R = r$ and $A = +10°$

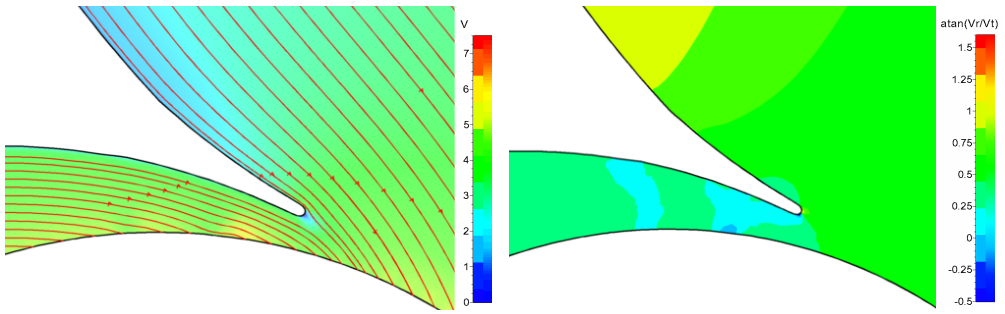

(c) Flow field for a cutwater of $S = 4L$, $R = r/4$ and $A = +0°$

Figure 5.20: Illustrations of three different cutwater at $\varphi = 0.0152$: the flow field [m/s](left) and α_2 [rad] coplanar with mid-flow cut-view (right).

The CFD post-processing allows to analyse the head and efficiency characteristics. At least four operating conditions are simulated to define the curves for each S, R, A variable set. In Fig. 5.21-5.22-5.23, the specific energy coefficient and efficiency are shown in function of the cutwater inclination angle, A, over the discharged unit, φ, normalized on the baseline BEP. Nine couples of sub-figures give an overview the multidimensional problem in $\Psi - \varphi$ and $\eta - \varphi$ for S, R, and A variables. Interestingly, stretching the cutwater produces a considerable increase of the PaT exploitable head, and shifts the efficiency peaks at lower discharges: by extending the cutwater length from 2 to 4 times, Ψ increases on average by 25 % and 32 % at low and high discharge, respectively. In this way, the flow leans along the cutwater walls, favouring a tangential component at the entrance of the runner.

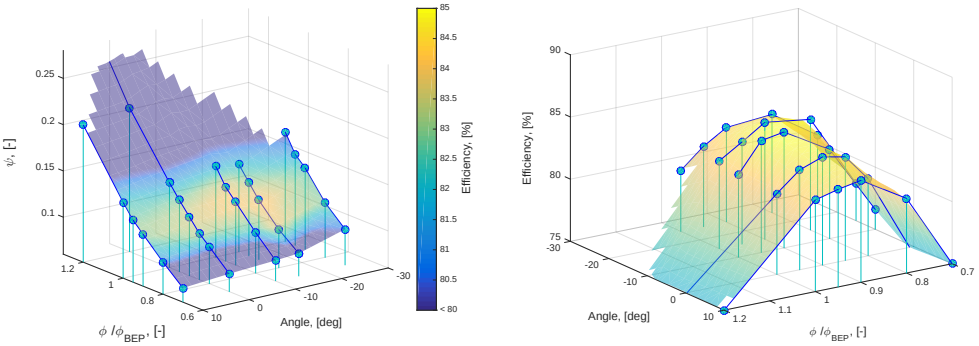

(a) Ψ and η for $S = 2L$ and $R = r/4$

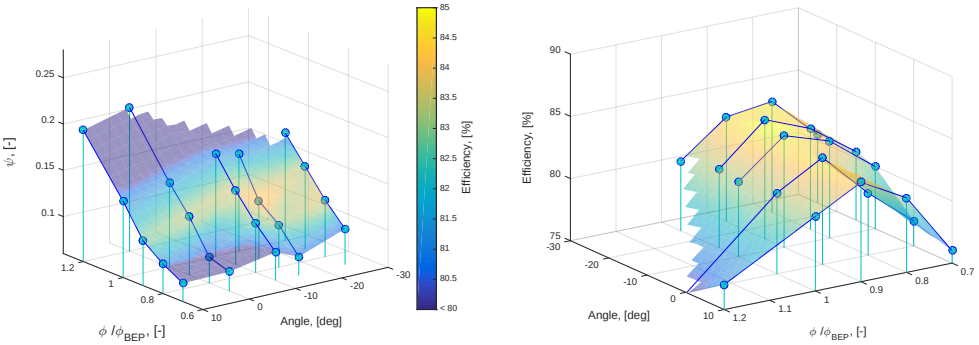

(b) Ψ and η for $S = 2L$ and $R = r/2$

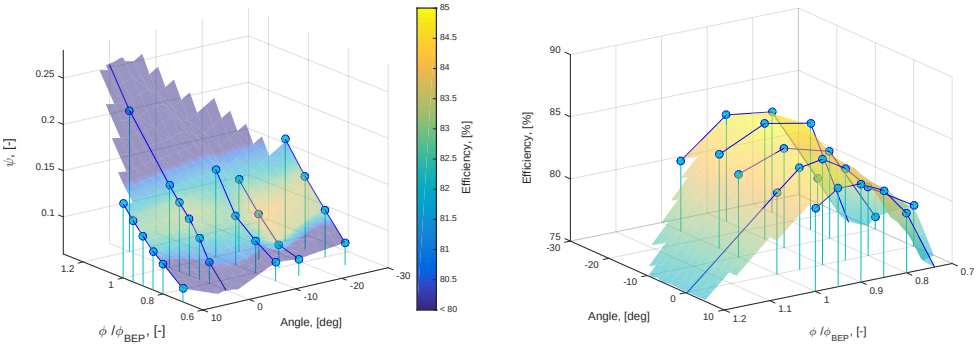

(c) Ψ and η for $S = 2L$ and $R = r$

Figure 5.21: Head and efficiency characteristics for cutwaters with $S = 2L$ as a function of the discharge number and the cutwater angle, A.

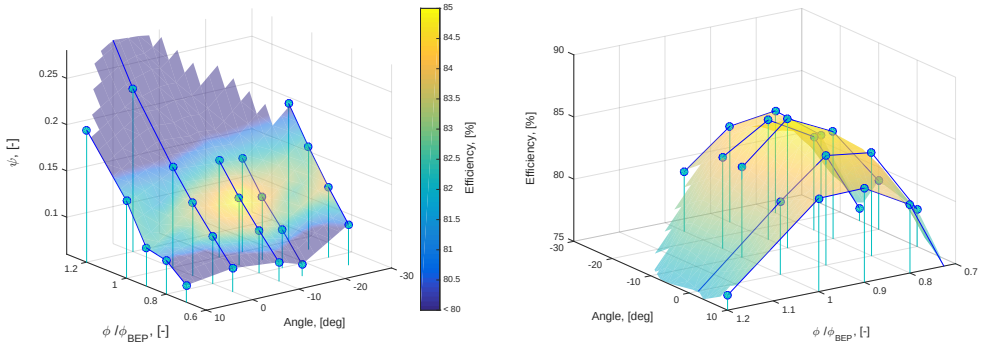

(a) Ψ and η for $S = 3L$ and $R = r/4$

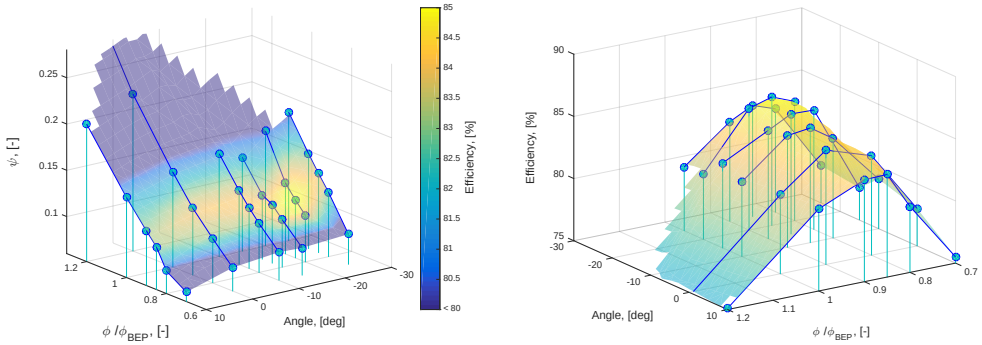

(b) Ψ and η for $S = 3L$ and $R = r/2$

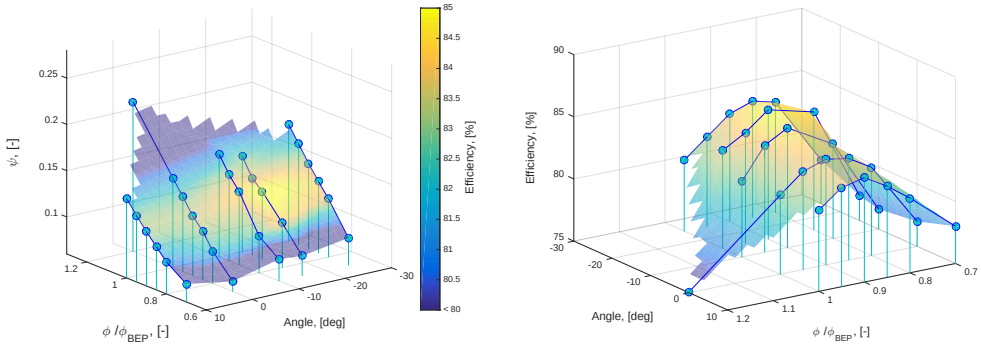

(c) Ψ and η for $S = 3L$ and $R = r$

Figure 5.22: Head and efficiency characteristics for cutwaters with $S = 3L$ as a function of the discharge number and the cutwater angle, A.

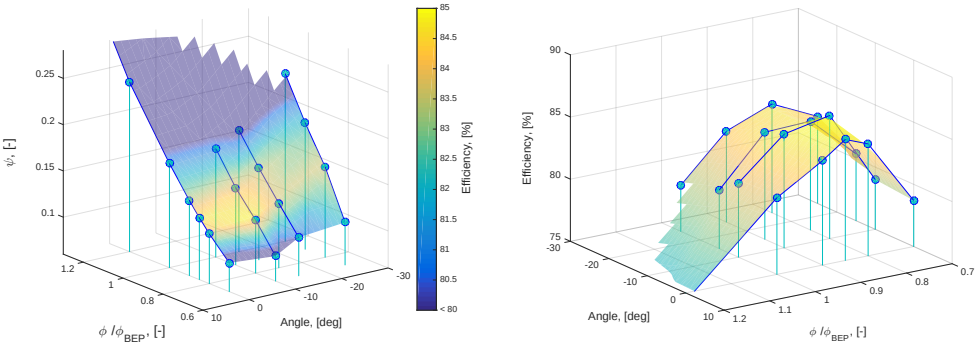

(a) Ψ and η for $S = 4L$ and $R = r/4$

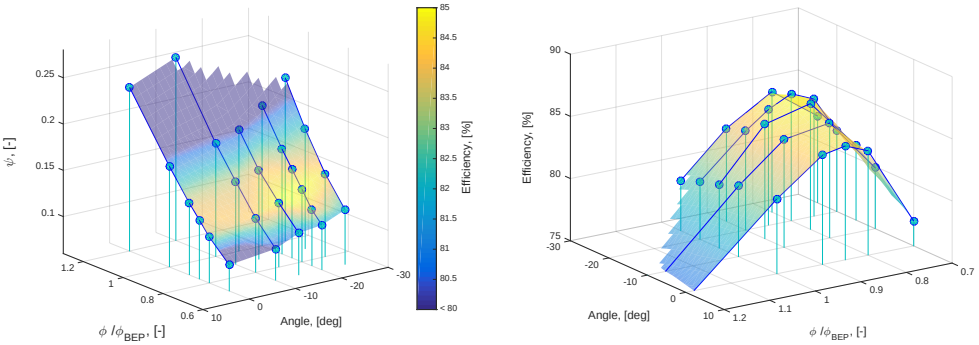

(b) Ψ and η for $S = 4L$ and $R = r/2$

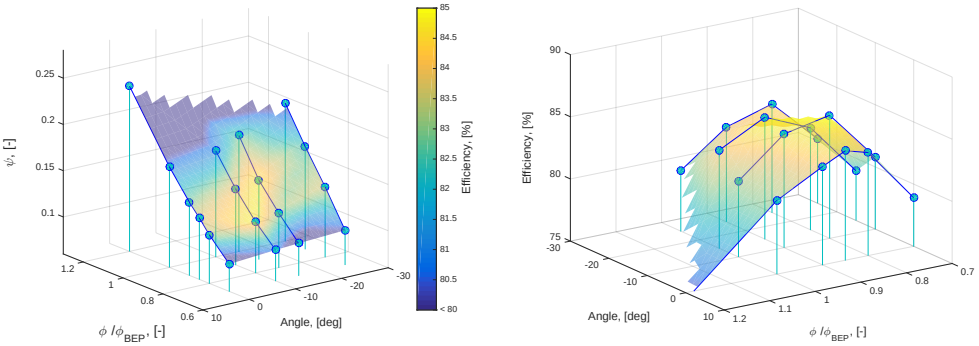

(c) Ψ and η for $S = 4L$ and $R = r$

Figure 5.23: Head and efficiency characteristics for cutwaters with $S = 4L$ as a function of the discharge number and the cutwater angle, A.

Due to the absence of diffuser vanes, the first approximation of α_2 is given by the cutwater incidence [Gulich 2010]. Therefore, in turbine operation, the volute determines the runner absolute flow angle, α_2, which directly affects the theoretical specific energy of the turbine, as expressed in Eq. 5.8.

Furthermore, it is highlighted an excess of negative inclination, A, causes an increase of the specific energy coefficient Ψ, between +0.04 and +0.08 (35-40%) in respect to the baseline characteristics. The water streamlines are stirred towards the outer wall of the volute, by rising considerably the absolute velocity circumferential component c_{2u} but also turbulence. As a consequence, the efficiency drops at high negative inclination ($A = -25$). Positive inclination ($A = +10°$) globally reduces both specific energy and hydraulic efficiency compared with the other analysed tilt angles.

In addition, the cutwater tip thickness, R, has a minor influence on the specific energy coefficient, Ψ, unless the cutwater is characterised by both a large stretch ($S > 3L$) and a high negative inclination angle ($A = -25°$). In these conditions, the head output is inversely proportional to the thickness of the cutwater tip: a sharp rounding as $R = r/4$ produces a 18-20 % raise in head compared to the baseline rounding ($R = r$).

To provide a quantification of the numerical accuracy, the numerical standard deviation of the mass flow balance is given. In Fig. 5.24, the errors computed during the CFD simulations over the discharge unit, φ, are normalized on the BEP of the baseline geometry. From the performance evaluation, it emerges that longer cutwaters than the baseline design pushes the peak of efficiency at lower discharge. Therefore, many tests occur in $0.7 < \varphi/\varphi_{BEP} < 0.9$, where most of the new design BEPs lay and the mass-error drops below 1 %. Finally, simulations at mid-severe partial load report high mass-error but they do not influence the optimization process as an operating condition far from the high performance.

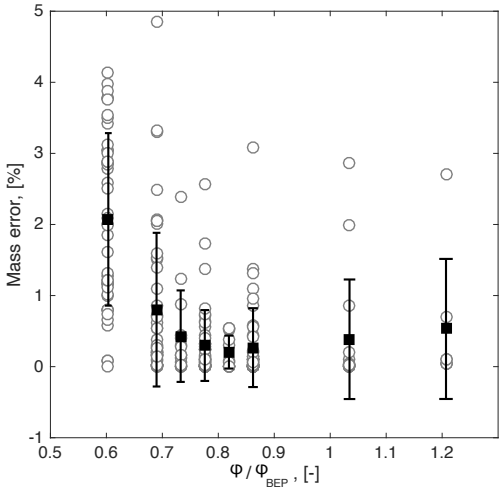

Figure 5.24: Numerical error for mass-flow mismatch between the inlet and outlet over the relative discharge number φ/φ_{BEP} for 224 simulations.

5.4.3 Surrogate model of the PaT hydraulic performance

The surrogate model of the predicted efficiency, $\hat{\eta}_{PAT}$, is built according the formulations expressed in Eq. 5.10. The training data-set to build each surrogate model is obtained by randomly selecting 80 % of the 224 simulated operating conditions and the test data-set is composed by the earmarked 20 % of the samples. The surrogate model $\hat{\eta}_{PAT}$ as a function of the cutwater dimensions and operating points is calculated and detailed in the Table 5.5. The final form of such multivariate regression model has the following arrangement:

$$\hat{\eta}_{PAT} = f(S, R, A, Q_{11}, n_{11}) \tag{5.13}$$
$$\hat{\eta}_{PAT} = intercept + \sum\nolimits_{BF_i \in \Lambda_{MARS}} BF_i$$

where the *intercept* is a constant independent of any variable and Λ_{MARS} is the dominion of all the allowed product combination of the variables in respect of the maximum polynomial degree adopted to produce the basis functions BFs. A quadratic degree of the fitting terms for $\hat{\eta}_{PAT}$ is found satisfactory. However, it includes a cubic expression of $\hat{Q}_{11}$. The complementary definition of $\hat{Q}_{11} = g(S, R, A, n_{11})$ links $\hat{\eta}_{PAT}$ to the constraints of the PaT characteristics. This additional and fundamental bond enables the solution to stick with admissible head-discharge relations for the investigated PaT. In other words, the variables Q_{11} and n_{11} are not independent but their relations must reflect the characteristics curves of the turbomachine under the cutwater modifications, and $\hat{Q}_{11}$ equation guarantees that.

Although including many knots may allow to fit a really good relationship with our training data, it may not generalize very well to new, unseen data [Boehmke & Greenwell 2019]. Consequently, once the full set of knots has been identified, knots that do not contribute significantly to predictive accuracy can be removed. This process is known as *"pruning"* and we can use cross-validation to find the optimal number of knots [Friedman 1991]. This *"pruning"* procedure assesses each predictor variable and estimates how much the error rate was decreased by including it in the model [Kuhn *et al.* 2013, Boehmke & Greenwell 2019]. The GCV score, driver of the *pruning* procedure, is meant to approximate a true cross-validation score by penalizing model complexity. GCV is an estimator of the predictive quality of a model. The reduction of GCV can thus be used as a criterion to optimize the number of selected variables with respect to the predicting the observations. A notable example is the determination of the smoothness parameter in splines. Finally, MARS model delivers for Eqn. 5.13 11 BFs. Similarly, the formulation for $\hat{Q}_{11}$ consists of only 16 enabled terms which are listed in the Table 5.6.

Fig. 5.25 illustrates the histogram of the model prediction error on the test data-set, and it assures the limited misstep of the surrogate model: 90 % of the tested data records an error within ±1 %. Likewise, another test on the $\hat{Q}_{11}$ prediction function is performed and the results confirm the good accuracy of the model (Fig. 5.26). The resulting values of R-squared and GCV are found to be adequate both for the $\hat{Q}_{11}$ constrain function (R-squared = 0.98 and GCV = 0.0002) and for the $\hat{\eta}_{PAT}$ final formulation (R-squared = 0.96 and GCV = 0.9906).

Table 5.5: Basis functions for $\hat{\eta}_{PAT}$ by the variables S, R, A Q_{11}, and n_{11}.

Basis Function, BF	Pruned	Coefficient
(Intercept)	No	84.2996
$h(n_{11} - 81.3415)$	Yes	None
$h(81.3415 - n_{11})$	No	0.917686
$Q_{11} * h(81.3415 - n_{11})$	No	-3.0256
$h(Q_{11} - 0.451706) * h(n_{11} - 81.3415)$	No	8.12082
$h(0.451706 - Q_{11}) * h(n_{11} - 81.3415)$	No	-4.7669
$h(n_{11} - 84.1156) * h(n_{11} - 81.3415)$	No	-0.0134891
$h(84.1156 - n_{11}) * h(n_{11} - 81.3415)$	Yes	None
$n_{11} * h(81.3415 - n_{11})$	Yes	None
$S * h(n_{11} - 81.3415)$	No	0.00384514
$h(Q_{11} - 0.408705)$	Yes	None
$h(0.408705 - Q_{11})$	Yes	None
$A * h(n_{11} - 81.3415)$	No	-0.00216247
$h(Q_{11} - 0.412572) * h(Q_{11} - 0.408705)$	Yes	None
$h(0.412572 - Q_{11}) * h(Q_{11} - 0.408705)$	No	290637
$A * h(Q_{11} - 0.408705)$	No	-1.27544
$S * h(Q_{11} - 0.408705)$	Yes	None
$n_{11} * h(Q_{11} - 0.408705)$	No	-0.439592
$h(n_{11} - 75.4268) * h(81.3415 - n_{11})$	Yes	None
$h(75.4268 - n_{11}) * h(81.3415 - n_{11})$	No	-0.0109386
$A * h(0.408705 - Q_{11})$	Yes	None

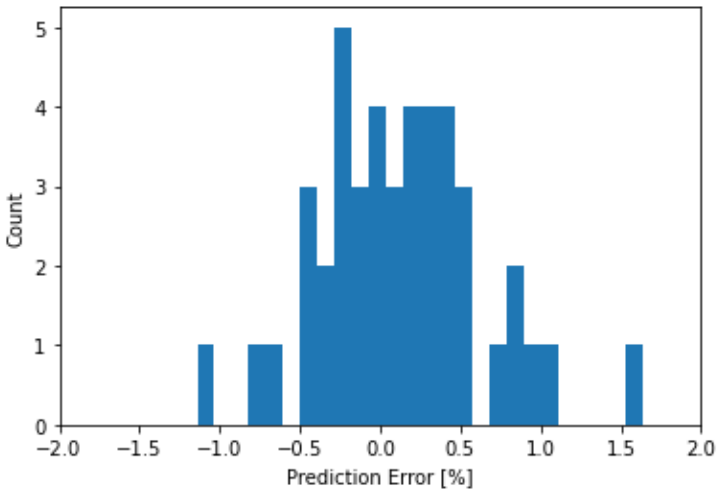

Figure 5.25: Test model accuracy for $\hat{\eta}_{PAT} = f(S, R, A, Q_{11}, n_{11})$.

Table 5.6: Basis functions for $\hat{Q}_{11}$ by the variables S, R, A, and n_{11} for third degree maximum fit spline.

Basis Function	Pruned	Coefficient
(Intercept)	No	0.497193
A	No	0.000802073
S	No	-0.00603202
R	Yes	None
$h(n_{11} - 106.309) * S$	No	0.000183678
$h(106.309 - n_{11}) * S$	Yes	None
$A * h(106.309 - n_{11}) * S$	No	5.99249e-06
A^2	No	0.00014047
A^3	No	5.7401e-06
$R * A$	Yes	None
$h(n_{11} - 102.63)$	No	-0.00411946
$h(102.63 - n_{11})$	Yes	None
$n_{11} * R$	Yes	None
$h(n_{11} - 96.0777) * h(102.63 - n_{11})$	Yes	None
$h(96.0777 - n_{11}) * h(102.63 - n_{11})$	Yes	None
$S * n_{11} * R$	No	-1.3619e-07
$A * h(102.63 - n_{11})$	No	-5.27589e-05
$S * R * A$	No	-6.76829e-07
$R * A^2$	No	-8.57713e-07
$S * A * h(102.63 - n_{11})$	No	-4.80337e-06
$A * h(n_{11} - 96.0777) * h(102.63 - n_{11})$	Yes	None
$R^2 * n_{11}$	No	9.76616e-08
$R * S$	Yes	None
$S^2 R$	Yes	None
S^2	No	0.000152352
S^3	No	-1.27029e-06

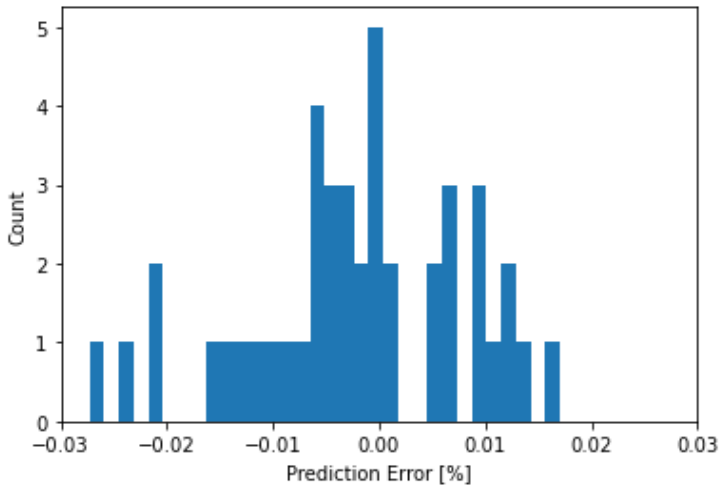

Figure 5.26: Test model accuracy for $\hat{Q}_{11} = g(S, R, A, n_{11})$.

5.4.4 Optimal cutwater design

An optimal solution is retrieved by solving Eq. 5.11 for multiple value of the variable n_{11}. At fixed n_{11}, a multi-start technique is coupled to the optimization problem. Thousands different variable assets are used as initial points in solving Eq. 5.11. Without this diversification, such methods can become localized in a small area of the solution space, eliminating the possibility of finding a global optimum [Tu & Mayne 2002]. In Table. 5.7, the efficiency values of the optimal geometry conditions found by solving the optimization problem are highlighted for different n_{11} values.

The PaT predicted peak of efficiency is found at $n'_{11} = 84.303$, corresponding to a set of variable geometry undoubtedly alike to most of the evaluated speed number: $S_{opt} = 3.54L$, $R_{opt} = r$ and $A_{opt} = -15°$. Such optimal geometrical asset for the cutwater in reverse mode is defined as Λ_{opt}. The resulting optimized geometry has been simulated and the following relative errors shows the modest discrepancy between the prediction and the simulations outputs of the optimal cutwater design:

$$\begin{aligned} \Delta\varphi &= \frac{\hat{\varphi} - \varphi_{opt}}{\hat{\varphi_{opt}}} = 0.01877 \\ \Delta\Psi &= \frac{\hat{\Psi} - \Psi_{opt}}{\hat{\Psi_{opt}}} = -0.07833 \\ \Delta\eta &= \frac{\hat{\eta} - \eta_{opt}}{\hat{\eta_{opt}}} = -0.00478 \end{aligned} \tag{5.14}$$

where $\hat{\varphi}, \hat{\Psi}, \hat{\eta}$ are the predicted values by the surrogate model and $\varphi_{opt}, \Psi_{opt}, \eta_{opt}$ are the results obtained by the numerical simulation on the Λ_{opt} geometry asset.

Fig. 5.27 compares the PaT characteristics curves with the baseline cutwater and the optimized geometry. Although the BEP moves to 13.0 % smaller discharge,the updated PaT cutwater records a raise in head by +7.5 % and the final gain in hydraulic efficiency is $\eta_{opt} - \eta = +3.9$. Therefore, significant improvements of the efficiency are reported at lower discharge in the broad range of $\varphi/\varphi_{BEP} = 0.6 - 0.9$, while the geometry update equalizes the baseline design for larger discharge values ($\varphi/\varphi_{BEP} > 1$).

Table 5.7: Predicted optimal cutwater geometry and the resulting efficiency by varying n_{11}.

n_{11} [-]	S [mm]	R [mm]	A [deg]	$\hat{Q}_{11}$ [-]	$\hat{\eta}$ [%]
110.378	60.40	65.0	-18.36	0.4364	79.00
103.250	56.67	65.0	-15.60	0.4107	80.91
97.345	56.25	65.0	-14.93	0.4107	83.33
92.349	55.94	65.0	-14.81	0.4106	84.68
88.051	55.63	65.0	-14.80	0.4106	85.32
84.303	55.11	65.0	-15.14	0.4106	85.48
80.996	24.21	60.0	-24.22	0.3435	84.12

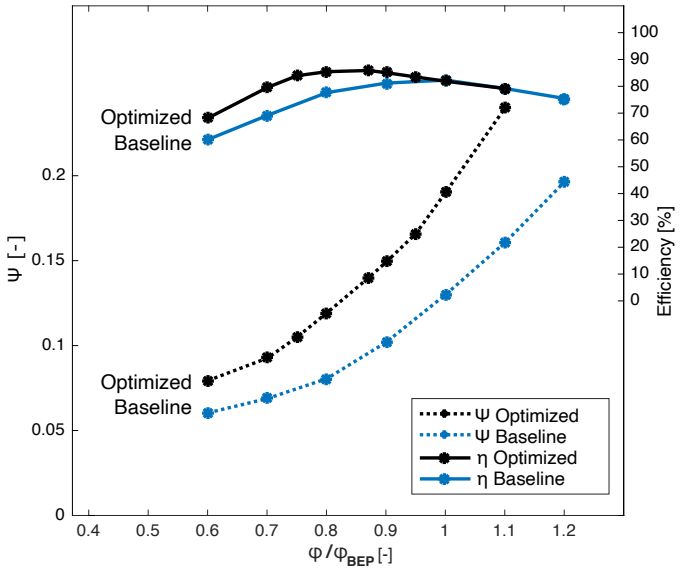

Figure 5.27: Ψ and η of the baseline and optimal cutwater designs at N_{PAT}.

In common hydraulic turbines, guide vanes are used to regulate the discharge and to impart a degree of swirl to the flow determined by the needs of the runner. Similarly, the water flow from the PaT inlet could be deflected by the cutwater towards a tangential direction and improve the efficiency. In the PaT baseline design, this deviation is not sufficient and an unbalanced water distribution occurs near the R/S gap. In this way, pump in reverse mode experiences a non-uniform speed and pressure profiles along the leading edge of the runner, generating local flaws in the velocity field in the cutwater area.

A cut-view of the optimal cutwater asset at mid-flow span is given in Fig. 5.28. The flow fields for high discharge ⓐⓑ, at their relative BEP conditions ⓒⓓ, and for low discharge ⓔⓕ are compared. In all the operating conditions of the PaT with the optimal cutwater, the flows appear to be slowed down upstream the cutwater and shifted to a circumferential direction. This path alteration dismisses the typical flow stall-area at the tip of the cutwater of baseline design that spoils the PaT hydraulic efficiency by generating flow separation and 3D turbulence.

In Fig. 5.29, two charts illustrate the static pressure profiles along the mid-flow arc length of the R/S half interface close to the cutwater for both cases. For the baseline geometry, a local velocity flaw occurs at the rotor inlet and it reflects in a static pressure spike beneath the cutwater. A dashed line indicates the x-coordinate of the tip of the cutwater (the orientation of the axes of the coordinate system is referenced to the one presented previously in Fig. 5.2). For the optimized geometry, any significant pressure perturbation is noted close to the cutwater nor elsewhere on the R/S interface.

In the contour plots, the pressure coefficient Cp, defined as in Eq.5.15, shows the effect of the new cutwater length and angle in dissipating this pressure peak on

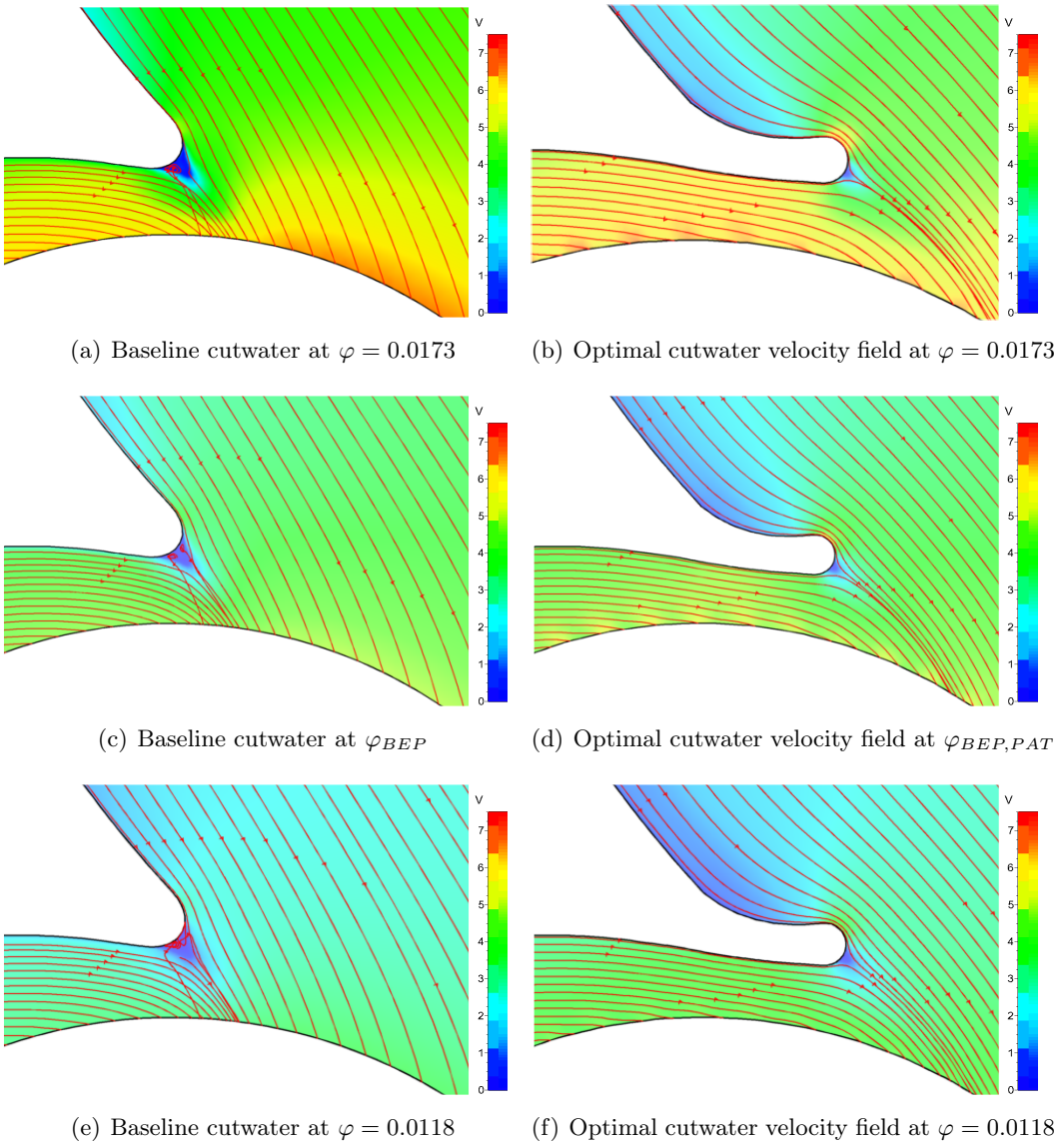

(a) Baseline cutwater at $\varphi = 0.0173$

(b) Optimal cutwater velocity field at $\varphi = 0.0173$

(c) Baseline cutwater at φ_{BEP}

(d) Optimal cutwater velocity field at $\varphi_{BEP,PAT}$

(e) Baseline cutwater at $\varphi = 0.0118$

(f) Optimal cutwater velocity field at $\varphi = 0.0118$

Figure 5.28: Velocity streamline and velocity magnitude [m/s] contour for the baseline geometry and the optimal asset at different discharge number

the rotor/stator interface by transferring radial flow into circumferential flow.

$$Cp = 2\frac{P - P_{inlet}}{\rho V_{inlet}^2} \tag{5.15}$$

The balanced Cp obtained in the optimized design underlines the advantage of increasing the flow circumferential component. The pressure peaks and deeps are deleted on the totality of the flow span before the impeller inlet $z = [-0.03, 0.03]$.

To validate the new incidence distribution at the runner inlet generated by the new design, the absolute velocity angle is compared to the volute mid-flow plan

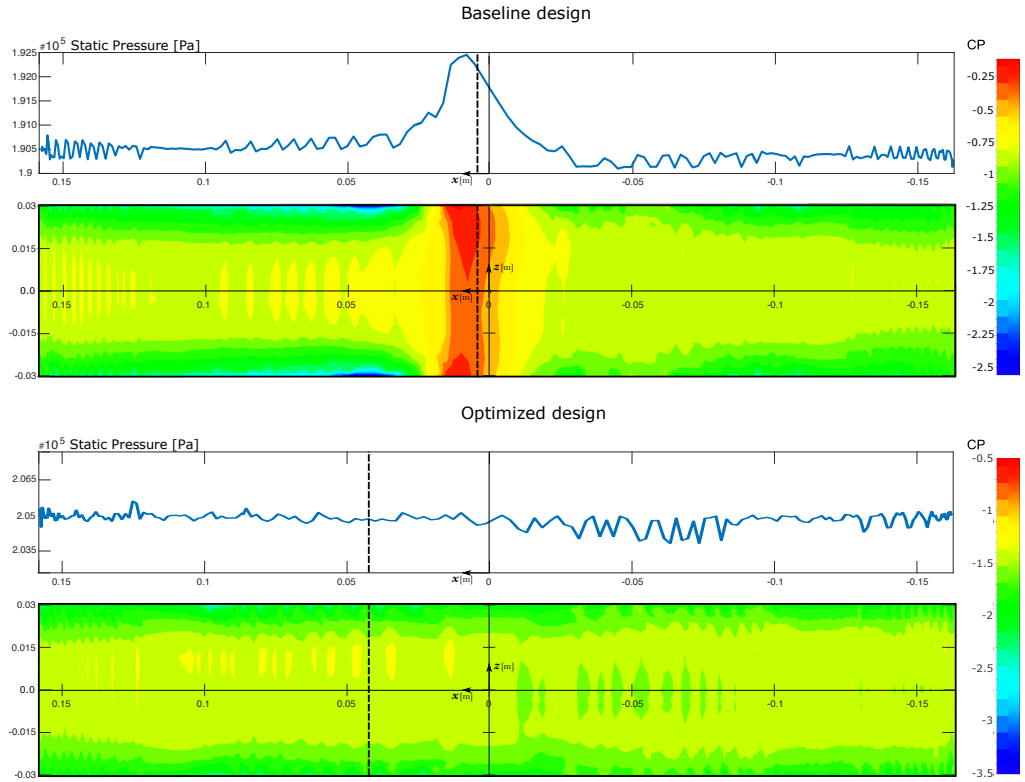

Figure 5.29: Static pressure profiles at mid-flow span and Cp contour for the rotor/stator interface in both baseline and optimized cutwater geometry.

across the volute at $\varphi/\varphi_{BEP} = 1$ (Fig. 5.30). A shorter cutwater corresponds to smaller flow deviation, allowing for a higher value of radial velocity in the near-cutwater region and higher turbulence on the runner inlet. Over an arc of 28°, the absolute velocity angle α_2 overpasses 0.75 rad at the mid-span flow before the runner inlet, raising the averaged value at the R/S interface to 0.48 rad in the baseline design. In the optimized design, the averaged value of α_2 is 0.28 rad.

Concerning the distribution of turbulent kinetic energy, k, the region with a high intensity involves the core flow in the volute for the baseline design and the volute outer wall surface of volute for the optimized design Fig. 5.31. For both cases, the highest gradients of k in the flow field are concentrated downstream the cutwater. Here, a peak of water turbulent kinetic energy occurs and indicates that the flow is relatively complex and with stronger velocity fluctuations. However, in the optimized solution the cutwater improves the turbulence kinetic energy distribution stability in the mid-flow, where k is reduced to near zero, and clearing the passage towards the runner inlet.

The flow models in the volute need to be extended into a three-dimensional overview to detect a comprehensive development of the flow path. A comparison of the BEP velocity vector profiles is given by Fig. 5.32 and Fig. 5.33. The velocity mag-

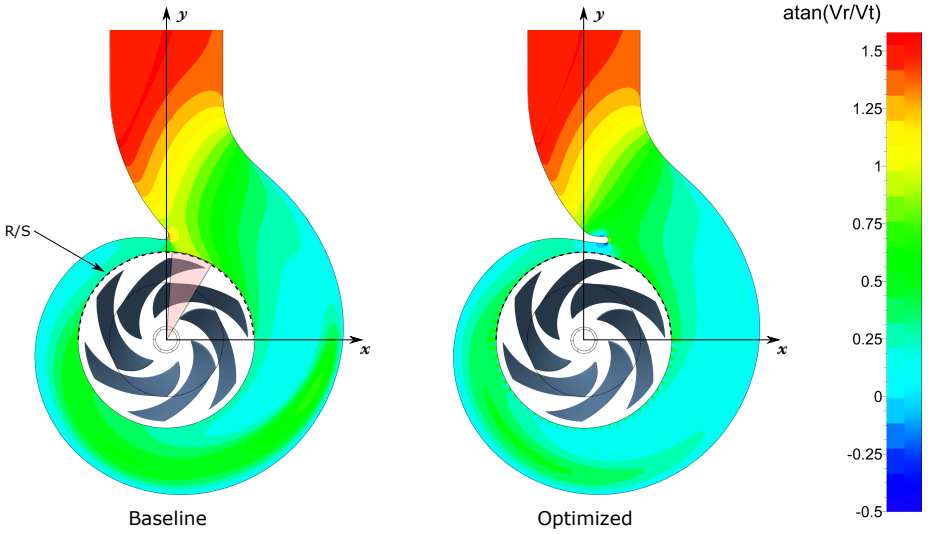

Figure 5.30: Contours of the absolute velocity angle [rad] across the volute cut-view and on the R/S used in Fig. 5.29.

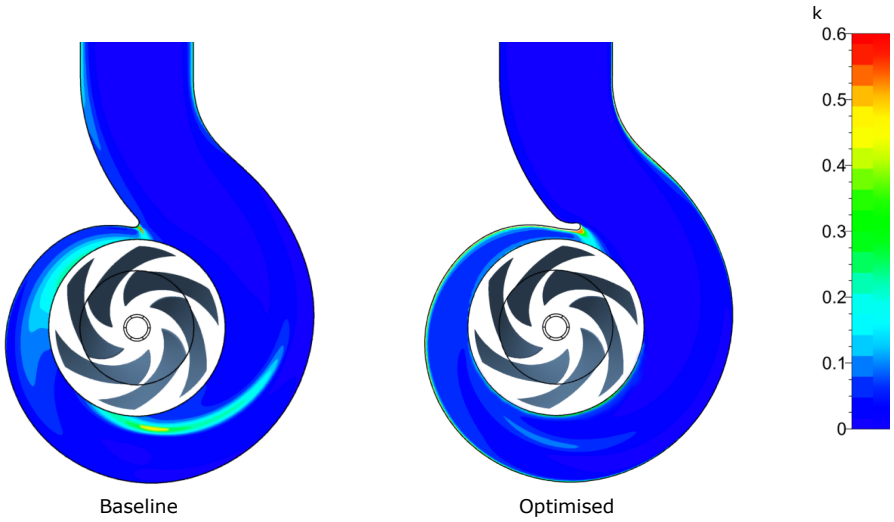

Figure 5.31: Contours of the turbulence kinetic energy k distribution [m^2/s^2] across the volute cut-view.

nitude [m/s] at the entrance of the volute is different among these two cases because the BEP for Λ_{opt} design lays at lower discharge than the baseline ($\varphi/\varphi_{BEP} = 0.87$). This distinction is confirmed by the colour map of the first volute cross-section in the aforementioned figures (sections A and B). However, the optimized geometry records a higher momentum at the R/S interfaces. The turbulence patterns are thus significantly different in the two cases. This is also demonstrated by how pressures and velocities are distributed uniformly in the optimized geometry while two strong symmetric vortices are clearly visible in the baseline case and defect the volute global performance.

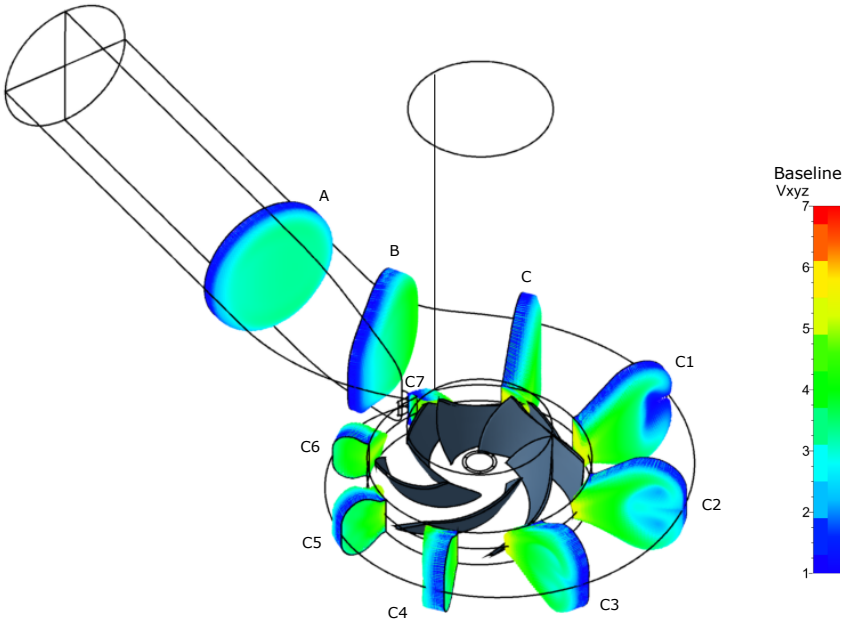

Figure 5.32: 3D overview of the absolute velocity vector profiles [m/s] in the baseline geometry.

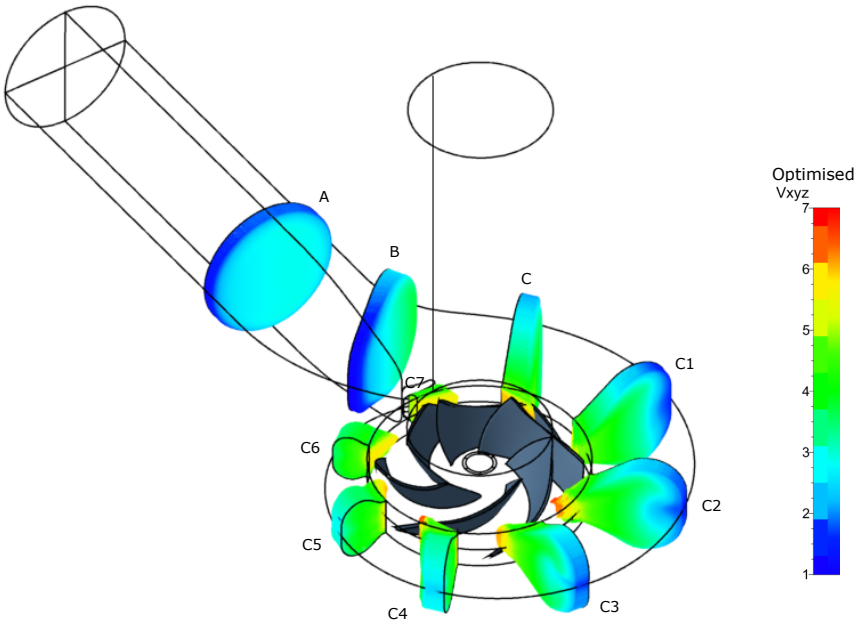

Figure 5.33: 3D overview of the absolute velocity vector profiles [m/s] in the optimized geometry.

The magnitude of the *vorticity* vector is represented in Fig. 5.34 for eight cuts of the volute (from C to C7), where

$$Vorticity = rot \times \vec{V} \tag{5.16}$$

The vorticity of a vector field captures the idea of how the fluid may rotate. The baseline geometry develops two intense swirls by a more extensive arc in the volute than in the optimized case. Various factors like initial curvature, the shrinking of the circular area of the spiral casing, the no-slip condition along the walls and a single opening to the rotor are some important parameters that affect the generation of secondary flow [Tao *et al.* 2019]. At the start of the casing (section C), the fluid flows evenly along the height of the casing. Due to an imbalance between the radial pressure gradient and the centrifugal force, secondary flow occurs as twin vortexes at the outer side of the volute: this happens early for the baseline geometry (from cross-section C1) than the optimized case (from cross-section C2). Indeed, the flow that accesses to the core of the volute with uneven distribution results in a higher static pressure gradient, as for the baseline case where the bulk of the fluid circulates mostly in the inner side of the casing (Fig. 5.32-sections C1 and C2). The strength of the vorticity changes from one cross-section to another, reaching its maximum at cross-section C4, at which point the vortexes are losing intensity. The vortexes disappear at cross-section C6 for both cases (Fig. 5.34).

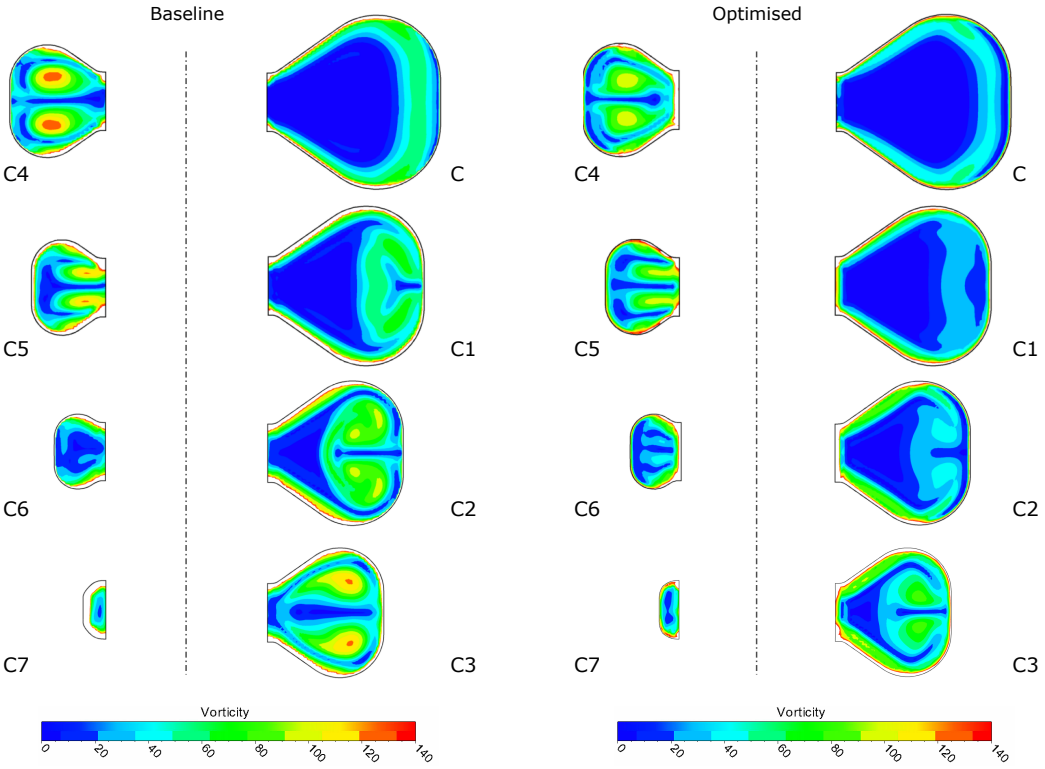

Figure 5.34: Through-flow vorticity contours over the volute cross-sections at BEP for the baseline and optimized geometry.

5.4.5 Unsteady verification of the PaT optimum

After the validation of the numerical model with the experimental results related to the PaT operating in turbine mode, the accuracy of the RANS simulated performance of the optimal geometry is compared by using the same asset in URANS simulations. In turbomachinery applications, time-averaging the results of a transient simulation is not necessarily equivalent to solving the steady-state model due to the rotor-stator interface effects. Fig. 5.35 shows the comparison between the RANS and URANS results of the PaT operating in turbine mode. The coloured areas of the unsteady simulations illustrate the minimum and maximum values of the results during an oscillation of a period.

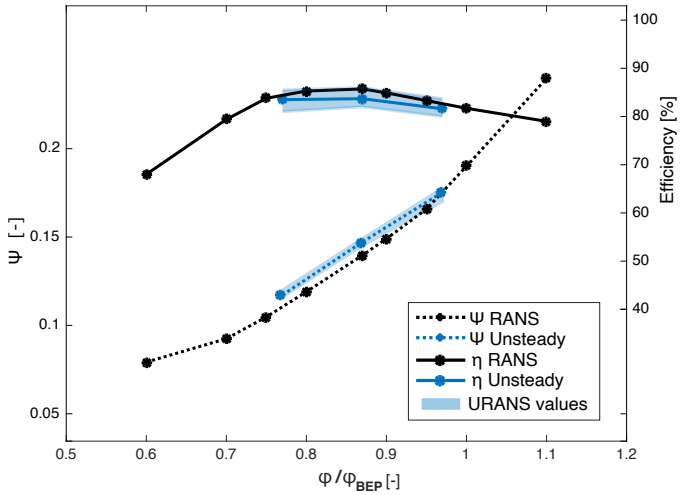

Figure 5.35: RANS and URANS characteristics of Λ_{opt} in PaT mode.

Different stations at mid-span are selected to report the variation of the α_2 during a complete rotation of the runner (360°). Alike sine waveforms of α_2 are recorded during the unsteady simulations, but with the same frequency. The peaks occur at the blade passage that produces momentary flow blockages. For this reason, the pairs at opposite locations are in phase but their amplitude changes along the volute. Fig. 5.36 describes the URANS α_2 fluctuations and it compares them with the results obtained for the same points in RANS analysis, represented in dashed lines. In the same way, other five stations are spread along the one blade passage. The results are plotted in Fig. 5.37. Table 5.8 reports the α_2 values of the steady state and the averaged value under a full period for unsteady simulations. Along with them, the relative differences, where the URANS results are taken as reference.

For sake of completeness, an overview of the absolute velocity angle of the steady state case and frames of the unsteady solutions at different time steps t is presented at the mid-span of the numerical domain. In Fig. 5.38 shows the comparisons of α_2 at $\varphi/\varphi_{BEP} = 0.87$, namely the PAT BEP. Four time steps are illustrated and precisely at $t = [0 + \theta], [1/4\theta + \theta], [1/2\theta + \theta]$, and $t = [3/4\theta + \theta]$ where θ is the blade passage period that corresponds to 60°. In the same way, a comparison at $\varphi/\varphi_{BEP} = 0.77$ and at $\varphi/\varphi_{BEP} = 0.97$ is produced in Fig. 5.39-5.40.

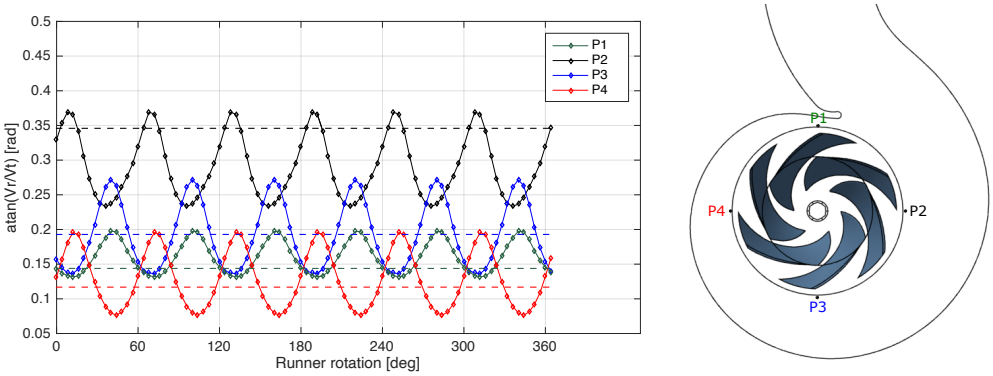

Figure 5.36: URANS α_2 fluctuations in points P1, P2, P3, and P4. The coordinates (x, y) of stations exhibited in Figure are as follows: P1(0, 0.162), P2(0.162, 0), P3(0, -0.162), and P4(-0.162, 0).

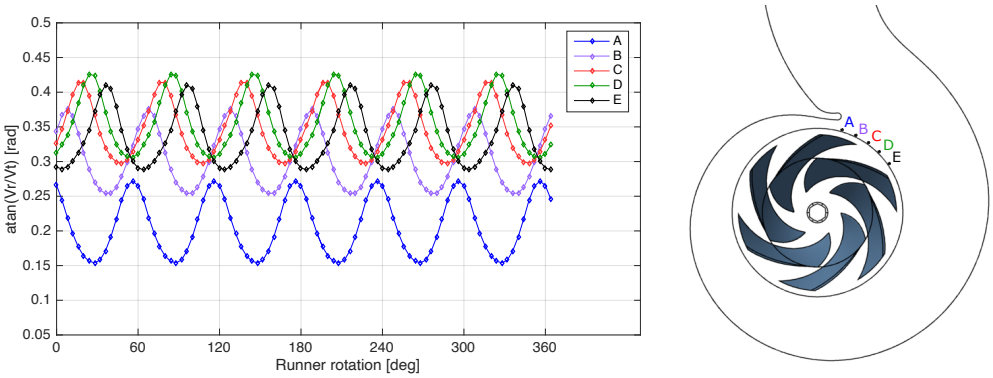

Figure 5.37: URANS α_2 fluctuations in points ad different span angles as in A(0°), B(12°), C(24°), D(36°), and E(48°).

Table 5.8: Divergence of the absolute velocity angle α_2 in RANS and URANS.

Station	RANS	URANS-AV	$\Delta\alpha_2$	Station	RANS	URANS-AV	$\Delta\alpha_2$
P1	0.144	0.159	-9.4%	A	0.205	0.206	-0.4%
P2	0.322	0.293	10.0%	B	0.383	0.309	23.9%
P3	0.193	0.191	1.0%	C	0.429	0.346	24.0%
P4	0.117	0.129	-9.3%	D	0.434	0.353	22.9%
				E	0.396	0.339	16.8%

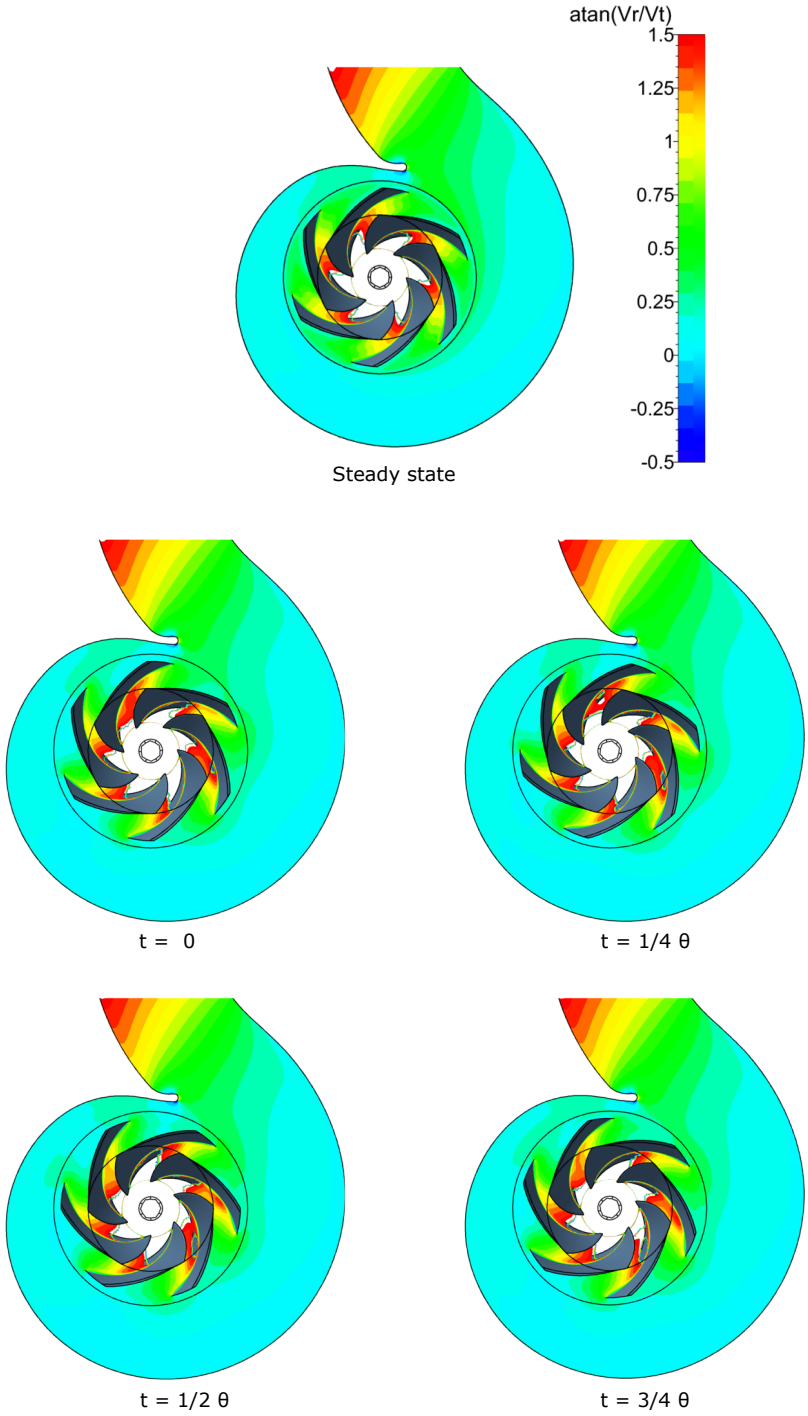

Figure 5.38: Comparison of α_2 for steady and unsteady states at $\varphi/\varphi_{BEP} = 0.87$.

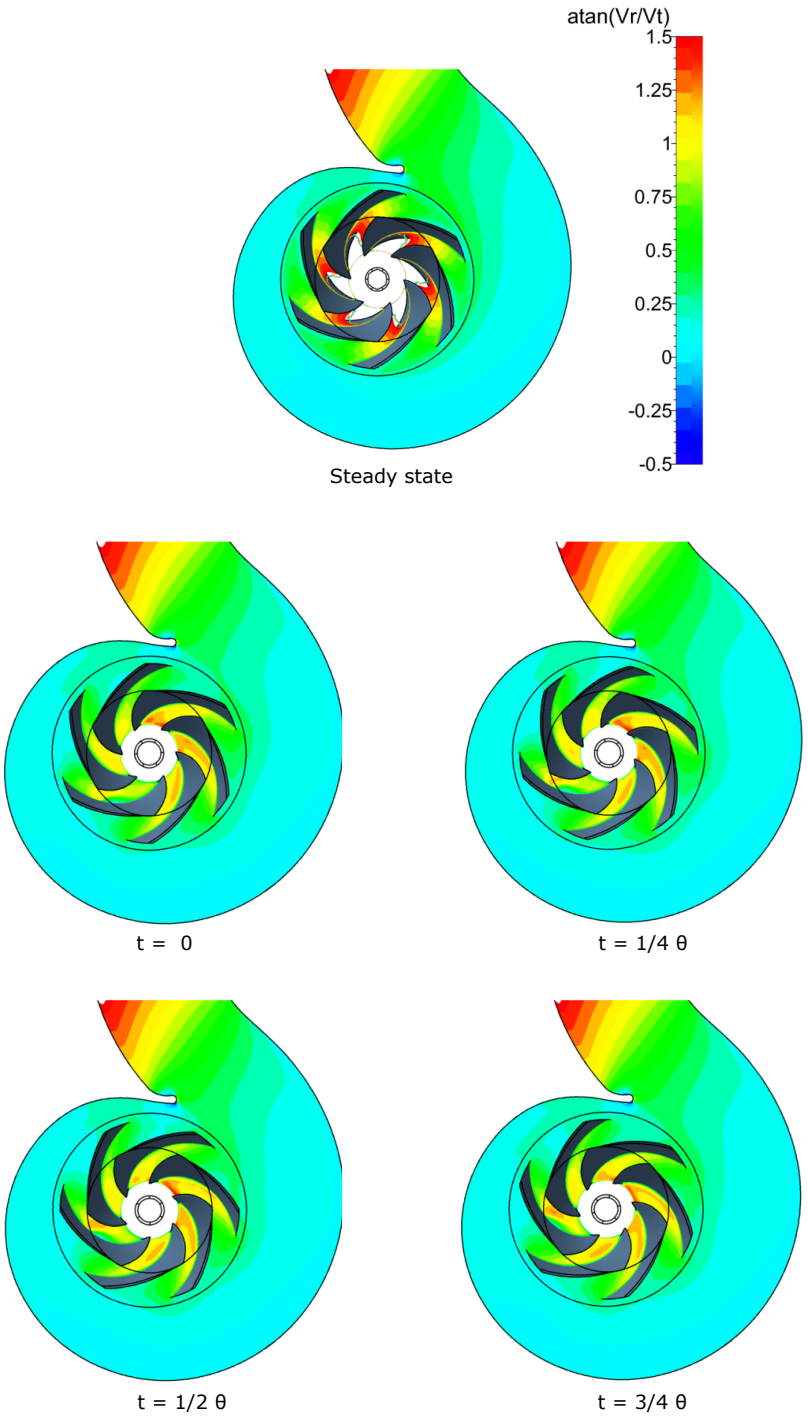

Figure 5.39: Comparison of α_2 for steady and unsteady states at $\varphi/\varphi_{BEP} = 0.77$.

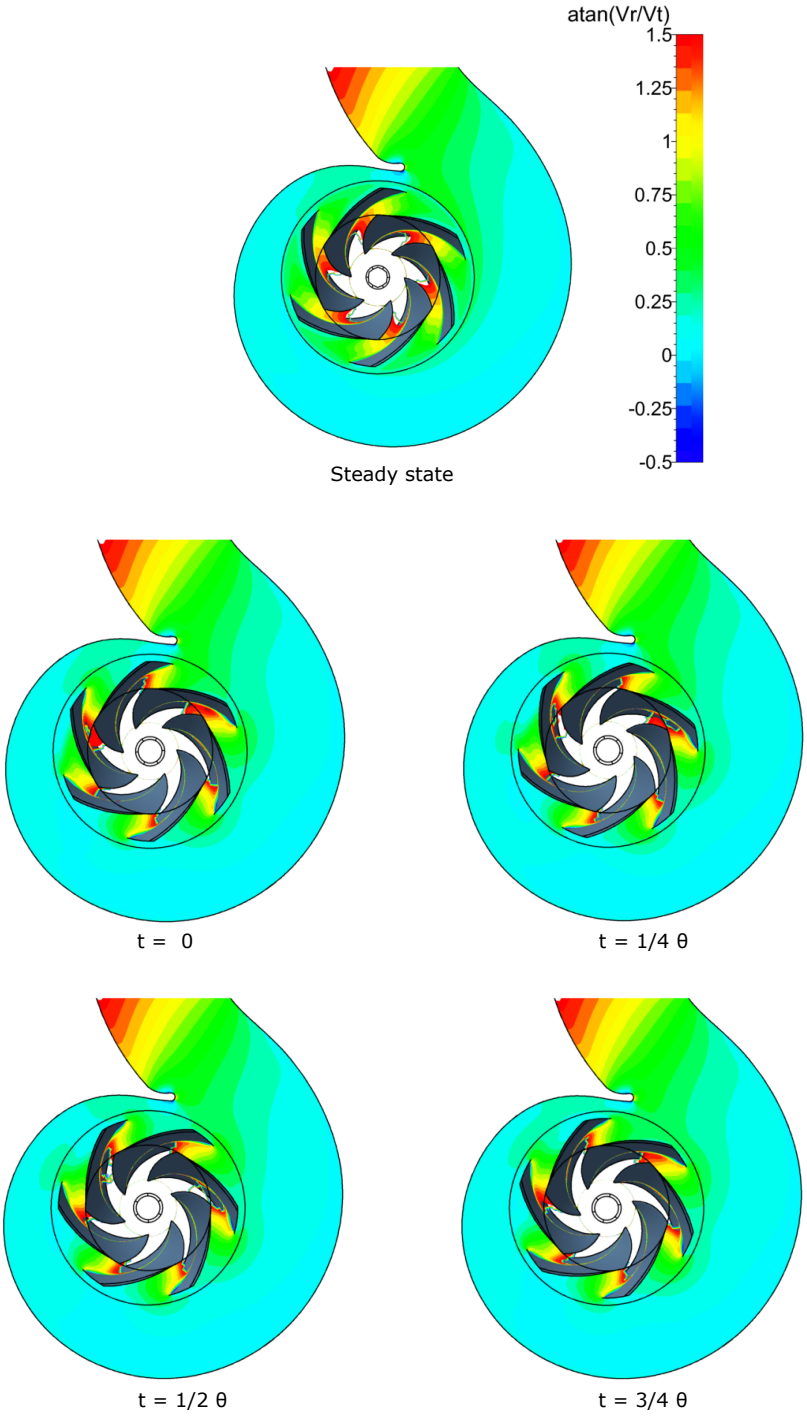

Figure 5.40: Comparison of α_2 for steady and unsteady states at $\varphi/\varphi_{BEP} = 0.97$.

5.4.6 Development of speed adjustment

The cutwater design generated by the solution of the optimization problem has improved the hydraulic efficiency and altered the PaT characteristics from its initial condition (Fig. 5.27). Although the performance is enhanced, this new PaT design would not satisfy the requirements of the starting duty point. This inconvenience could be solved by selecting another centrifugal pump that respects the assignments given for the site, as shown by the turbomachine decision tree in 4.10, considering this time the changes in the characteristics by the optimisation results.

Coupling the PaT-motor group with a VFD is another solution to this latest mismatch between the precedent (baseline) and new (optimized) working conditions. Re-positioning the optimized BEP coordinates to meet the original required head is possible by operating at different rotational speed. Rotational speed adjustments are commonly used to deal with variable load: varying the shaft speed allows to accommodate flow angles which result in higher performances [Mercier *et al.* 2019, Pérez-Díaz *et al.* 2015, Chazarra *et al.* 2018, Marchi & Simpson 2013]. As per the similarity laws, the non-dimensional parameter Psi obtained at different speeds shall collapse on a quadratic expression [Jain *et al.* 2015].

Fig. 5.41 shows that Ψ and η curves distinctly converge for both optimized and baseline cases. The PaT with the original geometry have been simulated for $\Omega = [0.85, 1.28]$ and the optimized within $\Omega = [0.85, 1.14]$, where $\Omega = N/N_{PAT}$. A quadratic polynomial fits the data for the specific energy coefficient by the least squares method (R-squared equals 0.9733), whereas a cubic regression returns the best fit for η. However, there are some deviations in the η curve fit by the Ω speed ratio (R-squared equals 0.8365). This may be due to the fact that the similarity laws are basically an approximation, based on the assumption of geometrical and dynamic similarity between the PaT working under different conditions

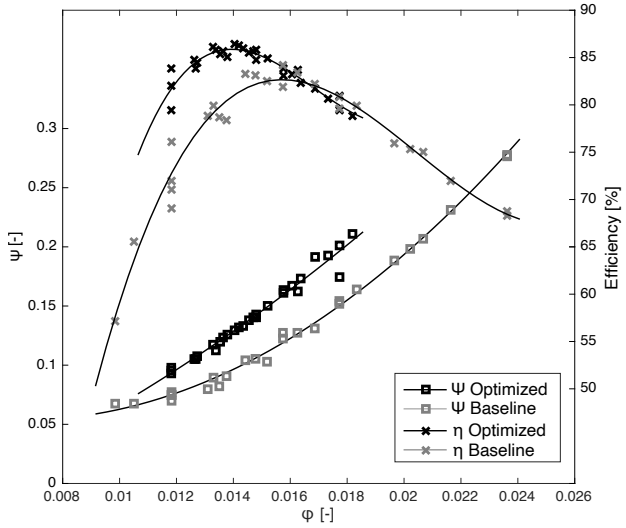

Figure 5.41: PaT performances with the baseline and optimal cutwater designs for $\Omega = [0.85, 1.28]$.

[Jain *et al.* 2015, Tahani *et al.* 2020]. The deviations may also be due to the different losses distribution by the flow. These losses also define the upper and lower hydrodynamic limits of the use of variable speed. When passing at high discharge in a convergent channel (as in a pump in reverse mode), the friction losses are more accentuated and cause the upper hydrodynamic bond on maximum rotational speed for turbomachines [Brennen 1994]. Nonetheless, substantial losses are due to shock losses at low discharge [Chapallaz *et al.* 1992], thus low rotational speed for PaTs are not recommended.

Finally, the divergences of the performances at variable speed, albeit modest, are shown in Fig. 5.42. Here, a zoom-in of the PaT yield illustrated in Fig. 5.41 describes the efficiency curves over the dimensionless discharge number and they are branched by the rotational speed ratio Ω. At this point, the effect of the speed variation (± 14 %) is traceable and the following regression equation describes the BEP efficiency line depending by φ and Ω:

$$\eta_{BEP} = a_1\varphi + a_2 + a_3\Omega \tag{5.17}$$

with the coefficients equal to $a_1 = 79.45, a_2 = 80.54$ and $a_3 = 4.22$, R-squared $= 0.959$ is obtained. According to the analysis of the PaTs performance at different rotational speed, corrections on the similarity law can be made in $a\left(\frac{N}{N_{ref}}\right)^b$ form by Eq. 5.18. Moreover, a new formulation can be computed and applied to predict the hydraulic efficiency by Eq. 5.19.

$$\begin{aligned} Q/Q_{ref} &= 0.984\,\Omega^{0.958} \\ H/H_{ref} &= 0.970\,\Omega^{1.920} \end{aligned} \tag{5.18}$$

$$\eta/\eta_{ref} = -0.047\,\Omega^2 + 0.1521\,\Omega + 0.8951 \tag{5.19}$$

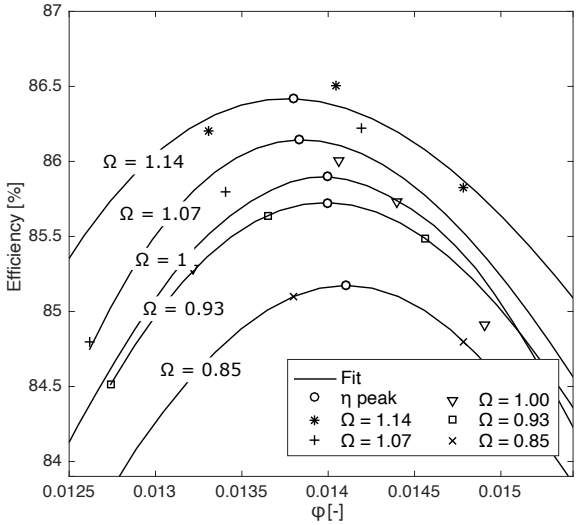

Figure 5.42: Detail of the PaT efficiency in Fig. 5.41 for the optimized geometry under speed variations Ω.

According to these correlations, a rotational speed adjustment by 2% (i.e. -15 rpm) allows reducing the available head from the H_{opt} to the initial baseline value, as such $H/H_{ref} = 1/1.075$. The efficiency peak would be predicted according to Eq. 5.19 and it is corrected by a factor $\eta/\eta_{ref} = 0.998$. Re-positioning the optimized BEP coordinates to meet the original required discharge rate requires a more significant speed variation. However, the effect of varying speed in turbine mode is different from the well-known effects in pump mode: while the variations in pump mode show a tendency to shift the head/flow curve in a direction approximately perpendicular to the curve [Chapallaz *et al.* 1992], in the turbine mode, each curve forms almost a continuation of the curve at a different speed (Fig. 4.23). Eventually, Eq. 5.18 predicts for $Q/Q_{ref} = 1/0.87$ a rotational speed raise of 17% and an efficiency improvement of $\eta/\eta_{ref} = 1.008$.

5.4.7 Pump performance

In the perspective of the studied turbomachine, that can work in both normal and inverse operations, additional investigation is carried out to assess the influence of the cutwater modifications on the pumping performance. During the normal operation of the pump, volute width and diameters play an important role in the definition of the discharge flow [Japikse *et al.* 1997, Lazarkiewicz & Troskolanski 1965]. One of the most important variables in casing design is the throat area, marked by the cutwater location. This area, together with the impeller geometry at the periphery, establishes the pump capacity at the best efficiency point. The throat area should be sized to accommodate the capacity at which the utmost efficiency is required [Lobanoff & Ross 2013].

Fine and limited modifications of the cutwater do not usually transfer relevant effects on the global efficiency as much the abrupt bend in the exit passage as stated in Section 5.3.2.2 (Fig. 5.6). However, substantial modifications could affect the volute capacity and hydraulic losses. Frequently, the throat area is small enough to act as a throttle and reduce the maximum flow rate otherwise obtainable from the pump impeller [Karassik *et al.* 2001]. Cutting back the tongue increases the throat area and increases the maximum flow rate; shortening the discharge nozzle may increase the diffusion losses a little and result in a lessened efficiency [Japikse *et al.* 1997, Karassik *et al.* 2001].

The CFD post-processing analysis of the pump in normal operation provides insights on the hydrodynamic phenomena for the cutwater modifications. The pump with the baseline cutwater defines the benchmark for the performance alteration given by the cutwater's length, S, and angle, A. The rounding variable, R, has been excluded by the investigation in pump mode after a preliminary sensitivity analysis. The minute modification of the tip radius of the cutwater generates a negligible effect on the pump hydraulic efficiency, at least in the range envisaged in this research.

Fig. 5.43 shows some 3D-propagations of the flow streamlines in the pump volute leaving the R/S interface. The baseline case ⓐ is compared with four other different

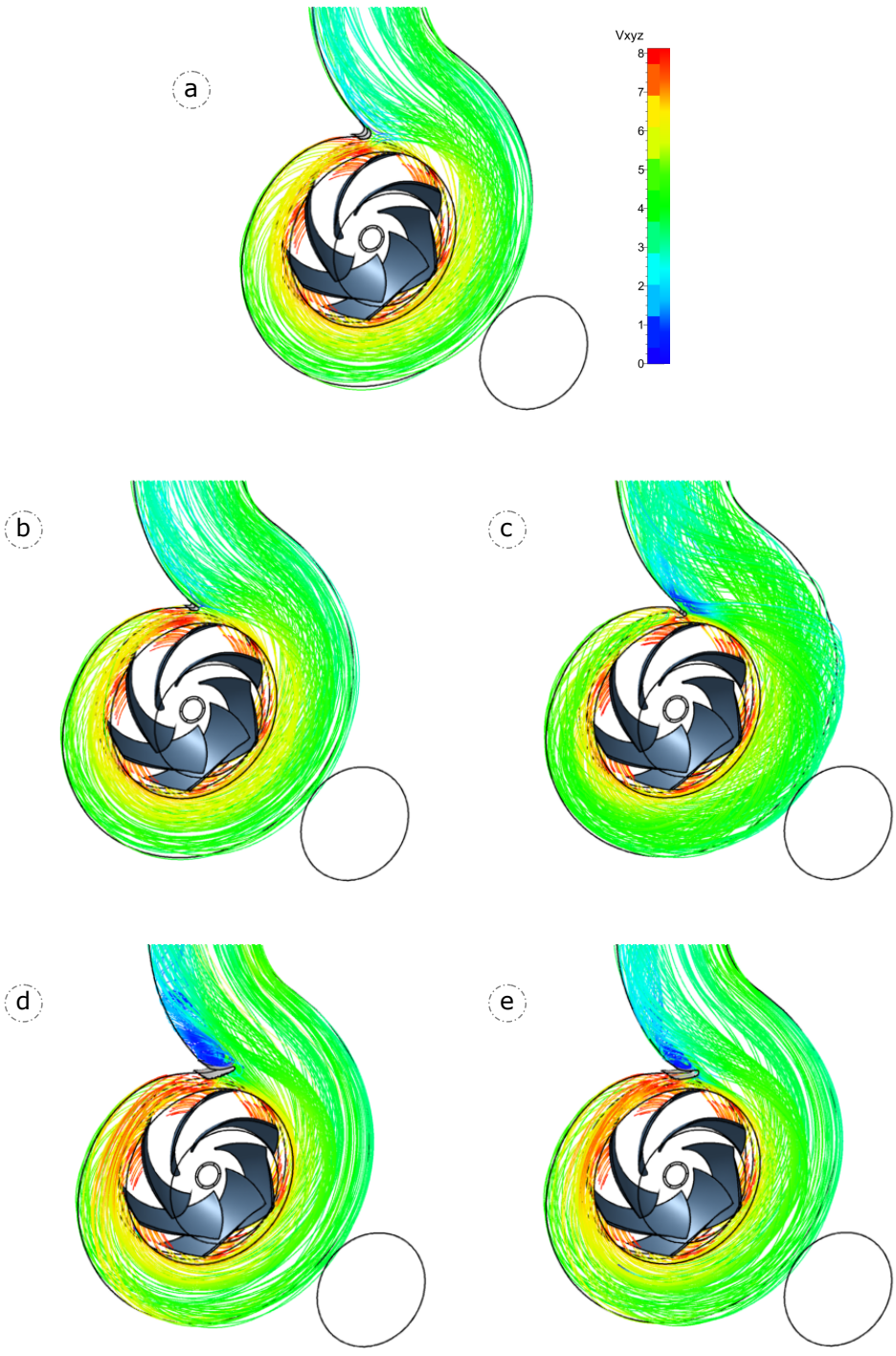

Figure 5.43: Velocity streamline of the pump with: ⓐ the baseline cutwater, ⓑ $2L, 0°$ case, ⓒ $3L, +10°$ case, ⓓ $4L, -25°$ case, and ⓔ the optimal geometry of the pump in reverse mode.

cutwater designs. All the simulations discussed in this figure are taken at pump BEP, equal to $\varphi_{BEP} = 0.017$. A $2L$-long cutwater without angle deviation ($A = +0°$) is represented by the subfigure ⓑ and it documents a clear similarity with baseline case in terms of flow distribution and velocity magnitude. A comparable flow field is recorded in the cutwater area and the final portion of the casing, after the throat section, lead smoothly the flow towards the exit. The $3L, +10°$ case ⓒ is characterized by a relevant and complex turbulent dissipation that slows down the flow speed in the volute casing. Moreover, the flow impacts abruptly on the cutwater-side of the throat. Such a movement contributes to raise the hydraulic losses in the volute and spoil the global pump efficiency. The cutwater implemented on the pump case ⓓ is $4L$-long and tilted by $-25°$. The extended pin obstructs the flow and induces a separation downstream. The flow separation implies a large zone of stalled fluid with local recirculation. The cutwater and the following stalled fluid block part of the cross-section available to the flow: the throat diameter drops by 14%. The unstalled fluid is therefore accelerated and high losses are generated through the strong exchange of momentum between the through-flow and the stalled zone. In the last subfigure ⓔ, the cutwater under Λ_{opt} modification ($3.54L, -15°$), is represented. Although to a lesser extent, it is subject to similar vortex dissipation phenomena of the previous case ⓓ.

The evolution of the relative total pressure integral in the pump volute is illustrated in Fig. 5.44. The sections A, B, C-C7 are previously defined in Fig 5.33. The cases ⓐ and ⓑ confirm their similarity in pressure distributions along all the cross-sections and ⓓ and ⓔ exhibit the larger pressure drop at the beginning of the spiral casing (C7-C6). The modifications carried out in case-ⓒ bring the most alteration from the baseline pressure profile. The negative cutwater inclination appears to flood the discharge passage in a such narrow area and only later the impeller

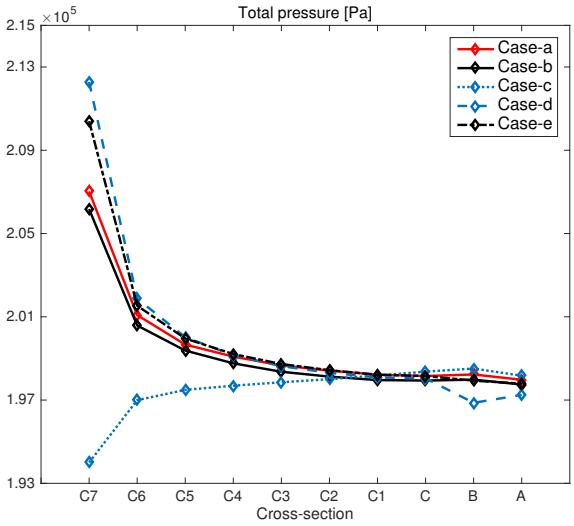

Figure 5.44: Absolute pressure distribution along the volute cross-section for five representative cases.

pump manages to deliver higher pressure.

Fig. 5.45 shows a close view of the streamlines bonded to the mid-flow surface around the cutwater for the aforementioned cases at $\varphi_{BEP} = 0.017$. Over posed, a contour of Cp is also given. ⓐ and ⓑ show evident affinity in the flow path and Cp distribution. The streamlines can often adapt well on the volute wall, limiting the pressure losses. Case ⓒ experiences a significant drop of static pressure directly after the impeller exits due to the forced fluid acceleration for the narrow

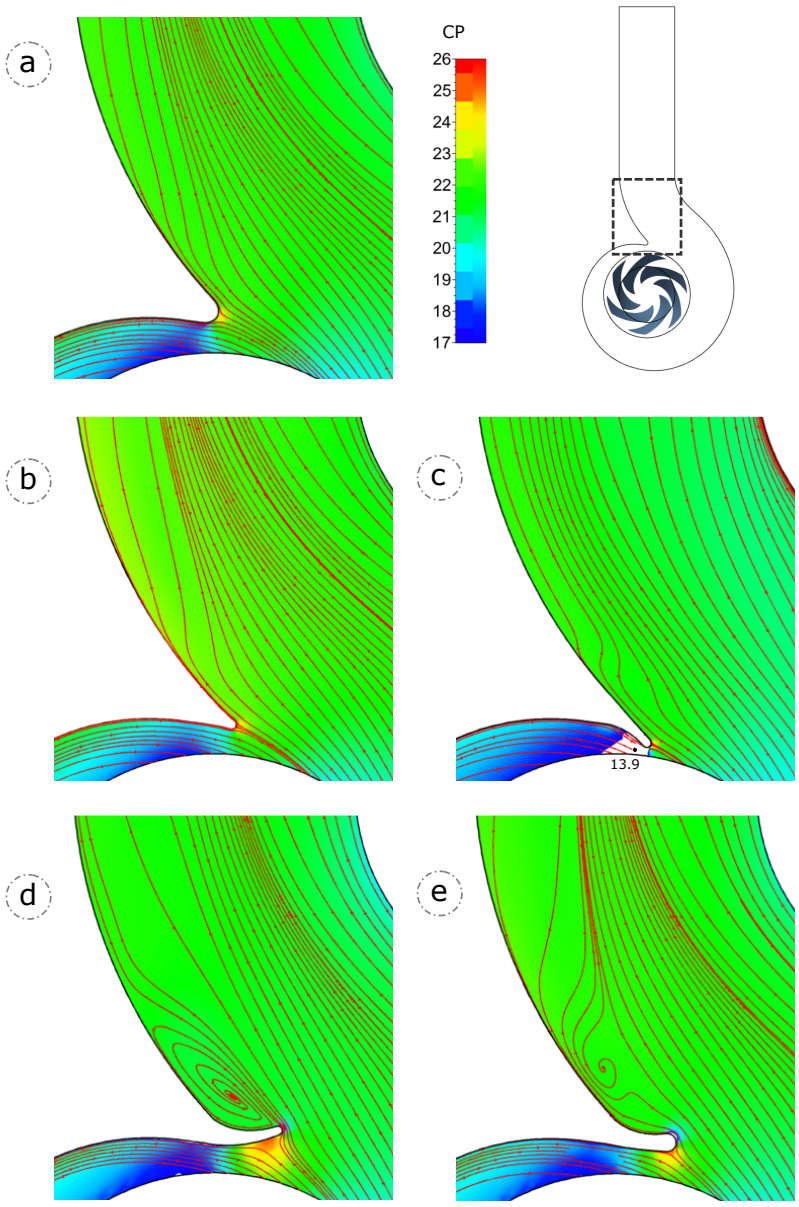

Figure 5.45: Velocity streamline and Cp contour of pumps with: ⓐ the baseline cutwater, ⓑ $2L, 0°$ case, ⓒ $3L, +10°$ case, ⓓ $4L, -25°$ case, and ⓔ the optimal geometry of the pump in reverse mode.

passage of the tilted cutwater. To maintain consistency with Cp range of the other subfigures, the minimum Cp local value is out-of-scale and only marked. In ⓓ a large deceleration area is shown on one side of the cutwater and stalled fluid fills the space downstream the throat with a wide vortex. The smaller angular incidence of the case ⓔ reshapes the streamline of the flow but a high degree of turbulence is still generated. Thick boundary layers are unfavourable to the diffuser flow and lead to not uniform velocity distributions.

The hydraulic efficiency of the pump at $\varphi/\varphi_{BEP} = 1$ according to the cutwater modifications is reported in Fig. 5.46. The data can be gathered in three regions distinguished by the variable S ($S = 4L, S = 3L$, and $S = 2L$). The inclination angle of the cutwater of each simulated design is indicated by the dark line. In addition, the PaT optimal geometrical asset, Λ_{opt}, and the efficiency for the baseline pump (dashed-red line) are shown in the figure. Limited improvements are obtained by stretching the cutwater up to 2L length at neutral or negative tilt angle ($-25 < A < 0$). Other two design sets bring an efficiency gain, but for punctual inclination angle: $S = 4L, A = +0°$ and $S = 3L, A = -15°$. The largest raise in efficiency is $+0.43\%$ with $S = 2L,\ A = -15°$. The Λ_{opt} configuration brings $+0.12\%$ compared to the baseline case.

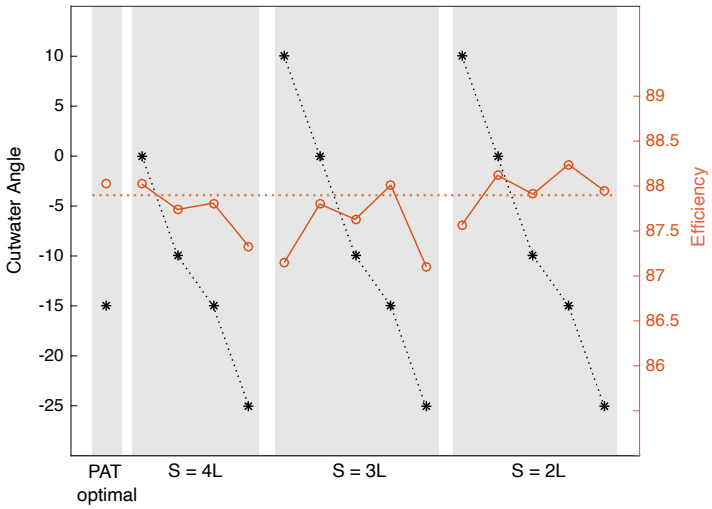

Figure 5.46: Pump hydraulic efficiency at $\varphi/\varphi_{BEP} = 1$ according to the cutwater modifications in stretching S and inclination A. Note that the baseline $\eta = 87.9\%$.

As described in the preceding section (Section 5.3.2.2), the spiral volute is designed to collect the flow discharging from an impeller in a way that would result in circumferentially uniform pressure and velocity. However, such a volute design is specific to a particular design discharge number [Brennen 1994]. At flow rates above or below nominal design, disturbed and separated flows can occur particularly in the vicinity of the cutwater. Some typical phenomena involve volute flow recirculation and separation on the inside and outside of the cutwater at flow coefficients below and above the designed discharge, respectively. For this reason, two other batches of simulation are computed to define the pump performance for

$\varphi/\varphi_{BEP} = 0.9$ (Fig. 5.47) and $\varphi/\varphi_{BEP} = 1.1$ (Fig. 5.48). The modifications globally spoil the hydraulic efficiency and considerably with extreme cutwater inclinations ($\Delta\eta$ about -1%). Neither a positive inclination appears to benefit any cutwater modifications nor out of the baseline BEP conditions. Moreover, a stretched geometry is further penalized at lower discharge, recording the most relevant efficiency detriment of -1.35% at $S = 3L, A = +10°$. The asset $S = 2L, A = -15°$, that shows a slight improvement in under $\varphi/\varphi_{BEP} = 1$ (Fig. 5.46), benefits to the efficiency by +0.16% and +0.34% at lower and higher discharge, respectively.

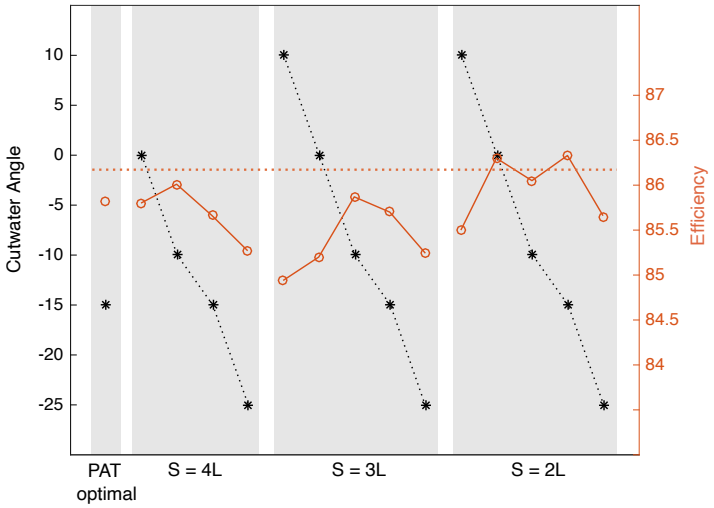

Figure 5.47: Pump hydraulic efficiency at $\varphi/\varphi_{BEP} = 0.9$ according to the cutwater modifications in stretching S and inclination A. Note that the baseline $\eta = 86.17\%$.

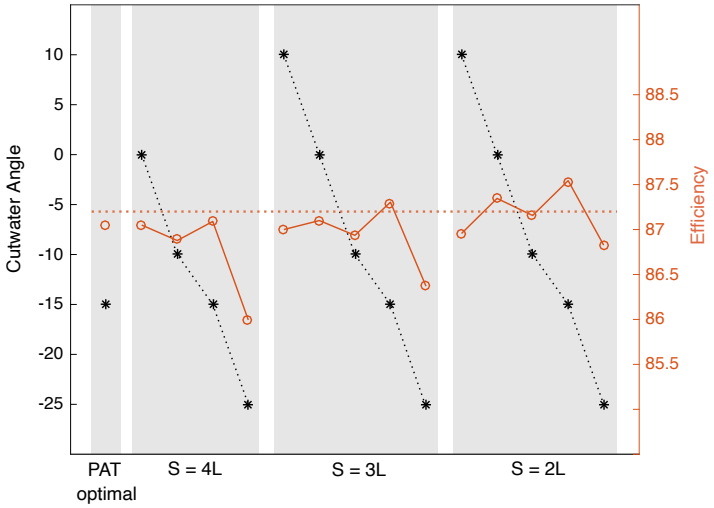

Figure 5.48: Pump hydraulic efficiency at $\varphi/\varphi_{BEP} = 1.1$ according to the cutwater modifications in stretching S and inclination A. Note that the baseline $\eta = 87.22\%$.

5.4.8 Unsteady verification of the pump performance in Λ_{opt}

The most comparable approach for a design study would be a transient simulation whose results are then time-averaged; this may yield very different results than a steady-state solution with mixing plane rotor stator. The limitations of the model could decrease the confidence on the results. Fig. 5.49 compares the pump head coefficient and the hydraulic efficiency of the baseline geometry and the optimum design for PaT mode. Moreover, unsteady simulations are computed to validate the pump performance in RANS. with Λ_{opt} asset. The performances of the optimized and baseline geometries matches at discharges close to φ_{BEP}.

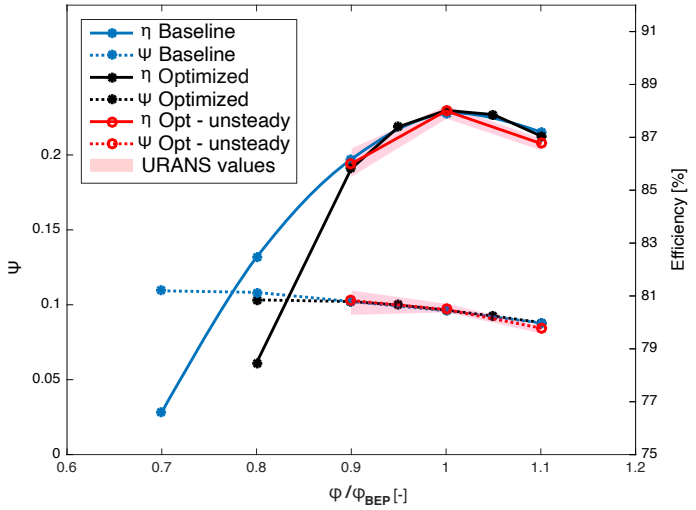

Figure 5.49: Comparison of the numerical pump characteristics with the baseline geometry and Λ_{opt}.

As presented in Section 5.4.7, the cutwater modifications affect the flow field downstream the runner and they have limited influence on the runner operating conditions. However, the extended tip of the cutwater produces a discharge obstruction that generates a stalling flow area with a wide recirculation. Fig. 5.50 illustrates the development of slow flow area ($V = 2$ [m/s]) in steady state pumping downstream the cutwater.

Unsteady simulations confirm the performance of the RANS simulations but show a further detriment in efficiency at $\varphi/\varphi_{BEP} = 1.1$ Larger discharges, and thus higher water velocity, corresponds to a higher pressure drop in the volute that reduces the global efficiency of the pump. The discrepancies of the RANS - URANS are as follow:

- $\varphi/\varphi_{BEP} = 0.9$, $\Delta\eta = 0.16$ % and $\Delta\Psi = 8.1 \cdot 10^{-4}$
- $\varphi/\varphi_{BEP} = 1.0$, $\Delta\eta = -0.20$ % and $\Delta\Psi = -4.0 \cdot 10^{-4}$
- $\varphi/\varphi_{BEP} = 1.1$, $\Delta\eta = -0.67$ % and $\Delta\Psi = -2.8 \cdot 10^{-2}$

The differences are based on the averaged value of the unsteady state simulations over a period of 60° of impeller rotation, namely a complete blade passage rotation.

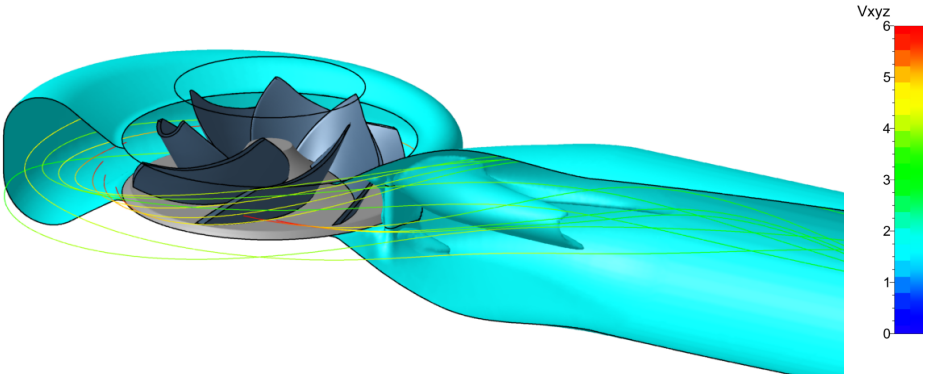

Figure 5.50: RANS velocity magnitude iso-surface ($V = 2$ m/s) downstream the cutwater of Λ_{opt} in pump mode.

Fig. 5.49 shows the characteristic oscillations during a whole period by the coloured red area that delimits the upper and lower values recorded.

Fig. 5.51 illustrates the URANS streamlines near the cutwater on the domain mid-span during pump mode working condition at $t = [0 + \theta], [1/4\theta + \theta], [1/2\theta + \theta]$, and $t = [3/4\theta + \theta]$, where θ is the blade passage period that corresponds to 60°. The shape of flow recirculation and detachment point are different of the steady state shown in Fig. 5.45-ⓔ but the magnitude velocity and the size of the stalled area downstream the cutwater are alike. This flow obstruction generates a three-

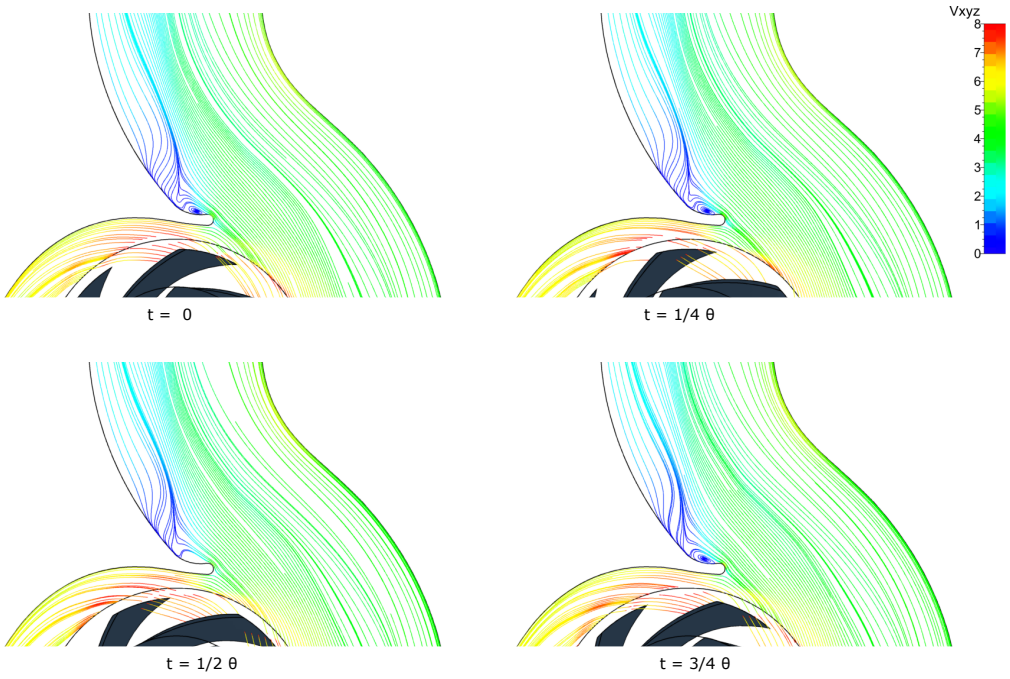

Figure 5.51: Water flow streamlines of the pump at $\varphi/\varphi_{BEP} = 1$ under Λ_{opt} asset.

dimensional turbulence affecting the normal profile of velocity at the final volute bend as presented similarly in steady state simulations. Iso-surfaces of velocity magnitude $V = 1$ [m/s] and $V = 2$ [m/s] show stalled flow areas downstream the cutwater in URANS simulations (Fig. 5.52 - 5.53). In comparison with steady state simulations, at $V = 2$ [m/s] the length of the slow speed area is similar but at its root it covers uniformly the cutwater height.

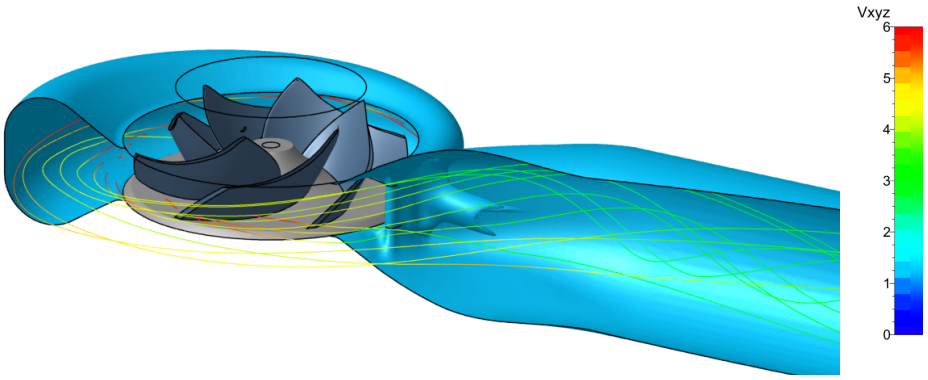

Figure 5.52: URANS velocity magnitude iso-surface ($V = 1$ m/s) downstream the cutwater of Λ_{opt} in pump mode.

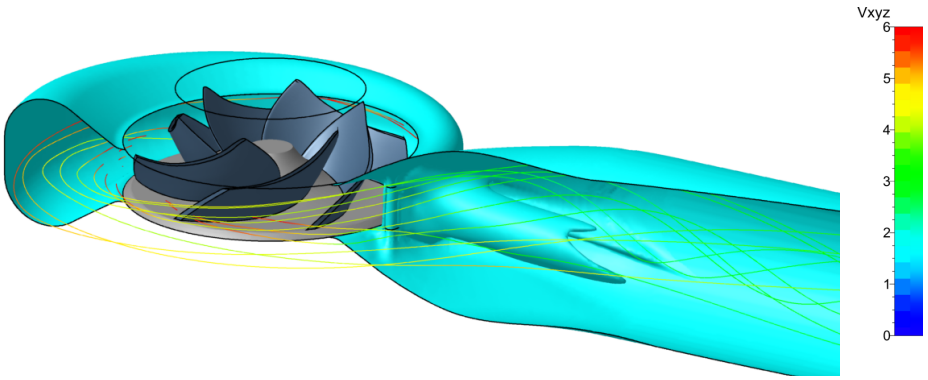

Figure 5.53: URANS velocity magnitude iso-surface ($V = 2$ m/s) downstream the cutwater of Λ_{opt} in pump mode.

5.5 Chapter conclusions

The cutwater is an important stationary part of the pump volute and it has a crucial role for defining the flow field in pumps functioning as turbines. In this chapter, a novel cutwater design is provided for improving the hydraulic efficiency of a PaT. A numerical investigation is computed for over two-hundred different duty points in order to produce a set of equations for modelling the PaT performance according to the cutwater geometry. Firstly, the research addresses the modification of the cutwater geometry in terms of length, rounding and angle. Then, the numerical simulations of the PaT baseline with the original cutwater design are validated by the experimental data available from the μ-PHES system where this centrifugal pump is installed. The CFD Ψ and η characteristic curves are obtained for the modified cutwater and the numerical outcome result in good agreement with the measurements within the accuracy of the experiments and the simulations. The results highlight the influence of the cutwater geometry in deflecting the inlet flow in the runner for improved performance. With a longer cutwater and within a limited range of the inclinations, the PaT's BEP moves to a higher head and lower discharge, obtaining considerable improvements in hydraulic efficiency.

Thanks to the outcomes achieved by the numerical simulations, a sufficient dataset of the PaT performance is available to train, validate and test a multivariate regression method. This process builds a model of the PaT efficiency as a function of the operating conditions and the cutwater geometrical parameters. By solving the optimization problem targeting the maximization of the PaT efficiency, the best cutwater geometry is found. This allows a drastic shortening of the investigation time. De facto, solving the complete optimization problem lasts less than one-tenth of the execution time needed for a single CFD set-point simulation.

The results of the model converge on a new cutwater design Λ_{opt} and the PaT's BEP gains 3.9 % in hydraulic efficiency. This is an outstanding performance improvement that doesn't require to modify the pump impeller. Unsteady simulations of the optimal geometry prove similar development of the absolute velocity angle at the runner inlet with limited discrepancy in the first 40° from the cutwater gap but, finally, RANS and URANS simulations agree on performances. The new BEP operates close to the nominal operating conditions of the baseline cutwater geometry at 87 % of the discharge and for 107.5 % of the available head. The change in operating condition reduces the theoretical power generation of the micro-turbine. However, such power subtraction is almost fully compensated by the performance improvement of the cutwater modification. Moreover, because the water volume of the upper reservoir is unaffected, the energy capacity of the hydropower system of the investigated PaT is augmented accordingly to its efficiency. In this way, the micro hydropower facility generates approximately the same power output and the water resource is exploited more responsibly. Variable speed technology is also foreseen and studied in order to revise the operating condition: a modest -2 % correction on the rotational speed allows the available head of the optimized PaT to be adjusted according the initial baseline requirement.

In the perspective to detect the alteration of the pump performance according to the cutwater modifications in normal operation, an additional investigation is carried out at pump BEP and part-load conditions. Most of the geometrical updates bring disadvantageous flow topologies that affect the pump hydraulic efficiency. Velocity streamlines and the pressure coefficient spot vortex and recirculation phenomena for cutwaters with negative tilt and strong pressure flaws in the volute for a positive inclination. However, no significant improvements are achievable in terms of hydrodynamic post-processing (from -1.35 % up to +0.43 %) in a short range of S-values and A-values. The optimal asset for PaT operation, Λ_{opt}, equals the baseline pump efficiency but exclusively at BEP discharge rate. Moreover, unsteady simulations of the modified pump verify the steady state performances and support the research outcomes.

Chapter 6

Conclusions and perspectives

Contents

6.1 Achievements

6.1.1 Review of the objectives

In Europe and most of the world, the main challenge of recent energy policy is to increase the share of RES with the aim of reducing greenhouse gas emissions to 80-95 % below 1990 levels by 2050 [European Commission 2012a]. In this context, energy, and more specifically, electricity energy storage plays a crucial role. As for PV panel systems, capacity factors lead towards over-dimensioning RES plants in order to satisfy energy demand even on cloudy days. To tackle this challenge, it appears necessary to develop a large storage capacity and to deal with issues caused by the mismatch between energy over-production and consumption, most often occurring on sunny days. These problems, that are particularly severe for hourly or sub-hourly operators in the energy markets, become consistent for grid stability and balancing.

Regarding PHES, large-scale power plants have made significant efforts towards flexibility to accommodate grid frequency stability supported by a significant share of intermittent RES. In small and micro scales plants, the target is to improve the energy efficiency of DESs, which are currently growing rapidly at residential and industrial levels. The major difficulties for the feasibility of decentralized μ-PHES are the low energy capacity of the system, limited by the maximum available height differential of the reservoirs, and the high costs involved. Also, the global efficiency and economic feasibility are importantly affected by the response of pumps and turbines to load variation. To face the frequent constraints linked to the site location and load variation, innovative options must be analysed and tested to better evaluate the potential of PHES at micro scale.

The achievements of the thesis can then be divided into three parts and they are shown in Fig. 6.1.

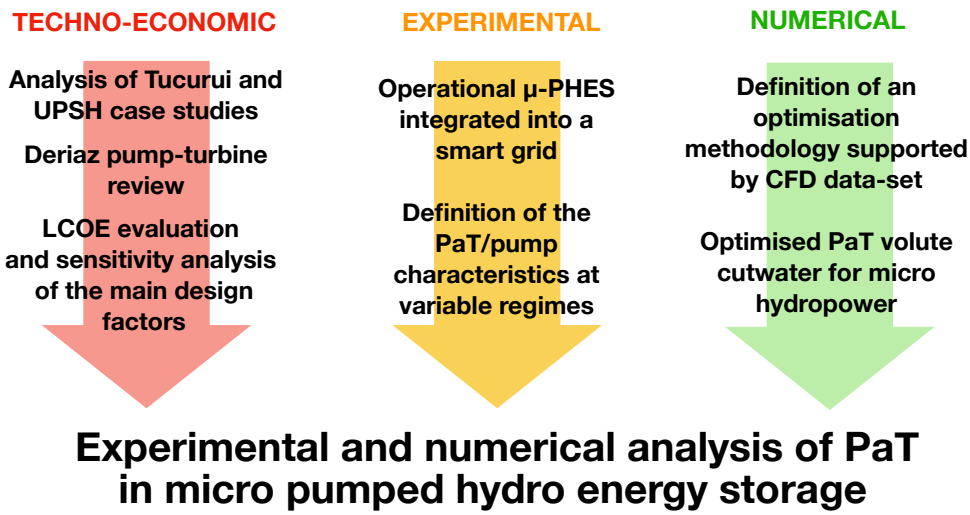

Figure 6.1: Achievements of the PhD thesis.

The first part of this PhD thesis reviews and provides the potential assessment of unconventional pumped hydro energy storage systems applied in synergy with existing infrastructures to escape the topographical requirements for such power plants. Such is the standpoint of the underground cavities used as lower reservoir in PHES plant. Two different case studies (Martelange and Pérronnes-lez-Binche) are discussed and their turbomachinery options are analysed. The analysis on the turbomachinery selection highlighted that the high variation of the head during generating cycles is critical for the machine reliability and it calls to non-traditional turbine set-up for preserving a profitable energy capacity, as well as to safeguard the turbines. Based on the options adopted in the Martelange case study, part-load conditions space from 35–107 % to 65–104 % and both Francis turbines and PATs with variable speed can be implemented to tackle high available head stretches. For the coal mine case study of Péronnes-lez-Binche, a series of separate Francis turbines can also be installed to deal with the extreme variable head operations. This concept is unusual and a complete feasibility study of this solution should be assessed but it succeeds in balancing the instant available head according to the operation in full series or in by-pass.

Moreover, another case study of an hybrid power system is presented. The integrated RES system with μ-PHES is a viable solution at the installation at Tucuruí locks in Brazil. One of the main obstacles to the socio-economic development of rural and remote areas, as most of the nearby Brazilian Amazon region, is the lack of electric energy grid (off-grid solution) in the numerous small isolated communities of the Amazon region that hampers value-added agricultural production, revenue growth and creation of jobs. One way to solve this problem is by setting up robust energy sources and storage appliance under a sustainable development perspective.

The system at Tucuruí reflects this purpose and it demonstrates the potential of using hydropower waterway locks for energy storage and RES integration.

To deepen the technological aspects of the turbine selection in PHES with variable load profiles, the Deriaz pump-turbine technology is examined especially in a downsized model for μ-PHES. This kind of pump-turbine is rare and its potential remains largely unknown. The work of this thesis provides a relevant gain of knowledge that can be exploited to fill this gap. The research methodology is presented and the results, that confirm the Deriaz flexibility in pump and turbine modes, are in agreement with the available data. This latter topic, along with UPSH and the Tucuruí case study, introduces the core research of this thesis on PaT.

Pumps used in reverse mode for micro hydropower were recently of high interest for industry and academics. PaTs are a legitimate cost-effective option in micro hydropower but there is no universal performance prediction, and their hydraulic efficiency can possibly shift from the higher efficiency of traditional hydraulic turbines. Nowadays, these reasons restrict PaTs exploitation. In this PhD, a μ-PHES equipped with a single PaT is designed, installed and intensively tested for integration into an existing smart-grid. The selections of characteristics of the turbomachine, pipeline, fittings, diffusers and instrumentation for performance metering and control achieved to set up an energy storage system with a round-trip efficiency of 42 %. This facility provides a unique and much sought guide to the pump/PaT performance, underlining the advantages of adopting a variable speed regulation for dealing with flexible loads. μ-PHES is, in closing, technically feasible. However when associated to local sources of energy in a urban area, it is still far from reaching grid parity. A cost-benefit analysis shows that additional design considerations are needed to make such system competitive with other energy storage technologies.

In pursuit of improving the hydropower yield of PaTs, a numerical analysis on the turbine volute is presented in the last chapter of this thesis. CFD simulations deliver essential data to identify the geometrical characteristics of the cutwater that impact on the PaT performance. Different values of stretching and thickness of the cutwater are studied at variable inclination by computational fluid dynamics simulations. A multivariate regression method is applied on the CFD results to build a surrogate model of the PaT hydraulic characteristics as a function of the geometrical parameters of the machine cutwater. Based on this model, an optimization problem is solved to identify the most advantageous geometrical asset of the PaT cutwater to maximize the hydraulic efficiency. The implemented methodology can be applied to all types of PaT. In this case, the results highlight the cutwater length and the angle are the most affecting variables in favouring a tangential component at the entrance of the runner. The hydraulic efficiency peak of the optimized geometry results to raise of 3.9 %, and the $\Psi - \varphi$ characteristic moves the BEP towards higher head (+7.5 %) and lower discharge (-13.0 %). The proposed methodology allows identifying the most suitable geometry of the PaT cutwater to maximize the performance while significantly reducing the computational time. The PaT characterisation and the efficiency improvement help the development and spreading of this technology in PHES application and in micro hydropower.

6.1.2 Work novelty

In the course of this PhD thesis, a few innovative, or at least not already publicly available, contributions have been made. Here is a list of the most important ones.

- To the intent to expand underground pumped storage plant potential, two specific case studies are demonstrated with regard to their operating conditions and hydropower yield.
- There is no precedent literature concerning the design, CFD, and experimental data analysis of the Deriaz pump-turbine, which is extremely suited to our current energy generation and storage needs in decentralized solutions.
- A novel micro-pumped hydro energy storage is designed and installed in a smart grid. Energy storage and energy recovery are achieved both via a single industrial centrifugal pump.
- PaT at variable rotational speed is demonstrated to be a valid turbomachinery alternative to conventional micro turbines in exploiting variable hydraulic power in distributed storage solutions. The PHES requires a calibrated evaluation of the hydraulic system performance taking in account energy fluctuation and the turbomachinery operating conditions.
- The experimental results and data obtained for μ-PHES on site allow for LCOE calculation and cost-saving improvements. Finally, they contribute to the awareness of PHES performance and feasibility in micro-scale, where there is a grave lack of practical information that strongly affects the reliability of any research done on the subject.
- There is no precedent literature concerning the methodology and design optimization of the cutwater in PaTs, providing a unique and much sought guide to its performance, improvements, and adaptation to hydropower.
- CFD simulations shed light on the performance of the PaT cutwater modifications and build a complete dataset to elaborate a predictive algorithm and an optimisation model.
- A novel cutwater design is provided for improving the hydraulic efficiency of a PaT. The modifications are executed in length, thickness and tilt angle.
- Perspectives are given by the development of correlations in rotational speed adjustments and pump performance of the modified cutwater geometry in PaTs.

6.2 Future work and perspectives

By the content of this report, three axes for further investigation and perspectives are identified.

- In the definition of the thesis framework, variable geometry pump-turbines and underground cavities used in PHES are two recent emerging subjects, whose potential calls more in-depth research.
- The outcome of the facility in the Negundo site delivers extensive recommendations to μ-PHES, addressing to additional improvements to mitigate the system weakness.
- Moreover, the methodology used to optimise the PaT cutwater can serve as a first brick of future work in finalising the optimal design.

6.2.1 Variable geometry Deriaz pump-turbine

In this work, it has been proven the extra degree of freedom present in a Deriaz pump-turbine allows a variable power produced and consumed better than other hydraulic pump-turbines in function of the needs of the grid. Thus, Deriaz in PHES applications is a very attractive solution for BRPs and TSOs in grid balancing and transmission. Nowadays, BRPs have to deal with the growing share of intermittent renewable energy sources that has led to increased interest in flexibility and EES capacity [Khan *et al.* 2018].

By 1960, when most of the Deriaz had been installed (Table 2.2), the energy mix has been diversifying significantly: the world had moved into nuclear electricity production and today's renewable sources (modern biofuels, wind, and solar) appeared only in the 1980-90s in the global total energy production. Compared to the applications of the 1960s, nowadays the regulation systems as the one applied to the adjustable runner blades are not more expensive, but more advanced materials and solutions are used to improve operational and power characteristics. Since then, the economics, the needs and the energy market have been also changed and it is necessary to explore different opportunities and reassess previous technologies in the need for flexible operations of hydro assets [Johnson *et al.* 2018].

Multiple storage solutions must now be analysed at all scales and in a decentralized context for various exploitable working conditions. RES fluctuations necessitate an efficient technology to manage energy storage and to match with the demands providing critical capacity during key energy periods. Deriaz high performance at part-load leads to high flexibility and allow the increase of the number of exploitable hydropower sites and revenues in PHES applications.

One remaining question is the effect of the manufacturing constraints, mechanical adjustments and servomotor requirements on the Deriaz pump-turbine design: a deeper analysis addressing this matter would need to consider the restrictions and considerations necessary for a more correct design that takes the mechanical and technological needs into account. Therefore, although the Deriaz pump turbine presents a formidable potential and it could help re-evaluate those sites previously discarded as *not-feasible*, today its application could not be affordable in micro scale until further techno-economic assessment.

6.2.2 UPSH

The possible investors who might be attracted by potential profit in PHES are repelled by the long payback period, by the regulatory uncertainties and topological risks, especially in UPSH installations. The economic adventure in such investment needs to compete, for instance, with the low price of natural gas used in gas turbines for brief spurts of peak power. The actual regulatory and economic climate should fight against avoidable use of fossil fuel and stir towards renewable and sustainability. For this reason, particular focus and value must be given to green power generation, storage and high energy efficiency.

A relevant benefit of the implemented UPSH is the avoided greenhouse gas emissions, resulting from using stored energy rather than energy coming from the national energy mix. According to the estimations given in [Spriet 2014], for 100 MW Martelange case study over the system lifetime, about 2 million tons of CO_2 equivalent can be avoided, which equals to about 10% of the total CO_2 emissions in Belgium for households in 2018 (26.8 million tons of CO_2 equivalent) [OECD 2019]. An additional environmental advantage in using groundwater instead of surface water is that it also reduces or eliminates the impact to fish populations [Yang & Jackson 2011]. However, in order to provide a more comprehensive analysis of the environmental effects generated by the implementation of the power system, additional impact on biodiversity, hydrogeology, geomorphology must be assessed.

The main concern for this type of mines is the damage that the water has done or will do while leaking in, and, in particular, the possible pressure relief openings in the mine because of erosion. These openings might cause higher leakage rates and lower structural sturdiness than expected. Even though it is expected mine structures can withstand the cyclic pressures, and that leakage will be acceptable, and partly compensated by inflows, on-site testing will still be necessary to determine the exact site-specific properties. Cracks in the soil are dependent on local conditions, and significant difference might occur from one site to another. The PHES can be relieved of the geological and structure risks of large underground cavities by the realisation of consolidation and membrane coatings.

The stability of the soil is also crucial to avoid that water erodes small particles of the cavity. This process forms debris in the water that can hit the turbine at high speed, causing damages. The use of water with a high content of debris, sand and muck, which is typical for an inactive quarry as the ones analysed, can cause wear of the gap between runner and casing of the turbine. Thus, the efficiency drops in a pump-turbine with closed impeller (e.g. fast Francis or some PaTs) as constant erosion takes place. Experimental investigations have shown a reduction of up to 5 % on centrifugal pump efficiency by the grow of the impeller gap [Mou *et al.* 2016]. The correct manufacturing material has to be picked up in a later stage of the project to deal with erosion corrosion and oxidation. This will only have an impact on price and not really on the hydraulics. In this regard, providing a sample of the water composition of the site to the turbomachinery manufacturer is necessary.

6.2.3 μ-PHES design recommendations

The μ-PHES in *Quartier Negundo* represents the prototype of such type of system that can be implemented to provide continuous electrical power to off-grid and remote communities when RES systems cannot meet demand. The growth interest in this topic has reached worldwide level and the development of the Tucuruí's case study is a clear example.

In urban environment, and in the context of energy decentralization, the push in innovation unbalances the traditional business model for RES that is focused on indirect revenues by self-consumption. Nowadays, in most of the European country, prosumers are allowed to sell their own-energy production directly under the regional and federal bills. But the legislation would quickly need to be adapted to enable small prosumers to participate at more complex energy market dynamics, where prosumers could sell their production and their flexibility too (when produce or consume). Each European country has responded differently in terms of time and legislation. The national issue of the energy sector (i.e., nuclear phase-out) and slow law's action hinder the Belgian answer to this fervent market opportunity for small players. These conditions and difficulties call for functional analysis of the micro energy storage system as an assisting tool to flexibility.

In this regard, a comprehensive comparison between the energy storage technologies for DES would be needed per case study in order to better propose the most sustainable and beneficial solution for the matter. Table 6.1 helps in this quest by gathering design key-points discussed in this thesis on μ-PHES about its strength, weakness, opportunities and threats (SWOT).

μ-PHES represents a robust EES alternative for rural and remote areas where technical expertise might be hard to find. Complex maintenance could jeopardize the system durability and the stability of the electricity provision. Grid-connected buildings or communities could also take advantage of pre-existing infrastructure to install a cost-effective μ-PHES. However, it is true PHES is a mature technology in which it is not expected any disruptive evolution that could make it more competitive to other storage growing technologies (e.g. electrochemical batteries or hydrogen). For instance, different kinds of batteries are present in today's market according to charging and discharging efficiency (or round-trip efficiency), life-time cycle, weight and peak voltage output [Palizban & Kauhaniemi 2016]. In the last decade, battery costs are falling quickly for the new growing market in electric vehicles and the global trend toward energy self-sufficiency.

On the other hand, the battery industry can generate considerable amounts of environmental pollutants (e.g., hazardous waste, greenhouse gas emissions and toxic gases) during different processes including mining, manufacturing, use, transportation, collection, storage, treatment, disposal and recycling [Poullikkas 2013b, Dehghani-Sanij *et al.* 2019]. Battery use will have significant social and environmental impacts; hence, it must be compared carefully with alternatives in terms of sustainability, while focusing on research to quantify externalities and reduce risk [Dehghani-Sanij *et al.* 2019]. Alternatives like pumped hydro must be encouraged

because of their low environmental impact compared to different types of batteries. The key concept for spreading of μ-PHES is to detect possible synergies with other appliances. Fire-safety systems are often located on rooftops of high buildings, and they could offer appealing water reservoirs for energy storage, but they are highly regulated and hard to adapt. μ-PHES can be integrated with stormwater basins, or irrigation appliances, or waterway locks or rainwater harvesting systems that today are more often implemented for sustainable drainage practises. These explorations would unveil new market scenarios and their possible evolution.

Table 6.1: SWOT analysis of μ-PHES.

Strengths	Weakness
- Although the land-take might be an issue, μ-PHES is environmental friendly. Furthermore it has minor disruptive effects on ecosystem than large scale PHES.	- Low energy density and electrical round-trip efficiency (42%) smaller than common lead-acid batteries (75-80%) and lithium ion batteries (95%).
- Robust and reliable back-up system of total grid-loss for vital function of industries of small communities.	- Time from zero to full-load is at least >30 s. Longer period from opposite operation regime.
- Low operating costs, long life-time and simple maintenance and refurbishment.	- Strong design dependence on the site space and elevation.
- Increase in the smart grid self-sufficiency and flexibility, especially with variable speed.	- Micro power-size limits the involvement in ancillary services.
Opportunities	**Threats**
- Effective synergies with other complementary systems such as water distribution, stormwater capacity, fire-extinguisher systems, and others.	- In case of μ-PHES equipped with PaTs, there are uncertainties linked to the performance prediction of the turbomachine.
- Easy access to the growing market opportunity of electrical demand-response (for time-base retribution or other financial incentives).	- A limited number of cycles penalises the LCOE of μ-PHES to grid parity and its competitiveness with other EES systems.
- The micro scale helps to reduce the geological constraints and it eases integration in small smart grid and buildings.	- A rapid economic growth of competitive EES technologies such as electrochemical batteries.

Other recommendations lay in the hydropower design guidelines that this research lets emerge. It is important to foresee civil engineering constraints and the consequent exceptional expenditures, as in the Negundo site. There, drilling the pipeline underground is the single way to link the two reservoirs without causing damage to the neighbour infrastructure (i.e. a pedestrian way and the local sewer line). However, the pipeline cost represents about 46% of the total expenses for the storage system (Table 4.7) and in other circumstances could have been reduced also by following the good practise for small hydropower of the ratio penstock length and available head (L/H) smaller than 3. Unfortunately, in Negundo site, $L/H = 8.0$.

The example of flexibility provided by the case study of *Quartier Negundo* can

constitute an alternative to upgrading the DES: the load outweighs are cut off by exploiting the capacity of the PHES and the intermittent energy injections produced by the renewable sources are efficiently stored in the hydraulic reservoir regardless the part load condition. This is successfully obtained by installing a PaT with variable speed control: it provides conditions for achieving a higher energy yield in exploiting variable hydraulic power while avoiding the onset of operation instabilities caused by the part load.

The use of the same machine for pumping and generating is related to the objective of saving cost of energy, space and maintenance. The PaT hydraulic efficiency recorded experimentally in the case study (about 72 %) may be smaller than with regular micro turbines but it is still very competitive and attractive for users. About simplifying the control operations, if it were not for the working condition variations, a gearbox would only set two rotational speeds on the shaft: one suitable for pumping and the second applied for generating mode. In these circumstances, the expenses would drop considerably, but no speed adjustment would be possible for the adaptation of the fluctuating head, nor for responding to an intermittent injection of renewable energy into the smart grid.

6.2.4 Optimal cutwater design finalisation in PaT

Although it is hard to expect any CFD method to be truly precise in all regards (e.g. for runner-volute coupling or passage gap at the blade tip) [Arani *et al.* 2019, Capurso *et al.* 2019c], CFD is an effective tool [Capurso *et al.* 2019a, Shah *et al.* 2013] that is necessary for high performance design studies. The presented numerical investigation on the PaT performance delivers decisive insights on the PaT functioning at its baseline geometry and with modified cutwater geometry. The accuracy of the CFD calculation is good from the standpoint of understanding the qualitative flow field, and it is good also in many quantitative areas. The findings in the cutwater effect depict the investigation area for flow development under different geometrical assets and offer opportunities in efficiency improvement. Moreover, the generated numerical data-set allows to develop an effective regression model of the PaT performance. The outcomes of the regression and optimisation process deliver a methodology that can be employed for a systematic volute adjustment by reducing the computational time and to promote furthermore the employment of PaTs in micro/mini hydropower applications (PHES included).

Finally, the PaT BEP of the updated cutwater geometry gains 3.9 % in hydraulic efficiency by a modest alteration of length and inclination that might require a limited use of resources by the manufacturer. Furthermore, the impeller pump design does not need to be changed nor the volute to be radically modified. The economic advantage of PaT on the traditional hydraulic turbines is so preserved. According the correlation developed for the case study in *Quartier Negundo* (Fig. 4.38), such raise in efficiency produces a reduction of LCOE by 3.8 %, equivalent to a 4 c€ cut per kWh produced by the μ-PHES. This performance improvement can be converted

in financial savings of 424 € per year or 12 thousand € in the system lifetime. The achieved results meet the objectives of this thesis in defining the PaTs potential in μ-PHES and providing a cost-effective geometrical optimisation.

The complete picture of the process of turbomachinery stage design and development consists in numerous analytical processes, involving a variety of steps and details. From a quasi-2D design then 3D design, CFD and finite element analysis are conducted to be integrated with rotor dynamic and laboratory evaluation, without eluding CAD and manufacturing constraints. The integrated agile engineering design system lies in a flow of progression and drop-back possibilities that iteratively optimises the final turbomachine design. Among the possible perspectives arising from the present work in finalising the optimal cutwater design, the following represents the most relevant: PaT behaviour under unsteady operating regimes and the structural/stress analysis.

The major sources of internal noise in pumps are usually associated with pressure dynamic pulsations, turbulence, vortex formation from separated flow around obstructions, and cavitation. In centrifugal pumps, in addition to recirculation noise, interaction of the impeller flow with the pump case (especially the cutwater), high-pressure gradients at the impeller blade tip, and flow separation can make significant contributions to pulsation levels and noise [Karassik *et al.* 2001]. Additional numerical simulations under unsteady conditions could be appropriate to ameliorate PaT performance driven by the cutwater modifications.

Finally, it needs to be said that centrifugal pumps are in generally machines that have either fluid or mechanically induced cyclic loading on their components. Although centrifugal pumps are for the most part steady-state rotational equipment and if any severe pressure gradient is encountered in the optimal PaT design, pulsations or fluctuating applied stresses might occur by the interaction between impeller exit vanes and the casing cutwater. A structural and stress analysis should be finally performed to assess the stability of the new asset modifications.

Appendices

Appendix A

Hydraulic design of a diagonal pump

A.1 Introduction

The content of this appendix is part of the peer-reviewed article *Deriaz pump-turbine for pumped hydro energy storage and micro applications*. The predictable pressure distribution inside a pump shows the fluid passes the impeller via an adverse pressure gradient. This further complicates the design of a turbine in pumping mode for all pump-turbines. The flow through the hydraulic turbine of the Deriaz type is quite complicated - as in most pump-turbines - and can require high demand of resources and high computer memory and CPU time [Lipej & Poloni 2000]. The purpose of this appendix is to develop a procedure for preliminary steps of Deriaz pump design. First, scaling laws are applied to determine the performance of the model ($D = 0.30$ m) from the prototype ($D = 0.95$ m). This allows to predict the operating point of the micro Deriaz for its design and, finally, analysis purpose (Section 3.4). A fast set of guidelines for designing mix-flow blades of Deriaz pumps is here presented: the design methodology is classical one but has no precedent in Deriaz application in the literature. Moreover, the hydrodynamic design of a new impeller using inverse method is usually based on a already existing base design [Muntean *et al.* 2015][Peng *et al.* 2002a] [Peng *et al.* 2002b], and the outcomes of this design process produces a significant starting point for further investigations.

Since turbomachines are designed for specific tasks, the sub-script N_s is used to denote the design value of the specific speed for a given machine. Thus general pump geometries, which have evolved over many decades, can be seen to fit into a single parameter family of shapes and applications. Overall efficiency rises as the specific speed increases, mainly due to decreased friction losses in the shrouds and a drop in volumetric losses [Brennen 1994].

In order to construct the starting point of the arc for the hub side, the shaft size and the hub diameter should be determined. Mechanical resistance determines the minimum size of the diameter of the shaft, which has to support the load and the blade pivots. The runner requires a larger diameter to accommodate the bearings. Considering also the complex internal mechanics, manufacturing is generally limited to no more than eight or ten blades [Houdeline & Verzeroli 1999]. The impeller selected has eight blades based on the experience of previous installed Deriza pump-turbine [Houdeline & Verzeroli 1999].

Evidently, the problem of calculating the dimensions of the impeller (and hence the whole turbomachine) for a given total head may have several solutions which vary from the point of view of efficiency and production costs. The best results will mostly likely be obtained for given operating conditions when the variables are chosen on the basis of experimental tests.

A.1.1 Scaling laws

Fluid mechanics and turbomachine performance are severely influenced by scaling laws. The affinity laws analysis is applied to the Deriaz prototype and Deriaz model in order to predict the performance of the turbomachine operating at different speeds and flow rates. Hardly the geometrical and kinematic similitude are achieved for a viscous fluid as water. In fact, on the turbomachine scaling it is not possible to use directly the Reynold's similitude

$$\mathrm{Re} = \left.\frac{\rho U_{ref} L_{ref}}{\mu}\right|_{pty} = \left.\frac{\rho U_{ref} L_{ref}}{\mu}\right|_{md} \tag{A.1}$$

where U_{ref} and L_{ref} are the flow speed in m/s and length in m adopted as reference [Commission *et al.* 1999]; the subscripts "pty" and "md" represent respectively prototype and model. In this analysis the velocity $U_{ref} = \omega D$ and the L_{ref} is mean flow diameter, D.

If the model testing is done using the same working fluid ($\nu_{md} = \nu_{pty}$) and the geometrical scale range is quite large, it is difficult to maintain a suitable velocity. As consequence, it is necessary to predict the possible variation of the velocity field and losses, due to dissimilar Reynolds number, Re (Eq. A.1).

Re is greater in the prototype than in the downsized model. Hydraulic losses have to be reviewed and the efficiency, η_h, has to be corrected as well. Since the hypothesis to consider the flow as completely turbulent remains valid, it is possible to use the Stodola-Ackeret's rule [Capata & Sciubba 2015] for the scaling of efficiency

$$\frac{1-\eta_{pty}}{1-\eta_{md}} = (1-V) + V\left(\frac{\mathrm{Re}_{md}}{\mathrm{Re}_{pty}}\right)^{n} \tag{A.2}$$

The first term of the equation represents the ratio of the losses prototype/model in two homologous functioning points. V represents the loss part due to the Re effect on the model and so $(1-V)$ is its complementary. The value V comes from the experience of the designer and from previous experiments: as the amount of previous statistical results is practically zero, the value assumed here is 0.5. n is an index offered by Nikuradse experiences [Gulich 2010] for localize the kind of fluid dynamic losses, here assumed at 0.2. The terms V and n are different according the literature depending by the accuracy of their data and dependency by the Reynolds number [Capata & Sciubba 2015, Pfleiderer 1952, Davis *et al.* 1951].

The analogy for two turbomachine is referred to the corresponding Best Efficiency Point (BEP). Eq. A.2 offers the estimation:

$$\Delta\eta_{opt} = \eta_{pty,opt} - \eta_{md,opt} \tag{A.3}$$

A.1.1.1 Application of the scaling in pump mode

The discussion of the efficiency in pump mode on the scale model is based on to the ratios D_{pty}/D_{md} and N_{pty}/N_{md}, where the fixed rotational speed of the model, N_{md}, is set to 1054 rpm. Other complementary information are listed in the Table 3.7. The assumption that the two machines are using the same fluid at comparable temperature and kinematic viscosity, ν, is maintained. From the definition of Reynolds number Eq. A.1

$$\left(\frac{\mathrm{Re}_{md}}{\mathrm{Re}_{pty}}\right)_{opt} = \frac{N_{md}D_{md}^2}{N_{pty}D_{pty}^2} = 0.140 \tag{A.4}$$

Finally, using Eq. A.2

$$\frac{1-\eta_{pty,opt}}{1-\eta_{md,opt}} = 0.837 \tag{A.5}$$

With $\eta_{md,opt} = 0.855$ (Table 3.7), the difference in the efficiency between the two machines in pump mode, $\Delta\eta_{h,pm}$, results

$$\Delta\eta_{h,pm} = \eta_{pty,opt} - \eta_{md,opt} = 2.81\ \% \tag{A.6}$$

A.1.1.2 Application of scaling in turbine mode

As is previously calculated for pump mode in Eq. A.6, an efficiency correction must be conducted for turbine mode as well. Using Eq. A.2 and the value reported for $\eta_{pty,opt} = 0.928$ in Table 3.7, the difference in the efficiency between the two machines in turbine mode, $\Delta\eta_{h,t}$, result in

$$\Delta\eta_t = \eta_{pty,opt} - \eta_{md,opt} = 1.40\ \% \tag{A.7}$$

The coefficients, n and V, in turbine mode are taken equal to the pump mode, because larger variation in velocity field are not expected[1].

A.1.1.3 Additional scaling considerations

The transposition is in agreement with the methodology provided by IEC code no. 60193 [Commission *et al.* 1999]. In this case, a reference Reynolds number of $7 \cdot 10^6$ is considered to minimize the deviation

$$(\Delta\eta_h)_{pty\to md} = \delta_{ref}\left[\left(\frac{Re_{ref}}{Re_{pty}}\right)^{0.16} - \left(\frac{Re_{ref}}{Re_{md}}\right)^{0.16}\right] \tag{A.8}$$

where $\delta_{ref} = (1-\eta_{h,\ pty,\ opt})/\left[\left(\frac{Re_{ref}}{Re_{pty,\ opt}}\right)^{0.16} + \frac{1-V_r}{V_r}\right]$ with V_r equal to 0.8 for operation as turbine and 0.6 for operation as pump [Commission *et al.* 1999]. The values of $\Delta\eta_{h,\ pty\to md}$ divergences with the results of Eq.A.6 and Eq.A.7 by less than 0,2 %.

The efficiency variation presented in Section A.1.1 is with respect to only the hydraulic aspects, η_h, and other considerations must be undertaken. In the reduced geometry, the inner domain of the machine is simpler than the prototype. For instance, a classic hydraulic machine for power production is equipped with internal access doors for maintenance and inspections. These can cause leaks and important efficiency losses. Moreover the hydraulic

[1] This value is indicative. It is necessary to adduce further researches for determining more calibrated n and V in pumping and generating mode.

turbomachine is usually connected to the whole gear apparatus and to the auxiliaries which produce additional load effects. All the subsequent discrepancies are summarized in variations of further hydraulic losses, leaks and mechanic losses:

$$\Delta\eta = \Delta\eta_h - \Delta\eta_{vol} - \Delta\eta_{mech} \tag{A.9}$$

Consider a same class of turbomachines that work under similar conditions. For these turbomachines a series of dimensionless coefficients are equal

$$\Psi = \frac{gH}{U_2^2} \qquad \varphi = \frac{Q}{U_2 R_2^2} \qquad \pi = \frac{P_p}{\rho U_2^3 R_2^2} \tag{A.10}$$

where Ψ is called the dimensionless *specific energy coefficient*, φ is the dimensionless *discharge number* and π is the dimensionless *power number*. Note that the mechanical losses and the total efficiency of a pump do not follow the similarity rules. The power coefficient is defined only for the internal power. For a constant value of the specific speed, N_s, the two machines belong in the same class. In order to treat each parameter individually, it is necessary to re-write the equation with $\Psi = gH/U_2^2 = \text{constant}$, which means $H \propto (D_n)^2$. Finally, it is possible to compute the term as

$$\frac{N_{md}Q_{md}^{1/2}}{{gH_{md}}^{3/4}} = \frac{N_{pty}Q_{pty}^{1/2}}{{gH_{pty}}^{3/4}} \quad \Rightarrow \quad \frac{NQ^{1/2}}{gH^{3/4}} \propto \frac{(ND)^{3/2}}{H^{3/4}} \propto \frac{ND}{H^{3/4}}H^{1/4} \propto \frac{ND}{\sqrt{H}} \tag{A.11}$$

Thus, the net head in pump mode of the model, $H_{p,md}$, respects the similitude

$$H_{pty} = H_{md}\frac{N_{pty}^2 D_{pty}^2}{N_{md}^2 D_{md}^2} = H_{md} \cdot 5.07 \tag{A.12}$$

Indeed, for $H_{md} = 10$ m, H_{pty} is equal to 50.7 m and it fits in the prototype head range according to Table 3.7. Likewise, the flow rate Q_{md} can be calculated according to

$$Q_{pty} = Q_{md}\frac{N_{pty}}{N_{md}}\left(\frac{D_{pty}}{D_{md}}\right)^3 = Q_{md} \cdot 22.59 \tag{A.13}$$

and with the prototype maximum flow rate $Q_{pty} = 5.50$ m^3/s (Table 3.7), Q_{md} is equal to 0.24 m^3/s. Table A.1 summarizes the operational data of the scale model.

Table A.1: Mechanical data of Deriaz prototype working in Naussac II.

Downsized model		
Geometrical reference, D	0.3	[m]
Design pumping head, $H_{p,n}$	10	[m]
Rotation speed, N	1054	[rpm]
Design pumping flow rate, $Q_{p,n}$	0.24	[m^3/s]
Pump efficiency, $\eta_{p,h}$	82.7	[%]
Turbine efficiency, $\eta_{t,h}$	91.4	[%]

A.1.2 Impeller inlet

The blade is shaped using a point by point method which defines the geometric parameters along five streamlines from the leading edge of the blade up to its trailing edge. The impeller layout design is highly dependent on previous studies and experience. However, these approaches have to be supported by theoretical approaches in fluid dynamics, numerical experimentation and experimental results. The estimation of the field of the velocities for the whole of the leading edge of the pump blade starts with the calculation of the flow and principal streamlines along the midstream.

For steady flow, the conservation of the angular momentum, T, expresses Euler's pump equation on the runner blade [Susan-Resiga *et al.* 2011] and, applied to one-dimensional simplification, it appears

$$T = \int_{blade} (\vec{r} \times \rho\vec{w})\ \vec{w}\ \mathrm{d}A \simeq \rho Q\ (c_{2u} r_2 - c_{1u} r_1) \tag{A.14}$$

where c_{2u} is the circumferential component of the flow velocity at the outlet of the control volume, r_2 is the outer radius of the impeller and c_{1u} and r_1 are the corresponding quantities at the inlet.

Euler's equation was deduced on the assumption that the flow though the impeller is axi-symmetric and the velocity field is created by an infinite number of contiguous stream surfaces and an infinite number of blades of thickness equal to zero [Lazarkiewicz & Troskolanski 1965]. In reality, the impeller has z number of blades of thickness which both reduce the cross-section area available for the flow through the impeller.

Blade thickness is a mechanical design consideration. It has to be thin enough to save material and weight, but also thick enough to handle fluctuating load flows and avoid the risk of fatigue cracks. The thickness of the blade is also dependent on the production technology used. If it is too thin and not adjusted with the other wall thickness at the root of the blade impeller, the desired casting of the impeller may not be achieved.

The effective flow rate is also affected by the volumetric efficiency; the volumetric and mechanical efficiency are assumed to be 98 % for an open impeller pump [Gulich 2010, Lazarkiewicz & Troskolanski 1965, Stepanoff 1957a]. The velocity in the impeller inlet and outlet in the meridional direction c_m is given by [Lazarkiewicz & Troskolanski 1965]

$$c_{m1} = K_1\sqrt{2gH}, \qquad c_{m2} = K_2\sqrt{2gH} \tag{A.15}$$

where K_{cm1} and K_{cm2} are respective velocity non dimensional coefficients [Lazarkiewicz & Troskolanski 1965, Stepanoff 1957a] which summarize the divergence from the theoretical value of the Bernoulli velocity.

The inlet flow direction is not normally considered completely axial and the peripheral component of the absolute velocity c_u is not equal to zero for most of the inlet edge of the blade. The theoretical head H_{th} is consequently affected by Euler's equation and this phenomenon is more pronounced at low partial loads. Pre-rotation and reverse flow result in an abnormal variation in pressure at the suction pipe wall and the rise in noise and vibration results in mechanical damage. In order to control these phenomena, IGVs (Inlet guide Vanes) can be placed a short distance from the impeller inlet. Variable angle adjustment of the IGVs can help regulate the head and increase efficiency over a fairly wide range of mass flow rates. However, IGVs need supplementary components and produce a pressure loss and a variation of the cavitation critical point [Tan *et al.* 2014].

In order to attain the required discharge, it is necessary to increase the blade angle β_1 calculate from Eq. A.16 by the angle of incidence i. Larger i values are used

for bigger D_2/D_1 ratios and for larger calculated β_1 angles (as in short blade impellers) [Lazarkiewicz & Troskolanski 1965]:

$$\beta_{1,th} = arctan\ \frac{c_{1m}}{u_{1m}}, \qquad \beta_1 = \beta_{1,th} + i_1 \tag{A.16}$$

If the approach flow angle drops below the blade angle ($i > 0$), the stagnation point is situated on the pressure surface of the blade. If the pump flow rate exceeds the shockless entry value, the incidence is negative and the stagnation point is located on the blade suction surface [Gulich 2010]. Values of i are in the range [2°, 6°] and the angle β_1 usually lies between 15° and 30° although in some cases it may be as high as 45° [Lazarkiewicz & Troskolanski 1965, Gulich 2010].

A.1.3 Impeller outlet

The theoretical head pump equation is defined as the head that a pump could generate if there were no hydraulic loss or mechanical friction during the operation of the pump. Combining this with and the velocity triangle at the outlet we obtain:

$$u_2 = \frac{c_{m2}}{\tan\beta_2} + \sqrt{\left(\frac{c_{m2}}{2\tan\beta_2}\right)^2 + gH_{th} + u_1 c_{u1}} \tag{A.17}$$

The hydraulic resistances in the passages and the disk friction of the shroud rotating in the liquid absorb a considerable part of the power of the machine and lower its efficiency. In the first model iteration, the velocity at the outlet, c_{m2}, is taken as being somewhat less than the velocity at the inlet according to the values for K_1 and K_2, within the range $c_{m2} = [0.7,\ 0.75]\ c_{m1}$ [Lazarkiewicz & Troskolanski 1965].

Since the velocity pattern in a turbomachine results from the pressure field around the blades, it can be concluded that different flow conditions are present on the pressure and suction sides of the blade. Hence, the flow is not able to follow the blades exactly. The condition of flow *blade-congruent* is theoretically reachable with an infinite number of blades [Gulich 2010]. The difference between the theoretical and absolute fluid tangential velocities is described by the following equation: slip $= c_{u2} - c_{u,\infty}$. Several values for the slip factor have been cited in the literature [Pfleiderer 1952, Wiesner 1967].

The components of the rotor exit velocity diagram are shown in Fig. A.1, which depicts the relationship between the absolute and relative velocities and flow angles.

The actual head rise is calculated iteratively in terms of the inlet and exit velocity triangles and the rotor hydraulic effectiveness, ε_h, which is the ratio of theoretical head to the theoretical head with infinite blades:

$$\varepsilon_h = \frac{H_{th}}{H_{th,\,\infty}} = \frac{1}{1 + C_p} \tag{A.18}$$

Pfleidere's correction, C_p, for a finite number of blades is calculated from the semi-empirical formula [Pfleiderer 1952]:

$$C_p = \psi \frac{r_2^2}{z\ M} \tag{A.19}$$

where r_2 denotes the external radius of the impeller with z blades, M the static moment of the midflow streamline with respect to the axis of rotation [Lazarkiewicz & Troskolanski 1965]:

$$M = \int_{r_1}^{r_2} r\,\mathrm{d}r = \frac{1}{2}(r_2^2 - r_1^2) \tag{A.20}$$

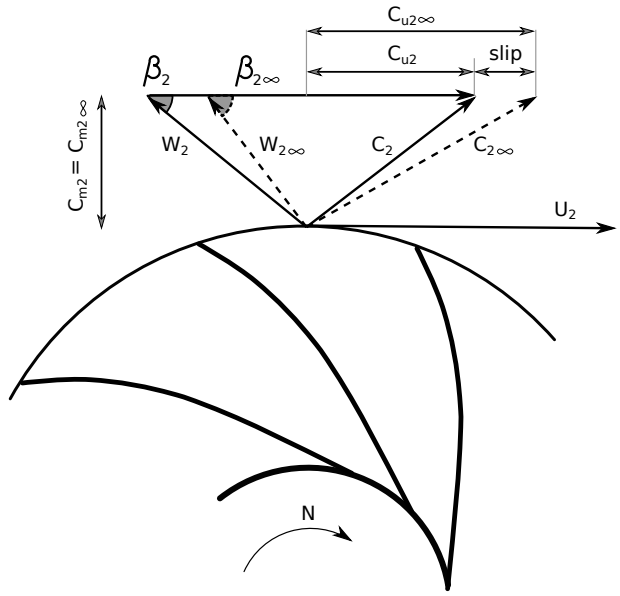

Figure A.1: Representation of the speed triangles and the the effect of the slip factor. The "slip" is defined as $\Delta c_u = c_{u2} - c_{u,\infty}$.

and the value of the coefficient ψ depends on the type of the impeller[2]. For impellers curved in three dimensions [Lazarkiewicz & Troskolanski 1965]

$$\psi = [1.0 \;\; 1.2](1 + \sin\beta_2)\left(\frac{r_1}{r_2}\right) \tag{A.21}$$

As shown by Fig. A.1, the vectorial tangential components of the fluid velocities are

$$c_{u2} = c_2 \cos\alpha_2 = u_2 + w_{u2} \tag{A.22}$$

$$w_{u2} = c_{m2} \tan\beta_{th,2} + u_2(1 - \tau) \tag{A.23}$$

The slip factor, τ, is defined as

$$\tau = 1 - \frac{\text{slip}}{u_2} \tag{A.24}$$

The deviation is the difference between the relative angle and the blade angle at the rotor exit as described by the following equation:

$$i_2 = \beta_2 - \beta_{th,2} \tag{A.25}$$

Values for the slip coefficient have been reported in the literature starting with Busemann in 1927 and later with several reviews [Wiesner 1967, von Backström 2005]:

$$\tau = 1 - \frac{(\sin\beta_{th,2})^{0.5}}{z^{\,0.7}} \tag{A.26}$$

[2]It has been confirmed experimentally that for angles $\beta < 90^\circ$ the number of the blades has negligible influence on the value of ψ. However, the influence of Reynolds number on ψ has not been satisfactorily explained. Conversely, with radial blades (having inlet and outlet angles of 90°) the slip factor is primarily caused by the Coriolis force.

Table A.2: Design values along five main streamlines.

Streamline	d_I [m]	β_1 [°]	$1+C_p$	β_2 [°]	τ_{Plf}/τ_{Sto}	w [m/s]
INT	-	19.12	1.323	9.63	1.0129	16.75
AA	0.0342	17.80	1.404	8.78	1.0128	18.34
BB	0.0324	16.78	1.490	8.13	1.0137	19.81
CC	0.0311	15.98	1.571	7.64	1.0140	21.07
EXT	0.0301	15.32	1.689	7.08	1.0183	22.71

or slip values as Pfleiderer's [Pfleiderer 1952]:

$$\text{slip}_{Pfleiderer} = \frac{g}{u_2}\frac{C_p}{1+C_p}H_{th} \tag{A.27}$$

or Stodola's:

$$\text{slip}_{Stodola} = \frac{\pi \sin \beta_{th,2} u_2}{z} \tag{A.28}$$

The relationship Eq. A.27 will be used in subsequent procedure for determine the slip coefficient. It is important to clearify that the slip does not represent a loss. It only affects magnitude of the head that the designed impeller can provide increasing the blade angle β_2.

In the case of study, the runner blades range has been chosen between 0° to +15° with the designed shape of the blade assigned at $\delta\beta = +10°$. Moreover the guide vanes opening is defined geometrically by the free distant a_0 offered by two couple of blades: from 0 mm to a maximum of 36 mm.

In order to calculate angles β_1 and β_2 and hence to determinate the shape of the blade, the impeller is divided in five elementary streams of equal rate flow. Assumed the the component velocity, c_m, maintains a constant mean value along each section [Lazarkiewicz & Troskolanski 1965] and that is used incompressible fluid, the streamlines are determined by trajectories which are able to divide the the blade in section with the same total flow size.

The results are divided by five different streamlines along the runner blade, starting from the line close to the shroud (INT) to the one at the root of the blade (EXT). The distance from the next streamline is represented by variable d that divide the blades in section tread by same amount of flow rate (Table.A.2). The higher value obtained for C_p at the tip of the blade underlines the discontinuity of the available head at the trailing edge. This has not to be considered as a loss but hydraulic consequence of having finite number of blades as described by effectiveness (Eq. A.18). The ratio of the two different slip factor provides a certain level of confidence of the results obtained concerning the estimation of the slip factor: the values of τ for Stodola (Eq. A.28) and for Pfleiderer (Eq. A.27) in agreement.

A.1.4 Blade profile

Deriaz machine runner blades are no more complex in shape than those of a Kaplan, but they have an important design feature already mentioned: adjacent blades can be made to come into contact with each other over their entire width in the closed position (Fig.2.16). This is an essential difference from the Kaplan where, in a closed position, the blades may be in contact at the periphery while a large gap remains between the blades near the hub [Deriaz & Warnock 1959b].

Basically, in the short passage the angle of divergence may suddenly increase to suddenly resulting in flow separation and relative losses; in the long passage the flow comes into contact with more surface, thereby increasing friction losses. The angle of overlap χ can be used to evaluate the case. The χ is easily shown in a 2D drawing in Fig. A.2 and usually stays in the range 30° - 40° for clean water pump [Lazarkiewicz & Troskolanski 1965].

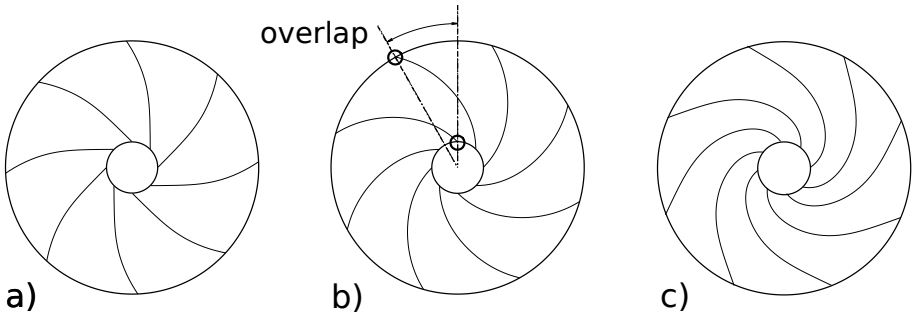

Figure A.2: Schematic representations of the overlap angle.

The blade of the impeller is shaped by adjusting the distributions of the velocity components from the leading edge to the trailing edge of the blade (Fig. A.3). The distributions must be adjusted in order to find the best blade angle distribution or stacking condition on the blade exit. After plotting all the streamlines, it might be necessary to examine the surface sketch of the blade to avoid frequent undesirable factors; the blade may be too long so that the overlap angle χ exceeds the maximum suggested and the inlet edge of the blade may deviate considerably from the correct radial direction.

One of the method to determine the shape of the blade is based as first draw on defining one or two arcs of a circle depending on the aims of the design. There are several method for determine the shape of the blade. In the *single arc method*the blade shape is drawn in the sketch Fig.A.4. From the point O we draw the line OB at the angle $\beta_1 + \beta_2$ on the circumference r_1 from any line OA. The straight line AB generate the point C as intersection with the circle r_1. The point G stays on the arc of angle β_2 of radius OA and on normal bisecting the line AC. The point G is the center of the single curvature of the blade of radius GA that may be calculated with the formula [Lazarkiewicz & Troskolanski 1965]:

$$GA = \frac{1}{2}\frac{r_2^2 - r_1^2}{r_2 cos\beta_2 - r_1 cos\beta_1} \tag{A.29}$$

After plotting all the streamlines, it could be necessary interview in the on the surface sketch of the blade to overcame frequent undesirable factor: the blade is too long so that the overlap angle χ exceeds the maximum suggested and the inlet edge of the blade may deviate considerably from the correct radial direction. It is then necessary to make iterative corrections by shortening some streamlines and lengthening others and assuming the

variation of the angle β_1 with a variation of the corresponding values of c_{m1} and the linked w_1. Specially this part is strongly affected by the designer's experience. It is necessary to iterate the analysis and select the suitable blade thickness, curvature and vane swept angles - all extremely important from the manufacturing point of view. Further attention must then be given to cavitation phenomena and the pressure distribution along the leading edge, trailing edge and the suction side of the blade adjusting the design each time as required.

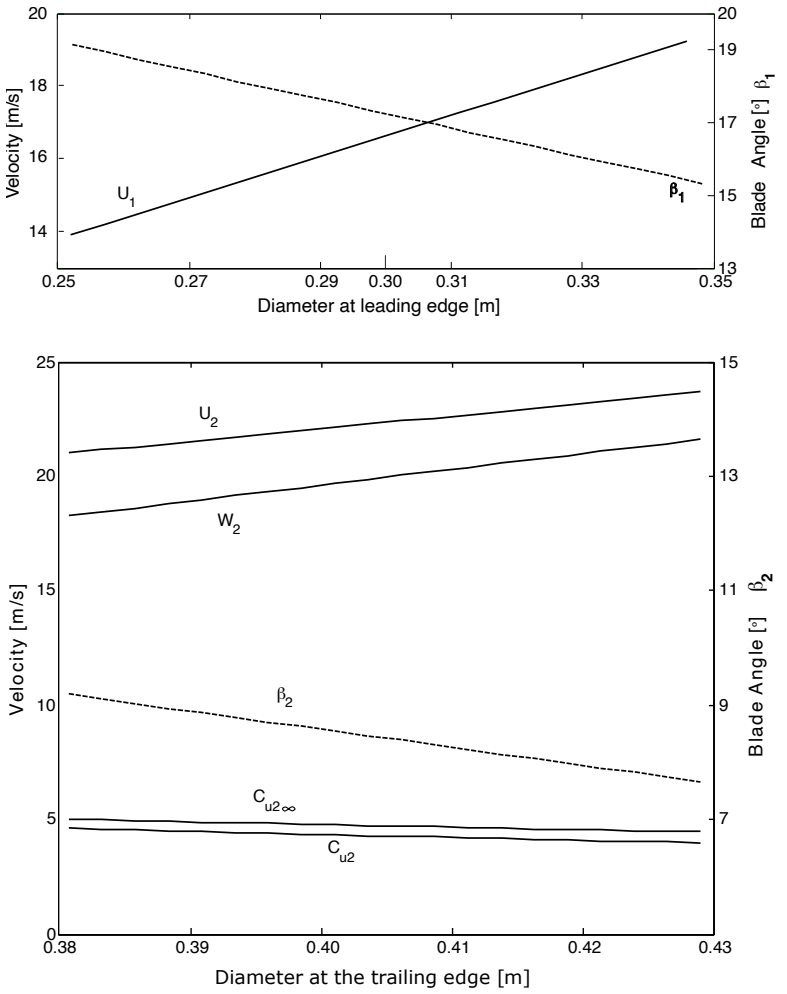

Figure A.3: Trailing edge parameters of the blade profile.

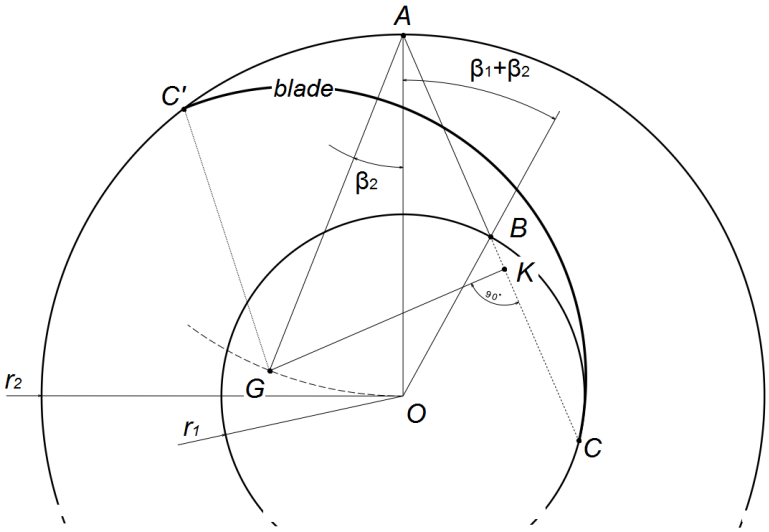

Figure A.4: Single-arc method of constructing blade profile

.

Appendix B

Fundamental notes on cavitation

A phenomenon of abnormal operation can occur in hydraulic machines, which goes under the name of cavitation and must be carefully considered because it can lead to structural damage to the machine.

Cavitation consists of a local evaporation of the fluid caused by a hydrodynamic lowering of the pressure. In fact, as a result of the motion of the fluid inside the machine, vacuum zones may occur within the fluid current. If the pressure drops below the vapour pressure of the fluid, vapour bubbles are formed which are carried by the fluid current. When the bubbles reach higher pressure zones, they implode in contact with the machine surfaces generating pressure waves that cause erosion phenomena by cavitation.

If a hydraulic system is designed to operate with a homogeneous liquid, additional vapour structures due to cavitation can be interpreted, by analogy with the case of mechanical systems, as mechanical clearances. The vapour structures are often unstable, and when they reach a region of increased pressure, they often violently collapse since the internal pressure hardly varies and remains close to the vapour pressure. The collapse can be considered analogous to shocks in mechanical systems by which clearances between neighbouring pieces disappear. Following this, a number of consequences can be expected [Franc & Michel 2006]:

- alteration of the performance of the system (reduction in lift and increase in drag of a foil, fall in turbomachinery efficiency, reduced capacity to evacuate water in spillways, energy dissipation, etc.);
- the appearance of additional forces on the solid structures;
- production of noise and vibrations;
- wall erosion, in the case of developed cavitation if the velocity difference between the liquid and the solid wall is high enough.

Consideration should also be given to the possibility of chemical corrosion due to gases dissolved in the liquid that tend to concentrate inside vapour bubbles formed during cavitation. In general, the onset of cavitation has a negative influence on the performance of the machine. In turbines it causes a decrease of the supplied power and of the efficiency, while in the pumps it leads to a decrease of the generated head and the capacity discharge. Indeed, bubbles obstacle the normal passage of the fluid and change the actual fluidynamic pattern.

However, the best machine performance conditions happen to be close to cavitation conditions and therefore the machines are often designed to operate in a field close to cavitation. This trend is consistent with the fact that for a given flow rate and head one tends to choose the fastest machine possible, as it is small in size and therefore of less weight and cost. The speed of the fluid in these machines is high and it is therefore more likely that the machine will work in close proximity to the cavitation.

For a hydraulic turbomachine the minimum pressure occurs at the point indicated by P in Fig. B.1.

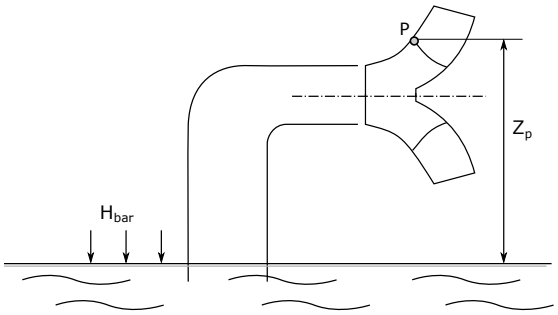

Figure B.1: Schematic view of the static head of the point P.

The value of overpressure with respect to vapour pressure in Figure P is given by the following relationship for Net Positive Suction Head Available ($NPSH_a$):

$$NPSH_a = H_{bar} - Z_p - H_{vp} \pm H_l - \frac{c_0^2}{2\rho} - H_h - FS \tag{B.1}$$

where the terms, express in energy per unit weight [J/N = m], represent:

- H_{bar}: barometric pressure of the upstream reservoir (downstream for turbines) - note that atmospheric conditions can influence the barometric pressure up to ±1% to an open-air reservoir;
- Z_p: static pressure of the point P;
- H_{vp}: vapour pressure;
- H_l: pressure losses (negative for pumps and positive for turbines);
- c_0: mean absolute speed at the point P;
- H_h: dynamic head due to internal friction of the turbomachine;
- FS: factor of safety used to account uncertainty in the hydraulic calculations and possible uneven velocity distribution. It is customary to consider no less than 20% of the $NPSH$ *required* and at least 1.5 m. $NPSH$ *required* is determined by the manufacturer at 3% drop in head by cavitation development.

Since H_h can be expressed as a function of speed through appropriate coefficients by $c_0^2/2\rho$ and $w_0^2/2\rho$, all the dynamic terms can be merged in a single term $\Delta H_h = c_0^2/2\rho + H_h$, thus:

$$NPSH_a = H_{bar} - Z_p - H_{vp} \pm H_l - \Delta H_h - FS \tag{B.2}$$

The equation in B.2 allows to evaluate the available height of the machine, that is the overpressure compared to the vapour pressure of the most disadvantaged point (P) of the machine. The boundary condition so that there is no cavitation will then occur when $h_{cav} = 0$, then at the maximum static suction height of the machine:

$$Z_p = H_{bar} - H_{vp} \pm H_l - \Delta H_h \tag{B.3}$$

The determination of the term dynamic ΔH_h is not always easy, so Thoma number is used to express the dynamic depression as a function of the machine head:

$$\sigma = \frac{\Delta H_h}{H} \tag{B.4}$$

According to the IEC standard nomenclature [Commission *et al.* 1999], Thoma number, σ, is the dimensionless term indicating the conditions of cavitation under which the machine operates. It is expressed as the ratio of Net Positive Suction specific Energy NPSE to a specific hydraulic energy $E = gH_1 - gH_2$.

$$\sigma = \frac{NPSE}{E} \simeq \frac{\frac{P_{bar} - P_{vp}}{\rho g} - Z}{H} \tag{B.5}$$

where Z is the machine setting level. Clearly every flow has a value of σ whether or not cavitation occurs. Because the specific speed N_s is an indication the shape and performance characterisation of a turbomachine it can be used to estimate σ and the onset of cavitation [Dixon & Hall 2010].

To avoid cavitation problem σ must be above a critical value σ_{cr}. Fig. B.2 shows an estimation of σ_{cr} for pumps, Kaplan turbines, Francis turbines and it illustrates a porposed region for PaTs [Chapallaz *et al.* 1992]. In fact,there exists a wide range of critical values of σ_{cr} for each value of specific speed and type of turbine due to the individual cavitation characteristics of the various runner designs [Dixon & Hall 2010]. The curves drawn are meant to assist preliminary selection procedures. The following design step is to perform tests on a reduced model of the turbomachine to determine σ_{cr}, namely when cavitation occurs or a marked decrease in efficiency is recorded [Dixon & Hall 2010]. It is also important to state that the value represented in the figure are referring to BEP operating conditions. A larger FS could solve this issue in off-design working point for reduce costs and for commercial applications [Jones *et al.* 2006].

Finally, at critical conditions, Eq. B.3 would be expressed by σ_{cr} as follow:

$$Z_{p,max} = H_{bar} - H_{vp} \pm H_l - \sigma_{cr} H \tag{B.6}$$

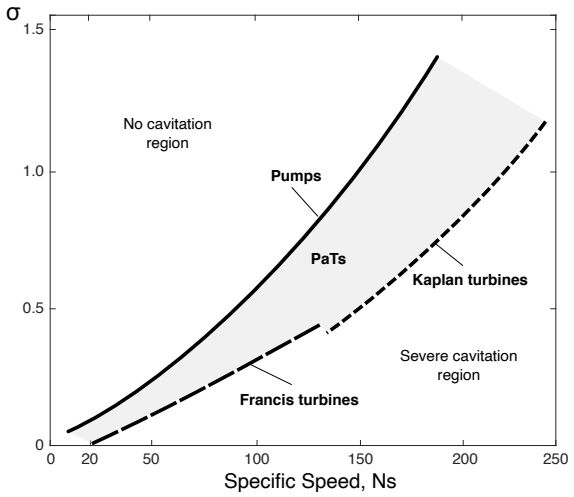

Figure B.2: Critical $\sigma_c r$ for pumps, Kaplan turbines, Francis turbines and PaTs. Adapted from [Chapallaz *et al.* 1992] .

Bibliography

[Abernethy *et al.* 1985] R. B. Abernethy, R. P. Benedict and R. B. Dowdell. *ASME Measurement Uncertainty*. Journal of Fluids Engineering, vol. 107, no. 2, pages 161–164, 06 1985. (Cited on page 109.)

[Adami *et al.* 2007] Paolo Adami, F. Martelli and S. Cecchi. *Analysis of the shroud leakage flow and mainflow interactions in high-pressure turbines using an unsteady computational fluid dynamics approach*. In Proceedings of the Institution of Mechanical Engineers, Part A: Journal of Power and Energy, 2007. (Cited on page 146.)

[Akinyele & Rayudu 2014] D. O. Akinyele and R. K. Rayudu. *Review of energy storage technologies for sustainable power networks*. Sustainable Energy Technologies and Assessments, vol. 8, pages 74–91, 2014. (Cited on page 19.)

[Alatorre-Frenk & Thomas 1990] C Alatorre-Frenk and T Thomas. *The pumps as turbines approach to small hydropower*. In World congress on Renewable energy, Reading, 1990. (Cited on pages 36 and 99.)

[Alatorre-Frenk 1994] Claudio Alatorre-Frenk. *Cost minimisation in micro-hydro systems using pumps-as-turbines*. PhD thesis, University of Warwick, 1994. (Cited on page 35.)

[Albadi *et al.* 2017] M. H. Albadi, A. S. Al-Busaidi and E. F. El-Saadany. *Using PHES to facilitate wind power integration in isolated systems - Case study*. Proceedings of the IEEE International Conference on Industrial Technology, 2017. (Cited on page 69.)

[Alemi Arani *et al.* 2019] Hamed Alemi Arani, Mohammad Fathi, Mehrdad Raisee and Seyed Ahmad Nourbakhsh. *The effect of tongue geometry on pump performance in reverse mode: An experimental study*. Renewable Energy, 2019. (Cited on pages 40 and 152.)

[Alvarado & Niemann 2015] Rodolfo Alvarado and André Niemann. *Underground Pumped-Storage Hydroelectricity Using Exisiting Coal Mining Infrastructure*. In 36th IAHR World Congress, pages 1–8, 2015. (Cited on page 13.)

[Andaroodi *et al.* 2005] M Andaroodi, Anton Schleiss and J.-L Boillat. *Standardization of civil engineering works of small hydropower plants and development of an optimization tool*. In Policy into Practice, pages 1–8, 2005. (Cited on page 58.)

[Andritz 2019] Andritz, 2019. https://www.andritz.com/resource/blob/34004/fd9cdefb249b7fa645228add62d9aa26/hy-andritz-pumps-as-turbines-en-data.pdf. (Cited on pages 34 and 86.)

[Aneke & Wang 2016] Mathew Aneke and Meihong Wang. *Energy storage technologies and real life applications - A state of the art review*. Applied Energy, vol. 179, pages 350–377, 2016. http://dx.doi.org/10.1016/j.apenergy.2016.06.097. (Cited on pages 20, 21 and 94.)

[Anilkumar *et al.* 2017a] T. T. Anilkumar, Sishaj P. Simon and Narayana Prasad Padhy. *Residential electricity cost minimization model through open well-pico turbine pumped storage system*. Applied Energy, 2017. (Cited on page 45.)

[Anilkumar *et al.* 2017b] T. T. Anilkumar, Sishaj P. Simon and Narayana Prasad Padhy. *Residential electricity cost minimization model through open well-pico turbine pumped storage system*. Applied Energy, 2017. http://dx.doi.org/10.1016/j.apenergy.2017.03.020. (Cited on page 93.)

[APERe 2019] APERe. *Association pour la Promotion des Energies Renouvelables*. Technical report, http://www.apere.org, 2019. (Cited on page 124.)

[Arani *et al.* 2019] Hamed Alemi Arani, Mohammad Fathi, Mehrdad Raisee and Seyed Ahamd Nourbakhsh. *A novel volute design for reducing radial force in pump and PAT*. In IOP Conference Series: Earth and Environmental Science, 2019. (Cited on pages 40, 152, 155 and 205.)

[Armendariz-Lopez *et al.* 2018] J. F. Armendariz-Lopez, A. P. Arena-Granados, M. E. Gonzalez-Trevizo, A. Luna-Leon and G. Bojorquez-Morales. *Energy payback time and Greenhouse Gas emissions: Studying the international energy agency guidelines architecture*. Journal of Cleaner Production, vol. 196, pages 1566–1575, 2018. (Cited on page 50.)

[Arriaga 2010] Mariano Arriaga. *Pump as turbine - A pico-hydro alternative in Lao People's Democratic Republic*. Renewable Energy, 2010. (Cited on page 38.)

[Asdrubali *et al.* 2019] F. Asdrubali, I. Ballarini, V. Corrado, L. Evangelisti, G. Grazieschi and C. Guattari. *Energy and environmental payback times for an NZEB retrofit*. Building and Environment, vol. 147, pages 461–472, 2019. (Cited on page 50.)

[Asomani *et al.* 2020] Stephen Ntiri Asomani, Jianping Yuan, Longyan Wang, Desmond Appiah and Kofi Asamoah Adu-Poku. *The impact of surrogate models on the multi-objective optimization of Pump-As-Turbine (PAT)*. Energies, 2020. (Cited on pages 39 and 152.)

[Avilés A. *et al.* 2019] Camilo Avilés A., Sebastian Oliva H. and D. Watts. *Single-dwelling and community renewable microgrids: Optimal sizing and energy management for new business models*. Applied Energy, 2019. (Cited on page 123.)

[Balkhair & Rahman 2017] Khaled S. Balkhair and Khalil Ur Rahman. *Sustainable and economical small-scale and low-head hydropower generation: A promising alternative potential solution for energy generation at local and regional scale*. Applied Energy, 2017. (Cited on page 9.)

[Barbarelli *et al.* 2016] S. Barbarelli, M. Amelio and G. Florio. *Predictive model estimating the performances of centrifugal pumps used as turbines*. Energy, 2016. (Cited on pages 36, 38 and 100.)

[Barbour *et al.* 2016] Edward Barbour, I. A.Grant Wilson, Jonathan Radcliffe, Yulong Ding and Yongliang Li. *A review of pumped hydro energy storage development in significant international electricity markets*. Renewable and Sustainable Energy Reviews, 2016. `http://dx.doi.org/10.1016/j.rser.2016.04.019`. (Cited on pages 42, 87 and 94.)

[Bardina *et al.* 1997] J. E. Bardina, P. G. Huang and T. J. Coakley. *Turbulence Modeling Validation, Testing, and Development*. Nasa Technical Memorandum, 1997. (Cited on page 155.)

[Barringer 1997] HP Barringer. *Reliability Engineering Principles. Barringer & Associates*. Inc., Vortrag, Texas, 1997. (Cited on pages 32 and 33.)

[Baumgarten & Guder 2005] Sven Baumgarten and Wolfgang Guder. *Pumpen als Turbinen*. KSB Pump company, Technik kompakt, no. 11, pages 2–9, 2005. (Cited on pages 2 and 138.)

[Baumgarten & Guder 2011] Sven Baumgarten and Wolfgang Guder. *Pumpen als Turbinen*. Technik Kompakt, no. 11, pages 2–9, 2011. (Cited on page 21.)

[Bear & Cheng 2010] Jacob Bear and Alexander H.-D. Cheng. Modeling Groundwater Flow and Contaminant Transport. Springer, 2010. (Cited on page 13.)

[Belderbos *et al.* 2016] Andreas Belderbos, Erik Delarue and William D'haeseleer. *Calculating the levelized cost of electricity storage*. In Energy: Expectations and Uncertainty, 39th IAEE International Conference, Jun 19-22, 2016. International Association for Energy Economics, 2016. (Cited on page 136.)

[Bhandari *et al.* 2015] Khagendra P. Bhandari, Jennifer M. Collier, Randy J. Ellingson and Defne S. Apul. *Energy payback time (EPBT) and energy return on energy invested (EROI) of solar photovoltaic systems: A systematic review and meta-analysis*, 2015. (Cited on page 50.)

[Bhattacharjee & Nayak 2019] Subhadeep Bhattacharjee and Pabitra Kumar Nayak. *PV-pumped energy storage option for convalescing performance of hydroelectric station under declining precipitation trend*. Renewable Energy, 2019. (Cited on page 45.)

[Binama *et al.* 2017] Maxime Binama, Wen Tao Su, Xiao Bin Li, Feng Chen Li, Xian Zhu Wei and Shi An. *Investigation on pump as turbine (PAT) technical aspects for micro hydropower schemes: A state-of-the-art review*. Renewable and Sustainable Energy Reviews, vol. 79, pages 148–179, 2017. (Cited on pages 2, 21, 31, 38, 92 and 99.)

[Bodeux *et al.* 2017] Sarah Bodeux, Estanislao Pujades, Philippe Orban, Serge Brouyère and Alain Dassargues. *Interactions between groundwater and the cavity of an old slate mine used as lower reservoir of an UPSH (Underground Pumped Storage Hydroelectricity): A modelling approach*. Engineering Geology, vol. 217, pages 71–80, 2017. (Cited on page 14.)

[Boehmke & Greenwell 2019] Brad Boehmke and Brandon M Greenwell. Hands-on machine learning with r. CRC Press, 2019. (Cited on pages 158 and 168.)

[Botterud *et al.* 2014] Audun Botterud, Todd Levin and Vladimir Koritarov. *Pumped storage hydropower: benefits for grid reliability and integration of variable renewable energy*. Technical report, Argonne National Lab.(ANL), Argonne, IL (United States), 2014. (Cited on page 139.)

[Bozorgi *et al.* 2013] A. Bozorgi, E. Javidpour, A. Riasi and A. Nourbakhsh. *Numerical and experimental study of using axial pump as turbine in Pico hydropower plants*. Renewable Energy, vol. 53, pages 258–264, 2013. http://dx.doi.org/10.1016/j.renene.2012.11.016. (Cited on page 9.)

[Braun & Hazelroth 2015] Gerry Braun and Stan Hazelroth. *Energy Infrastructure Finance: Local Dollars for Local Energy*. Electricity Journal, 2015. (Cited on pages 41 and 42.)

[Brennen 1994] C. E. Brennen. Hydrodynamics of pumps. Concepts ETI, Inc., 1 édition, 1994. (Cited on pages 148, 184, 189 and 209.)

[Brugel 2020] Brugel. *Brussels regulator for the electricity and gas markets.*, 2020. (Cited on pages 124, 125 and 126.)

[Brun *et al.* 2015] Pierre Brun, Bernard Mahiou and Michel Ayoub. *The Petit Canal Sea water pumped storage plant in Guadeloupe island: a tool to allow the intermittent renewable energy development*. Houille Blanche, pages 7–13, 2015. (Cited on page 11.)

[BSG 2020] BSG. *Bendigo Mines Pumped Hydro Project - Bendigo Sustainability Group*, 2020. https://www.bsg.org.au/bendigo-pumped-hydro-project/ [Accessed 2020-01-02]. (Cited on page 13.)

[Buckingham 1914] E. Buckingham. *On physically similar systems; Illustrations of the use of dimensional equations*. Physical Review, vol. 4, no. 4, pages 345–376, 1914. http://dx.doi.org/10.1103/PhysRev.4.345. (Cited on page 101.)

[Bueno & Carta 2006] C. Bueno and J. A. Carta. *Wind powered pumped hydro storage systems, a means of increasing the penetration of renewable energy in the Canary Islands*, 2006. (Cited on page 1.)

[Burke 2017] James J. Burke. Power distribution engineering: Fundamentals and applications. CRC Press, 2017. (Cited on page 125.)

[Callio 2020] Callio. *Energy Storage in Mine - Northern Ostrobothnia Centre for Economic Development Transport envionment*, 2020. https://callio.info [Accessed 2020-01-20]. (Cited on page 13.)

[Capata & Sciubba 2015] Roberto Capata and Enrico Sciubba. *Experimental fitting of the re-scaled Balje maps for low-reynolds radial turbomachinery*. Energies, vol. 8, no. 8, pages 7986–8000, 2015. http://dx.doi.org/10.3390/en8087986. (Cited on page 210.)

[Capelo *et al.* 2017] Bernardo Capelo, Modesto Pérez-Sánchez, João F.P. Fernandes, Helena M. Ramos, P. Amparo López-Jiménez and P. J.Costa Branco. *Electrical behaviour of the pump working as turbine in off grid operation.* Applied Energy, 2017. http://dx.doi.org/10.1016/j.apenergy.2017.10.039. (Cited on pages 33 and 92.)

[Capurso *et al.* 2019a] T Capurso, L Bergamini and M Torresi. *Design and CFD performance analysis of a novel impeller for double suction centrifugal pumps.* Nuclear Engineering and Design, vol. 341, pages 155–166, 2019. (Cited on pages 40 and 205.)

[Capurso *et al.* 2019b] Tommaso Capurso, Lorenzo Bergamini, Sergio Mario Camporeale, Bernardo Fortunato and Marco Torresi. *CFD analysis of the performance of a novel impeller for a double suction centrifugal pump working as a turbine.* In 13 th European Conference on Turbomachinery Fluid dynamics & Thermodynamics. EUROPEAN TURBOMACHINERY SOCIETY, 2019. (Cited on page 40.)

[Capurso *et al.* 2019c] Tommaso Capurso, Michele Stefanizzi, Giuseppe Pascazio, Sergio Ranaldo, Sergio M. Camporeale, Bernardo Fortunato and Marco Torresi. *Slip factor correction in 1-D Performance prediction model for paTs.* Water (Switzerland), 2019. (Cited on pages 155 and 205.)

[Carravetta *et al.* 2012] Armando Carravetta, Giuseppe Del Giudice, Oreste Fecarotta and Helena M. Ramos. *Energy Production in Water Distribution Networks: A PAT Design Strategy.* Water Resources Management, vol. 26, no. 13, pages 3947–3959, 2012. http://dx.doi.org/10.1007/s11269-012-0114-1. (Cited on pages 34, 92 and 93.)

[Carravetta *et al.* 2013] Armando Carravetta, Giuseppe Del Giudice, Oreste Fecarotta and Helena M. Ramos. *Pump as turbine (PAT) design in water distribution network by system effectiveness.* Water (Switzerland), vol. 5, no. 3, pages 1211–1225, 2013. http://dx.doi.org/10.3390/w5031211. (Cited on pages 34, 38 and 92.)

[Carravetta *et al.* 2018] A. Carravetta, O. Fecarotta and H. M. Ramos. *A new low-cost installation scheme of PATs for pico-hydropower to recover energy in residential areas.* Renewable Energy, 2018. (Cited on pages 38 and 93.)

[Castillo 1964] M. Castillo. *El Aprovechamiento Hidroeléctrico del tajo inferior y las centrales des bombeo*, 1964. Revista de obras publicas. (Cited on page 29.)

[Ceglia *et al.* 2020] F. Ceglia, P. Esposito, E. Marrasso and M. Sasso. *From smart energy community to smart energy municipalities: Literature review, agendas and pathways.* Journal of Cleaner Production, vol. 254, 2020. (Cited on page 53.)

[Chang *et al.* 2013] Martin K. Chang, Joshua D. Eichman, Fabian Mueller and Scott Samuelsen. *Buffering intermittent renewable power with hydroelectric generation: A case study in California.* Applied Energy, 2013. (Cited on page 1.)

[Chapallaz *et al.* 1992] Jean-Marc Chapallaz, Peter Eichenberger and Gerhard Fischer. Manual on pumps used as turbines. Vieweg Braunschweig, Germany, 1992. (Cited on pages 184, 185 and 223.)

[Chazarra *et al.* 2018] Manuel Chazarra, Juan I. Pérez-Díaz, Javier García-González and Roland Praus. *Economic viability of pumped-storage power plants participating in the secondary regulation service.* Applied Energy, 2018. http://dx.doi.org/10.1016/j.apenergy.2018.02.025. (Cited on pages 1, 93, 115 and 183.)

[Chen *et al.* 2009] Haisheng Chen, Thang Ngoc Cong, Wei Yang, Chunqing Tan, Yongliang Li and Yulong Ding. *Progress in electrical energy storage system: A critical review.* Progress in Natural Science, 2009. (Cited on page 69.)

[Chen *et al.* 2015] Gang Chen, Ryan P. Powers, Luis M.T. de Carvalho and Brice Mora. *Spatiotemporal patterns of tropical deforestation and forest degradation in response to the operation of the Tucuruí hydroelectricdam in the Amazon basin.* Applied Geography, 2015. (Cited on page 45.)

[Childs 1962] SM Childs. *Convert pumps to turbines and recover HP.* Hydrocarbon Processing and Petroleum Refiner, vol. 41, no. 10, pages 173–174, 1962. (Cited on pages 35, 36 and 99.)

[Choi *et al.* 2013] Hyen Jun Choi, Mohammed Asid Zullah, Hyoung Woon Roh, Pil Su Ha, Sueg Young Oh and Young Ho Lee. *CFD validation of performance improvement of a 500 kW Francis turbine.* Renewable Energy, vol. 54, pages 111–123, 2013. http://dx.doi.org/10.1016/j.renene.2012.08.049. (Cited on page 77.)

[Ciocan *et al.* 2012] Gabriel Dan Ciocan, Olivier Teller and Francois Czerwinski. *Variable speed pump-turbines technology.* UPB Scientific Bulletin, Series D: Mechanical Engineering, 2012. http://dx.doi.org/10.1111/j.2042-3306.1984.tb01832.x. (Cited on pages 2 and 93.)

[ČKD Blansko 2012a] ČKD Blansko. *Company's reference project - ČKD Blansko Engineering.* http://www.ckdlh.cz/en/about-us/companys-reference-projects, 2012. [Visited online: 30 November 2017]. (Cited on page 29.)

[ČKD Blansko 2012b] ČKD Blansko. *New hydropower projects under construction in India*, 2012. [Visisted online: 30 November 2017]. (Cited on page 29.)

[Coll-Mayor *et al.* 2007] Debora Coll-Mayor, Mia Paget and Eric Lightner. *Future intelligent power grids: Analysis of the vision in the European Union and the United States.* Energy Policy, vol. 35, no. 4, pages 2453–2465, 2007. (Cited on page 123.)

[Commision 2020] European Commision. *EU climate action and the European Green Deal.* EU Action, 2020. (Cited on page 8.)

[Commission *et al.* 1999] International Electrotechnical Commission*et al. Hydraulic Turbines, Storage Pumps and Pump-Turbines-Model Acceptance Tests.* IEC 60193 Standard - International Electrotechnical Commission Geneva, vol. 60193, page 578, Nov. 1999. (Cited on pages 101, 106, 210, 211 and 223.)

[Commission 2011] European Commission. *A Roadmap for moving to a competitive low carbon economy in 2050.* COM(2011) 112 final, 2011. (Cited on page 54.)

[CONCERE-CNC 2019] CONCERE-CNC. *Plan national energie-climat PNEC 2030.* Technical report, Service public federal Economie, 2019. (Cited on page 53.)

[Connolly *et al.* 2011] D Connolly, H Lund, P Finn, B V Mathiesen and M Leahy. *Practical operation strategies for pumped hydroelectric energy storage (PHES) utilising electricity price arbitrage.* Energy Policy, vol. 39, no. 7, pages 4189–4196, 2011. (Cited on page 59.)

[Cornut *et al.* 2006] Pierre Cornut, David Aubin, Mathieu Van Criekingen, Olivier Dubois, Christian Dessouroux and Jean Michel Decroly. *Public, "club" and individual management of natural resources: The case of domestic rainwater tanks in Belgium.* Erde, vol. 137, no. 4, pages 273–292, 2006. (Cited on page 133.)

[Corporation 2015] IFC International Finance Corporation. Hydroelectric power: A guide for developers and investors. World Bank, 2015. (Cited on pages 58 and 59.)

[Corsini *et al.* 2013] Alessandro Corsini, Giovanni Delibra and Anthony G Sheard. *A critical review of computational methods and their application in industrial fan design.* International Scholarly Research Notices, vol. 2013, 2013. (Cited on page 155.)

[CREG 2020] CREG. *Commission de régulation de l'électricité et du gaz*, 2020. (Cited on pages 60 and 125.)

[Daily & Nece 1960] James W Daily and Ronald E Nece. *Chamber dimension effects on induced flow and frictional resistance of enclosed rotating disks.* ASME Journal of Fluids Engineering, vol. 82, pages 217–232, 1960. (Cited on page 146.)

[Dassault 2019] Dassault. *Catia V5 R20 - Dassault Systemes*, 2019. (Cited on page 144.)

[Davis *et al.* 1951] H Davis, H Kottas and A Moody. *The Influence of Reynolds Number on the Performance of Turbomachinery.* Trans. ASME, vol. 73, July 1951. (Cited on page 210.)

[de Almeida *et al.* 2003] Anibal T. de Almeida, Paula Fonseca, Hugh Falkner and Paolo Bertoldi. *Market transformation of energy-efficient motor technologies in the EU.* Energy Policy, no. 6, pages 563–575, 2003. (Cited on pages 52 and 53.)

[de Oliveira e Silva & Hendrick 2016] Guilherme de Oliveira e Silva and Patrick Hendrick. *Pumped hydro energy storage in buildings.* Applied Energy, vol. 179, pages 1242–1250, 2016. http://dx.doi.org/10.1016/j.apenergy.2016.07.046. (Cited on pages 10, 94, 136 and 139.)

[de Oliveira e Silva 2017] Guilherme de Oliveira e Silva. Characterisation and optimisation of electrical energy storage in residential buildings. Université libre de Bruxelles, 2017. (Cited on page 126.)

[De Vos 2015] Kristof De Vos. *Negative Wholesale Electricity Prices in the German, French and Belgian Day-Ahead, Intra-Day and Real-Time Markets.* Electricity Journal, vol. 28, no. 4, pages 36–50, 2015. (Cited on page 53.)

[Deane *et al.* 2010] J. P. Deane, B. P. Ó Gallachóir and E. J. McKeogh. *Techno-economic review of existing and new pumped hydro energy storage plant.* Renewable and Sustainable Energy Reviews, vol. 14, no. 4, pages 1293–1302, 2010. (Cited on pages 2, 54, 58 and 94.)

[Dehghani-Sanij *et al.* 2019] AR Dehghani-Sanij, E Tharumalingam, MB Dusseault and R Fraser. *Study of energy storage systems and environmental challenges of batteries.* Renewable and Sustainable Energy Reviews, vol. 104, pages 192–208, 2019. (Cited on page 203.)

[Deloitte 2018] Deloitte. *Assessing the economic conditions of Belgian pumped-hydroelectric storage: comparative review of profitability drivers in Europe and evaluation of the current situation*, 2018. (Cited on page 59.)

[Denton 2010] John D Denton. *Some limitations of turbomachinery CFD.* In Turbo Expo: Power for Land, Sea, and Air, volume 44021, pages 735–745, 2010. (Cited on page 155.)

[Derakhshan & Nourbakhsh 2008a] Shahram Derakhshan and Ahmad Nourbakhsh. *Experimental study of characteristic curves of centrifugal pumps working as turbines in different specific speeds.* Experimental Thermal and Fluid Science, vol. 32, no. 3, pages 800–807, 2008. http://dx.doi.org/10.1016/j.expthermflusci.2007.10.004. (Cited on pages 35, 36, 47, 100, 146 and 160.)

[Derakhshan & Nourbakhsh 2008b] Shahram Derakhshan and Ahmad Nourbakhsh. *Theoretical, numerical and experimental investigation of centrifugal pumps in reverse operation.* Experimental Thermal and Fluid Science, vol. 32, no. 8, pages 1620–1627, 2008. http://dx.doi.org/10.1016/j.expthermflusci.2008.05.004. (Cited on pages 36, 100 and 102.)

[Derakhshan *et al.* 2009] Shahram Derakhshan, Bijan Mohammadi and Ahmad Nourbakhsh. *Efficiency improvement of centrifugal reverse pumps.* Journal of Fluids Engineering, Transactions of the ASME, 2009. (Cited on pages 39 and 40.)

[Deriaz & Warnock 1959a] P. Deriaz and J. G. Warnock. *Reversible Pump-Turbines for Sir Adam Beck-Niagara Pumping-Generating Station.* Journal of Basic Engineering, vol. 81, no. 4, pages 521–529, 1959. (Cited on pages 17 and 71.)

[Deriaz & Warnock 1959b] P Deriaz and JG Warnock. *Reversible pump turbine for Sir Adam Beck-Niagara Pumping-Generating Station.* Trans. ASME, vol. 81, no. 1, pages 521–533, December 1959. (Cited on pages 25, 27, 28 and 217.)

[Deriaz 1926] Paul Deriaz. *Hydraulic turbine*, December 21 1926. US Patent 1611341. (Cited on page 24.)

[Deriaz 1955] Paul Deriaz. *La turbine-pompe réversible axio-centrifuge à pas variable: le développement d'une nouvelle machine hydraulique.* Bulletin technique de la Suisse romande, vol. Ecole polytechnique federale Zurich: centenaire 1855-1955, fasc.no 2, no. 81, pages 382–387, December 1955. http://dx.doi.org/10.5169/seals-61375. (Cited on pages 18, 25, 26 and 27.)

[Dieck 1997] Ronald H. Dieck. *Measurement uncertainty models.* ISA Transactions, vol. 36, no. 1, pages 29 – 35, 1997. (Cited on page 108.)

[Dixon & Hall 2010] S. Dixon and Cesare Hall. Fluid mechanics and thermodynamics of turbomachinery. Elsevier, 2010. (Cited on pages 19, 64, 86, 105 and 223.)

[DNIT - National Department of Transport Infrastructure 2018] DNIT - National Department of Transport Infrastructure. *Tucuruí Locks-PA 2020:1.*, 2018. (Cited on page 46.)

[Doshi *et al.* 2017] Ashish Doshi, Salim Channiwala and Punit Singh. *Inlet impeller rounding in pumps as turbines: An experimental study to investigate the relative effects of blade and shroud rounding.* Experimental Thermal and Fluid Science, 2017. (Cited on pages 40, 146 and 160.)

[Dostál & Ladányi 2018] Zdeněk Dostál and Libor Ladányi. *Demands on energy storage for renewable power sources.* Journal of Energy Storage, vol. 18, pages 250–255, 2018. http://dx.doi.org/0.1016/j.est.2018.05.003. (Cited on page 8.)

[Dunlap 2020] Richard A Dunlap. Renewable Energy: Volumes 2. Morgan & Claypool Publishers, 2020. (Cited on page 67.)

[e Silva & Hendrick 2016] Guilherme e Silva and Patrick and Hendrick. *Lead-acid batteries coupled with photovoltaics for increased electricity self-sufficiency in households.* Applied Energy, vol. 178, pages 856–867, 2016. https://doi.org/10.1016/j.apenergy.2016.06.003. (Cited on pages 1 and 8.)

[Economie SPF 2019] Economie SPF. *Service Public Fédéral Economie, P.M.E., Classes moyennes et Energie - Federal Public Service Economy, S.M.E.s, Self-employed and Energy*, 2019. (Cited on page 53.)

[EEX GROUP 2020] EEX GROUP. *EPEX SPOT*, 2020. (Cited on page 127.)

[ELIA Group 2020] ELIA Group. *Belgian transmission system operator*, 2020. (Cited on pages 43, 126, 127 and 128.)

[Elia.be 2018] Elia.be. *Solar-PV power generation data*, 2018. http://www.elia.be/en/grid-data/power-generation/solar-power-generation-data/graph. [Accessed 28 Feb. 2018]. (Cited on pages 130 and 131.)

[Energiasalv 2020] Energiasalv. *The Muuga seawater pumped hydroelectricity storage project - Energiasalv Pakri OU*, 2020. http://www.tuuleenergia.ee/en/2018/02/ [Accessed 2020-01-20]. (Cited on page 13.)

[Engeda 1988] A Engeda. *Auswahl von Kreiselpumpen als Turbinen.* Pumpentagung Karlsruhe, vol. A6, 1988. (Cited on page 102.)

[Engelken *et al.* 2016] Maximilian Engelken, Benedikt Römer, Marcus Drescher, Isabell M. Welpe and Arnold Picot. *Comparing drivers, barriers, and opportunities of business models for renewable energies: A review.* Renewable and Sustainable Energy Reviews, vol. 60, pages 795–809, jul 2016. (Cited on page 53.)

[ENGIE 2020] ENGIE. *Electrabel - La centrale d?acc umulation par pompage de Coo*, 2020. (Cited on page 55.)

[Erskine & Van Rooy 2004] A Erskine and O Van Rooy. *The complete refurbishment of Culligran underground hydropower station.* In Hydropower Developments - New Projects, Rehabilitation, and Power Recovery, volume 2004 6, pages 125–140, 2004. (Cited on pages 31, 71 and 76.)

[European Commission 2010] European Commission. Energy 2020, 2010. https://doi.org/10.2833/78930. (Cited on page 8.)

[European Commission 2012a] European Commission. *Energy roadmap 2050*, 2012. http://dx.doi.org/10.2833/10759. (Cited on pages 1, 41 and 197.)

[European Commission 2012b] European Commission. *Liberalisation of the electricity and gas markets*, 2012. http://ec.europa.eu/competition/sectors/energy/overview_en.html [Accessed 2020-01-15]. (Cited on page 52.)

[European Committee for Standardization 2002] European Committee for Standardization. *Eurocode 1: Actions on structures - Part 1-1: General actions - Densities, self-weight, imposed loads for buildings*. European Committee for Standardization, vol. 2, no. 2005, pages 1–5, 2002. (Cited on page 133.)

[European Parliament and the Council 2013] European Parliament and the Council. *Report from the Commission to the European Parliament, the Council, the European economic and social Committee and the Committee of the regions: Renewable energy progress report*, 2013. (Cited on page 8.)

[Favrel 2019] A. Favrel. Prediction of hydro-acoustic resonances in hydropower plants by a new approach based on the concept of swirl number. Journal of Hydraulic Research, 2019. doi:10.1080/00221686.2018.1555556. (Cited on pages 67 and 68.)

[Ferreira *et al.* 2013] Helder Lopes Ferreira, Raquel Garde, Gianluca Fulli, Wil Kling and Joao Pecas Lopes. *Characterisation of electrical energy storage technologies*. Energy, vol. 53, pages 288–298, 2013. http://dx.doi.org/10.1016/j.energy.2013.02.037. (Cited on page 139.)

[Fessenden 1917] Reginald A. Fessenden. *System of Storing Power*, 1917. (Cited on page 12.)

[Fischer *et al.* 2015] David Fischer, Andreas Härtl and Bernhard Wille-Haussmann. *Model for electric load profiles with high time resolution for German households*. Energy and Buildings, 2015. (Cited on page 127.)

[FPS-Public Health 2017] FPS-Public Health. *4th National Climate Survey*, 2017. (Cited on pages 123 and 124.)

[Franc & Michel 2006] Jean-Pierre Franc and Jean-Marie Michel. Fundamentals of cavitation, volume 76. Springer science & Business media, 2006. (Cited on pages 157 and 221.)

[Friedman 1991] Jerome H Friedman. *Multivariate adaptive regression splines*. The annals of statistics, pages 1–67, 1991. (Cited on pages 157 and 168.)

[Geth *et al.* 2015] F. Geth, T. Brijs, J. Kathan, J. Driesen and R. Belmans. *An overview of large-scale stationary electricity storage plants in Europe: Current status and new developments*. Renewable and Sustainable Energy Reviews, 2015. (Cited on page 54.)

[Gicquel *et al.* 2011] Laurent Y.M. Gicquel, N. Gourdain, J.-F. Boussuge, H. Deniau, G. Staffelbach, P. Wolf and Thierry Poinsot. *High performance parallel computing of flows in complex geometries*. Comptes Rendus Mécanique, vol. 339, no. 2-3, pages 104–124, 2011. https://doi.org/10.1016/j.crme.2010.11.006. (Cited on pages 78 and 80.)

[Giosio *et al.* 2015] D. R. Giosio, A. D. Henderson, J. M. Walker, P. A. Brandner, J. E. Sargison and P. Gautam. *Design and performance evaluation of a pump-as-turbine micro-hydro test facility with incorporated inlet flow control*. Renewable Energy, vol. 78, pages 1–6, 2015. (Cited on pages 2, 38, 39, 147 and 160.)

[Golub *et al.* 1979] Gene H Golub, Michael Heath and Grace Wahba. *Generalized cross-validation as a method for choosing a good ridge parameter*. Technometrics, vol. 21, no. 2, pages 215–223, 1979. (Cited on page 159.)

[Grid-Scale Energy Storage 2018] Grid-Scale Energy Storage. *Gravity Power Module - Energy Storage*, 2018. http://www.gravitypower.net. [Accessed 03 July 2018]. (Cited on page 12.)

[Gronemeier & Jäckel 2013] Klaus Gronemeier and Bernhard Jäckel. *Pumped-Storage Hydroelectricityplan <Martelange> Pre-Feasibility-Study*, sep 2013. (Cited on pages 57 and 70.)

[Grover 1980] KM Grover. *Conversion of pumps to turbines*. GSA Inter corp., Katonah, New York, 1980. (Cited on page 35.)

[Gulich 2010] J. F. Gulich. Centrifugal pumps. Springer, 2 édition, 2010. (Cited on pages 72, 102, 146, 149, 151, 160, 167, 210, 213 and 214.)

[Guo *et al.* 2017] Pengcheng Guo, Zhaoning Wang, Longgang Sun and Xingqi Luo. *Characteristic analysis of the efficiency hill chart of Francis turbine for different water heads*. Advances in Mechanical Engineering, vol. 9, no. 2, page 1687814017690071, 2017. (Cited on page 15.)

[Hager 2014] Willi Hager. Hydraulicians in europe 1800-2000: Volume 2, volume 2. CRC Press, 2014. (Cited on page 24.)

[Hanckock 1963] J Hanckock. *Centrifugal pump or water turbine*. Pipe Line News, vol. 6, pages 25–27, 1963. (Cited on page 35.)

[Hendriks *et al.* 2018] Mary Hendriks*et al. South Australia leads the way in energy storage integration*. Energy News, vol. 36, no. 1, page 15, 2018. (Cited on page 11.)

[Hergt 1982] P Hergt. *The influence of the volute casing on the position of the best efficiency point*. In 11th IAHR Symposium, Amsterdam, volume 3, 1982. (Cited on page 35.)

[Hickernell & xiang Yuan 1997] Fred J. Hickernell and Ya xiang Yuan. *A Simple Multistart Algorithm for Global Optimization*, 1997. (Cited on page 159.)

[Hiratsuka *et al.* 1993] Akitaka Hiratsuka, Takashi Arai and Tsukasa Yoshimura. *Seawater pumped-storage power plant in Okinawa island, Japan*. Engineering geology, vol. 35, no. 3-4, pages 237–246, 1993. (Cited on page 11.)

[Höglund-Isaksson *et al.* 2012] Lena Höglund-Isaksson, Wilfried Winiwarter, Pallav Purohit, Peter Rafaj, Wolfgang Schöpp and Zbigniew Klimont. *EU low carbon roadmap 2050: Potentials and costs for mitigation of non-CO2greenhouse gas emissions*. Energy Strategy Reviews, vol. 1, no. 2, pages 97–108, 2012. http://dx.doi.org/10.1016/j.esr.2012.05.004. (Cited on page 7.)

[Houdeline & Verzeroli 1999] J Houdeline and J Verzeroli. Deriaz pump-turbine for naussac 2 plant in france. ALSTOM Power Hydro, 1999. (Cited on pages 29, 72, 73, 75 and 209.)

[Huang & Yu 2017] Dikai Huang and Tai Yu. *Study on energy payback time of building integrated photovoltaic system*. Procedia Engineering, vol. 205, pages 1087–1092, 2017. (Cited on page 50.)

[Huart 2019] Michel Huart. *Les chercheurs belges avancent sur la flexibilité*, 2019. (Cited on pages 127 and 128.)

[Hughes 2010] Darren Hughes. *Investigation into the feasibility of a West of Ireland Pumped Storage System*, 2010. (Cited on page 11.)

[IEA 2020] IEA. *Renewables Information 2020 Overview*. Climate Change 2013 - The Physical Science Basis, vol. 53, no. 9, pages 1–30, 2020. (Cited on pages 1, 9, 52, 85 and 87.)

[Iliev *et al.* 2019] Igor Iliev, Chirag Trivedi and Ole Gunnar Dahlhaug. *Variable-speed operation of Francis turbines: A review of the perspectives and challenges*. Renewable and Sustainable Energy Reviews, vol. 103, pages 109–121, 2019. (Cited on page 71.)

[Imanishi 1964] Atsuo Imanishi. *Fuji hydraulic turbine and generator II*. http://www.fujielectric.com/company/tech_archives/pdf/10-06/FER-10-06-198-1964.pdf, 1964. (Cited on pages 29 and 31.)

[International Energy Agency 2013] International Energy Agency. *World Energy Outlook: Executive Summary*. Paris: International Energy Agency, pages 1–7, 2013. (Cited on page 123.)

[International Energy Agency 2018] International Energy Agency. *Renewable information: database documentation 2018*, 2018. https://www.iea.org. (Cited on page 52.)

[Ioakimidis & Genikomsakis 2018] Christos S Ioakimidis and Konstantinos N Genikomsakis. *Integration of seawater pumped-storage in the energy system of the Island of São Miguel (Azores)*. Sustainability, vol. 10, no. 10, page 3438, 2018. (Cited on page 11.)

[IRENA 2019] IRENA. *Renewable energy statistics*. International Renewable Energy Agency, 2019. www.irena.org/Publications. (Cited on pages 7 and 8.)

[Jain & Patel 2014] Sanjay V. Jain and Rajesh N. Patel. *Investigations on pump running in turbine mode: A review of the state-of-the-art*. Renewable and Sustainable Energy Reviews, vol. 30, pages 841–868, 2014. http://dx.doi.org/10.1016/j.rser.2013.11.030. (Cited on pages 2, 38, 92 and 140.)

[Jain *et al.* 2015] Sanjay V. Jain, Abhishek Swarnkar, Karan H. Motwani and Rajesh N. Patel. *Effects of impeller diameter and rotational speed on performance of pump running in turbine mode*. Energy Conversion and Management, 2015. (Cited on pages 2, 39, 40, 183 and 184.)

[Jannuzzi & de Melo 2013] Gilberto de Martino Jannuzzi and Conrado Augustus de Melo. *Grid-connected photovoltaic in Brazil: Policies and potential impacts for 2030*. Energy for Sustainable Development, vol. 17, no. 1, pages 40–46, 2013. (Cited on page 46.)

[Japikse *et al.* 1997] David Japikse, William D Marscher and Raymond B Furst. *Centrifugal pump design and performance*. Wilder, VT: Concepts ETI, Inc, 1997., 1997. (Cited on pages 147, 148 and 185.)

[Jaumotte *et al.* 1994] André L. Jaumotte, Pierre Decock, Lucien Megnint and Georges Verdurand. *Turbines hydrauliques: Description et évolution [Hydraulic turbine: description and evolution]*. Archives, 1994. (Cited on pages 19, 64, 71 and 86.)

[Javed *et al.* 2020] Muhammad Shahzad Javed, Tao Ma, Jakub Jurasz and Muhammad Yasir Amin. *Solar and wind power generation systems with pumped hydro storage: Review and future perspectives*, 2020. (Cited on pages 1 and 45.)

[J.Kirejczyk 2001] J.Taulan J.Kirejczyk J.Verzeroli. Non-polluting pump turbine: Naussac 2. Hydrovision 2000, Charlotte - USA, alstom power hydro édition, 2001. (Cited on page 75.)

[Johnson *et al.* 2018] M Johnson, P O'Connor and Rocio Uria-Martinez. *2017 Hydropower Market Report - Update (April)*. Technical report, Oak Ridge National Laboratory, 2018. (Cited on page 201.)

[Johnson 2016] Richard W Johnson. Handbook of fluid dynamics. Crc Press, 2016. (Cited on pages 17 and 22.)

[Johnston & Dean 1966] J. F. Johnston and R. C. Dean. *Losses an vaneless diffusers of centrifugal compressors and pumps: Analysis, experiment, and design*. Journal of Engineering for Gas Turbines and Power, vol. 88, no. 1, pages 49–60, 1966. (Cited on pages 147 and 148.)

[Jones *et al.* 2006] Garr M Jones, Robert L Sanks, Bayard E Bosserman, George Tchobanoglous*et al.* Pumping station design. Gulf Professional Publishing, 2006. (Cited on page 223.)

[Jonsson *et al.* 2012] P. P. Jonsson, B. G. Mulu and M. J. Cervantes. *Experimental investigation of a Kaplan draft tube - Part II: Off-design conditions*. Applied Energy, vol. 94, pages 71–83, 2012. https://doi.org/10.1016/j.apenergy.2012.01.032. (Cited on page 15.)

[Jülch 2016] Verena Jülch. *Comparison of electricity storage options using levelized cost of storage (LCOS) method*. Applied Energy, 2016. http://dx.doi.org/10.1016/j.apenergy.2016.08.165. (Cited on pages 118 and 139.)

[Kaldellis *et al.* 2010] J. K. Kaldellis, D. Zafirakis and E. Kondili. *Energy pay-back period analysis of stand-alone photovoltaic systems.* Renewable Energy, vol. 35, no. 7, pages 1444–1454, 2010. (Cited on page 50.)

[Karassik *et al.* 2001] Igor J Karassik, Joseph P Messina, Paul Cooper, Charles C Heald*et al.* Pump handbook, volume 3. McGraw-Hill New York, 2001. (Cited on pages 112, 185 and 206.)

[Katsaprakakis & Christakis 2014] Dimitris Al Katsaprakakis and Dimitris G Christakis. *Seawater pumped storage systems and offshore wind parks in islands with low onshore wind potential. A fundamental case study.* Energy, vol. 66, pages 470–486, 2014. (Cited on page 11.)

[Katsaprakakis *et al.* 2013] Dimitris Al Katsaprakakis, Dimitris G Christakis, Ioannis Stefanakis, Petros Spanos and Nikos Stefanakis. *Technical details regarding the design, the construction and the operation of seawater pumped storage systems.* Energy, vol. 55, pages 619–630, 2013. (Cited on page 11.)

[Khan *et al.* 2018] Agha Salman M. Khan, Remco A. Verzijlbergh, Ozgur Can Sakinci and Laurens J. De Vries. *How do demand response and electrical energy storage affect (the need for) a capacity market?* Applied Energy, vol. 214, pages 39–62, 2018. http://dx.doi.org/10.1016/j.apenergy.2018.01.057. (Cited on page 201.)

[Kocaman & Modi 2017] Ayse Selin Kocaman and Vijay Modi. *Value of pumped hydro storage in a hybrid energy generation and allocation system.* Applied Energy, 2017. (Cited on page 1.)

[Koohi-Kamali *et al.* 2013] Sam Koohi-Kamali, VV Tyagi, NA Rahim, NL Panwar and H Mokhlis. *Emergence of energy storage technologies as the solution for reliable operation of smart power systems: A review.* Renewable and Sustainable Energy Reviews, vol. 25, pages 135–165, 2013. https://doi.org/10.1016/j.rser.2013.03.056. (Cited on page 28.)

[Kroposki *et al.* 2012] Ben Kroposki, Kari Burman, Jamie Keller, Alicen Kandt, John Glassmire and Peter Lilienthal. *Integrating High Levels of Renewables in to the Lanai Electric Grid.* Technical report, National Renewable Energy Lab.(NREL), Golden, CO (United States), 2012. (Cited on page 11.)

[Kuhn *et al.* 2013] Max Kuhn, Kjell Johnson*et al.* Applied predictive modeling, volume 26. Springer, 2013. (Cited on pages 158 and 168.)

[Landry 2015] C. Landry. Hydroacoustic modeling of a cavitation vortex rope for a francis turbine. EPFL PhD Thesis 6547, 2015. (Cited on page 66.)

[Lazarkiewicz & Troskolanski 1965] Stephen Lazarkiewicz and A. T Troskolanski. Impeller pumps. Pergamon Press, 1965. (Cited on pages 23, 72, 148, 185, 213, 214, 215, 216 and 217.)

[Levieux *et al.* 2019] Luis Ignacio Levieux, Fernando A. Inthamoussou and Hernán De Battista. *Power dispatch assessment of a wind farm and a hydropower plant: A case study in Argentina.* Energy Conversion and Management, vol. 180, pages 391–400, 2019. (Cited on page 1.)

[Lewinsky-Kesslitz 1987] H.P. Lewinsky-Kesslitz. *Pumps as turbines for small-scale hydropower plants.* WASSERWIRTSCHAFT, vol. 77, no. 10 , Oct. 1987, pages 531–537, 1987. (Cited on pages 36 and 100.)

[Lian *et al.* 2019] Jijian Lian, Yusheng Zhang, Chao Ma, Yang Yang and Evance Chaima. *A review on recent sizing methodologies of hybrid renewable energy systems*, 2019. (Cited on pages 1 and 45.)

[Limpens & Jeanmart 2018] Gauthier Limpens and Hervé Jeanmart. *Electricity storage needs for the energy transition: An EROI based analysis illustrated by the case of Belgium.* Energy, 2018. (Cited on pages 52, 123 and 128.)

[Lipej & Poloni 2000] A Lipej and C Poloni. *Design of Kaplan runner using multiobjective genetic algorithm optimization.* Journal of Hydraulic Research, vol. 38, no. 1, pages 73–79, 2000. http://dx.doi.org/10.1080/00221680009498361. (Cited on page 209.)

[Lobanoff & Ross 2013] Val S Lobanoff and Robert R Ross. Centrifugal pumps: design and application. Elsevier, 2013. (Cited on page 185.)

[Luthander *et al.* 2015] Rasmus Luthander, Joakim Widén, Daniel Nilsson and Jenny Palm. *Photovoltaic self-consumption in buildings: A review.* Applied Energy, 2015. (Cited on page 124.)

[Manolakos *et al.* 2004] D. Manolakos, G. Papadakis, D. Papantonis and S. Kyritsis. *A stand-alone photovoltaic power system for remote villages using pumped water energy storage.* Energy, vol. 29, no. 1, pages 57–69, 2004. (Cited on page 10.)

[Marchi & Simpson 2013] Angela Marchi and Angus R. Simpson. *Correction of the EPANET Inaccuracy in Computing the Efficiency of Variable Speed Pumps.* Journal of Water Resources Planning and Management, vol. 139, no. 4, pages 456–459, 2013. http://dx.doi.org/10.1061/(ASCE)WR.1943-5452.0000273. (Cited on pages 115 and 183.)

[Maricic *et al.* 2009] Tihomir Maricic, Don Haber and Stanislav Pejovic. *Niagara pump generating station proven functionality unique in Canada.* In Electrical Power & Energy Conference (EPEC), 2009 IEEE, pages 1–6. IEEE, 2009. (Cited on pages 29 and 30.)

[Martin 2011] Gregory G. Martin. *Underground pumped hydroelectric energy storage.* Technical report, Pacific Northwest Lab., Richland, WA (USA), 2011. (Cited on pages 12, 13, 18 and 55.)

[Martins *et al.* 2008] F. R. Martins, E. B. Pereira, S. A.B. Silva, S. L. Abreu and Sergio Colle. *Solar energy scenarios in Brazil, Part one: Resource assessment.* Energy Policy, vol. 36, no. 8, pages 2853–2864, 2008. (Cited on page 46.)

[Mathworks 2016] Mathworks. *MATLAB version 9.1. (R2016b).* Natick, Massachusetts, vol. 698, 2016. (Cited on page 159.)

[Matsuo *et al.* 2020] Yuhji Matsuo, Seiya Endo, Yu Nagatomi, Yoshiaki Shibata, Ryoichi Komiyama and Yasumasa Fujii. *Investigating the economics of the power sector under high penetration of variable renewable energies.* Applied Energy, 2020. (Cited on pages 1 and 52.)

[Meeus *et al.* 2012] Leonardo Meeus, Isabel Azevedo, Claudio Marcantonini, Jean Michel Glachant and Manfred Hafner. *EU 2050 Low-Carbon Energy Future: Visions and Strategies.* Electricity Journal, vol. 25, no. 5, pages 57–63, 2012. (Cited on page 54.)

[Menéndez *et al.* 2020] Javier Menéndez, Jesús Manuel Fernández-Oro and Jorge Loredo. *Economic feasibility of underground pumped storage hydropower plants providing ancillary services.* Applied Sciences (Switzerland), 2020. (Cited on pages 58 and 59.)

[Mercier *et al.* 2019] Thomas Mercier, Clément Hardy, Pierre Van Tichelen, Mathieu Olivier and Emmanuel De Jaeger. *Control of variable-speed pumps used as turbines for flexible grid-connected power generation.* Electric Power Systems Research, vol. 176, page 105962, 2019. (Cited on pages 115 and 183.)

[MHI Japan 2017] MHI Japan. *Individual Units for Hydro in Japan.* http://globalenergyobservatory.org, 2017. [Visited online: 30 November 2017]. (Cited on page 29.)

[Miao *et al.* 2015] Sen Chun Miao, Jun Hu Yang, Guang Tai Shi and Ting Ting Wang. *Blade profile optimization of pump as turbine.* Advances in Mechanical Engineering, 2015. (Cited on page 39.)

[Mikhail *et al.* 2001] S Mikhail, MG Khalafallah and M El-Nady. *Disk friction loss in centrifugal and mixed flow pumps.* In Seventh International Congress on Fluid Dynamics and Propulsion, pages 1–6, 2001. (Cited on page 146.)

[Min 1984] A. P. N Min. *Ondergrondse Pomp Accumulatie Centrale: effectiviteitsverbetering dmv verschillende pomp-turbinevermogens.* Master thesis, DTU, 1984. (Cited on page 13.)

[Minakov *et al.* 2015] A. V. Minakov, D. V. Platonov, A. A. Dekterev, A. V. Sentyabov and A. V. Zakharov. *The numerical simulation of low frequency pressure pulsations in the high-head Francis turbine.* Computers and Fluids, 2015. http://dx.doi.org/10.1016/j.compfluid.2015.01.007. (Cited on page 77.)

[Miyagawa *et al.* 1998] K Miyagawa, N Fukuda, K Tsuji, K Suzuki and J Saotome. *Development of a Deriaz type pump-turbine with high head, large capacity and variable speed.* In Proceedings of the XIX IAHR symposium on hydraulic machinery and cavitation, page 39, 1998. (Cited on pages 28 and 87.)

[Montomoli *et al.* 2015] Francesco Montomoli, Mauro Carnevale, Antonio D'Ammaro, Michela Massini and Simone Salvadori. Uncertainty Quantification in Computational Fluid Dynamics and Aircraft Engines. Springer, 2015. (Cited on page 146.)

[Motwani *et al.* 2013] K. H. Motwani, S. V. Jain and R. N. Patel. *Cost analysis of pump as turbine for pico hydropower plants - A case Study.* In Procedia Engineering, volume 51, pages 721–726, 2013. http://dx.doi.org/10.1016/j.proeng.2013.01.103. (Cited on pages 2, 33, 92 and 138.)

[Mou *et al.* 2016] Jiegang Mou, Zhenfu Chen, Yunqing Gu and Tianxing Fan. *Effect of sealing ring clearance on pump performance.* World Pumps, vol. 2016, no. 3, pages 38–41, 2016. (Cited on page 202.)

[Muller *et al.* 2016] A. Muller, Arthur Favrel, Christian Landry and Francois Avellan. *Fluid structure interaction mechanisms leading to dangerous power swings in Francis turbines at full load.* Journal of Fluids and Structures, vol. 69, 2016. (Cited on page 67.)

[Muntean *et al.* 2015] Sebastian Muntean, Ionel Draghici, Gheorghiţă Gînga, Liviu Eugen Anton and Alexandru Baya. *Hydrodynamic design of a storage pump impeller using inverse method and experimental investigation of the global performances.* WasserWirtschaft Extra, vol. 1, pages 28–32, 2015. (Cited on page 209.)

[National Electric Energy Agency 2018] National Electric Energy Agency. *Normative Resolution 2.433/2018*, 2018. (Cited on pages xv and 50.)

[Nautiyal *et al.* 2011] Himanshu Nautiyal, Anoop Kumar and Sanjay Yadav. *Experimental Investigation of Centrifugal Pump Working as Turbine for Small Hydropower Systems.* Energy Science and Technology, vol. 1, no. 1, pages 79–86, 2011. http://dx.doi.org/10.3968/j.est.1923847920110101.006. (Cited on pages 21, 35, 36, 38 and 92.)

[Nicolet *et al.* 2002] Christophe Nicolet, François Avellan, Philippe Allenbach, Alain Sapin and Jean Jacques Simond. *New tools for the simulation of transient phenomena in francis turbine power plants.* In Proceedings of the 21st IAHR Symposium on Hydraulic Machinery and Systems, Lausanne, Switzerland, volume 1, pages 519–528. International Association For Hydraulic Research, 2002. (Cited on page 65.)

[Nicolet *et al.* 2007] C Nicolet, B. Greiveldinger, J. J. Herou, B. Kawkabani, P. Allenbach, J. Simond and F. Avellan. *High-Order Modeling of Hydraulic Power Plant in Islanded Power Network.* IEEE Transactions on Power Systems, vol. 22, pages 1870–1880, 2007. (Cited on page 66.)

[Nicolet 2007] C. Nicolet. Hydroacoustic modelling and numerical simulation of unsteady operation of hydroelectric systems. EPFL Ph.D. Thesis, 2007. (Cited on pages 65 and 66.)

[Niedzica 2017] Elektrownia Wodna Niedzica. http://www.zzw-niedzica.com.pl/elektrownia.htm, 2017. [Visited online: 30 November 2017]. (Cited on page 29.)

[Nikolaidis & Poullikkas 2018] Pavlos Nikolaidis and Andreas Poullikkas. *Cost metrics of electrical energy storage technologies in potential power system operations.* Sustainable Energy Technologies and Assessments, 2018. (Cited on page 69.)

[Nolden *et al.* 2020] C. Nolden, J. Barnes and J. Nicholls. *Community energy business model evolution: A review of solar photovoltaic developments in England.* Renewable and Sustainable Energy Reviews, 2020. (Cited on page 126.)

[Nourbakhsh *et al.* 2007] Ahmad Nourbakhsh, André Jaumotte, Charles Hirsch and Hamideh B Parizi. Turbopumps and pumping systems. Springer Science & Business Media, 2007. (Cited on pages 24, 99, 111 and 147.)

[Nourbakhsh *et al.* 2010a] A Nourbakhsh, S Derakhshan, E Javidpour and A Riasi. *Centrifugal & axial pumps used as turbines in small hydropower stations.* In Hidroenergia 2010: International Congress on Small Hydropower International Conference and Exhibition on Small Hydropower, pages 16–19, 2010. (Cited on pages 34, 36, 91 and 99.)

[Nourbakhsh *et al.* 2010b] Ahmad Nourbakhsh, Shahram Derakhshan, E Javidpour and Alireza Riasi. *Centrifugal & axial pumps used as turbines in small hydropower stations.* In Hidroenergia 2010: International Congress on Small Hydropower International Conference and Exhibition on Small Hydropower, pages 16–19, 2010. (Cited on page 20.)

[Novara *et al.* 2019] D. Novara, A. Carravetta, A. McNabola and H. M. Ramos. *Cost Model for Pumps as Turbines in Run-of-River and In-Pipe Microhydropower Applications.* Journal of Water Resources Planning and Management, vol. 145, no. 5, page 04019012, 2019. (Cited on page 21.)

[NUM 2013] NUMECA International. *User manual FINE/Turbo 90.3*, 2013. (Cited on pages 78, 79 and 80.)

[NUM 2019a] NUMECA International. *User manual AutoGrid5^{TM} 13.2*, 2019. (Cited on page 151.)

[NUM 2019b] NUMECA International. *User manual FINE/Open 8.1*, 2019. (Cited on pages 155 and 156.)

[NUM 2019c] NUMECA International. *User manual Hexpress^{TM} 8.1*, 2019. (Cited on page 152.)

[NUM 2019d] NUMECA International. *User manual HexpressView^{TM} 8.1*, 2019. (Cited on page 152.)

[O. Thapar 2017] O. Thapar. *Modern Hydroelectric Engineering Practice In India: Electro-Mechanical Works.* http://ahec.org.in/publ/Modern_Hydroelectric_Engineering_Practice_Prof_OD_Thapar/Volume_I/Chapter-3_Hydraulic_Turbine_Classification_and_Selection.pdf, 2017. [Visited online: 30 November 2017]. (Cited on page 29.)

[OECD 2019] OECD. *OECD Environmental Data.* Technical report, Organisation for Economic Co-operation and Development, 2019. https://stats.oecd.org/ [Accessed 2020-02-06]. (Cited on page 202.)

[Ogayar & Vidal 2009] B Ogayar and P G Vidal. *Cost determination of the electro-mechanical equipment of a small hydro-power plant.* Renewable Energy, vol. 34, no. 1, pages 6–13, 2009. (Cited on pages 57 and 58.)

[Ogayar *et al.* 2009] B. Ogayar, P. G. Vidal and J. C. Hernandez. *Analysis of the cost for the refurbishment of small hydropower plants.* Renewable Energy, 2009. (Cited on pages 58 and 66.)

[Olsen *et al.* 2015] Jan Olsen, Kasper Paasch, Benny Lassen and Christian T. Veje. *A new principle for underground pumped hydroelectric storage.* Journal of Energy Storage, vol. 2, pages 54–63, 2015. http://dx.doi.org/10.1016/j.est.2015.06.003. (Cited on pages 11 and 12.)

[Orchard & Klos 2009] Bryan Orchard and Sander Klos. *Pumps as turbines for water industry.* World Pumps, vol. 2009, no. 8, pages 22–23, 2009. http://dx.doi.org/10.1016/S0262-1762(09)70283-4. (Cited on pages 33, 92 and 99.)

[Otero & Sanz 2000] L. Otero and P. D. Sanz. *High-pressure shift freezing. Part 1. Amount of ice instantaneously formed in the process.* Biotechnology Progress, vol. 16, no. 6, pages 1030–1036, 2000. http://dx.doi.org/10.1021/bp000122v. (Cited on page 107.)

[Paish 2002] O. Paish. *Micro-hydropower: Status and prospects.* Proceedings of the Institution of Mechanical Engineers, Part A: Journal of Power and Energy, vol. 216, no. 1, pages 31–40, 2002. (Cited on pages 17, 33, 34, 86, 92 and 140.)

[Palizban & Kauhaniemi 2016] Omid Palizban and Kimmo Kauhaniemi. *Energy storage systems in modern grids?Matrix of technologies and applications.* Journal of Energy Storage, vol. 6, pages 248–259, 2016. (Cited on pages 53 and 203.)

[Patel *et al.* 2015] JB Patel, RN Mevada, D Sardana and VP Rajput. *Experimental and numerical investigation of centrifugal pump performance in reverse mode.* Int. J. Adv. Technol. Eng. Sci, vol. 3, no. 1, pages 1066–1072, 2015. (Cited on page 40.)

[Peng *et al.* 2002a] Guoyi Peng, Shuliang Cao, Masaru Ishizuka and Shinji Hayama. *Design optimization of axial flow hydraulic turbine runner: Part I-an improved Q3D inverse method.* International Journal for Numerical Methods in Fluids, vol. 39, no. 6, pages 517–531, 2002. http://dx.doi.org/10.1002/fld.342. (Cited on page 209.)

[Peng *et al.* 2002b] Guoyi Peng, Shuliang Cao, Masaru Ishizuka and Shinji Hayama. *Design optimization of axial flow hydraulic turbine runner: Part II-multi-objective constrained optimization method.* International Journal for Numerical Methods in Fluids, vol. 39, no. 6, pages 533–548, 2002. http://dx.doi.org/10.1002/fld.343. (Cited on page 209.)

[Peng *et al.* 2013] Jinqing Peng, Lin Lu and Hongxing Yang. *Review on life cycle assessment of energy payback and greenhouse gas emission of solar photovoltaic systems*, 2013. (Cited on page 50.)

[Pereira 2019] J. Gomes Pereira. Predicting the dynamic behavior of francis turbine generating units. EPFL PhD Thesis 7131, 2019. (Cited on page 67.)

[Pérez-Díaz *et al.* 2015] Juan I. Pérez-Díaz, M. Chazarra, J. García-González, G. Cavazzini and A. Stoppato. *Trends and challenges in the operation of pumped-storage hydropower plants.* Renewable and Sustainable Energy Reviews, 2015. http://dx.doi.org/10.1016/j.rser.2015.01.029. (Cited on pages 1, 93, 115 and 183.)

[Pérez-Sánchez *et al.* 2017] Modesto Pérez-Sánchez, Francisco Javier Sánchez-Romero, Helena M. Ramos and P. Amparo López-Jiménez. *Energy recovery in existing water networks: Towards greater sustainability.* Water (Switzerland), 2017. http://dx.doi.org/10.3390/w9020097. (Cited on page 34.)

[Pfleiderer 1952] C. Pfleiderer. Turbomachines. Springer-Verlag, 1952. (Cited on pages 210, 214 and 216.)

[Pickard 2011] William F Pickard. *The history, present state, and future prospects of underground pumped hydro for massive energy storage.* Proceedings of the IEEE, vol. 100, no. 2, pages 473–483, 2011. (Cited on page 12.)

[Pinto *et al.* 2017] Runa Nivea Pinto, Asif Afzal, Loyan Vinson D?Souza, Zahid Ansari and AD Mohammed Samee. *Computational fluid dynamics in turbomachinery: a review of state of the art.* Archives of Computational Methods in Engineering, vol. 24, no. 3, pages 467–479, 2017. (Cited on page 155.)

[Poulain *et al.* 2018] Angélique Poulain, Jean Raynald de Dreuzy and Pascal Goderniaux. *Pump Hydro Energy Storage systems (PHES) in groundwater flooded quarries.* Journal of Hydrology, 2018. http://dx.doi.org/10.1016/j.jhydrol.2018.02.025. (Cited on page 93.)

[Poullikkas 1995] Andreas Poullikkas. *Surface roughness effects on induced flow and frictional resistance of enclosed rotating disks.* ASME Journal of Fluids Engineering, vol. 117, pages 526–528, 1995. (Cited on page 146.)

[Poullikkas 2013a] Andreas Poullikkas. *A comparative overview of large-scale battery systems for electricity storage*. Renewable and Sustainable Energy Reviews, 2013. (Cited on page 69.)

[Poullikkas 2013b] Andreas Poullikkas. *A comparative overview of large-scale battery systems for electricity storage*. Renewable and Sustainable Energy Reviews, vol. 27, pages 778–788, 2013. (Cited on page 203.)

[Pugliese *et al.* 2016] Francesco Pugliese, Francesco De Paola, Nicola Fontana, Maurizio Giugni and Gustavo Marini. *Experimental characterization of two Pumps As Turbines for hydropower generation*. Renewable Energy, vol. 99, pages 180–187, 2016. http://dx.doi.org/10.1016/j.renene.2016.06.051. (Cited on pages 2, 36, 38 and 92.)

[Pujades *et al.* 2017] Estanislao Pujades, Philippe Orban, Sarah Bodeux, Pierre Archambeau, Sébastien Erpicum and Alain Dassargues. *Underground pumped storage hydropower plants using open pit mines: How do groundwater exchanges influence the efficiency?* Applied Energy, vol. 190, pages 135–146, 2017. (Cited on pages 11, 13, 14 and 93.)

[Pujades *et al.* 2018] Estanislao Pujades, Philippe Orban, Pierre Archambeau, Sebastien Erpicum and Alain Dassargues. *Numerical study of the Martelange mine to be used as underground reservoir for constructing an Underground Pumped Storage Hydropower plant*. Advances in Geosciences, vol. 45, pages 51–56, 2018. (Cited on pages 12, 14, 69 and 70.)

[Pujades *et al.* 2020] Estanislao Pujades, Philippe Orban, Pierre Archambeau, Vasileios Kitsikoudis, Sebastien Erpicum and Alain Dassargues. *Underground pumped-storage hydropower (UPSH) at the Martelange mine (Belgium): Interactions with groundwater flow*. Energies, 2020. (Cited on page 70.)

[Qian *et al.* 2016] Zhongdong Qian, Fan Wang, Zhiwei Guo and Jie Lu. *Performance evaluation of an axial-flow pump with adjustable guide vanes in turbine mode*. Renewable Energy, 2016. (Cited on page 38.)

[Ramos & Borga 1999] H. Ramos and A. Borga. *Pumps as turbines: An unconventional solution to energy production*. Urban Water, 1999. (Cited on page 38.)

[Rehman *et al.* 2015a] Shafiqur Rehman, Luai M. Al-Hadhrami and Md Mahbub Alam. *Pumped hydro energy storage system: A technological review*. Renewable and Sustainable Energy Reviews, vol. 44, pages 586–598, 2015. (Cited on pages 8, 45, 69, 87 and 94.)

[Rehman *et al.* 2015b] Shafiqur Rehman, Luai M Al-Hadhrami and Md Mahbub Alam. *Pumped hydro energy storage system: A technological review*. Renewable and Sustainable Energy Reviews, vol. 44, pages 586–598, 2015. (Cited on page 29.)

[Reynders *et al.* 2017] Glenn Reynders, Jan Diriken and Dirk Saelens. *Generic characterization method for energy flexibility: Applied to structural thermal storage in residential buildings*. Applied Energy, vol. 198, pages 192–202, 2017. https://doi.org/10.1016/j.apenergy.2017.04.061. (Cited on page 8.)

[Roberts *et al.* 1965] C M Roberts, E B Wilson and J G Wiltshire. *DESIGN ASPECTS OF THE STRATHFARRAR AND KILMORACK HYDROELECTRIC SCHEME.* Proceedings of the Institution of Civil Engineers, vol. 30, no. 3, pages 449–487, 1965. http://dx.doi.org/10.1680/iicep.1965.9522. (Cited on pages 29 and 30.)

[Rossi & Renzi 2017] Mosè Rossi and Massimiliano Renzi. *Analytical Prediction Models for Evaluating Pumps-As-Turbines (PaTs) Performance*. In Energy Procedia, 2017. (Cited on page 38.)

[RTBF 2017] RTBF. *Le climat, votre préoccupation: les résultats de notre enquête*, 2017. (Cited on page 124.)

[Rudy 2013] Jason Rudy. *Package sklearn-contrib-py-earth Version 0.1.0*, 2013. (https://contrib.scikit-learn.org/py-earth/index.html. (Cited on page 159.)

[Rüther & Zilles 2011] Ricardo Rüther and Roberto Zilles. *Making the case for grid-connected photovoltaics in Brazil.* Energy Policy, vol. 39, no. 3, pages 1027–1030, 2011. (Cited on page 46.)

[Ruud 1976] F. O. Ruud. *Vibration of Deriaz Pumps at Dos Amigos Pumping Plant.* Journal of Fluids Engineering, vol. 98, no. 8, pages 674–679, 1976. http://dx.doi.org/10.1115/1.3448447. (Cited on page 29.)

[Sabihuddin *et al.* 2015] Siraj Sabihuddin, Aristides E. Kiprakis and Markus Mueller. *A numerical and graphical review of energy storage technologies.* Energies, 2015. (Cited on page 69.)

[Sandia 2016] Sandia. *DOE Global Energy Storage Database.* Database, page 1464 projects, 2016. (Cited on page 9.)

[Schiffer *et al.* 2017] Jürgen Schiffer, Helmut Benigni and Helmut Jaberg. *Analysis of the leakage behavior of francis turbines and its impact on the hydraulic efficiency?a validation of an analytical model based on computational fluid dynamics results.* Journal of Fluids Engineering, vol. 139, no. 2, 2017. (Cited on page 78.)

[Schlunegger & Thöni 2013] Hans Schlunegger and Andreas Thöni. *100 MW full-size converter in the Grimsel 2 pumped-storage plant.* In Proc. 2013 HYDRO Conference, 2013. (Cited on pages 28 and 87.)

[Schmiedl 1988a] E Schmiedl. *Pumpen als Turbinen.* Pumpentagung, Karlsruhe (A6), 1988. (Cited on page 102.)

[Schmiedl 1988b] E Schmiedl. *Serien-Kreiselpumpen im Turbinenbetrieb.* Pumpentagung: Karlsruhe, Germany, 1988. (Cited on pages 35, 36, 38 and 100.)

[Schoenung & Hassenzahl 2003] S.M. Schoenung and W.V. Hassenzahl. *Long- vs. Short-Term Energy Storage Technologies Analysis A Life-Cycle Cost Study A Study for the DOE Energy Storage Systems Program.* Technical report August, Sandia National Laboratories, 2003. http://infoserve.sandia.gov/sand{_}doc/2003/032783.pdf. (Cited on page 24.)

[Scorza 2019] Daniel Scorza. *Stranded Nuclear Asset Provides Opportunity for Seawater Pumped Storage.* http:www.powermag.com/solving-renewable-transmission-constraints-with-water-infrastructure, 2019. [Visited online: 21 December 2020]. (Cited on page 11.)

[Service public de Wallonie 2020] Service public de Wallonie. *Géoportail de la Wallonie*, 2020. https://geoportail.wallonie.be [Accessed 2020-06-29]. (Cited on page 57.)

[Shah *et al.* 2013] S. R. Shah, S. V. Jain, R. N. Patel and V. J. Lakhera. *CFD for centrifugal pumps: A review of the state-of-the-art.* In Procedia Engineering, 2013. (Cited on pages 80 and 205.)

[Sharma 1985] K Sharma. *Small hydroelectric projects - use of centrifugal pumps as turbines.* Kirloskar Electric Co., Bangalore, India, 1985. (Cited on pages 35, 36 and 100.)

[Sibelga 2020] Sibelga. *Brussels' distribution system operator.*, 2020. (Cited on page 126.)

[Singh & Nestmann 2010] Punit Singh and Franz Nestmann. *An optimization routine on a prediction and selection model for the turbine operation of centrifugal pumps.* Experimental Thermal and Fluid Science, vol. 34, no. 2, pages 152–164, 2010. http://dx.doi.org/10.1016/j.expthermflusci.2009.10.004. (Cited on pages 20 and 100.)

[Singh & Nestmann 2011] Punit Singh and Franz Nestmann. *Internal hydraulic analysis of impeller rounding in centrifugal pumps as turbines.* Experimental Thermal and Fluid Science, 2011. (Cited on page 40.)

[Singh *et al.* 2004] Punit Singh, J. T. Kshirsagar, Saban Caglar, Franz Nestmann and Natanasabapathi. *Experimental and computational studies of the effect of 'casing eye rib' on the swirl flow at the exit of a pump as turbine.* In Proceedings of the ASME Heat Transfer/Fluids Engineering Summer Conference 2004, HT/FED 2004, 2004. (Cited on page 40.)

[Singh 2005] Punit Singh. *Optimization of internal hydraulics and of system design for PUMPS AS TURBINES with field implementation.* PhD thesis, Institut für Wasserwirtschaft und Kulturtechnik, Universität Karlsruhe (TH), 2005. (Cited on page 40.)

[Skotak & Stegner 2014] A Skotak and P Stegner. *Choosing Turbines for Low-Head Pumped-Storage Plants.* HRW-Hydro Review Worldwide, vol. 22, January 2014. (Cited on pages 25 and 27.)

[Slovenske Elektrarne 2017] Slovenske Elektrarne. https://www.seas.sk/liptovska-mara-hpp, 2017. [Visited online: 30 November 2017]. (Cited on page 29.)

[Spänhoff 2014] Bernd Spänhoff. *Current status and future prospects of hydropower in Saxony (Germany) compared to trends in Germany, the European Union and the World.* Renewable and Sustainable Energy Reviews, 2014. http://dx.doi.org/10.1016/j.rser.2013.10.035. (Cited on page 14.)

[Spriet 2014] Jan Spriet. *A Feasibility study of pumped hydropower energy storage systems in underground cavities.* Master thesis, Bruface (ULB-VUB Faculty of Engineering, 2014. (Cited on pages 13, 55, 56, 58, 70 and 202.)

[Statista 2018] Statista. *Prices of electricity for the industry in Belgium from 2008 to 2018.* Technical report, www.statista.com, 2018. (Cited on page 128.)

[Statistical Office of the European Communities 2018] Statistical Office of the European Communities. *EUROSTAT: Electricity prices for household consumers - bi-annual data*, 2018. http://appsso.eurostat.ec.europa.eu/nui/show.do?dataset=nrg_pc_204&lang=en. [Accessed 03 July 2018]. (Cited on page 139.)

[Štefan *et al.* 2020] David Štefan, Mosè Rossi, Martin Hudec, Pavel Rudolf, Alessandra Nigro and Massimiliano Renzi. *Study of the internal flow field in a pump-as-turbine (PaT): Numerical investigation, overall performance prediction model and velocity vector analysis.* Renewable Energy, 2020. (Cited on pages 144 and 152.)

[Steimes *et al.* 2016a] J. Steimes, G. Al Zohbi, P. Hendrick, B. Haut and S. Doucement. *Cost and revenue breakdown for a pumped hydroelectric energy storage installation in Belgium.* In Sustainable Hydraulics in the Era of Global Change - Proceedings of the 4th European Congress of the International Association of Hydroenvironment engineering and Research, IAHR 2016, 2016. (Cited on pages 54, 55 and 70.)

[Steimes *et al.* 2016b] J. Steimes, P. Hendrick, B. Haut and S. Doucement. *Cost and revenue breakdown for a pumped hydroelectric energy storage installation in Belgium.* In Sustainable Hydraulics in the Era of Global Change - Proceedings of the 4th European Congress of the International Association of Hydroenvironment engineering and Research, IAHR 2016, 2016. http://dx.doi.org/10.1201/b21902-49. (Cited on pages 58 and 93.)

[Stepanoff 1957a] A. J. Stepanoff. Centrifugal and axial flow pumps, design and applications. John Wiley and Sons Inc, 1 édition, 1957. (Cited on pages 35, 36, 72, 100 and 213.)

[Stepanoff 1957b] Alexey Joakim Stepanoff. Centrifugal and axial flow pumps: theory, design, and application. Wiley New York, 1957. (Cited on page 38.)

[Stoppato *et al.* 2016] Anna Stoppato, Alberto Benato, Nicola Destro and Alberto Mirandola. *A model for the optimal design and management of a cogeneration system with energy storage.* Energy and Buildings, vol. 124, pages 241–247, 2016. http://dx.doi.org/10.1016/j.enbuild.2015.09.036. (Cited on pages 1 and 10.)

[Sulzer 2019] Sulzer, 2019. https://www.sulzer.com/en/shared/applications/2017/05/29/09/07/hydraulic-power-recovery-turbine. (Cited on pages 34 and 86.)

[Sun-Sheng *et al.* 2012] Yang Sun-Sheng, Kong Fan-Yu, Fu Jian-Hui and Xue Ling. *Numerical research on effects of splitter blades to the influence of pump as turbine.* International Journal of Rotating Machinery, 2012. (Cited on page 40.)

[Sun *et al.* 2019] Kaiqi Sun, Ke Jun Li, Jiuping Pan, Yong Liu and Yilu Liu. *An optimal combined operation scheme for pumped storage and hybrid wind-photovoltaic complementary power generation system.* Applied Energy, vol. 242, pages 1155–1163, 2019. (Cited on pages 1 and 45.)

[Susan-Resiga *et al.* 2011] R.F. Susan-Resiga, S. Muntean, F. Avellan and I. Anton. *Mathematical modelling of swirling flow in hydraulic turbines for the full operating range.* Applied Mathematical Modelling, vol. 35, no. 10, pages 4759–4773, 2011. http://dx.doi.org/10.1016/j.apm.2011.03.052. (Cited on page 213.)

[Tahani *et al.* 2020] Mojtaba Tahani, Ali Kandi, Mahdi Moghimi and Shahram Derakhshan Houreh. *Rotational speed variation assessment of centrifugal pump-as-turbine as an energy utilization device under water distribution network condition.* Energy, vol. 213, page 118502, 2020. (Cited on page 184.)

[Tam & Clinch 1979] Shiu W. Tam and J.M. Clinch. *Study of certain economic aspects of turbomachinery for underground pumped hydroelectric storage plants.* Technical report, Argonne National Lab., IL (USA), 1979. (Cited on page 70.)

[Tan *et al.* 2014] Lei Tan, Baoshan Zhu, Shuliang Cao, Yuchuan Wang and Binbin Wang. *Influence of prewhirl regulation by inlet guide vanes on cavitation performance of a centrifugal pump.* Energies, vol. 7, no. 2, pages 1050–1065, 2014. https://doi.org/10.3390/en7021050. (Cited on page 213.)

[Tan *et al.* 2017] P. Tan, H. R. Jiang, X. B. Zhu, L. An, C. Y. Jung, M. C. Wu, L. Shi, W. Shyy and T. S. Zhao. *Advances and challenges in lithium-air batteries.* Applied Energy, 2017. http://dx.doi.org/10.1016/j.apenergy.2017.07.054. (Cited on page 118.)

[Tao *et al.* 2019] Yi Tao, Shouqi Yuan, Jianrui Liu and Fan Zhang. *Influence of cross-sectional flow area of annular volute casing on transient characteristics of ceramic centrifugal pump.* Chinese Journal of Mechanical Engineering, vol. 32, no. 1, page 4, 2019. (Cited on page 177.)

[Teuteberg 2010] B.H. Teuteberg. *Design of a Pump-As-Turbine Microhydro System for an Abalone Farm.* M.Engineering, 2010. (Cited on page 38.)

[Thépot *et al.* 1999] R Thépot, J Clérin, C Sudour and JP Taulan. *Naussac 2: mise en œuvre des pompes turbines Deriaz.* La Houille Blanche, no. 3-4, pages 41–45, 1999. (Cited on pages 72 and 74.)

[Thoma & Kittredge 1931] D. Thoma and C.P. Kittredge. *Centrifugal pumps operated under abnormal conditions.* Power, vol. 73, pages 881–884, 1931. (Cited on page 34.)

[Trianni *et al.* 2016] Andrea Trianni, Enrico Cagno and Stefano Farné. *Barriers, drivers and decision-making process for industrial energy efficiency: A broad study among manufacturing small and medium-sized enterprises.* Applied Energy, vol. 162, pages 1537–1551, 2016. (Cited on page 123.)

[Truong *et al.* 1988] Q. M. Truong, Y. Bouvet and C. Periolat. *Ultra high head units for France's Super Bissorte pumped-storage plant.* International Water Power and Dam Construction, vol. 40, no. 11, pages 11–15, 1988. (Cited on page 71.)

[Tu & Mayne 2002] W Tu and RW Mayne. *Studies of multi-start clustering for global optimization.* International journal for numerical methods in engineering, vol. 53, no. 9, pages 2239–2252, 2002. (Cited on pages 159 and 171.)

[Turton 2012] Robert Keith Turton. Principles of turbomachinery. Springer Science & Business Media, 2012. (Cited on page 87.)

[U. Tsuneo et al. 1964] U. Tsuneo et al. *DERIAZ TYPE PUMP-TURBINE FOR KUROMATAGAWA No. 2 POWER STATION, ELECTRIC POWER DEVELOPMENT CO. LTD.* FUJI ELECTRIC REVIEW, vol. 10, no. 1, 1964. (Cited on page 26.)

[US Army Corps of Engineers 1981] US Army Corps of Engineers. *An Assessment of Hydroelectric Pumped Storage*. Technical report, National hydroelectric power resources study. The U.S. Army Engineer Institute for water resources, 1981. (Cited on page 13.)

[Vagnoni *et al.* 2018] E. Vagnoni, L. Andolfatto, S. Richard, C. Münch-Alligné and F. Avellan. *Hydraulic performance evaluation of a micro-turbine with counter rotating runners by experimental investigation and numerical simulation*. Renewable Energy, vol. 126, pages 943–953, 2018. http://dx.doi.org/10.1016/j.renene.2018.04.015. (Cited on page 9.)

[Valentín *et al.* 2017] David Valentín, Alexandre Presas, Eduard Egusquiza, Carme Valero, Mònica Egusquiza and Matias Bossio. *Power swing generated in Francis turbines by part load and overload instabilities*. Energies, 2017. (Cited on page 65.)

[Vallés *et al.* 2016] Mercedes Vallés, Javier Reneses, Rafael Cossent and Pablo Frías. *Regulatory and market barriers to the realization of demand response in electricity distribution networks: A European perspective*. Electric Power Systems Research, 2016. (Cited on page 53.)

[Vanbellingen *et al.* 1982] R. Vanbellingen, A. Lejeune, J. Marchal, M. Poels and M. Salhoul. *Vibration of screen at La Plate Taille hydro storage power station in Belgium.* In Proceedings of the Congress of International Association for Hydraulic Research, 1982. (Cited on page 54.)

[Versteeg & Malalasekera 2007] Henk Kaarle Versteeg and Weeratunge Malalasekera. An introduction to computational fluid dynamics: the finite volume method. Pearson Education, 2007. (Cited on pages 77 and 78.)

[von Backström 2005] Theodor W. von Backström. *A Unified Correlation for Slip Factor in Centrifugal Impellers*. Journal of Turbomachinery, 2005. (Cited on page 215.)

[Wang *et al.* 2017] Tao Wang, Chuan Wang, Fanyu Kong, Qiuqin Gou and Sunsheng Yang. *Theoretical, experimental, and numerical study of special impeller used in turbine mode of centrifugal pump as turbine*. Energy, 2017. (Cited on pages 39 and 152.)

[Wiesner 1967] FJ Wiesner. *A review of slip factors for centrifugal impellers*. Journal of Engineering for power, vol. 89, no. 4, pages 558–566, 1967. (Cited on pages 214 and 215.)

[Williams 1994a] A. A. Williams. *The Turbine Performance of Centrifugal Pumps: A Comparison of Prediction Methods*, 1994. (Cited on pages 19 and 38.)

[Williams 1994b] AA Williams. *The turbine performance of centrifugal pumps: a comparison of prediction methods*. Proceedings of the Institution of Mechanical Engineers, Part A: Journal of Power and Energy, vol. 208, no. 1, pages 59–66, 1994. (Cited on pages 36 and 92.)

[Witt *et al.* 2016] Adam Witt, Dol Raj Chalise, Boualem Hadjerioua, Michael Manwaring and Norm Bishop. *Development and Implications of a Predictive Cost Methodology for Modular Pumped Storage Hydropower (m-PSH) Projects in the United States*, 2016. (Cited on page 93.)

[Wong 1996] I. H. Wong. *An underground pumped storage scheme in the Bukit Timah granite of Singapore*. Tunnelling and Underground Space Technology, vol. 11, no. 4, pages 485–489, 1996. (Cited on page 13.)

[Worrell *et al.* 2003] Ernst Worrell, John A. Laitner, Michael Ruth and Hodayah Finman. *Productivity benefits of industrial energy efficiency measures*. Energy, 2003. (Cited on page 53.)

[Wu *et al.* 2007] Jingchun Wu, Katsumasa Shimmei, Kiyohito Tani, Kazuo Niikura and Joushirou Sato. *CFD-based design optimization for hydro turbines*. Journal of Fluids Engineering, Transactions of the ASME, vol. 129, no. 2, pages 159–168, 2007. (Cited on page 77.)

[Wu *et al.* 2012] Yulin Wu, Shuhong Liu, Hua Shu Dou, Shangfeng Wu and Tiejun Chen. *Numerical prediction and similarity study of pressure fluctuation in a prototype Kaplan turbine and the model turbine*. Computers and Fluids, 2012. http://dx.doi.org/10.1016/j.compfluid.2011.12.005. (Cited on page 77.)

[Xu *et al.* 2019] Beibei Xu, Diyi Chen, M. Venkateshkumar, Yu Xiao, Yan Yue, Yanqiu Xing and Peiquan Li. *Modeling a pumped storage hydropower integrated to a hybrid power system with solar-wind power and its stability analysis.* Applied Energy, vol. 248, pages 446–462, 2019. (Cited on pages 1 and 47.)

[Yang & Jackson 2011] Chi Jen Yang and Robert B. Jackson. *Opportunities and barriers to pumped-hydro energy storage in the United States.* Renewable and Sustainable Energy Reviews, 2011. (Cited on page 202.)

[Yang & Yang 2019] Weijia Yang and Jiandong Yang. *Advantage of variable-speed pumped storage plants for mitigating wind power variations: Integrated modelling and performance assessment.* Applied Energy, vol. 237, pages 720–732, 2019. http://dx.doi.org/10.1016/j.apenergy.2016.06.097. (Cited on page 93.)

[Yang *et al.* 2012a] Sun Sheng Yang, Shahram Derakhshan and Fan Yu Kong. *Theoretical, numerical and experimental prediction of pump as turbine performance.* Renewable Energy, vol. 48, pages 507–513, 2012. http://dx.doi.org/10.1016/j.renene.2012.06.002. (Cited on pages 35, 36 and 38.)

[Yang *et al.* 2012b] Sun Sheng Yang, Fan Yu Kong, Hao Chen and Xiang Hui Su. *Effects of blade wrap angle influencing a pump as turbine.* Journal of Fluids Engineering, Transactions of the ASME, 2012. (Cited on pages 40 and 146.)

[Yang *et al.* 2012c] Sun Sheng Yang, Fan Yu Kong, Wan Ming Jiang and Xiao Yun Qu. *Effects of impeller trimming influencing pump as turbine.* Computers and Fluids, 2012. (Cited on page 40.)

[Yang *et al.* 2013] Sun Sheng Yang, Hou Lin Liu, Fan Yu Kong, Cui Dai and Liang Dong. *Experimental, numerical, and theoretical research on impeller diameter influencing centrifugal pump-as-turbine.* Journal of Energy Engineering, 2013. (Cited on page 40.)

[Yang *et al.* 2014a] Sun Sheng Yang, Hou Lin Liu, Fan Yu Kong, Bin Xia and Lin Wei Tan. *Effects of the radial gap between impeller tips and volute tongue influencing the performance and pressure pulsations of pump as turbine.* Journal of Fluids Engineering, Transactions of the ASME, 2014. (Cited on pages 40, 146 and 160.)

[Yang *et al.* 2014b] Sun Sheng Yang, Chao Wang, Kai Chen and Xin Yuan. *Research on blade thickness influencing pump as turbine.* Advances in Mechanical Engineering, 2014. (Cited on page 40.)

[Yang 1983] CS Yang. *Performance of the vertical turbine pumps as hydraulic turbines.* Proceedings of Performance Characteristics of Hydraulic Turbines and Pumps, 1983. (Cited on page 102.)

[Ye *et al.* 2020] Jiawei Ye, Wei Zeng, Zhigao Zhao, Jiebin Yang and Jiandong Yang. *Optimization of pump turbine closing operation to minimizewater hammer and pulsating pressures during load rejection.* Energies, vol. 13, no. 4, 2020. (Cited on page 67.)

[Yekini Suberu *et al.* 2014] Mohammed Yekini Suberu, Mohd Wazir Mustafa and Nouruddeen Bashir. *Energy storage systems for renewable energy power sector integration and mitigation of intermittency.* Renewable and Sustainable Energy Reviews, 2014. http://dx.doi.org/10.1016/j.rser.2014.04.009. (Cited on page 42.)

[Yüksel 2010] Ibrahim Yüksel. *Hydropower for sustainable water and energy development.* Renewable and Sustainable Energy Reviews, 2010. (Cited on page 9.)

[Zavadil & Meduna 1981a] M Zavadil and M Meduna. Essais sur le modele reduit. GEC. ALSTOM Neyrpic, Hampton, Virginia, 1981. (Cited on pages 76, 81 and 83.)

[Zavadil & Meduna 1981b] M Zavadil and M Meduna. Performances en turbine. GEC. ALSTOM Neyrpic, Hampton, Virginia, 1981. (Cited on pages 76 and 83.)

[Zavadil & Meduna 1981c] M Zavadil and M Meduna. Performances en turbine model test. GEC. ALSTOM Neyrpic, Hampton, Virginia, 1981. (Cited on page 83.)

[Zeng *et al.* 2018] Chongji Zeng, Yexiang Xiao, Yongyao Luo, Jin Zhang, Zhengwei Wang, Honggang Fan and Soo Hwang Ahn. *Hydraulic performance prediction of a prototype four-nozzle Pelton turbine by entire flow path simulation.* Renewable Energy, vol. 125, pages 270–282, 2018. http://dx.doi.org/10.1016/j.renene.2018.02.075. (Cited on page 9.)

[Zhang *et al.* 2015] Sufang Zhang, Philip Andrews-Speed and Pradeep Perera. *The evolving policy regime for pumped storage hydroelectricity in China: A key support for low-carbon energy.* Applied Energy, vol. 150, no. Supplement C, pages 15 – 24, 2015. https://doi.org/10.1016/j.apenergy.2015.03.103. (Cited on page 29.)

[Zhang *et al.* 2019] Yusheng Zhang, Chao Ma, Jijian Lian, Xiulan Pang, Yanan Qiao and Evance Chaima. *Optimal photovoltaic capacity of large-scale hydro-photovoltaic complementary systems considering electricity delivery demand and reservoir characteristics.* Energy Conversion and Management, vol. 195, pages 597–608, 2019. (Cited on page 1.)

[Židonis & Aggidis 2015] Audrius Židonis and George A. Aggidis. *State of the art in numerical modelling of Pelton turbines.* Renewable and Sustainable Energy Reviews, vol. 45, pages 135–144, 2015. (Cited on page 20.)

[Zillmann & Perau 2015] A. Zillmann and E. Perau. *A conceptual analysis for an underground pumped storage plant in rock mass of the Ruhr region.* In Geotechnical Engineering for Infrastructure and Development - Proceedings of the XVI European Conference on Soil Mechanics and Geotechnical Engineering, ECSMGE 2015, volume 7, pages 3789–3794, 2015. (Cited on page 13.)